



UNIVERSITAT DE  
BARCELONA

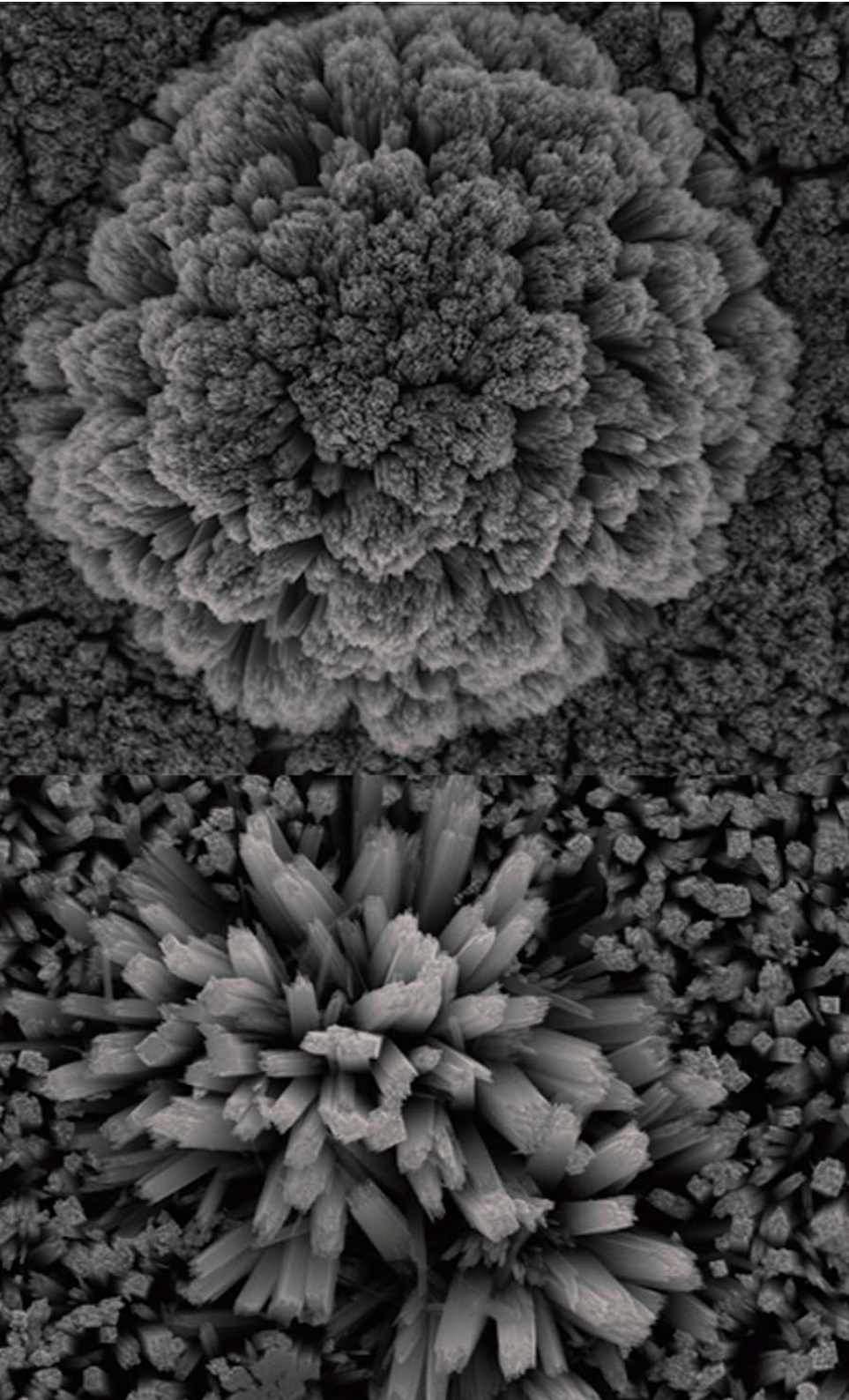
# Towards Artificial Photosynthesis: Photoelectrochemical CO<sub>2</sub> Reduction to Solar Fuels

Andrés Parra Puerto

**ADVERTIMENT.** La consulta d'aquesta tesi queda condicionada a l'acceptació de les següents condicions d'ús: La difusió d'aquesta tesi per mitjà del servei TDX ([www.tdx.cat](http://www.tdx.cat)) i a través del Dipòsit Digital de la UB ([diposit.ub.edu](http://diposit.ub.edu)) ha estat autoritzada pels titulars dels drets de propietat intel·lectual únicament per a usos privats emmarcats en activitats d'investigació i docència. No s'autoritza la seva reproducció amb finalitats de lucre ni la seva difusió i posada a disposició des d'un lloc aliè al servei TDX ni al Dipòsit Digital de la UB. No s'autoritza la presentació del seu contingut en una finestra o marc aliè a TDX o al Dipòsit Digital de la UB (framing). Aquesta reserva de drets afecta tant al resum de presentació de la tesi com als seus continguts. En la utilització o cita de parts de la tesi és obligat indicar el nom de la persona autora.

**ADVERTENCIA.** La consulta de esta tesis queda condicionada a la aceptación de las siguientes condiciones de uso: La difusión de esta tesis por medio del servicio TDR ([www.tdx.cat](http://www.tdx.cat)) y a través del Repositorio Digital de la UB ([diposit.ub.edu](http://diposit.ub.edu)) ha sido autorizada por los titulares de los derechos de propiedad intelectual únicamente para usos privados enmarcados en actividades de investigación y docencia. No se autoriza su reproducción con finalidades de lucro ni su difusión y puesta a disposición desde un sitio ajeno al servicio TDR o al Repositorio Digital de la UB. No se autoriza la presentación de su contenido en una ventana o marco ajeno a TDR o al Repositorio Digital de la UB (framing). Esta reserva de derechos afecta tanto al resumen de presentación de la tesis como a sus contenidos. En la utilización o cita de partes de la tesis es obligado indicar el nombre de la persona autora.

**WARNING.** On having consulted this thesis you're accepting the following use conditions: Spreading this thesis by the TDX ([www.tdx.cat](http://www.tdx.cat)) service and by the UB Digital Repository ([diposit.ub.edu](http://diposit.ub.edu)) has been authorized by the titular of the intellectual property rights only for private uses placed in investigation and teaching activities. Reproduction with lucrative aims is not authorized nor its spreading and availability from a site foreign to the TDX service or to the UB Digital Repository. Introducing its content in a window or frame foreign to the TDX service or to the UB Digital Repository is not authorized (framing). Those rights affect to the presentation summary of the thesis as well as to its contents. In the using or citation of parts of the thesis it's obliged to indicate the name of the author.



2015

PhD Thesis

Andrés Parra Puerto

# Towards Artificial Photosynthesis: Photoelectrochemical CO<sub>2</sub> Reduction to Solar Fuels

Andrés Parra Puerto





UNIVERSITAT DE  
BARCELONA



Thesis submitted to apply for the degree of Doctor, in the *Molecular Inorganic Chemistry* Program of the University of Barcelona.  
Departament de Química Inorgànica, Facultat de Química

*Towards Artificial Photosynthesis:  
Photoelectrochemical CO<sub>2</sub> Reduction to Solar Fuels*

**Andrés Parra Puerto**

Supervisors:

**Dra. Teresa Andreu Arbella**

Institut de Recerca en Energia de Catalunya  
Departament de Ciència dels Materials i Enginyeria Metal·lúrgica,  
Universitat de Barcelona

**Prof. Dr. Joan Ramon Morante Lleonart**

Institut de Recerca en Energia de Catalunya  
Departament d'Electrònica, Universitat de Barcelona

Tutor: **Prof. Dr. Narcís Homs Martí**

Institut de Recerca en Energia de Catalunya  
Departament de Química Inorgànica de la Universitat de Barcelona

September 2015



La Dra. Teresa Andreu Arbella, investigadora del Institut de Recerca en Energia de Catalunya (IREC) y profesora asociada del Departamento de Materiales e Ingeniería Metalúrgica de la Universidad de Barcelona,

El Prof. Dr. Joan Ramon Morante Leonart, investigador de Institut de Recerca en Energia de Catalunya (IREC) y Catedrático del Departamento de Electrónica de la Universidad de Barcelona,

CERTIFICAN:

Que la memoria titulada **Towards Artificial Photosynthesis: Photoelectrochemical CO<sub>2</sub> Reduction to Solar Fuels**, presentada por Andrés Parra Puerto para optar al grado de Doctor en el Programa de Química Inorgánica Molecular de la Universidad de Barcelona ha sido realizada bajo su dirección en el Institut de Recerca en Energia de Catalunya (IREC).

Barcelona, Septiembre de 2015

Dra. Teresa Andreu Arbella

Prof. Dr. Joan Ramon Morante Leonart



El Prof. Dr. Narcís Homs Martí, investigador de Institut de Recerca en Energia de Catalunya (IREC) y Catedrático del Departamento de Química Inorgánica de la Universidad de Barcelona,

CERTIFICA: que ha sido el tutor responsable de los estudios de Doctorado realizados dentro del programa de Doctorado de Química Inorgánica Molecular por Andrés Parra Puerto.

Barcelona, Septiembre de 2015.

Prof. Dr. Narcís Homs Martí



*“Life is not complex.  
We are complex.  
Life is simple,  
and the simple thing is the right thing.”*

*“La vida no es complicada.  
Nosotros somos complicados.  
La vida es simple,  
y lo simple es lo correcto”*

*Oscar Wilde*



# Abstract

Greenhouse-gas emissions from the energy sector represent roughly two-thirds of all anthropogenic greenhouse-gas emissions and CO<sub>2</sub> emissions from the sector have risen over the past century to ever higher levels. Effective action in the energy sector is, consequently, essential to tackling the climate change problem.

This thesis is devoted to prove the concept of the CO<sub>2</sub> reduction to CH<sub>4</sub> with a decreasing in the voltage requirements using a photocatalytic mechanism. Subsequently, part of the solar energy is transferred to the reaction, obtaining an improvement in the total energy balance. The work developed intends first, to take advantage of the know features of the photoactive nanostructured materials obtained by anodization and hydrothermal synthesis (allowing to obtain better surface areas and improving the photon collection, light photosynthetic reactions). Second investigate the copper and copper oxide cathodes for the CO<sub>2</sub> electroreduction activity to CH<sub>4</sub> (dark photosynthetic reactions) using a complete cell to understand the parameters involved in the process and the products selectivity for each cathodes. And third the implementation of the photoanode and cathode in a photoelectrochemical complete cell.



# Acknowledgments

Bueno pues este viaje parece llegar a su fin aunque tiene sus baches por el camino al final se llega y cuando se llega seguramente más adelante, ahora seguramente no que tanto bache te deja mareado, se recordará esta época con mucha nostalgia y buenos momentos siendo una de las mejores épocas vividas ya que enseña mucho y más viniendo de la Alcarria hasta Barcelona para pasarla aquí. Pero que sea una buena época viene de la gente que ha pasado por tu vida en esta temporada (que no es poca 4 añazos madre, que al final se pasa más rápido de lo que uno se piensa). Por ello es mi turno el agradecer a toda esta gente que ha hecho que esta sea una gran experiencia hasta llegar aquí.

En primer lugar agradecer a mis directores de tesis por haberme elegido para poder realizarla y por el apoyo que han ido dándome a lo largo de la misma. Teresa Andreu muchas gracias por la dirección para la realización de este trabajo y la paciencia en algunos casos debido a mi carácter “disperso”. A Joan Ramon Morante, por las explicaciones económicas en el ámbito de la ciencia que no se tienen muy en cuenta pero son cosas bastante importantes además del aporte que ha dado a este trabajo bajo su dirección. A Narcís Homs por apadrinarme en el departamento de química inorgánica de la Universidad de Barcelona y por el trabajo de tutor que ha realizado.

La andadura que comencé por 2011 en este laboratorio con los pocos miembros que había, los postdoc que estaban Marcel, Cristina y Javi, con los primeros que fui a tomar unas cervezas, las

cuales agradecí mucho. Con ellos he pasado grandes momentos en esta época, con Marcel el que es uno de mis referentes de aprendizaje de catalán, su gran habilidad para poner motes como su carácter característico pero muy divertido. A Cristina una compadre de Castilla la Manca a la cual tengo mucho cariño por su apoyo, cariño y por su puesto grandes momentos de cervezas. Y Javi como no, al cual a lo largo del tiempo que hemos estado juntos hemos tenido muchos grandes momentos divertidos y un poco locos (y los que quedan) pero el cual he compartido mucho considerándolo como un hermano. Por supuesto a Cristian que le pille en la época de escritura pero luego ha sido un gran apoyo tanto científico como personal. A Marta, la compañera con la que empecé a tratar gracias a juego de tronos y la primera boda por aquí, pero que al final se ha convertido en una gran amiga como compañera (a parte de mi otra referencia del catalán) a la cual quiero mucho, ya que es como mi hermana mayor y gracias por presentarme a Nacho (su marido) con el cual hemos congeniado muy bien a pesar de vernos menos. Edgar aunque fue corto pero fue una muy buena influencia por su práctica manera de pensar y su grato conocimiento. A Damián por supuesto, por sus muy buenas lecciones en las vitrinas de laboratorio como su personalidad. Por supuesto al turco del lab, Erdem por su gran amistad y ayuda en estos últimos años ya que hemos compartido bastantes cosillas y como no a la adquisición más reciente de Sevilla, Javi (Mr. Hyde) que aunque al principio era más reacio se ha convertido en un gran amigo.

Por supuesto a todos los compañeros de IREC que me han ayudado t he conocido a lo largo de estos años, Albert, Elisabeth que aunque no son de la parte científica me han ayudado mucho y

dejan un buen recuerdo. Doris, María, Silvia las chicas de Cabot a las cuales tengo mucho cariño. Raquel por la ayuda que me ha dado siempre, Alex Carreté que empezó también conmigo. A Diouldé por el apoyo que siempre ha tenido conmigo. A todo el laboratorio de nanoiónica Dolors, Saranya, Bibiana, Albert, Alex, Mark y de las últimas adquisiciones pero no menos importante Elba por la simpatía y buen rollo que siempre tiene, pero especialmente a Laura aunque ya no esté en el lab pero la cual ha sido una grandísima amiga y la cual me acogió como uno más cuando vine a Barcelona, y gracias a ella conocí a Viti, Kike, Dodi, Delfi, Ana, Xavi, Paola con los cuales he pasado grandes momentos. Por supuesto a Eleonora, nuestra catadora de cerveza por esas búsquedas de bares con picho gratis por Barcelona, y a toda la gente del departamento de electrónica de la UB que he conocido estos años.

Por supuesto a los compañeros que he conocido en esgrima, con los cuales he aprendido bastante y he conocido muy buena gente, en especial a Lluís por esas cervezas y buenos momentos como a la Dra. Bea (su señora) por acogerme tan bien.

Aunque este en otro grupo y haya pasado todo el doctorado en la UB, Alberto, el otro componente junto a Javi del círculo de confianza con el cual he recorrido todo este camino y con el cual hemos tenido muy buenos momentos (esos jueves tontos de subirse a muros), vacaciones por la costa brava (con sus momentos de tensión), la buena acogida por parte suya y de su familia (buena gente coño) como el apoyo muto en la escritura ya que terminaremos a la vez. Y por su puesto a la gente que he conocido gracias a él, Andrés, Miriam, Marta, Lucaz, Raúl, etc.

A todos mis amigos de Guadalajara, especialmente Natalia con la cual por desgracia veo poco pero es una gran persona y amiga a la cual quiero mucho. Por supuesto a Álvaro y Jose David (nene) con los cuales he pasado prácticamente toda la vida y con los que siempre he podido contar aunque estemos lejos y nos veamos poco, aunque fugaz en algún caso o alguna semana cada año han venido a verme a Barcelona. También a Lidia, una persona muy querida para mí, que conocerla en un viaje de “locura” as su Bierzo querido ha sido muy positivo, por toda la ayuda, apoyo moral, los buenos consejos, los buenos momentos y sobretodo que gracias a ella he podido desconectar de todo un poco haciéndolo todo más llevadero y volviendo con más energía a la carga y como no por aguantarme en el periodo de tesis.

Y por supuesto a toda mi familia por el apoyo que siempre he recibido por parte de toda ella, especialmente a mi abuela que siempre se ha interesado mucho por “el catalán”. Y por supuesto a mi cuñada y mis padres los cuales me han apoyado en todo lo que hecho y les quiero mucho y como no a mi hermano al cual tengo como una referencia y quiero mucho, que siempre está ahí para darme la colleja o para ayudarme en todo lo que puede,

Muchas Gracias.

Barcelona 23 de Septiembre de 2015

# Index

1.	Introduction.....	3
1.1	Frame of the Thesis .....	3
1.2	The Photosynthesis.....	22
1.3	CO <sub>2</sub> Photoreduction for Solar Fuels Generation.....	28
1.4	Photoanode for Solar Water Splitting (Light Reaction) ..	34
1.5	CO <sub>2</sub> Electroreduction (Dark Reaction) .....	41
1.6	Scope of the Research.....	49
1.7	References .....	51
2.	Experimental Methods .....	57
2.1	Chapter Overview.....	57
2.2	TiO <sub>2</sub> Synthesis Methods.....	57
2.2.1	<i>Anodization</i> .....	57
2.2.2	<i>Hydrothermal</i> .....	59
2.3	Photoelectrochemical and Electrochemical Measurements (PEC/EC).....	61
2.3.1	<i>Photoelectrochemical Setup (PEC)</i> .....	62
2.3.2	<i>Electrochemical Setup (EC)</i> .....	66
2.3.3	<i>Electrodes Conditioning</i> .....	69
2.4	References .....	73
3.	Light Reaction: Photoanodes for Water Splitting .....	77
3.1	Chapter Overview.....	77
3.2	Titanium Dioxide Nanotubes, TiNTs.....	78
3.2.1	<i>Hierarchical TiNTs Synthesis by Anodization</i> .....	83

3.2.2	<i>Structural and Morphological Characterization</i> .....	86
3.2.3	<i>Optical Characterization and PEC Measurements</i> ...	95
3.3	<b>Titanium Dioxide Nanorods</b> .....	103
3.3.1	<b><i>TiO<sub>2</sub> Nanorods Hydrothermal Synthesis Optimization</i></b> .....	105
3.3.1.1	<i>Effect of Titanium Precursor Concentration</i> .....	108
3.3.1.2	<i>Chlorine Concentration Effect</i> .....	113
3.3.2	<b><i>TiO<sub>2</sub> Nanorods Doping</i></b> .....	121
3.3.2.1	<i>Tin Doping</i> .....	121
3.3.2.2	<i>Vanadium Doping</i> .....	123
3.3.2.3	<i>Nitrogen Doping</i> .....	140
3.4	<b>Conclusions</b> .....	149
3.5	<b>References</b> .....	155
4.	<b>Dark Reaction: CO<sub>2</sub> Electroreduction with Cu-Based Electrodes</b> .....	161
4.1	<b>Chapter Overview</b> .....	161
4.2	<b>Copper Based Electrodes as Catalyst</b> .....	162
4.2.1	<b><i>Cu Mesh as Gas Diffusion Electrode (GDE) and Copper Foil Electrode for CO<sub>2</sub> Reduction</i></b> .....	162
4.2.1.1	<i>Electrocatalytic Reduction of CO<sub>2</sub> in KHCO<sub>3</sub> and NaHCO<sub>3</sub> over a Copper Surface</i> .....	167
4.2.1.2	<i>Electrolyte Concentration Effect and Cu foil experiment</i> .....	175
4.2.2	<b><i>Cu<sub>x</sub>O Mesh as Gas Diffusion Electrode</i></b> .....	179
4.2.2.1	<i>Electrocatalytic reduction of CO<sub>2</sub> in KHCO<sub>3</sub> and NaHCO<sub>3</sub> over a Copper Oxide (Cu<sub>x</sub>O) surface</i> .....	182

4.2.2.2	<i>Electrochemical evolution of the Cu<sub>x</sub>O layers in the CO<sub>2</sub> reduction.</i>	192
4.3	<b>CO<sub>2</sub> Pre-Humidification Effect</b>	201
4.4	<b>Conclusions</b>	207
4.5	<b>References</b>	209
5.	<b>Photoelectrochemical (PEC) Cell Assembling</b>	215
5.1	<b>Evaluation of Photoanodes</b>	215
5.2	<b>Evaluation of Cathodes</b>	219
5.3	<b>Evaluation of the Overall Process</b>	222
6.	<b>Conclusions</b>	229
	<b>Annexes</b>	237
A.	<b>Electrochemical Reduction of Supercritical CO<sub>2</sub> in Ionic Liquids</b>	237
B.	<b>Characterization and Analysis Techniques</b>	241
B.1.	<b>Gas Chromatography (GC)</b>	241
B.2.	<b>Scanning Electronic Microscopy (SEM)</b>	245
B.3.	<b>Atomic Force Spectroscopy (AFM)</b>	246
B.4.	<b>X – Ray Diffraction (XRD)</b>	247
B.5.	<b>Thermal Treatments</b>	249
B.6.	<b>Diffuse Reflectance Ultraviolet – Visible Spectroscopy (UV – Vis)</b>	251
C.	<b>Calculations</b>	253
C.1.	<b>Mott – Schottky plots</b>	253
C.2.	<b>Electrochemical Standard Potential and Gibbs Energy (<math>\Delta Gf^\circ</math>)</b>	259
	<b>References</b>	265

D.	Resumen de la Tesis.....	267
D.1.	Introducción.....	267
D.1.1.	<i>Producción de Combustibles Solares Mediante Fotorreducción de CO<sub>2</sub></i> .....	269
D.1.2.	<i>Fotoánodos para la Ruptura del Agua Mediante Energía Solar (Reacción Luminosa)</i> .....	271
D.1.3.	<i>Electrorreducción de CO<sub>2</sub> (Reacción Oscura)</i> .....	272
D.1.4.	<i>Objetivos de la Tesis</i> .....	273
D.2.	Reacción Luminosa: Fotoánodos para la Ruptura de Agua.....	273
D.2.1.	<i>Nanotubos de Óxido de Titanio, TiNTs</i> .....	273
D.2.2.	<i>Nanohilos de Óxido de Titanio</i> .....	276
D.2.3.	<i>Dopaje de Nanohilos</i> .....	279
D.3.	Reacción Oscura: Electrorreducción de CO <sub>2</sub> con Electrodo Basados en Cobre .....	284
D.4.	Ensamblado de la Celda PEC.....	288
D.5.	Conclusiones.....	290
D.6.	Bibliografía .....	298

# Chapter I

## Introduction

<b>1.</b>	<b>Introduction.....</b>	<b>3</b>
<b>1.1</b>	<b>Frame of the Thesis .....</b>	<b>3</b>
<b>1.2</b>	<b>The Photosynthesis.....</b>	<b>22</b>
<b>1.3</b>	<b>CO<sub>2</sub> Photoreduction for Solar Fuels Generation.....</b>	<b>28</b>
<b>1.4</b>	<b>Photoanode for Solar Water Splitting (Light Reaction) ..</b>	<b>34</b>
<b>1.5</b>	<b>CO<sub>2</sub> Electroreduction (Dark Reaction) .....</b>	<b>41</b>
<b>1.6</b>	<b>Scope of the Research.....</b>	<b>49</b>
<b>1.7</b>	<b>Reference .....</b>	<b>51</b>

# **1. Introduction**

## **1.1 Frame of the Thesis**

The world is at a critical juncture in its efforts to combat climate change. Since the first Conference of the Parties (COP) in 1995, greenhouse-gas (GHG) emissions have risen by more than one-quarter and the atmospheric concentration of these gases has increased steadily to 435 parts per million carbon dioxide equivalent (ppm CO<sub>2</sub>-eq) in 2012 [1]. The International Panel on Climate Change (IPCC) has concluded that, in the absence of fully committed and urgent action, climate change will have severe and irreversible impacts across the world. The international commitment to keep the increase in long-term average temperatures to below two degrees Celsius (2°C) relative to pre-industrial levels, will require substantial and sustained reductions in global emissions.

The long lifetime of greenhouse gases means that it is the accumulation in the atmosphere what matters most. In its latest report, the Intergovernmental Panel on Climate Change (IPCC) estimated that to preserve the 50% change of limiting global warming to 2°C, the world can support a maximum carbon dioxide (CO<sub>2</sub>) emissions “budget” of 3000 gigatons (Gt) (the mid-point in a range of 2900 Gt to 3200 Gt) [2], of which an estimated 1970 Gt had been already emitted before 2014. Taking into account CO<sub>2</sub> emissions from industrial processes and land use, land-use change and forestry over the rest of the 21<sup>st</sup> century; the energy sector will

have a carbon budget of 980 Gt (the midpoint in a range of 880 Gt to 1180 Gt) from the start of 2014 onwards (*Figure 1.1*). The carbon legacy that is locked-in by new development of fossil-fuelled energy infrastructure underlines the importance that attaches to success in achieving a step change in efforts to contain GHG emissions in the COP21 meeting to be held in Paris in December 2015.

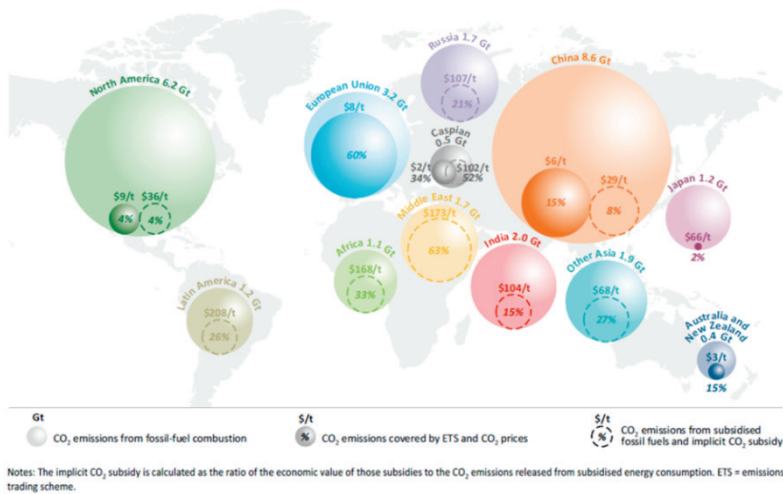
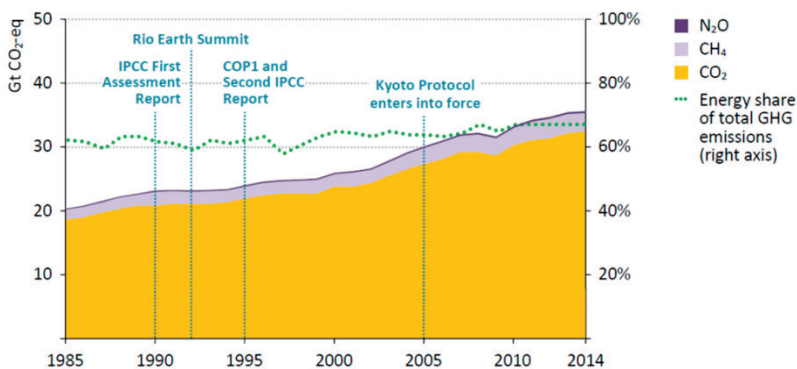


*Figure 1.1. CO<sub>2</sub> emissions of energy sector in selected regions in 2014 [3].*

Greenhouse-gas emissions from the energy sector represent roughly two-thirds of all anthropogenic greenhouse-gas emissions (*Figure 1.2*) and CO<sub>2</sub> emissions from the sector have risen over the past century to ever higher levels. Effective action in the energy sector is, consequently, essential to tackling the climate change problem.

One indicator of the scale of the challenge to the energy sector is the fact that the total volume of global energy sector CO<sub>2</sub> emissions

over the past 27 years matched the total level of all previous years. Fossil fuels continue to meet more than 80% of total primary energy demand and over 90% of energy-related emissions are CO<sub>2</sub> from fossil-fuel combustion. Since 2000, the share of coal has increased from 38% to 44% of energy-related CO<sub>2</sub> emissions, the share of natural gas stayed flat at 20% and that of oil declined from 42% to 35% in 2014. While smaller in magnitude (and less long-lasting in the atmosphere, though with higher global warming potential), methane (CH<sub>4</sub>) and nitrous oxide (N<sub>2</sub>O) are other powerful greenhouse gases emitted by the energy sector. Methane accounts for around 10% of energy sector emissions, which are originated mainly from oil and gas extraction, transformation and distribution. Most of the remaining emissions are nitrous oxide from energy transformation, industry, transport and buildings.



Notes: CO<sub>2</sub> = carbon dioxide, CH<sub>4</sub> = methane, N<sub>2</sub>O = nitrous oxide. CH<sub>4</sub> has a global warming potential of 28 to 30 times that of CO<sub>2</sub>, while the global warming potential of N<sub>2</sub>O is 265 higher than that of CO<sub>2</sub>.

**Figure 1.2.** Global anthropogenic energy - related greenhouse - gas emissions by type [3].

An important change in the energy sector from 2014 to 2015 has been the rapid drop in world oil prices and, to a lesser extent,

natural gas and coal prices. After a prolonged period of high and relatively stable prices, oil dropped from over \$100 (US dollars) per barrel in mid-2014 to below \$50 in early-2015. Natural gas prices also declined, but the pace and extent were dependent on prevailing gas pricing policies and other regional factors: in the United States they fell from \$0.014 per watts-hour (W·h) in mid-2014 to below \$0.01/W·h in early-2015; German import prices moved below \$0.027/W·h from \$0.029/W·h during the summer of 2014, while average Japan liquefied natural gas (LNG) import prices (a weighted average of long-term contracts and spot trading) declined to around \$0.051/W·h from \$0.055/W·h in mid-2014. Coal prices in northwest Europe declined from \$73 per tons in mid-2014 to around \$60/ton at the start of 2015 due to persistent overcapacity in the market. Despite lower fossil-fuel prices, there were no signs of weakening appetite for renewables in 2014: global investment in renewable-based power generation was \$270 billion and positive policy moves have continued in many countries. India has declared an aim to have an installed non-hydro renewable energy capacity of 175 gigawatts (GW) by 2022 (of which solar PV is 100 GW).

Renewable technologies are becoming increasingly cost competitive in a number of countries and circumstances, but public support schemes are still required to facilitate deployment in many others. Renewables-based power generation capacity is estimated to have increased by 128 GW in 2014, of which 37% is wind power, almost one-third solar power and more than a quarter from hydropower (*Figure 1.3*). This amounted to more than 45% of world power generation capacity additions in 2014, consistent with

the general upward trend in recent years. Lower oil prices proved to be a challenge for other forms of renewable energy, including biofuels in transport and renewable heat, as the latter competes directly with natural gas heating (the price of which is still, in many cases, linked to the oil price). While biofuels face challenges arising from lower oil prices, some other developments served to improve their outlook: to counter current bleak prospects for biofuels in Brazil, the government increased the ethanol blending rate from 25% to 27% and that for biodiesel from 5% to 7%, and increased gasoline taxes, while Argentina and Indonesia raised their biofuel mandates.

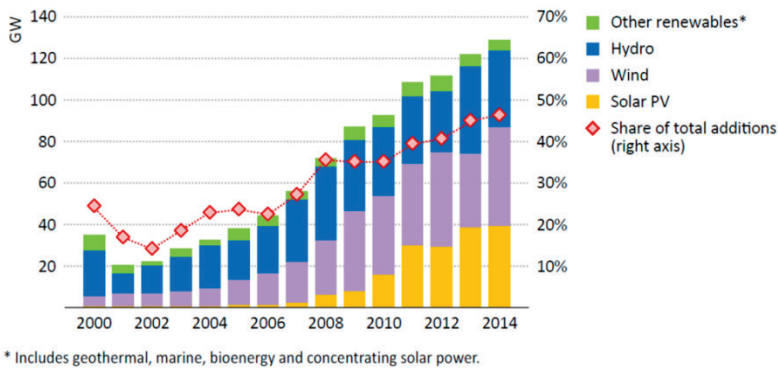
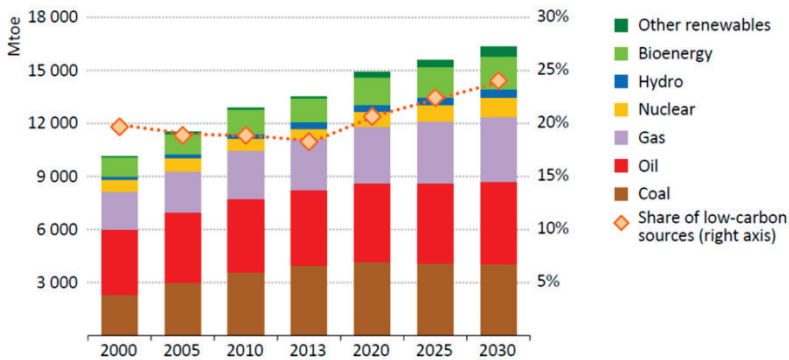


**Figure 1.3.** Global renewables-based power capacity additions by type and share of the total capacity additions [3].

There are three scenarios for the world energy outlook that are covered in the annual report of the IEA (International Energy Agency) [3]:

(a) The first scenario was proposed in the COP20 in Lima, Peru. The countries made an agreement for the communication of

the individual climate contribution, called *Intended Nationally Determined Contributions (INDCs)*. The INDC Scenario represents a preliminary assessment of the implications of the submitted INDCs and statements of intended INDC content for some countries. All INDCs that had been formally submitted to the UNFCCC Secretariat by 14 May 2015 (including Switzerland, European Union, Norway, Mexico, United States, Gabon, Russia, Liechtenstein and Andorra), which collectively represent 34% of global energy-related CO<sub>2</sub> emissions. The transition away from fossil fuels is gradual in the INDC Scenario, with the share of fossil fuels in the world’s primary energy mix declining from more than 80% today to around three-quarters in 2030 (*Figure 1.4*).



Note: "Other renewables" includes wind, solar (photovoltaic and concentrating solar power), geothermal, and marine.

**Figure 1.4.** Global primary energy demand by type in the INDC scenario [3].

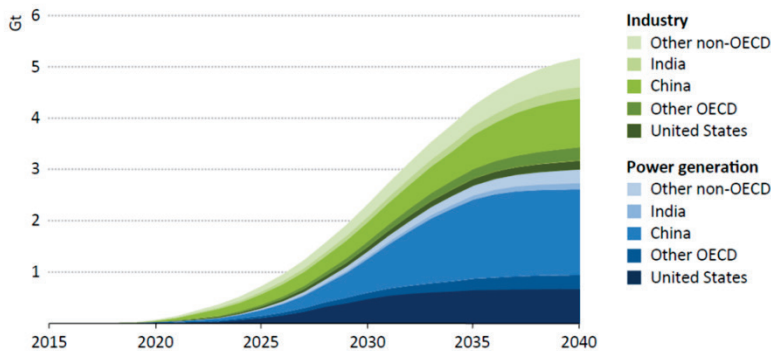
(b) The second scenario is the *Bridge Scenario*. The objective is to facilitate adoption by each country or region individually and using only existing technology of a pragmatic near-term strategy, that is compatible with the same level of development and

economic growth, that underlies the energy sector policies and climate pledges which are reflected in the INDC Scenario. This scenario is not, itself, a pathway to the 2°C target, additional technology and policy needs for such a pathway are set out in the 450 Scenario. However, it indicates a strategy for near-term action as a bridge to higher levels of decarbonisation at a later stage compatible with the 2°C goal.

(c) The *450 Scenario* which takes a different approach. It adopts a specified outcome achievement of the necessary action in the energy sector to serve the internationally adopted goal; to limit the rise in long-term average global temperature (with a likelihood of around 50%) to 2°C and illustrating steps by which that might be achieved.

An important action to decrease the CO<sub>2</sub> in the atmosphere is the Carbon capture and Storage (CCS) which achieved an important milestone in 2014, with Boundary Dam unit 3 (net capacity of 120 megawatts) in Canada becoming the first commercial power plant of CO<sub>2</sub> capture to come online. The 22 large-scale CCS projects either in operation or under construction have a collective CO<sub>2</sub> capture capacity of around 40 million tons (Mt) per year [4]. The present pace of progress, however, falls short of that needed in order to achieve the pace and scale of CCS deployment necessary to achieve a 2°C pathway. Carbon capture and storage, through a suite of technologies, separates and captures CO<sub>2</sub> from power and industrial sources, then transports CO<sub>2</sub> to a suitable site for injection into deep underground formations for permanent storage. CCS makes possible the strong reduction of net CO<sub>2</sub> emissions from

fossil-fuelled power plants and industrial processes, providing a protection strategy for power plants that would otherwise be decommissioned, mothballed or suffer reduced operations in a carbon-constrained world [5,6]. As well as fossil fuels, CCS may also be used in combination with sustainable biomass, resulting in so-called “negative emissions”. In the 450 Scenario, CCS is increasingly adopted from around the mid-2020s, with deployment accelerating in the 2030s and capturing around 5.1 Gt of CO<sub>2</sub> emissions per year by 2040 (*Figure 1.5*), close to 4.9 Gt higher than in the Bridge Scenario. Over the period 2015 to 2040, about 52 Gt of CO<sub>2</sub> emissions are captured.



Note: Industry includes the following sectors: steel, cement (energy- and process-related), chemicals and paper production; oil refining; coal-to-liquids, gas-to-liquids and natural gas processing.

*Figure 1.5. CO<sub>2</sub> captured in the 450 scenario by sector and region [3].*

This involves a massive increase in CCS deployment over the 13 large-scale projects in operation today, which capture a total of about 27 Mt CO<sub>2</sub> per year (though only 5.6 Mt CO<sub>2</sub> at present is being stored with full monitoring and verification). To date, CCS investments have been made in sectors in which costs are relatively

manageable (e.g. natural gas processing or refining) and where the captured CO<sub>2</sub> has a valuable application, such as for enhanced oil recovery. But if instead of CO<sub>2</sub> which is stored, this gas could be transformed to a valuable product will be a good method to recover some part of the investment in CCS technology avoiding the CO<sub>2</sub> storage.

CCS alone is a technology directed to CO<sub>2</sub> abatement, removing carbon from the economy. Another technology to reduce the CO<sub>2</sub> levels is the carbon capture and utilization (CCU). CCU takes CO<sub>2</sub> from point sources and then converts it into commercially valuable products [7]. However, CCU alone cannot realistically remediate all emissions because of the volumes involved and the potential markets for the individual products. Furthermore, due to the energy penalty with CCU, it is likely that the conversion steps will take place at times of low energy demand, when renewable electricity is comparatively cheaper. Other factors that govern the commercial viability of CCU also need to be considered. These include the availability of hydrogen and other feedstocks in the supply chain and a systems approach to integration of resources, energy and land use. The reutilization of the CO<sub>2</sub> can go by three pathways:

(a) *Mineral carbonation*. The concept of storage of CO<sub>2</sub> as calcium and magnesium carbonate minerals is commonly referred to as mineral carbonation (IPCC, 2005). Calcium and magnesium carbonates are poorly soluble in water and are environmentally harmless minerals that could provide a permanent storage solution for CO<sub>2</sub>. Mineral carbonation could be an alternative for long-term

geological storage, especially for regions where CO<sub>2</sub> underground storage is not possible (*Figure 1.6*). In mineral carbonation, (captured) CO<sub>2</sub> is reacted with silicate minerals to form carbonates. As mineral feedstock, rocks that are rich in alkaline earth silicates can be used. Examples are olivine (MgSiO<sub>4</sub>) and wollastonite (CaSiO<sub>3</sub>). These silicates of magnesium and calcium react with CO<sub>2</sub> to form the corresponding carbonates and SiO<sub>2</sub> providing storage on a geological time scale. Carbon dioxide storage by mineral carbonation mimics the naturally occurring rock weathering which is known to have played an important role in the historical reduction of the CO<sub>2</sub> concentration in the atmosphere after the creation of the earth. This “weathering” depends on the initial chemical composition, the characteristics of the minerals and the amount of CO<sub>2</sub> uptake. The natural carbonation reaction is very slow. Therefore, a key challenge for large-scale industrial deployment of CO<sub>2</sub> mineralisation is acceleration of the carbonation process, using heat, pressure, and mechanical and chemical pre-treatment of the mineral. The technology of accelerated carbonation has been used in the treatment of solid wastes in which toxic compounds are stabilized by carbonated materials, so that the treated solid waste material can be utilized in construction. The *advantages* of mineral carbonation for CO<sub>2</sub> storage are:

- I. It is a permanent CO<sub>2</sub> storage system, leak-free fixation with no requirements of long term monitoring.
- II. Very large capacity. The calcium and magnesium carbonate mineral rock deposits on earth are theoretically sufficient to fix all

the CO<sub>2</sub> that could be produced by the combustion of all available fossil fuel reserves [8].

III. The exothermic carbonation chemical reactions indicating that in principle no energy is required for the reactions and theoretically even give useful energy i.e. heat could be produced.

IV. Waste materials like steel converter slag or asbestos can be converted into “valuable” calcium or magnesium carbonates.

V. Finally, it is technically possible to operate the carbonation process directly with flue gases, making the expensive CO<sub>2</sub> capture step superfluous.

But this process generates some *disadvantages*:

I. Large amount of minerals are required to be transported from the mining place to the carbonation plant. Transport distance can be minimized by situating the carbonation plant at the site of the mine.

II. The fixation process of CO<sub>2</sub> requires about 1.6 to 3.7 tonnes of rock, so that more than six times more rock than coal is required to be mined to fix the CO<sub>2</sub> from its combustion.

III. In principle there are no energy requirements for the carbonation process. The overall storage efficiency will be less than 70% due to energy consumption related to mining, transport and pre-processing of the minerals, requiring grinding to around 100 microns.

IV. Extensive mining operations necessary, which will have environmental impact.

V. There is the potential for asbestos to be present in the mineral deposit.

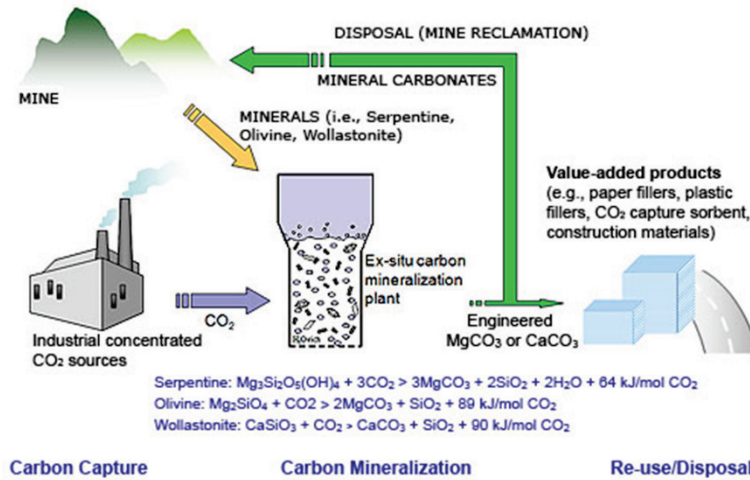
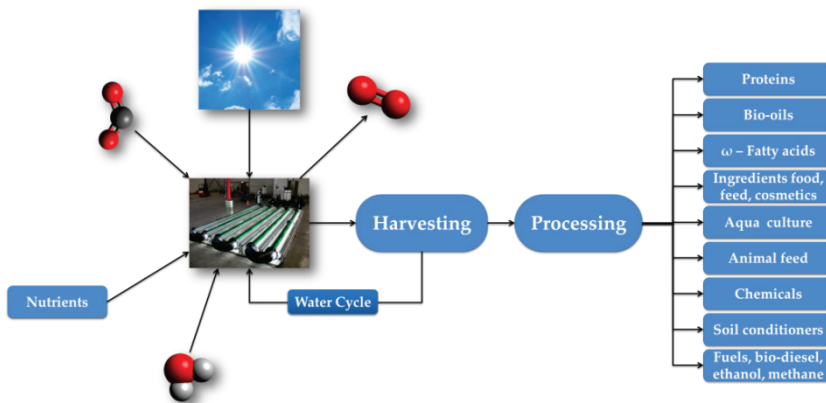


Figure 1.6. Summary of mineral carbonation options [9].

(b) Value-added  $CO_2$  utilization through algae. Biological mitigation of  $CO_2$  relies on photosynthesis by green plants or algae. In this process organic compounds are synthesized from carbon dioxide and water powered by energy derived from sunlight. The resulting biomass can be used for electricity generation or as raw material for production of transportation fuels, bio-based chemicals and materials (Figure 1.7). An option for direct capture and utilization of  $CO_2$  emitted from point sources could involve the cultivation and processing of plants growing in an aquatic environment especially microalgae. Microalgae are microscopic, single-celled plants growing in fresh water or seawater. They use sunlight as their energy source, and  $CO_2$  and inorganic nutrients (mainly N-compounds ( $NO_3^-$ ,  $NH_4^+$ ) and phosphates) for growth.

The CO<sub>2</sub> growth of algae can be derived from concentrated sources such as flue gas. Per ton of algal biomass ca. 0.5 ton carbon (from 1.8 tons of CO<sub>2</sub> taken up by the algae) are fixed and converted to valuable products. Microalgae biomass is a versatile raw material that can potentially be used as a source for a range of non-fuel and fuel products, including bio-oils and proteins, high value chemicals and ingredients, food and feed, fertilizers and fuels.



*Figure 1.7. Overview of algae production process and the options in the products generated.*

In recent years large investments have taken place in the sector by private investors and governments in the US, the EU and elsewhere predominantly aimed at fuel production. However, to date no successful large-scale production of algal biofuels has been realized. An important feature is the high growth rate and productivity of microalgae, which is several fold higher than most terrestrial plants. This is due to more efficient use of light and highly efficient utilization of nutrients by the microalgae. Cultivation takes place in open-pond systems or in (semi)closed

photobioreactors that could be located on marginal, non-arable land. Many algal species can use salt or brackish water or effluents so in these applications there is no competition with conventional agriculture. Due to evaporation, some form of salt management must be used such as brine removal. A disadvantage is the relatively high energy requirement for continuous mixing of the cultivation system and for dewatering of the algal biomass.

Even though CO<sub>2</sub> utilization through algae has advantages and potential, there are several major challenges. Even at higher productivities microalgae systems have a substantial land requirement, which may not be available in the direct surroundings of power plants. Furthermore, costs are still high. Significant R&D and technological development and cost reductions related to cultivation and harvesting of the algae are required to enable large-scale production systems.

(c) *Conversion of CO<sub>2</sub>: chemical feedstock.* As a consequence of its low reactivity, in order to convert CO<sub>2</sub> into economically valuable products it is need a reduction in the activation energy for the reaction through the use of catalysts. Because of the enormous quantities of CO<sub>2</sub> emitted through anthropogenic activities, it is necessary for these processes to be diverse because of supply chain requirements and global capacity.

A pathway for investment in carbon dioxide utilization will be the ability to maintain security in the supply of fuels and commodity chemicals that have traditionally relied on petrochemical feedstock. Petrochemical prices are indexed to crude oil prices and fluctuation can lead to supply and price instabilities.

By utilizing CO<sub>2</sub> it is possible to retain carbon within a cycle, in a closed loop. It may be that the carbon is trapped in a permanent form, such as through accelerated mineralization, to produce construction materials and polymer formation, or stored within an energy vector, such as a synthetic liquid fuel. However, considering its conversion to fuels, capture of CO<sub>2</sub> from the air would ultimately be necessary to maintain the cycle. Within the wide spectrum of possible products there are valuable intermediates including synthesis gas and small molecule organics that can be targeted.

In *Figure 1.8* it is presented some of the main products obtained from CO<sub>2</sub> that have been reported. This represents a small sub-set of the whole chemicals landscape and it is only recently that efforts have been focused on diversifying the portfolio of reactions. This is an area that has been identified by the Engineering and Physical Sciences Research Council (EPSRC) in their Grand Challenges looking towards a sustainable chemical economy by 2050. Therefore, research into how CO<sub>2</sub> can be effectively utilized is an area of great interest and prime for investment. Indeed, the International Conference on Carbon Dioxide and Utilization [10] is growing year by year and new reaction pathways are being discovered at an increasing rate.

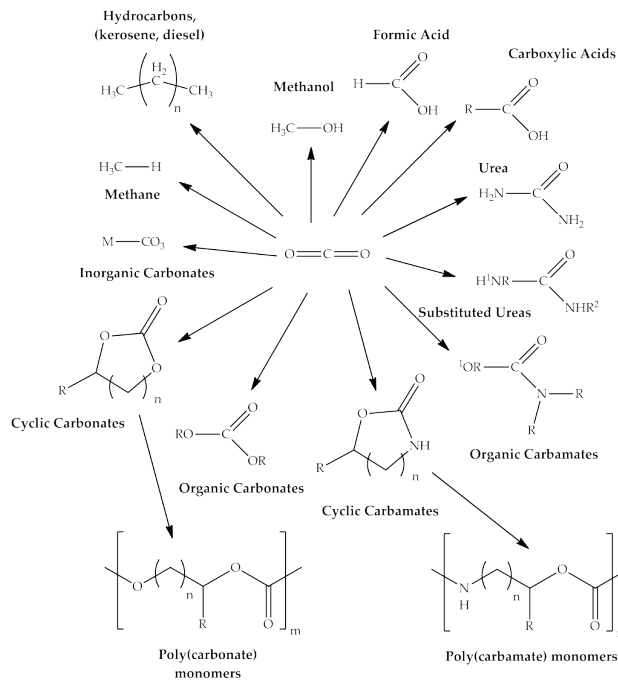


Figure 1.8. A short overview of the more common chemicals obtained from  $\text{CO}_2$ .

Consequently, CCU has the potential of easing our dependence on crude oil by creating alternative pathways (chemical or biological) to synthesizing products, such as substitutes for transportation fuel. Utilizing the  $\text{CO}_2$  captured by carbon capture units for algal growth, chemical feedstock or mineral carbonation, may help overcome investment barriers due to the high investment costs associated with capture equipment.

Currently in Europe, the only long-term incentive to capture carbon is provided through the EU ETS (Emission trading system), however for the foreseeable future it is doubtful whether the price per ton of carbon abated will reach levels high enough to stimulate

CCS beyond a demonstration phase. In the case of CCU technology, enables the recovery of initial and running costs by using the CO<sub>2</sub> as a valuable commodity, and such technologies have the potential to complement CO<sub>2</sub> storage pathways. For example, a power plant combined with both CCS and CCU could theoretically select a CO<sub>2</sub> pathway dependent on market dynamics (*i.e.* price of EU ETS *vs.* synthetic fuel price).

Mineral carbonation in the European Union could be of interest for those countries that have limited geological storage capacities either on or offshore. Finland is an example of such a country, as well as Portugal, Greece, Hungary, Lithuania and countries in the Baltic region where saline aquifers are less suitable for CO<sub>2</sub> storage. An interesting niche market for the European Union is the carbonation of alkaline waste materials like blast furnace slag and fly & bottom ash. This could be very attractive for European steel plants, where 1 ton of slag can capture 250 kg of CO<sub>2</sub>. However this would only reduce the steel mill emissions by 1.5%. An additional benefit is that the quality of the carbonated steel slag would be improved. But the mineral carbonation will be restricted to those regions in Europe with a good infrastructure for bulk goods. Typically harbors like Rotterdam (almost 400,000 metric tons per year) and Antwerp have terminals equipped for bulk solid handling. The economic feasibility of this route depends on the value of the specific carbonate minerals and needs to be further researched.

In the case of the algae process a large scale fixation of CO<sub>2</sub> with algae demands a large cultivation surface. Typically for a 600 MW

coal fuelled power plant at least 200 km<sup>2</sup> is needed to fix the CO<sub>2</sub> emissions. So this route for use of CO<sub>2</sub> use would fit more in the rural regions of Europe where (farming) land could be used for algal biomass. As a consequence, CO<sub>2</sub> needs to be transported to these areas.

Outside the European Union, in the USA, CCU is viewed as an important technology. Announcing \$106 million of investment in CCU processes such as carbonation, algae capture to produce biofuels and production of polycarbonates. The US Energy Secretary stated: “These innovative projects convert carbon pollution from a climate threat to an economic resource. This is part of our broad commitment to unleash the American innovation machine and build the thriving, clean energy economy of the future” [11]. The perceived benefits to the US economy are clearly recognized and alongside investment in CCS, there has been investment in CCU processes. Due to its geographical, economical and scientific situation the USA has potential to use any of the processes described in this report and is currently conducting research in all of them.

The climate and geographical situation in Australia make the country particularly suited to algal capture and utilization. The large amounts of solar radiation plus land available and the economic benefits are driving the technology forward. MDB Energy in Australia has received \$3.5 million of funding which is matched with a \$3.5 million investment from the company to commercialize a bio-carbon capture and storage process at three major Australian power plants. The process will use algae to

produce bio-oils and animal feeds which can be sold at a higher cost than operational costs. This process when at full scale on a single 80 hectare site would use more than 70 Megatons of flue gas emissions and produce over 11 million liters of oil, approximately enough for 18,000 cars per year (based on consumption of 1 tank of fuel per month) [12].

Australia also has significant activities in mineral carbonation. New South Wales has been found to be not well suited to geological storage and mineralization is being investigated as an alternative. The Australian government has invested \$2.1 million into building a pilot plant for capturing CO<sub>2</sub>, mineralising it and using the product for building materials, bricks, pavers, cement and agricultural additives [13].

In summary, even though both CCS and CCU technologies is possible to mitigate climate change, they can only be regarded as temporary solutions, particularly those options which merely delay the emissions of CO<sub>2</sub> rather than eliminate them permanently. Although from an economic perspective, CCU would appear to be a better option than CCS as the latter is an unprofitable activity, the cost-effectiveness as well as the environmental impacts of CCU must to be evaluated carefully on a life cycle basis to ensure a positive economic and environmental balance. Moreover, the potential of CCU is still limited as the current global demand of chemicals and other products does not have the capacity to sink enough CO<sub>2</sub> emissions to contribute significantly to meeting the carbon reduction targets. A further significant issue for CCU is that the 'storage' time of CO<sub>2</sub> is limited by the short lifespans of the

chemicals and fuels produced. Therefore, future research should focus on the development of materials and products with longer lifetimes to enable long-term storage of CO<sub>2</sub>. In the case of CCS overcomes this problem through long-term storage, but there is a risk of CO<sub>2</sub> leakage which could potentially cause more damage than if dilute emissions were to continue unabated. Equally significant is the fact that deployment of large scale CCS is not expected until well into the 2020s by which time it may be too late to reverse the impacts of climate change. Nevertheless, if the above concerns can be addressed, both CCS and CCU could play a role in mitigating climate change, together with other options such as energy demand reduction, renewables and other low-carbon technologies [14].

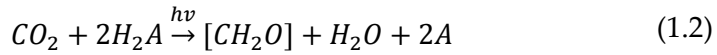
### 1.2 The Photosynthesis

Concerning to the CCU technology of transforming the CO<sub>2</sub> to a valuable product there is a natural known process which allows the reutilization of this recovered CO<sub>2</sub> transforming to a chemical valuable product using renewable energy, the *Photosynthesis*. The photosynthetic process is based on the carbohydrate generation using solar power for the energy production in plants. This process is involved in the incorporation of carbon in the biosphere and as source of O<sub>2</sub> for the atmosphere.



In the formula the term [CH<sub>2</sub>O], represents a generalized carbohydrate. In a general point of view the photosynthetic

reaction involves the  $\text{CO}_2$  reduction. For plants, most algae and cyanobacteria  $\text{H}_2\text{O}$  is the reductant, but there are some bacteria in which the reductant molecule change. For this reason, a more general reaction for photosynthesis is given by Eq. (2).



In this reaction  $\text{H}_2\text{A}$  is a general reductant agent and  $\text{A}$  is the oxidized product. In 1930 Van Niel confirm by isotopic labeling experiments that the  $\text{O}_2$  generated in the photosynthetic process did not proceed from  $\text{CO}_2$  [15].

However, in the real pathway of the reaction, photons has not direct effect over this reaction and  $\text{H}_2\text{O}$  cannot reduce the  $\text{CO}_2$  directly. The global process explained before are separated in two subprocesses for all the photosynthetic organisms (*Figure 1.9*).

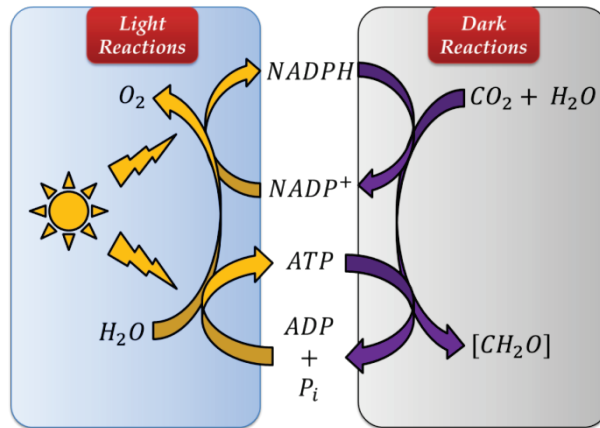


*Figure 1.9. Simple scheme of the two subprocesses of photosynthesis [16].*

All the photosynthetic process is carried out in the chloroplast, a plant organelle, in higher plants and algae. In this organelle the two reaction are carried out, the water oxidation and the  $\text{CO}_2$

reduction. First the light reactions in detail (water oxidation) are shown in the scheme below.

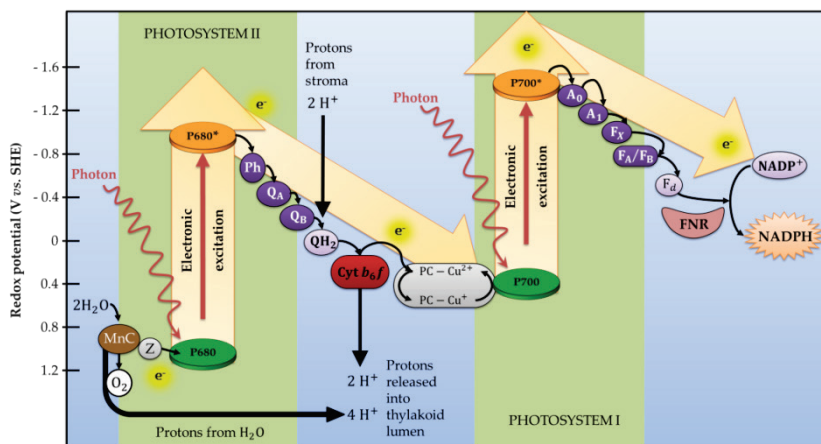
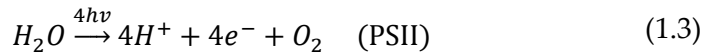


**Figure 1.10.** Light reactions with the corresponding potential level. MnC (Manganese center), Z (P680 donor center), P680 (PSII-chlorophyll reaction center), Ph (pheophytin a, electron acceptor),  $Q_A$ ,  $Q_B$  (plastoquinone),  $QH_2$  (plastoquinol, reduced plastoquinone), Cyt  $b_6f$  (cytochrome complex), PC (plastocyanin, copper protein), P700 (PSI-chlorophyll reaction center),  $A_0$  (chlorophyll acceptor),  $A_1$  (phylloquinone, vitamin K1);  $F_A$ ,  $F_B$ ,  $F_X$  (proteins with FeS clusters);  $F_d$  (soluble ferredoxin, another FeS protein) and FNR (enzyme ferredoxin:  $NADP^+$  oxidoreductase) [16].

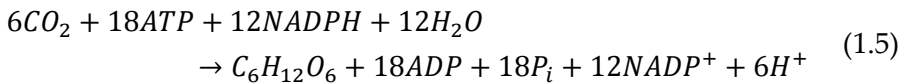
Both photosystem II (PSII) and photosystem I (PSI) contain an electron transport chain, which extracts energy when an excited electron loses its energy of excitation in a stepwise fashion. The photosystem carries out a series of oxidation/reduction reactions similar to those in electron transport (Figure 1.10). In summary, the PSII provides the electrons to stabilize the PSI. However, to recover the P680 in PSII took the electrons for the water, which split in the presence of an electron acceptor, releasing oxygen. This electron acceptor is a protein containing a cluster of four oxygen-bridged manganese atoms (MnC). The process dissociates two water

molecules, releasing oxygen, which diffuses out of the chloroplast. The four protons that are produced from the two water molecules are released into the thylakoid lumen, creating a pH gradient between the lumen and stroma. In the case of PSI the electrons excited from P700 arrives to  $NADP^+$  forming NADPH (powerful reductant agent) which will be used in the Calvin cycle [17] (the dark reactions). At the end the overall reactions of the tow PS can be summarized:



NADPH and ATP (adenosine triphosphate, which transports chemical energy) generated in the light reactions were used in the dark reactions.

The dark reactions occur in the stroma of the chloroplast and are shown schematically in *Figure 1.11*. The cycle can be resumed in three steps. In step I, carbon dioxide is trapped as a carboxylate. In step II  $CO_2$  was reduced to the aldehyde-ketone level found in sugars. In stage III, the molecule that accepts  $CO_2$  is regenerated. The overall equation for the Calvin Cycle is:



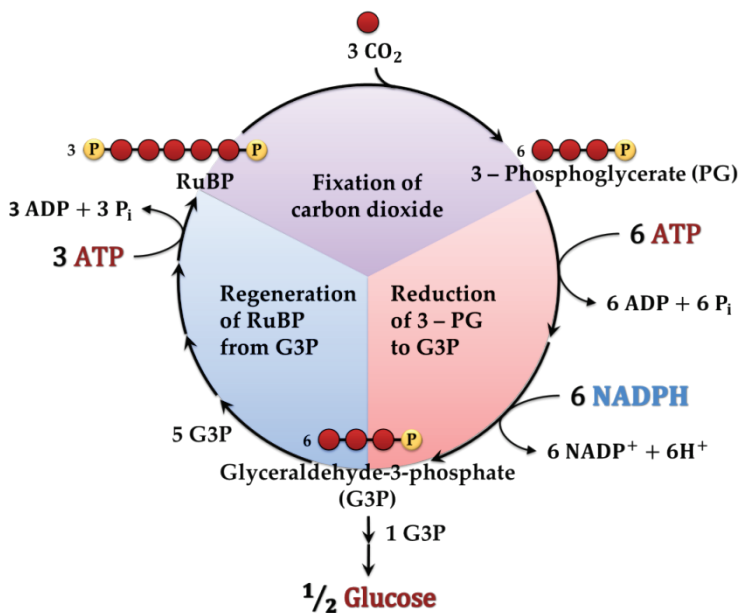


*Figure 1.11. Calvin cycle scheme which is separated in three parts CO<sub>2</sub>: fixation, glucose generation and regeneration of the RuBP (Ribulose-1,5-BiPhosphate).*

If this process could be exported to the technological point of view (artificial photosynthesis inside CCU technology) would be a very interesting method for the revalorization of CO<sub>2</sub> decreasing the gas storage investments. With this process is possible to storage the energy into chemical bonds. The energy required for this process could be obtained from solar (using electrolyzers or photoelectrochemical cells) and wind power (electrolyzers) which require storage systems to use the energy when is needed. From the technological point of view the **artificial photosynthesis** is possible to include in the concept of Solar Refinery as shown in *Figure 1.12*.

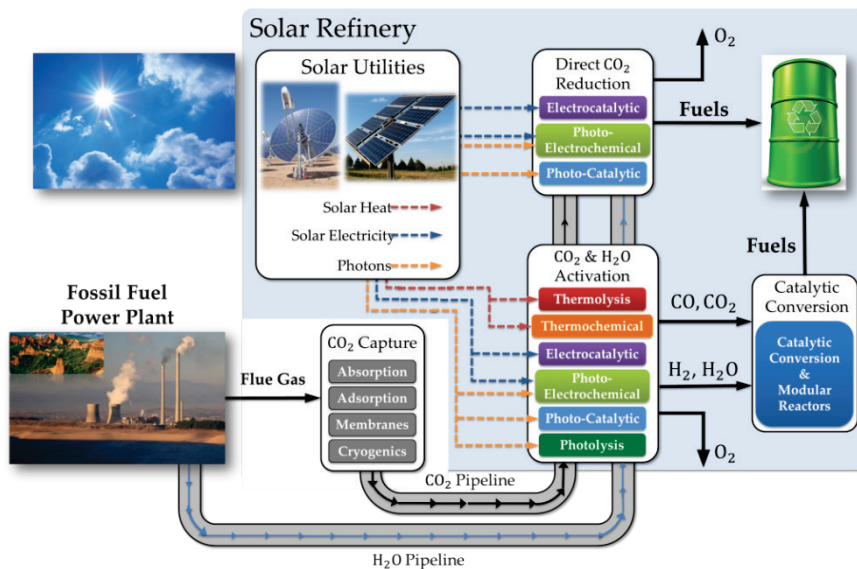


*Figure 1.12. Solar Refinery concept  $\text{CO}_2$  and  $\text{H}_2\text{O}$  conversion into fuels.*

The solar refinery concept is based on the  $\text{CO}_2$  circular economy. This concept is based on the generated  $\text{CO}_2$  from fossil fuels combustion must be captured and transformed (recycled) to valuable products using different methodologies. The energy requirements can be supplied by solar power (solar heat, solar electricity or photons) as shown in *Figure 1.12*. These generated products can be interested for the petrochemistry industry or as fuels for energy generation, obtaining zero  $\text{CO}_2$  emissions in the overall process. This means that the generated  $\text{CO}_2$  is completely recycled to a valuable product closing the  $\text{CO}_2$  life cycle, as the photosynthetic process. In the last five years, several research initiatives around the world have been emerged, considering artificial photosynthesis a strategic technology. In USA, U.S. Department of Energy (DOE) Energy Innovation Hub has launched

JCAP (Joint Center on Artificial Photosynthesis), one of the largest research program. In Asia, Nedo from Japan has launched specific actions involving Tokyo University, NIMS and AIST. Also, Korea Center for Artificial Photosynthesis (KCAP) has centralized all the research groups devoted to solar-to-fuel technologies. In Europe, EERA has included this topic in one of their working groups, Joint Programme on Advanced Materials and Processes for Energy Application (AMPEA), and there are many networks and research institutes that are now being initiated: UK Solar Fuel Network (SFN), Solar Fuels Institute (SOFI, Denmark) and Institute for Solar Fuels (Helmholtz-Zentrum, Germany).

### 1.3 CO<sub>2</sub> Photoreduction for Solar Fuels Generation

The first results of photocatalytic CO<sub>2</sub> reduction in aqueous media were reported by Honda *et al.* [18]. Another research groups have been done some investigations about the mechanism and efficiencies in the CO<sub>2</sub> reduction using the simulated solar light. The major products obtained from the photocatalytic CO<sub>2</sub> reduction are methane (CH<sub>4</sub>), methanol (MeOH), carbon monoxide (CO) or formic acid (HCOOH) and in a minor level C<sub>2</sub> products, which could be utilized as new and clean energy sources, more simple products as the generated in the photosynthesis but with the same objective.

As mentioned before in the Photosynthesis part, the CO<sub>2</sub> photoreduction process is based on the physical phenomena of the

excitation and charge transfer, where the electron ( $e^-$ ) and hole ( $h^+$ ) photo-generated must be separated, avoiding the recombination. In the case of the photosynthesis the excitation is generated by the solar irradiation over the P680 and P700, the charge transfer is carried on by some intermediate molecular species. Extrapolated to inorganic materials, the excitation is generated over a semiconductor material in which the electron from the valence band is excited to the conduction band generating an electron-hole pair. The semiconductor requires an optimal energy band alignment for achieving an adequate charge transfer and separation (*Figure 1.13*) allowing the reaction under interest [19]. For the water oxidation ( $H_2O/O_2$ ) reaction the generated hole must have a positive energy level for the valence band. In the other hand, the electron excited in the conduction band must have a negative energy position level which can carry on the water reduction ( $H_2/H_2O$ ) or carbon dioxide reduction ( $CO/CO_2$ ,  $HCOO^-/CO_2$ ).

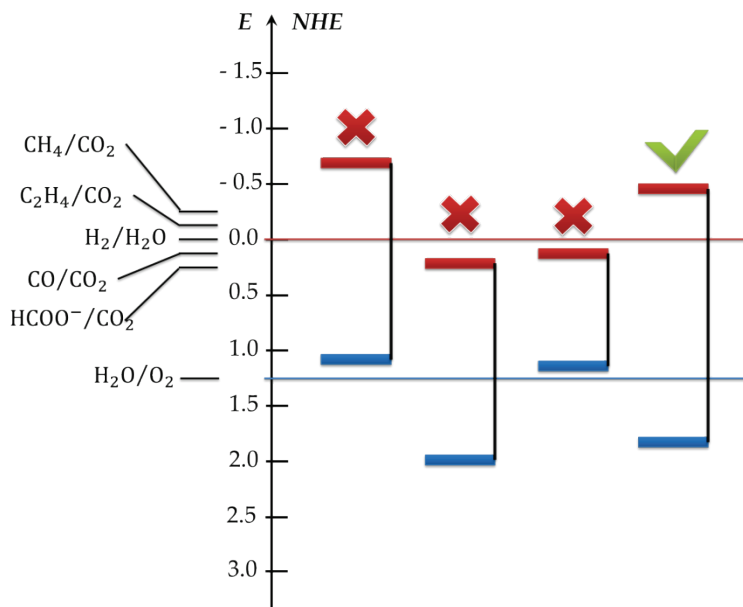


**Figure 1.13.** Scheme of the different possibilities in the energy bands alignments for semiconductor, marked with a green tick the optimal values for the valence band for water oxidation and the conduction band for water or  $CO_2$  reduction.

As seen in **Figure 1.13** the theoretical semiconductor with the green tick has the adequate energy bands position for  $CO_2$  and  $H_2$  catalytic conversion. There are many materials with the good energy alignment for this purpose, but some materials suffer from lack of stability under aqueous or gas media required for the reaction [20]. In this context,  $TiO_2$  is a suitable candidate for the process: good band alignment for both reactions, chemical stability, cheap material with high optical and electronic quality, no toxic, etc. [21].

There are two approaches for the CO<sub>2</sub> reduction, (1) the direct photocatalysis and (2) the photoelectrochemical (PEC) process. In *Figure 1.14* it is illustrated a scheme of both approaches.

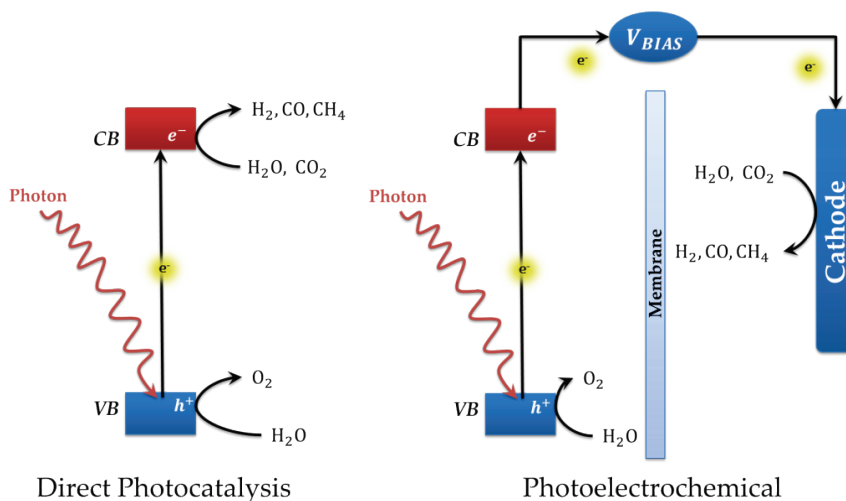


*Figure 1.14.* Direct photocatalytic conversion and photoelectrochemical approach for CO<sub>2</sub> or water reduction process.

For the first approach, with the properties of TiO<sub>2</sub> is possible to use for the direct CO<sub>2</sub> reduction process. Both oxidation and reduction processes occur at the surface of the same material. In this case there is an important property of the material, the crystallographic facets, which might have different reactivity depending on the facet direction: ones are adequate for the oxidation process and others for the reduction, avoiding somehow the recombination process [22,23]. However, due to the proximity of the reactions that occurs at the surface of the particles there is a high probability for the recombination process, limiting the efficiency [24]. Nevertheless, another method to enhance more the efficiency is using co-catalysis acting as trap for the photogenerated

electrons, decreasing the direct recombination in the bulk material and increasing the efficiency.

In reported works with the highest efficiency Varghese *et al.* [25] using TiO<sub>2</sub> nanotubes with copper and platinum as co-catalyst reach to a conversion speed of 32 nmol cm<sup>-2</sup> h<sup>-1</sup> to methane which requires 8 e<sup>-</sup> and other products which requires additional e<sup>-</sup> for C<sub>1+x</sub> products (x = 1, 2, 3, etc.) or less than 8 electrons for CO (2 e<sup>-</sup>). This values is equivalent to an approximately 0.01 % of the energy usage of the solar power (100 mW cm<sup>-2</sup>) or in fotogenerated current density terms less than 10 μA cm<sup>-2</sup>.

This low efficiency comes from the band energy disposition as shown in *Figure 1.13* which improves the electrons transition from the molecules to the valence band, known as oxidation power of the semiconductor/electrolyte system. This effect allows the reoxidation of the products obtained from the CO<sub>2</sub> photoreduction (hydrocarbons and alcohols). These products act as sacrificial agents displacing the water oxidation (oxygen evolution reaction, OER) which requires more energy. This mechanism limits the productivity of direct photoreduction of CO<sub>2</sub>.

However, to avoid this problem from the direct photocatalysis (products reoxidation) the system requires a revising of how is possible to avoid the presence in the same place of the products from the oxidation and reduction reaction. As mentioned in *Figure 1.14* the second approach for the CO<sub>2</sub> reduction reaction is using a photoelectrochemical process (PEC), which adjusts perfectly for the mentioned requirements and is closer to the photosynthetic process mentioned before, where the reactions take place in a physical

separated compartments. The first author whom propose this idea was Hitachi [26] and more recently by Ampelli *et al.* [27]. In this setup an external potential ( $V_{BIAS}$ ) can be applied which allows to control the potential between the two electrodes. In a semiconductor material the potential drop occurs at the surface and helps to modulate the bandwidth in the depletion width region (the bulk part of the semiconductor keep neutral). With high depletion width the electric field is large, generating a better charge separation of the photogenerated  $e^-/h^+$  pairs avoiding the recombination process at the surface, enhancing the solar energy conversion.

In this situation, the photoelectrochemical process shows better efficiencies in solar  $H_2$  production versus the direct conversion [28]. Actually there are modifications of PEC setup based on electrolyzers working in flow and separated by a membrane [29,30]. The basic improvement obtained when a photoactive anode (photoanode) is assembled in a classical electrolyzer setup is shown in *Figure 1.15*. In this scheme is represented the reduction of the potential requirements for an electrochemical process with the input of energy coming from the solar light, as sequence, decreasing the overall energy requirements in the process. Until this moment there is not an industrial PEC cell for the photoelectrochemical  $CO_2$ reduction.

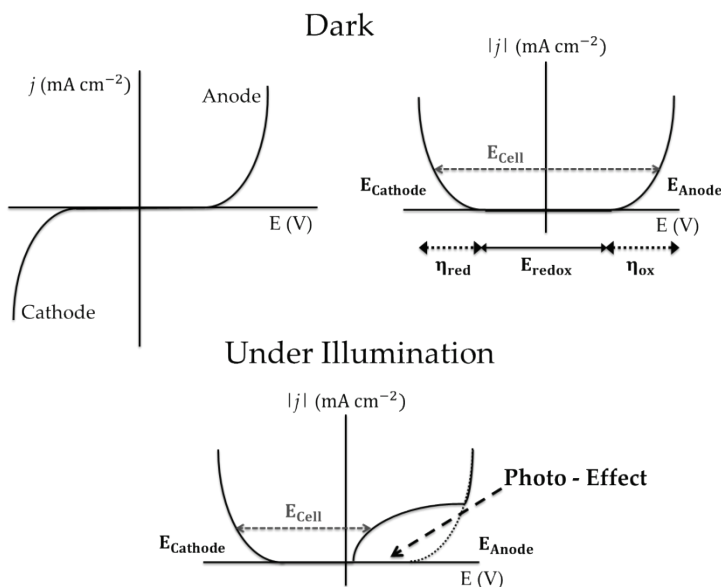


**Figure 1.15.** Scheme of the photo-effect in a photoelectrochemical (PEC) setup in dark and under illumination (photoanode illuminated).

## 1.4 Photoanode for Solar Water Splitting (Light Reaction)

The light reactions in the photosynthetic process supply the electrons required for the  $\text{CO}_2$  reduction involving water splitting reaction and generating oxygen. In artificial photosynthesis the reduction reaction can be adjusted depending on the final product interest and the oxidation process not ever generate oxygen as final product, depends on the media used. The semiconductor materials have the properties to excite electrons from the valence band to the conduction band generating  $e^- - h^+$  pair, required for the redox reaction. As mentioned before, the band positioning of the semiconductor is very important because can decrease the external

bias potential requirements in the electrochemical setup. However, there are two types of semiconductor in both cases a depletion region is generated at the interface semiconductor/electrolyte, for an n-type semiconductor, electrons migrate to the bulk of the material while holes are accumulated at the surface (interface semiconductor/electrolyte) acting as photoanodes for the oxidation reaction (GaAs,  $\text{TiO}_2$ ,  $\text{WO}_3$ ,  $\text{Fe}_2\text{O}_3$ , etc). In the case of the p-type, which act as photocathodes for the reduction reaction (Si,  $\text{Cu}_2\text{O}$ , etc.), goes in the opposite way with an accumulation of electrons at the surface (*Figure 1.16*).

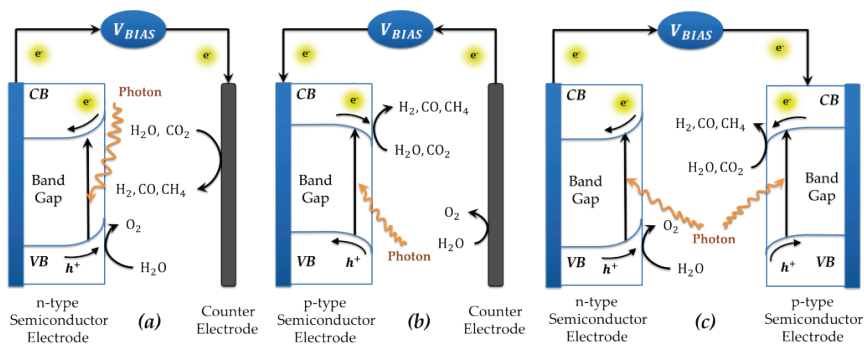


*Figure 1.16. Semiconductor type working setup schemes, (a) n-type, (b) p-type and (c) n,p-type coupled.*

For the water splitting reaction, the electrons photoexcited to the conduction band must be close to the water reduction potential and the holes generated in the valence band must react with the water molecules for oxygen evolution (OER) [31,32]. The potential values (*Table 1.1*) for the water splitting reactions can be calculated from tabulated thermodynamic data [33].

## Chapter I

**Table 1.1.** Potential values of the half reactions involved water splitting reaction vs. SHE reference electrode, considering acid and basic media.

<b>Acid Media (pH,0)</b>	<b><math>E^\circ</math> (V vs. SHE)</b>
$2\text{H}^+ + 2\text{e}^- \rightarrow \text{H}_2 (\text{g})$	0
$\text{O}_2 + 4\text{H}^+ + 4\text{e}^- \rightarrow 2\text{H}_2\text{O}$	1.23
<b>Basic Media (pH, 14)</b>	<b><math>E^\circ</math> (V vs. RHE)</b>
$2\text{H}_2\text{O} + 2\text{e}^- \rightarrow \text{H}_2 (\text{g}) + 2\text{OH}^- (\text{aq})$	-0.83
$\text{O}_2 (\text{g}) + 2\text{H}_2\text{O} + 4\text{e}^- \rightarrow 4\text{OH}^- (\text{aq})$	0.40

A more detailed schematic illustration of the basic principles of overall water splitting on a semiconductor particle, which is essentially the same to a water-splitting PEC cell, is shown below (Figure 1.17).

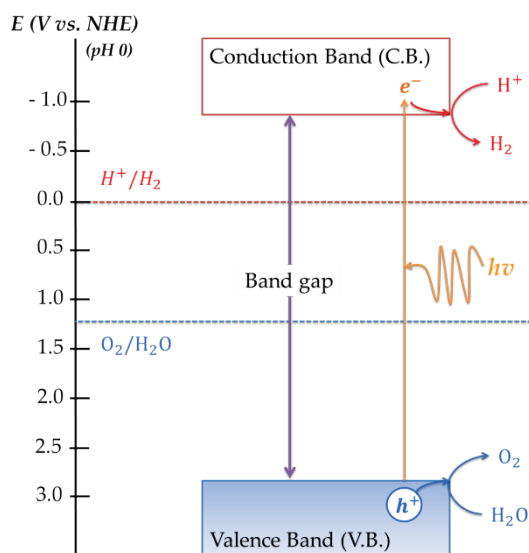


**Figure 1.17.** Basic principle of overall water splitting on a semiconductor particle [34].

Artero *et al.* made a representation of the conduction band and valence bands levels of the commonly semiconductors used in an aqueous electrolyte at pH 1 [35].

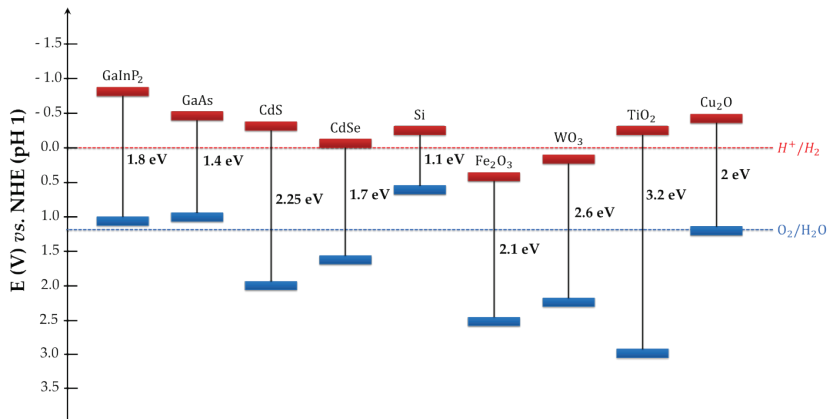


**Figure 1.18.** Band positions of several semiconductor materials in contact with aqueous electrolyte at pH 1 (blue lines represent the upper edge of the valence band whereas the red ones represent the lower edge of the conduction band). The visible spectrum corresponds to energies from 1.56 eV (800 nm) to 3.12 eV (400 nm) [35].

From the serial of semiconductors exposed before we focus on the metal-oxide material due to the expertise generated in our research group, but there are many different kind of semiconductors [34]. In the metal-oxides semiconductors the most studied are the hematite ( $\text{Fe}_2\text{O}_3$ ),  $\text{WO}_3$  and  $\text{TiO}_2$ , being the last one the best due to the cost and the natural abundance [36]. In **Figure 1.18** is possible to observe for  $\text{Fe}_2\text{O}_3$  and  $\text{WO}_3$  that the conduction band energy is lower than the water reduction potential, in this case an external bias potential is required, decreasing the efficiency of the process for the water splitting reaction.

Hematite ( $\text{Fe}_2\text{O}_3$ ) has received a lot of interest as the ideal candidate as photoanode for the PEC cells. The theoretical current density due to its band gap is possible to reach for this material to  $11.6 \text{ mA cm}^{-2}$  for the solar to hydrogen (STH) values 14.1%. However the reported values arrives only to  $3 \text{ mA cm}^{-2}$  with an onset potential of  $0.9 \text{ V vs. RHE}$  [37,38] and this material requires a high external potential obtaining a lower overall energy efficiency (*Figure 1.19*).

In the case of the tungsten oxide ( $\text{WO}_3$ ) the theoretical values of current density is around  $5.1 \text{ mA cm}^{-2}$  [39,40] with a STH efficiency of 6.3%. The maximum experimental value reached is  $2.4 \text{ mA cm}^{-2}$  [41] with an onset potential of  $0.48 \text{ V vs. RHE}$  [42]. The problem of this material is the external potential requirements due to the conduction band position and the non-stability in neutral and alkaline media (*Figure 1.19*).

Recent studies on  $\text{BiVO}_4$  (bismuth vanadate) have focused on the preparation of  $\text{BiVO}_4$  as the electrode-type material for use as the photoanode for photoelectrochemical cells. However, the typical efficiencies of unmodified  $\text{BiVO}_4$  photoanodes for water-oxidation were not impressive as they suffer from excessive-hole recombination, poor charge transport properties and poor water oxidation kinetics.  $\text{BiVO}_4$  is a promising photoanode material due to the fact that it is composed of inexpensive elements and has a band gap of  $2.4 \text{ eV}$  with the valence band (VB) edge located at ca.  $2.4 \text{ eV vs. RHE}$  (reversible hydrogen electrode), providing sufficient overpotential for holes to photooxidize water while the conduction band (CB) edge is located just short of the thermodynamic level for

H<sub>2</sub> [43]. Its band gap is slightly larger than that is desired for a photoanode (ca. 2.0 eV), but its very negative CB position may compensate for this disadvantage. [32,44].

In the case of the TiO<sub>2</sub>, in both stable crystallographic forms has lower values of theoretical current density and STH respect the mentioned oxides, in anatase form 1.1 mA cm<sup>-2</sup> with a STH of 1.3 % and for rutile 1.8 mA cm<sup>-2</sup> with a maximum STH value of 2.2 %. The experimental values of current density are around 0.6 mA cm<sup>-2</sup> with an onset potential of 0.2 V *vs.* RHE. The stability of this material is well known in alkali and acidic media. The absorption range in the solar spectra is lower due to the large bandgap value (3.2 eV and 3 eV for anatase and rutile respectively). However, the position of the conduction band is in a upper energy level than the water or carbon dioxide reduction [45] and the reaction can be spontaneous demonstrated in the reported works in the direct photoreduction process unlike the mentioned materials. For this reason, and the more negative value of onset potential, the external potential requirements for the photoelectrochemical cell is lower for TiO<sub>2</sub> compared with the other oxides, giving a better efficiency in the overall process [32], despite of the lower current density reached (*Figure 1.19*).

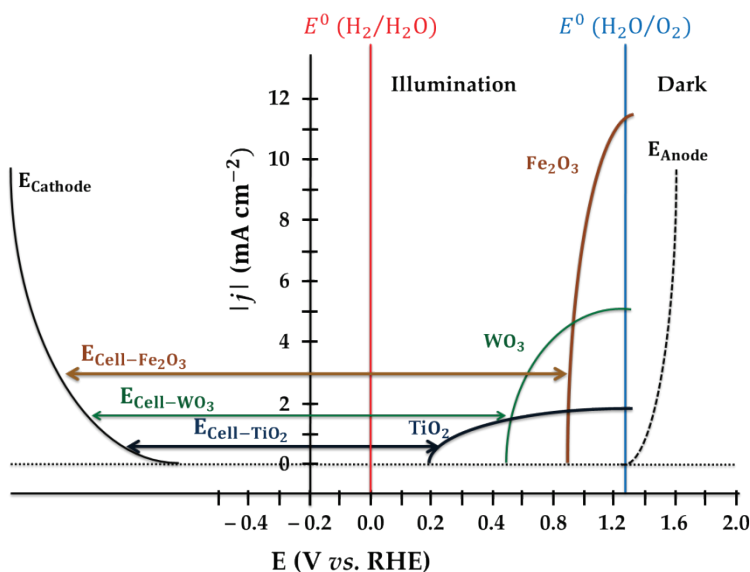


**Figure 1.19.** Schematic showing of the qualitative effect of the photoanode onset potential on the overall voltage performance in a PEC cell for the metal-oxides mentioned before. The dotted line corresponds to a classical anode in dark. For the photoanodes the theoretical current densities were used and the onset potentials reported in bibliography.

As mentioned before, this external potential enhances the photogenerated electron-hole separation improving the efficiency of the reaction compared with the direct photoreduction process. In addition, all the photocatalytic process take place on the material surface which could be modified in the synthesis process and with the thermal treatments done after the preparation, this opened a large reported works with different synthetic methods [46,47].

## 1.5 CO<sub>2</sub> Electroreduction (Dark Reaction)

Similar to the photosynthesis, the electrochemical CO<sub>2</sub> reduction corresponds with the Calvin cycle (dark reactions) with the difference of the final reduced products from CO<sub>2</sub>. The variety of products obtained from CO<sub>2</sub> reduction in aqueous media goes from liquid fuels (formic acid, isopropanol, methanol...), hydrocarbons (methane, ethane, ethylene) to fuels precursors as carbon monoxide (Syngas) [48,49]. Using tabulated thermodynamic data [33] as used on the paragraph above, the potential values from the different half reactions involved in the CO<sub>2</sub> electroreduction versus SHE (Standard Hydrogen Electrode pH 0) were calculated (*Table 1.2*). This data can give an idea of the theoretical potential range in which the CO<sub>2</sub> reduction moves and the differences with the H<sub>2</sub> evolution reaction in this case all the reaction are considered in basic media. The calculations are explained in detail in **Annex C**.

## Chapter I

---

*Table 1.2. Potential values of the half reactions involved in the CO<sub>2</sub> electroreduction vs. SHE reference electrode.*

<b>CO<sub>2</sub>(g) Reduction Half Reactions</b>	<b>E° (V vs. SHE)</b>
CO <sub>2</sub> + H <sup>+</sup> + 2e <sup>-</sup> ↔ HCOO <sup>-</sup>	-0.22
CO <sub>2</sub> + 2H <sup>+</sup> + 2e <sup>-</sup> ↔ CO + H <sub>2</sub> O	-0.10
CO <sub>2</sub> + 6H <sup>+</sup> + 6e <sup>-</sup> ↔ CH <sub>3</sub> OH + H <sub>2</sub> O	0.03
CO <sub>2</sub> + 8H <sup>+</sup> + 8e <sup>-</sup> ↔ CH <sub>4</sub> + 2H <sub>2</sub> O	0.18
2CO <sub>2</sub> + 12H <sup>+</sup> + 12e <sup>-</sup> ↔ C <sub>2</sub> H <sub>4</sub> + 4H <sub>2</sub> O	0.06
2CO <sub>2</sub> + 12H <sup>+</sup> + 12e <sup>-</sup> ↔ C <sub>2</sub> H <sub>5</sub> OH + 3H <sub>2</sub> O	0.09
2CO <sub>2</sub> + 14H <sup>+</sup> + 14e <sup>-</sup> ↔ C <sub>2</sub> H <sub>6</sub> + 4H <sub>2</sub> O	0.14
<b>H<sub>2</sub> Reduction Half Reaction</b>	
2H <sup>+</sup> + 2e <sup>-</sup> → H <sub>2</sub>	0.00

In aqueous media the CO<sub>2</sub> reduction potential values are not very negative compared with the H<sub>2</sub> evolution reaction (HER), however the activity for CO<sub>2</sub> reduction are relatively low. The theoretical reduction potentials decrease when the pH values increase, following the Nernst equation [50]. Gattrell *et al.* [51] obtained the tendency of the potentials versus pH of the half reaction of CO<sub>2</sub> reduction. With our calculations we obtain a very similar plot shown *Figure 1.20* at the working pH range mentioned by Gattrell. But in our case we use the data obtained from the reactions done in basic media.

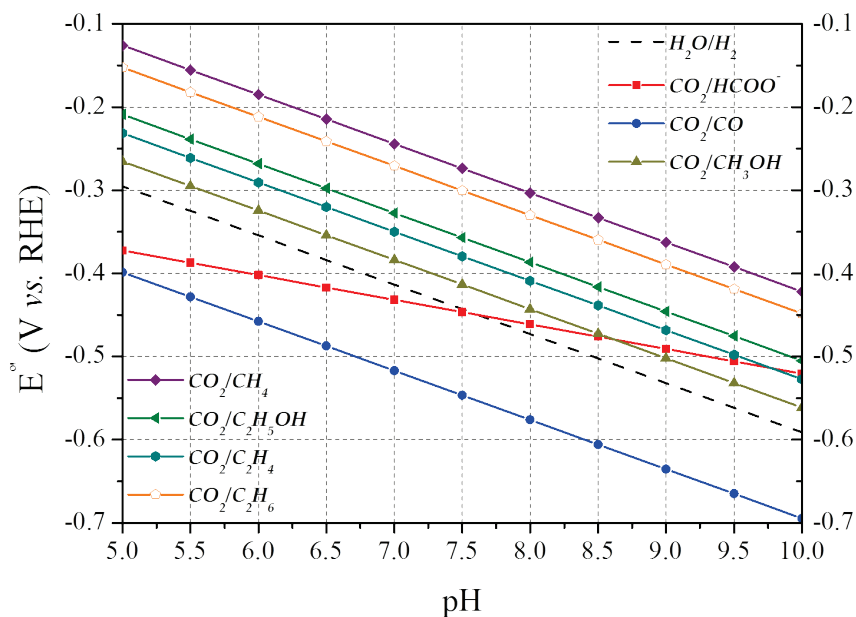


**Figure 1.20.** Formal standard reduction potentials ( $E^\circ$ ) versus pH at 25°C using the basic approximation. The dotted line corresponds to the hydrogen ( $H_2$ ) evolution reaction at the same conditions.

Nevertheless, the  $CO_2$  reduction requires higher overpotential decreasing the energy efficiency for the process the same happened for the  $H_2$  reduction. The limiting step in the  $CO_2$  reduction is the formation of the  $CO_2^{\bullet-}$  radical anion intermediate. The standard potential value is shown below being the responsible for the high overpotential [52–54].



This reaction has very high activation energy ( $E_a$ ) limiting kinetically the reaction. The energy requirements for the  $CO_2$  activation are high the electronic reorganization and opening the

very stable initial linear geometry to an angled one, allowing the  $\text{CO}_2$  reduction (*Figure 1.21*).

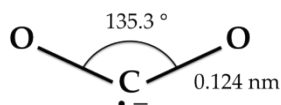


*Figure 1.21.* Atomic configuration of  $\text{CO}_2^{\cdot-}$  employed in scf into study by Pacansky et al. [55].

The overvoltage generated by the activation energy could be decreased using a catalyst which improves the  $\text{CO}_2$  coordination and adsorption over the surface, opening the molecule and decreasing the overpotential (*Figure 1.22*).

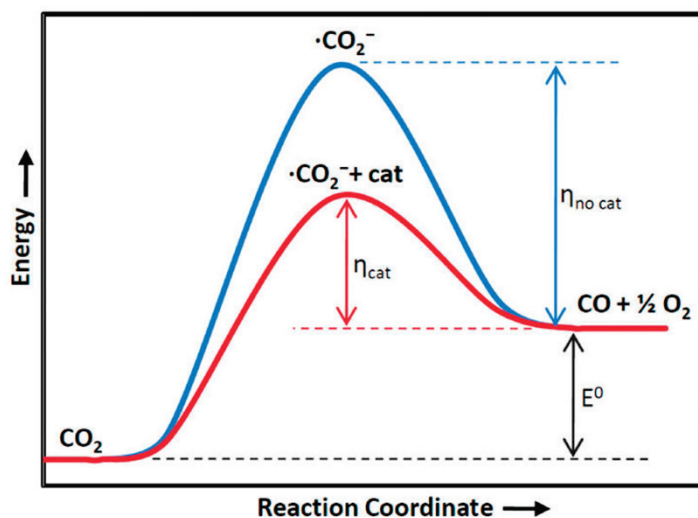


*Figure 1.22.* Qualitative reaction scheme for  $\text{CO}_2$  conversion. Catalysts and electrolytes acting as cocatalyst can lower the energy of the intermediate, improving the energetic efficiency of the conversion ( $\eta$ , overpotential) [53].

For example, in the case of Hg (mercury) electrodes the potential required for the reduction reaction is 300 mV less than the expected for the  $\text{CO}_2^{\bullet-}$  radical. The activation energy requirements changes if the intermediate specie are stabilized or not in the electrode surface (ad).



Sullivan et al. [56] and Vassiliev et al. [57] propose that in aqueous media the first reaction step is the hydration of a  $\text{CO}_2$  molecule followed by a completion to become adsorbed onto an active site. This implies that the  $\text{CO}_2(\text{ad})$  species is a critical limiting step within the aqueous system.

The principal challenge of the  $\text{CO}_2$  reduction to fuels is to understand the electrocatalytic electron transference mechanisms and the reaction intermediates species adsorption. Hori *et al.* [58] made an study about the product distribution from the  $\text{CO}_2$  reduction over a pure Cu electrode at pH 7. Thermodynamically the methane and ethylene must be more favorable than hydrogen evolution (HER) which not corresponds with the experimental values obtained, in the case of hydrogen requires only two electrons and for methane and ethylene 8 and 12 respectively, for this reason the kinetics of the reaction changes.

The  $\text{CO}_2$  reduction generates CO and  $\text{HCOO}^-$  under 1.12 V. At this potential the hydrocarbons generation stars giving ethylene ( $\text{C}_2\text{H}_4$ ) and after methane ( $\text{CH}_4$ ). The methane production has a strong potential dependency [59] increasing the partial current

density, reaching to higher productivity at -1.35 V than CO and formate. The working potential window for aqueous electrolyte is reduced to neutral pH (6.8–8) due to HER takes place at the working potential competing with the CO<sub>2</sub> reduction improving the efficiency at lower pH, and at high pH CO<sub>2</sub> is not stable. A study using different electrolytes for the CO<sub>2</sub> reduction using a Cu electrode, was reported by Hori [58] giving the faradaic efficiencies of the products generated in the electroreduction of CO<sub>2</sub>. The products distribution depends on the electrolyte used, for ethylene and alcohols, KCl, K<sub>2</sub>SO<sub>4</sub> and KClO<sub>4</sub> and dilute HCO<sub>3</sub><sup>-</sup> solutions. However, methane is preferentially produced in phosphate and relatively concentrated HCO<sub>3</sub><sup>-</sup> solutions. The methane production is improved when protons or hydrogen are available in the electrode surface, having a strong dependence with the pH [60]. The hydrogen carbonate electrolyte gives an equilibrated efficiency in the CO<sub>2</sub> process, for this reason is the most used electrolyte for all the CO<sub>2</sub> reported works. However to avoid the deactivation of the electrode the electrolyte requires a pre-electrolysis before the test. Hori *et al.* [61] reported a study of the metallic copper deactivation by depositing heavy metals impurities contained in the reagent chemicals, very small amount of organic substances in the water and the generation of reaction intermediates could poison the electrode surface.

As mentioned before the reaction is kinetically controlled and the product selectivity depends over many factors in the electrolyte as ionic strength, temperature and composition (aqueous or non-aqueous). Nevertheless consider the same conditions the metallic

electrode drive the selectivity in the CO<sub>2</sub> reduction. Hori *et al.* [62] reported a study over a large variety of metal electrodes with the faradic efficiency for each products generated in the CO<sub>2</sub> reduction at 19°C bubbling CO<sub>2</sub> in the electrolyte at pH 7. The metals can be divided in four groups based on the selectivity.

- *First group*, metals with negligible CO adsorption strength and high overpotential for the HER and for CO<sub>2</sub> as *Pb, Hg, In, Sn, Cd, Ti, Bi*, etc. The CO<sub>2</sub><sup>•-</sup> intermediate is weakly stabilized, giving formate as mayor product (HCOO<sup>-</sup>) [63].
- *Second group*, metals with weak CO adsorption strength and intermediate overpotential for the HER as *Au, Ag, Zn*, etc. CO<sub>2</sub> is catalyzed to CO and by desorption is liberated giving as mayor product.
- *Third group*, metals with better CO adsorption than the others keeping the overpotential for HER. There is only one metal with these properties, *Cu*. The CO<sub>2</sub> is catalyzed to more reduced states as hydrocarbons (CH<sub>4</sub>, C<sub>2</sub>H<sub>4</sub>, etc.) with interesting efficiencies.
- *Fourth group*, metals with strong CO adsorption and low HER overpotential as *Ni, Fe, Pt, Ti*, etc. Is favored the water reduction than the CO<sub>2</sub> reduction obtaining H<sub>2</sub> as mayor product.

Sakata and his coworkers applied 32 metals to CO<sub>2</sub> reduction at -2.2 V *vs.* SCE in 0.05 M KHCO<sub>3</sub>. They mostly confirmed the results obtained by Hori and coworkers, and showed that Ni and Pt electrodes, which scarcely give products in CO<sub>2</sub> reduction

at ambient temperature and pressure, can reduce  $\text{CO}_2$  to  $\text{CO}$  or formic acid under elevated pressure (60 atm) [64,65]. Recently Hori prepared a review in which are collected the references of the different metals used in the  $\text{CO}_2$  reduction in aqueous and nonaqueous media [50]. Jaramillo *et al.* reported a study using Au, Ag, Zn, Cu, Ni, Pt and Fe obtaining methane and methanol as products from  $\text{CO}_2$  reduction at low selectivity, apart in the same work describes the catalytic activity and selectivity in the framework of  $\text{CO}$  binding energy for the different metals [49].

A global view of the metal activity in the periodic table for  $\text{CO}_2$  reduction was reported by Azuma *et al.* [64], improved by Lee *et al.* [66].

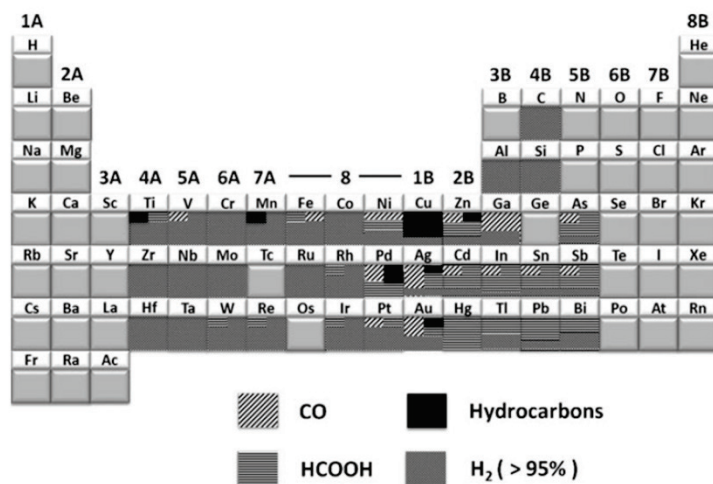


Figure 1.23. Periodic Table showing  $\text{CO}_2$  reduction products at ambient operating conditions [66].

## 1.6 Scope of the Research

This thesis is devoted to prove the concept of the CO<sub>2</sub> reduction to CH<sub>4</sub> with a decreasing in the voltage requirements using a photocatalytic mechanism. Subsequently, part of the solar energy is transferred to the reaction, obtaining an improvement in the total energy balance. The work developed intends first, to take advantage of the know features of the photoactive nanostructured materials obtained by anodization and hydrothermal synthesis (allowing to obtain better surface areas and improving the photon collection, light photosynthetic reactions). Second investigate the copper and copper oxide cathodes for the CO<sub>2</sub> electroreduction activity to CH<sub>4</sub> (dark photosynthetic reactions) using a complete cell to understand the parameters involved in the process and the products selectivity for each cathodes. And third the implementation of the photoanode and cathode in a photoelectrochemical complete cell.

In addition, it is expected that the synthesis methods, fabrication techniques and experimental setups used and optimized in this work, will serve as background and inspiration for the future people of the “Energy Storage and Energy Harvesting group”, in the Advance Materials Department at IREC in which this thesis starts, four years ago.

This thesis is organized as described below,

- ❖ **Chapter II** shows the main synthetic and electrochemical techniques employed during this thesis and the experimental setups used for the electrochemical test.
- ❖ **Chapter III** describes the TiO<sub>2</sub> photoelectrodes synthesized by anodization (anatase nanotubes) and hydrothermal (rutile nanorods). For the nanotubes a method to improve the surface area and light trapping property was introduced. For the rutile nanorods, a hydrothermal optimization study was done and the incorporation of new materials to improve the charge carrier density and the activity in the visible region.
- ❖ **Chapter IV** presents the electrochemical CO<sub>2</sub> reduction activity and selectivity using metallic copper and copper oxide as cathodes. An addition, the copper oxide cathode was deeply study to understand the electrochemical process and the parameters involved.
- ❖ **Chapter V** presents the evaluation and discussion of the assembling of the complete photoelectrochemical cell setup with the electrodes studied.

The conclusions are summarized in **Chapter VI**. In addition, at the end of the thesis some **Annexes** were included: Supercritical CO<sub>2</sub> reactor optimization for CO<sub>2</sub> electroreduction to methane, characterization and measurements techniques used in the thesis and some calculations required for the **Chapter III** and **IV** were explained.

---

## 1.7 References

- [1] EEA (European Environment Agency). *Atmospheric Greenhouse Gas Concentrations*. Copenhagen: **2015**.
- [2] IPCC (Intergovernmental Panel on Climate Change). *Climate Change 2014: Synthesis Report: Contribution of Working Group I, II and III to the Fifth Assessment Report of the Intergovernmental Panel on Climate Change*. Geneva: **2014**.
- [3] IEA (International Energy Agency). *Energy Climate and Change World Energy Outlook Special Report*. **2015**.
- [4] Global CCS Institute. *The Global Status of CCS: 2014*. Melbourne: **2015**.
- [5] OECD/IEA. *Redrawing the Energy-Climate Map: World Energy Outlook Special Report*. Paris: **2013**.
- [6] OECD/IEA. *Southeast Asia Energy Outlook: World Energy Outlook Special Report*. Paris: **2013**.
- [7] Styring P., Jansen D., de Conick H., Reith H., Armstrong K. *Carbon Capture and Utilisation in the green economy*. **2011**.
- [8] Lackner K.S., Wendt C.H., Butt D.P., Joyce E.L., Sharp D.H. *Energy*. **1995**, 20, 1153.
- [9] Ah-Hyung A.  
[http://www.columbia.edu/~ap2622/research\\_carbon.html](http://www.columbia.edu/~ap2622/research_carbon.html).  
[Accessed: September 4, 2015].
- [10] <http://www.iccdu2015.sg/>. [Accessed: September 4, 2015].
- [11] <http://energy.gov/fe/office-fossil-energy>. [Accessed: September 4, 2015].
- [12] <http://www.mbdenergy.com/>. [Accessed: September 4, 2015].
- [13] <http://scinews.com.au/releases/410/view>. [Accessed: September 4, 2015].
- [14] Cuéllar-Franca R.M., Azapagic A. *J CO2 Util.* **2015**, 9, 82.
- [15] Niel C.B. *Arch Mikrobiol.* **1932**, 3, 1.
- [16] Mathews C.K., Van Holde K.E., Ahern K.G. *BIOQUÍMICA*. Tercera Ed. Madrid: Pearson Educacion; **2002**.
- [17] Bassham J.A., Benson A.A., Calvin M. *J Biol Chem.* **1950**, 185, 781.
- [18] INOUE T., FUJISHIMA A., KONISHI S., HONDA K. *Nature.* **1979**, 277, 637.
- [19] Grätzel M. *Nature.* **2001**, 414, 338.

- [20] Hoffmann M.R., Martin S.T., Choi W., Bahnemann D.W. *Chem Rev.* **1995**, 95, 69.
- [21] Schneider J., Matsuoka M., Takeuchi M., Zhang J., Horiuchi Y., Anpo M., et al. *Chem Rev.* **2014**, 140919080959008.
- [22] Ohno T., Sarukawa K., Matsumura M. *New J Chem.* **2002**, 26, 1167.
- [23] Diebold U. *Surf Sci Rep.* **2003**, 48, 53.
- [24] Ohtani B. *Catalysts.* **2013**, 3, 942.
- [25] Varghese O.K., Paulose M., Latempa T.J., Grimes C.A. *Nano Lett.* **2009**, 9, 731.
- [26] Ichikawa S., Doi R. *Catal Today.* **1996**, 27, 271.
- [27] Ampelli C., Centi G., Passalacqua R., Perathoner S. *Energy Environ Sci.* **2010**, 3, 292.
- [28] Mor G.K., Shankar K., Paulose M., Varghese O.K., Grimes C.A. *Nano Lett.* **2005**, 5, 191.
- [29] Carver C., Ulissi Z., Ong C.K., Dennison S., Kelsall G.H., Hellgardt K. *Int J Hydrogen Energy.* **2012**, 37, 2911.
- [30] Li Y., Yu H., Song W., Li G., Yi B., Shao Z. *Int J Hydrogen Energy.* **2011**, 36, 14374.
- [31] Maeda K. *J Photochem Photobiol C Photochem Rev.* **2011**, 12, 237.
- [32] Walter M.G., Warren E.L., McKone J.R., Boettcher S.W., Mi Q., Santori E.A., et al. *Chem Rev.* **2010**, 110, 6446.
- [33] Bard A.J., Parsons R., Jordan J. *Standard Potentials in Aqueous Solution.* **1985**.
- [34] Maeda K., Domen K. *J Phys Chem C.* **2007**, 111, 7851.
- [35] Artero V., Fontecave M. *Comptes Rendus Chim.* **2011**, 14, 799.
- [36] Bhatt M.D., Lee J.S. *J Mater Chem A.* **2015**.
- [37] Sivula K., Le Formal F., Grätzel M. *ChemSusChem.* **2011**, 4, 432.
- [38] Tilley S.D., Cornuz M., Sivula K., Grätzel M. *Angew Chem Int Ed Engl.* **2010**, 49, 6405.
- [39] Liu X., Wang F., Wang Q. *Phys Chem Chem Phys.* **2012**, 14, 7894.
- [40] Lee W.J., Shinde P.S., Go G.H., Ramasamy E. *Int J Hydrogen Energy.* **2011**, 36, 5262.
- [41] Brillet J., Yum J.-H., Cornuz M., Hisatomi T., Solarska R., Augustynski J., et al. *Nat Photonics.* **2012**, 6, 824.
- [42] Amano F., Tian M., Wu G., Ohtani B., Chen A. *ACS Appl Mater Interfaces.* **2011**, 3, 4047.
- [43] Xie B., Zhang H., Cai P., Qiu R., Xiong Y. *Chemosphere.* **2006**, 63, 956.

- [44] Bak T., Nowotny J., Rekas M., Sorrell C.. *Int J Hydrogen Energy*. **2002**, 27, 991.
- [45] Scanlon D.O., Dunnill C.W., Buckeridge J., Shevlin S.A., Logsdail A.J., Woodley S.M., et al. *Nat Mater*. **2013**, 12, 798.
- [46] Chen X., Liu L., Yu P.Y., Mao S.S. *Science*. **2011**, 331, 746.
- [47] Bourikas K., Kordulis C., Lycourghiotis A. *Chem Rev*. **2014**.
- [48] Kuhl K.P., Cave E.R., Abram D.N., Jaramillo T.F. *Energy Environ Sci*. **2012**, 5, 7050.
- [49] Kuhl K.P., Hatsukade T., Cave E.R., Abram D.N., Kibsgaard J., Jaramillo T.F. *J Am Chem Soc*. **2014**, 136, 14107.
- [50] Hori Y. Electrochemical CO<sub>2</sub> Reduction on Metal Electrodes. In: Vayenas CG, White RE, Gamboa-Aldeco ME, editors. *Mod. Asp. Electrochem.*, Springer New York; **2008**, p. 89–189.
- [51] Gattrell M., Gupta N., Co A. *J Electroanal Chem*. **2006**, 594, 1.
- [52] Chaplin R.P.S., Wragg A.A. *J Appl Electrochem*. **2003**, 33, 1107.
- [53] Whipple D.T., Kenis P.J.A. *J Phys Chem Lett*. **2010**, 1, 3451.
- [54] Tryk D.A., Fujishima A. *Electrochem Soc Interface*. **2001**, 32.
- [55] Pacansky J. *J Chem Phys*. **1975**, 62, 2740.
- [56] Sullivan B.P., Krist K., Guard H.E. *Electrochemical and Electrocatalytic Reactions of Carbon Dioxide*. Elsevier; **1993**.
- [57] Vassiliev Y.B., Bagotsky V.S., Osetrova N.V., Khazova O.A., Mayorova N.A. *J Electroanal Chem Interfacial Electrochem*. **1985**, 189, 271.
- [58] Hori Y., Murata A., Takahashi R. *J Chem Soc Faraday Trans 1 Phys Chem Condens Phases*. **1989**, 85, 2309.
- [59] Cook R.L., MacDuff R.C., Sammells A.F. *J Electrochem Soc*. **1987**, 134, 1873.
- [60] Hori Y., Takahashi R., Yoshinami Y., Murata A. *J Phys Chem B*. **1997**, 101, 7075.
- [61] Hori Y., Konishi H., Futamura T., Murata A., Koga O., Sakurai H., et al. *Electrochim Acta*. **2005**, 50, 5354.
- [62] Hori Y., Kikuchi K., Suzuki S. *Chem Lett*. **1985**, 1695.
- [63] Jitaru M., Lowy D.A., Toma M., Toma B.C., Oniciu L. *J Appl Electrochem*. **1997**, 27, 875.
- [64] Azuma M., Watanabe M. *J Electrochem Soc*. **1990**, 137, 1772.
- [65] Azuma M., Hashimoto K., Hiramoto M., Watanabe M., Sakata T. *J Electroanal Chem Interfacial Electrochem*. **1989**, 260, 441.
- [66] Lee J., Kwon Y., Machunda R.L., Lee H.J. *Chem Asian J*. **2009**, 4, 1516.



# Chapter II

Experimental

Methods

<b>2</b>	<b>Experimental Methods .....</b>	<b>57</b>
2.1	Chapter Overview.....	57
2.2	TiO <sub>2</sub> Synthesis Methods.....	57
2.2.1	<i>Anodization .....</i>	<i>57</i>
2.2.2	<i>Hydrothermal.....</i>	<i>59</i>
2.3	Photoelectrochemical            and            Electrochemical Measurements (PEC/EC).....	61
2.3.1	<i>Photoelectrochemical Setup (PEC).....</i>	<i>62</i>
2.3.2	<i>Electrochemical Setup (EC).....</i>	<i>66</i>
2.3.3	<i>Electrodes Conditioning.....</i>	<i>69</i>
2.4	References .....	73

## **2. Experimental Methods**

### **2.1 Chapter Overview**

The **aim of this chapter** is to give a general overview of the specific experimental methods and tools employed in this thesis emphasizing their main interest for the following chapters. The main experimental setups shown herein are the synthetic methods for the nanostructured TiO<sub>2</sub>, the (photo)-electrochemical measurements setups and methods, as well as the copper electrodes preparation methodologies for CO<sub>2</sub> reduction reaction explained in **Chapter IV**.

### **2.2 TiO<sub>2</sub> Synthesis Methods**

#### *2.2.1 Anodization*

TiO<sub>2</sub> nanotubes photoelectrodes of **Chapter III** has been synthesized by anodization. The setup (*Figure 2.1*) is based on a two electrode cell (working and counter electrode) connected to a voltage controller (Gtelco-GVD1444 and TTi EX752M, Multi-Mode PSU, 75V/150V, 300W).

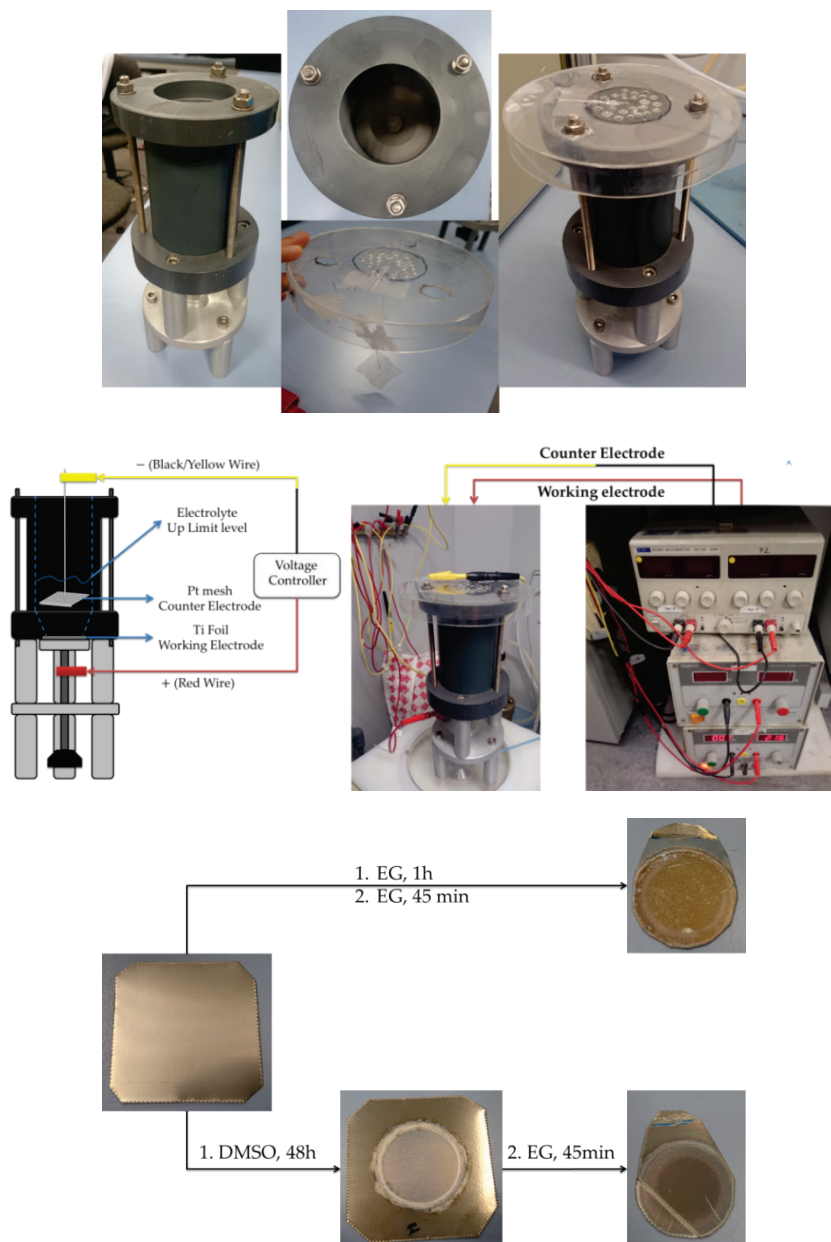


**Figure 2.1.** First and second images correspond to the anodization reactor and setup. Third image samples aspect in each synthetic step, in detailed explained in **Chapter III**. EG and DMSO corresponds to the electrolytes used Ethylene Glycol and Dimethyl sulfoxide.

Platinum mesh was used as counter electrode (9 cm<sup>2</sup>), placed parallel to the titanium foil as working electrode, which was polarized positively by the DC source, in a homemade PVP reactor that allows the exposure of one side of the sample.

Ti foil was cut in 3 × 3 cm<sup>2</sup> pieces to use it in the anodization reactor, but the exposed surface in the reactor was 3.14 cm<sup>2</sup> (circular area, r = 1 cm<sup>2</sup>). The cleaning protocol for these Ti consisted in two sonication steps: (1) in a mixture of isopropanol, acetone and ethanol during 15 min to degrease and clean de surface and (2) 15 min in Mili Q water. After them the sample was dried under N<sub>2</sub> stream. The synthesis protocol is shown in **Chapter III**.

### **2.2.2**      *Hydrothermal*

For the hydrothermal synthesis of TiO<sub>2</sub> nanorods a Teflon-lined stainless steel autoclave (125 ml, Parr Instrument Co.) was used. A Binder furnace was used for the heat source.

The samples preparation on glass conductive substrate is explained in **Chapter III** but the real aspect of the substrate and the samples after the hydrothermal synthesis is shown below (*Figure 2.2*).

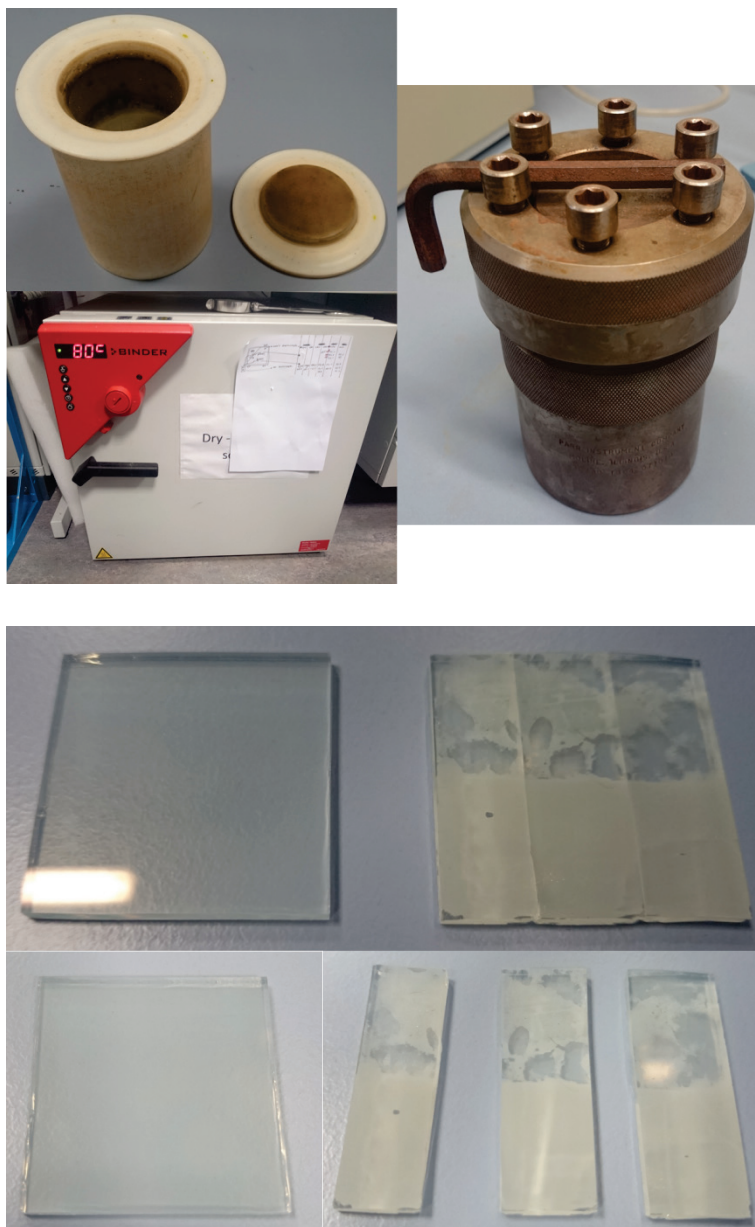


*Figure 2.2. (a) Hydrothermal Teflon cup for the substrate and electrolyte, stainless steel cover and oven used. (b) Cleaned Substrate and samples cut in pieces after the hydrothermal synthesis for the electrochemical test.*

## 2.3 Photoelectrochemical and Electrochemical Measurements (PEC/EC)

A potentiostat is an electronic instrument which controls the voltage difference between a working and a reference electrode. It implements this control by injecting a current into the cell through an auxiliary electrode. The potentiostat measures the current flow between the working and the auxiliary electrodes. It becomes galvanostat when the injection of the controlled variable is switched from cell voltage to cell current. **In this work** two systems to monitor the potential-intensity of the electrochemical cells were used a potentiostat/galvanostat Parstat 2273 (Princeton Applied Research) with impedance analyzer and Biologic SAS, SP-50. From this type of measurements it should be possible to obtain the typical current density - voltage (iV) curves, Mott-Schottky plots for the photoanodes and potentiostatic/galvanostatic experiments for the CO<sub>2</sub> reduction.



*Figure 2.3. Parstat 2273 and Biologic SP-50 potential monitor systems.*

### 2.3.1 Photoelectrochemical Setup (PEC)

The components in a PEC cell are a photoelectrode or photoanode, which can typically be for example an n-type semiconductor in order to absorb photons, a counter electrode (cathode or p-type semiconductor photocathode) immersed in an aqueous electrolyte (*Figure 2.4*). The working principle of this system starts with a surface charge space zone in the semiconductor-electrolyte interface. For an n-type semiconductor, there is a bending potential associated to this surface depletion zone. According to the Maxwell laws applied to solid electromagnetism, this bending potential,  $V_s$ , is due to the existence of an internal electric field that scans the free carriers. Electrons,  $n$ , are removed from this zone towards the inner part of the semiconductor whereas holes,  $p$ , are scanned towards the interface semiconductor/electrolyte. In thermodynamic equilibrium, according to the Gauss theorem, the free,  $n$  and  $p$  and fix charges, doping  $N_D$  and surface states density  $N_{ss}$ , introduced by impurities or dopant specimens are directly connected with the bending potential  $V_s$  and consequently with the geometrical size of this space charge zone,  $W$ .

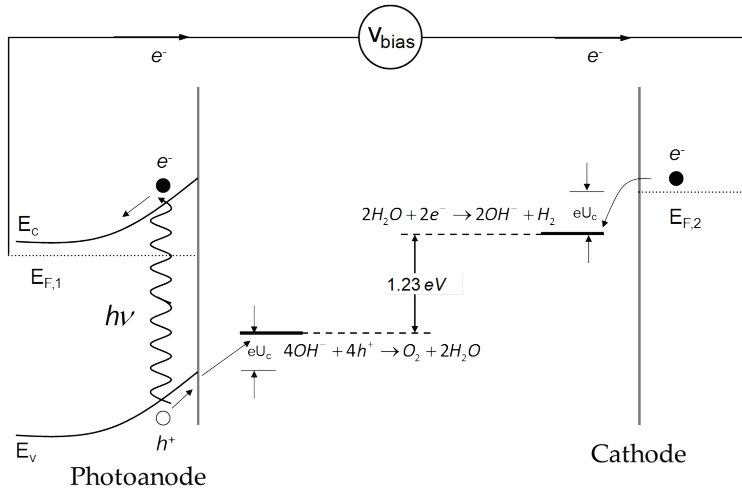


**Figure 2.4.** PEC cell energy diagram with the correspondent redox reactions for each side. Photoanode (n-type semiconductor), cathode (metal, Pt),  $E_f$  (Fermi level),  $U_c$  (overpotential).

Therefore, the holes generated in the semiconductor valence band are pulling by the electrical field for the surface accumulation in the semiconductor surface. If the band position have the adequate energy level, this level must be below the other one, is possible to obtain the water oxidation reaction (oxidation half reaction). The energetic difference ( $eU$ ) between the holes in the photoanode and the energetic position of the water oxidation associated level gives the oxidation reaction overpotential value ( $U$ ). However, the holes in the surface can suffer recombination due to the surface defects or semiconductor structural defects. Finally the electrolyte must be capable for maintain the needed ion conduction levels able for closing the overall electric circuit [1].

All electrochemical experiments, involving photoanodes (working electrode), were performed in 1M NaOH (pH 13.6)

## Chapter II

---

electrolyte using a platinum mesh as counter electrode and an Ag/AgCl electrode as reference electrode, inside a quartz cell and. The illumination source is a 150 W xenon lamp equipped with AM.1.0 and AM.1.5G filters (Solar Ligth Co. AIR MASS 1.5 SIMULATOR).

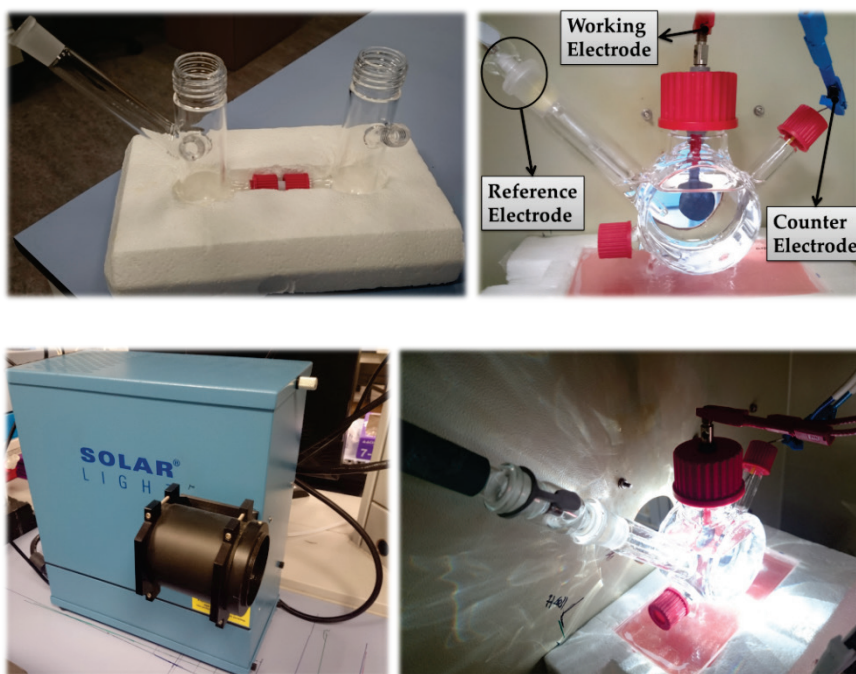


*Figure 2.5. Quartz cells used for the PEC measurements, solar simulator lamp and a running intensity ( $I$ ) versus potential ( $V$ ) experiment.*

A Bentham Tmc-300 V-U- LS with triple grating and 300 mm focal length were used as monochromatic light source to perform the incident photon-to-electron conversion efficiency (IPCE) measurements coupled with a Abet Technologies, Inc. Solar simulator AM1.5G (LS 150)

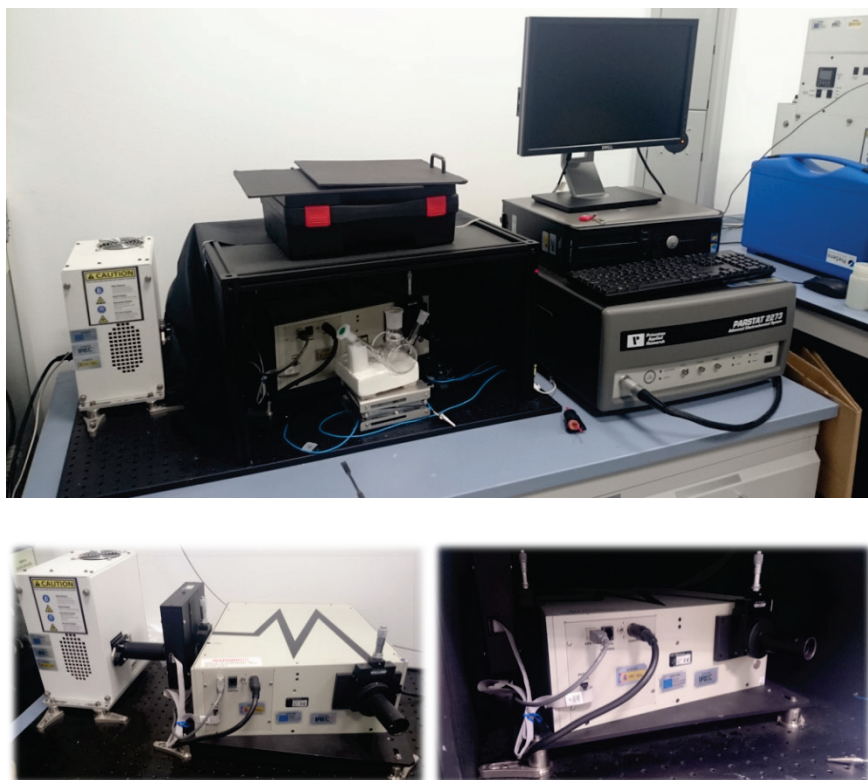


*Figure 2.6. Equipment for the incident-to-photon (IPCE) measurements.*

## 2.3.2 Electrochemical Setup (EC)

The basic electrochemical cell is a MicroFlowCell from Electrocell A/S with an electroactive area of  $10\text{ cm}^2$  [2]. This type of cells have already been used before in reported works in  $\text{CO}_2$  reduction [3–5].

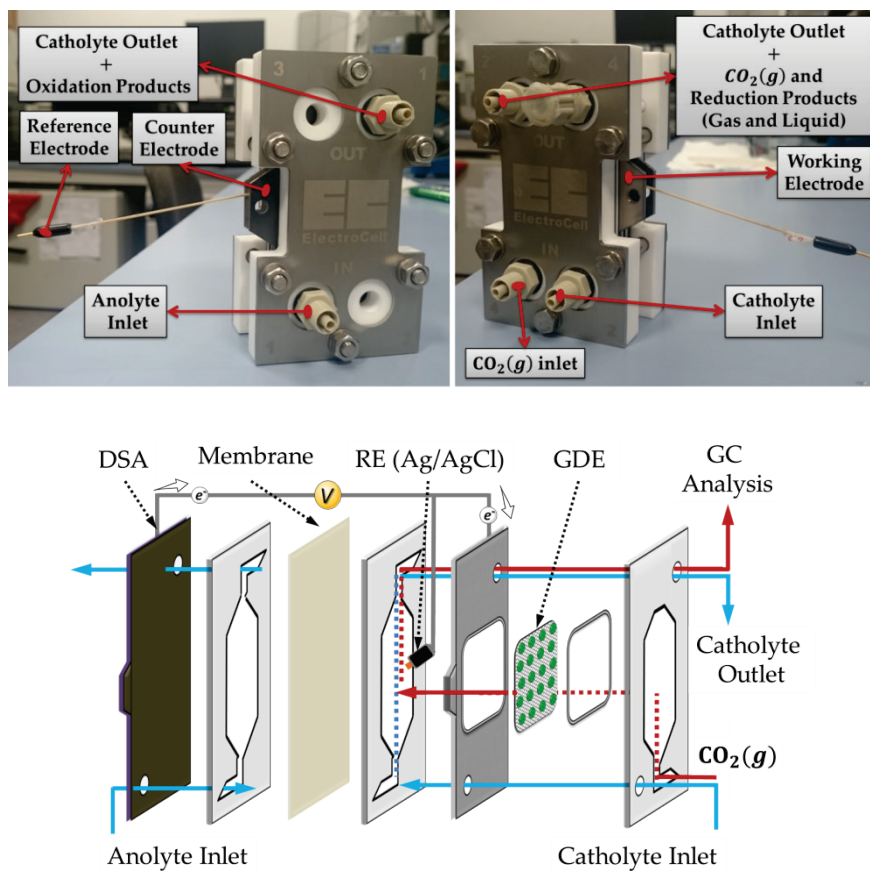


*Figure 2.7. Electrochemical cell images and detailed cell scheme.*

The cell was constructed by stacking rubber gaskets, Polytetrafluoroethylene (PTFE) flow channels, and metal current

collectors at the cathode and anode parts. After stacking of layers and assembled, the cell was closed and fitted with a torque of using 2 N·m using an automatic wrench. The cathode and anode compartments were separated by a polymer membrane, Nafion 117 (DuPont®) of which was permeable to cations ( $H^+$ ,  $Na^+$  or  $K^+$ ). The cathode holder is a frame of metallic titanium in which is possible to allocate a metallic electrode or a gas diffusion electrode; the anode is a DSA –  $O_2$  (Dimensionally Stable Anode,  $Ta_2O_5 - IrO_2$ ) and the reference is Ag/AgCl/3 M KCl Leak Free miniature Reference Electrode from Harvard Apparatus (*Figure 2.8*), located in the catholyte compartment.

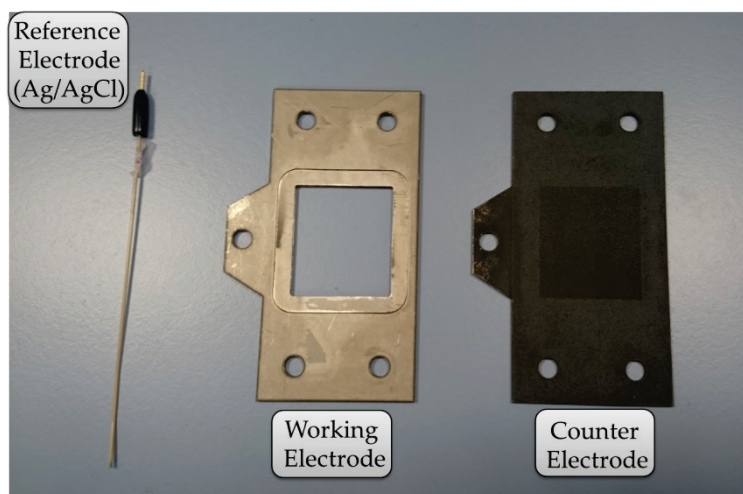


*Figure 2.8. Electrodes used in the electrochemical flow cells*

The  $CO_2$  electrochemical bench is shown in *Figure 2.9*. The EC cell is connected to the catholyte and anolyte containers by a Tygon® flexible pipe. The anolytes used in the experiments was sodium and potassium hydroxide using the same concentration and positive ions as the catholyte. The electrolytes were pump at 11

$\text{mL min}^{-1}$  flowing speed fixed for all the experiments. The catholyte container is connected to the Micro-GC for the gas analysis.

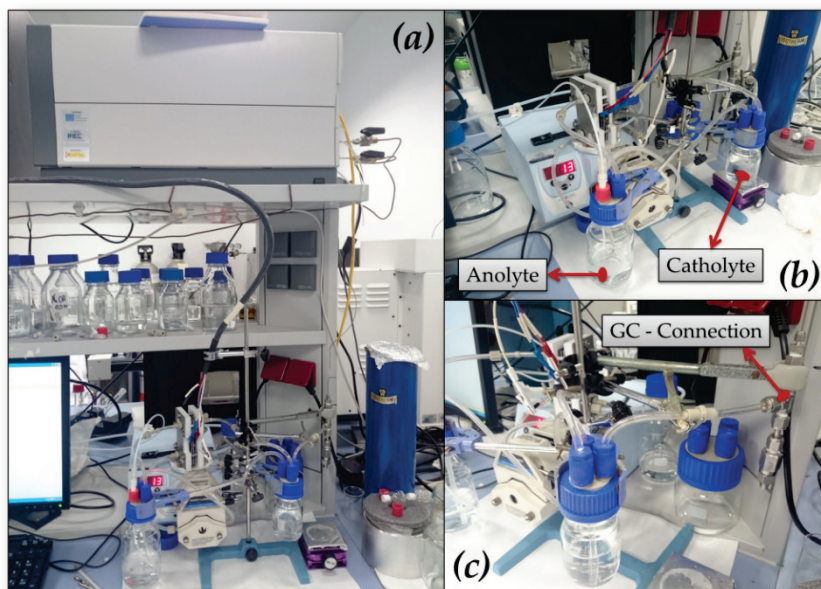


*Figure 2.9. Electrochemical bench used in the  $\text{CO}_2$  reduction experiments.*

For the gas source, pure  $\text{CO}_2$  or Ar was used and regulated by a mass flow (Bronkhorst® HIGH-TECH) set at  $10 \text{ mL min}^{-1}$  for the electrochemical experiments. The mass flows were incorporated in a homemade methacrylate panel.

The electrochemical working conditions used for all the experiments in **Chapter IV**, were in galvanostatic mode in a three-electrode setup, being the cathode the working electrode. During the experiment, the counter electrode (anode) potential was registered in parallel simultaneously to evaluate the overall cell

potential during electrolysis. The products obtained were measured in constant flow by gas chromatography (**Annex B**).

The pre-electrolysis of the catholyte was performed in a two electrode cell at -2.0 V for more than 12 hours using two platinum meshes. The mass flows and pre-electrolysis setups are shown in **Figure 2.10**.



**Figure 2.10.** Left image, methacrylate panel with three mass flow one at 50 and two at  $200 \text{ mL min}^{-1}$  maximum flows, calibrated for  $\text{CO}_2$ . One of the  $200 \text{ mL min}^{-1}$  mass flow is used for the Ar and the rest for  $\text{CO}_2$ . Right image, catholyte pre-electrolysis setup with stirring system.

### 2.3.3 Electrodes Conditioning

For the conditioning of the electrode a home-developed protocol was used. A scheme of the method and images of the electrodes are shown in

The copper electrodes used for all of these experiments was a copper gauze (100 mesh woven from, 0.11 mm (0.0045in) dia wire, Alfa Aesar) and copper foil (1.0 mm (0.04in) thick, Puratronic® 99.9999% (metal basis) from Alfa Aesar). Electrodes were cut with two different sizes  $10 \text{ cm}^2$  only for the mesh and  $1 \text{ cm}^2$  for both of them. The protocol used starts with a cleaning by sonication in a

mixture of ethanol, isopropanol and acetone (Panreac) during 15 min to eliminate the fat and the dust coming from the factory. The second step the samples were immersed in DI water another 15 min and then dried with N<sub>2</sub> stream. And the third one is a HCl:H<sub>2</sub>O bath (3:1) during 5 min to clean the surface eliminating the oxide layer which could be formed and the impurities attached reaching to a shiny electrode, this step is used in the pristine copper to clean the surface before any test. After this step some tests were carried on using these electrodes only with the chemical cleaning (*Chem*). To improve the roughness and surface area after the third step an electropolishing (*Epol*) (technique commonly used) was done over the cleaned copper surface. The electrode was immersed in orthophosphoric acid solution (H<sub>3</sub>PO<sub>4</sub>, 85%) and potentiostatically 2 V was applied during 1 minute (it is typical method to clean the surface of metal impurities [6,7]). The electropolish technique was done in a two electrode cell setup with the reference connected to the counter electrode; a platinum mesh was used as counter electrode and a copper mesh as electrode.

To synthesize the copper oxide cathode electrodes after while the third step a thermal treatment was done at 500°C in air during two hours obtaining a core-shell organization in which a metallic copper is covered with the different oxide layers. The structure generated in to this organization: CuO/Cu<sub>2</sub>O/Cu.

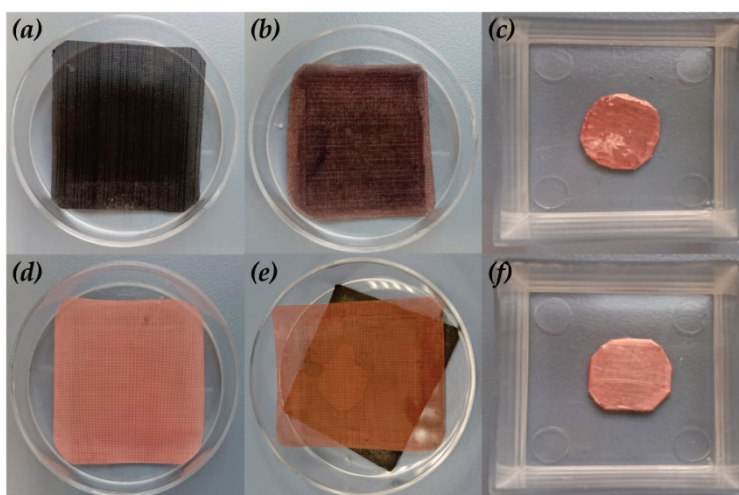
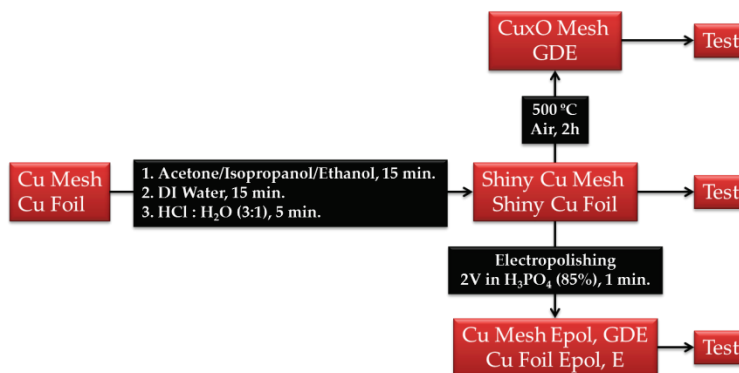


**Figure 2.11.** First image, copper electrodes preparation scheme. Second image, Copper electrodes used in the CO<sub>2</sub> reduction. (a) Fresh Cu<sub>2</sub>O, (b) Cu<sub>x</sub>O after test, (c) Cu foil mechanically polished, (d) Cu mesh after cleaning protocol, (e) Cu mesh after test and (f) Cu foil electropolished.

To use the copper mesh like gas diffusion electrode a carbon Toray paper (TGP-H-60, Alfa Aesar) with the same size of the electrodes was used in the back part. The carbon paper is used to block the liquid crossing through the mesh going to the gas compartment but allowing the gas pass to the liquid part for the

carbon dioxide supplying to improve the mass transfer problem due to the low  $\text{CO}_2$  solubility in the aqueous media [8]. In this particular zone where all phases are at the same time is called triple reaction point. For this reaction gas phase, liquid and solid surface (catalyst) are at the same time taking place the reaction (*Figure 2.12*) [9,10]. For the carbon Toray paper cleaning the same protocol of the chemical cleaning in the copper electrodes was used, to be sure that there are any deposited particle over the the carbon paper.

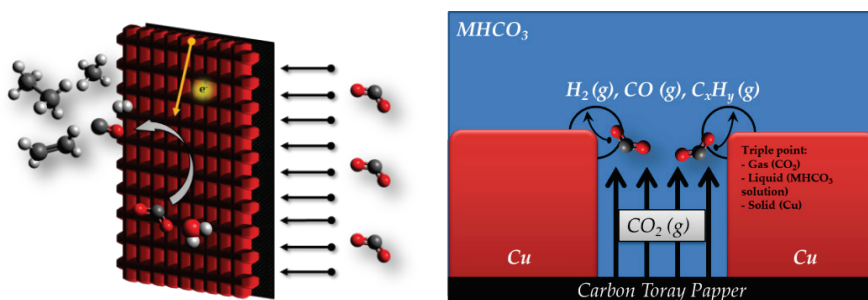


*Figure 2.12. Gas diffusion electrode scheme and triple point reaction center*

## 2.4 References

- [1] Chen Z., Dinh H.N., Miller E. *Photoelectrochemical Water Splitting: Standards, Experimental Methods, and Protocols*. New York, NY: Springer New York; **2013**.
- [2] <http://www.electrocell.com/micro-flow-cell.html>. [Accessed: July 15, 2015].
- [3] Alvarez-Guerra M., Quintanilla S., Irabien A. *Chem Eng J*. **2012**, 207-208, 278.
- [4] Dufek E.J., Lister T.E., McIlwain M.E. *J Appl Electrochem*. **2011**, 41, 623.
- [5] Innocent B., Liaigre D., Pasquier D., Ropital F., Léger J.-M., Kokoh K.B. *J Appl Electrochem*. **2008**, 39, 227.
- [6] Kuhl K.P., Cave E.R., Abram D.N., Jaramillo T.F. *Energy Environ Sci*. **2012**, 5, 7050.
- [7] Chen C.S., Handoko A.D., Wan J.H., Ma L., Ren D., Yeo B.S., et al. *Catal Sci Technol*. **2014**, 2.
- [8] Sánchez-Sánchez C.M., Montiel V., Tryk D.A., Aldaz A., Fujishima A. *Pure Appl Chem*. **2001**, 73.
- [9] Delacourt C., Ridgway P.L., Newman J. *J Electrochem Soc*. **2010**, 157, B1902.
- [10] Delacourt C., Ridgway P.L., Kerr J.B., Newman J. *J Electrochem Soc*. **2008**, 155, B42.



# Chapter III

Light Reaction:

Photoanodes for

Water Splitting

<b>3</b>	<b>Light Reaction: Photoanodes for Water Splitting .....</b>	<b>77</b>
<b>3.1</b>	<b>Chapter Overview.....</b>	<b>77</b>
<b>3.2</b>	<b>Titanium Dioxide Nanotubes, TiNTs.....</b>	<b>78</b>
<b>3.2.1</b>	<i>Hierarchical TiNTs Synthesis by Anodization.....</i>	<b>83</b>
<b>3.2.2</b>	<i>Structural and Morphological Characterization .....</i>	<b>86</b>
<b>3.2.3</b>	<i>Optical Characterization and PEC Measurements ...</i>	<b>95</b>
<b>3.3</b>	<b>Titanium Dioxide Nanorods.....</b>	<b>103</b>
<b>3.3.1</b>	<i>TiO<sub>2</sub> Nanorods Hydrothermal Synthesis Optimization.....</i>	<b>105</b>
<b>3.3.1.1</b>	<i>Effect of Titanium Precursor Concentration.....</i>	<b>108</b>
<b>3.3.1.2</b>	<i>Chlorine Concentration Effect.....</i>	<b>113</b>
<b>3.3.2</b>	<i>TiO<sub>2</sub> Nanorods Doping .....</i>	<b>121</b>
<b>3.3.2.1</b>	<i>Tin Doping .....</i>	<b>121</b>
<b>3.3.2.2</b>	<i>Vanadium Doping .....</i>	<b>123</b>
<b>3.3.2.3</b>	<i>Nitrogen Doping .....</i>	<b>140</b>
<b>3.4</b>	<b>Conclusions.....</b>	<b>149</b>
<b>3.5</b>	<b>References .....</b>	<b>155</b>

## **3. Light Reaction: Photoanodes for Water Splitting**

### **3.1 Chapter Overview**

This chapter is focused on the photoactive  $\text{TiO}_2$  based nanostructured materials for water splitting. The first  $\text{TiO}_2$  nanostructuring strategy under study was the synthesis of nanotubes by anodization of a titanium foil using organic electrolytes. The  $\text{TiO}_2$  crystal phase obtained by this technique was anatase. Lately, the anodization process was done using two electrolytes in different steps seeking a surface modification to improve the efficiency. Consequently, a porous surface with an increment in the surface area was obtained, which was assessed by an increment on its photoactivity.

The second nanostructured materials under study were  $\text{TiO}_2$  nanorods obtained by hydrothermal synthesis over a conductive glass substrate, Fluorine Tin Oxide (FTO) coated glass. The nanorods using this technique had rutile structure. An optimization of two parameters involved in the hydrothermal synthesis was studied: (1) initial titanium precursor concentration and (2) increasing the chlorine concentration to obtain larger and thinner rods. To increase the photoactivity of  $\text{TiO}_2$ , we pursued the incorporation of dopants inside the structure. The dopants selected were tin (Sn) which improves the charge carriers, vanadium (V) which allows the absorption in the visible range and nitrogen (N) to enhance the efficiency in the photoactivity of the material.

## **3.2 Titanium Dioxide Nanotubes, TiNTs**

For the preparation of photoanodes for water splitting, the work has been focused on one-dimensional (1D) semiconductor nanostructures grown over a conductive substrate, which according to the background of the group are the best candidates for obtaining highly efficient photoelectrodes. The thesis of C. Fàbrega [1] was devoted to nanostructured ( $\text{TiO}_2$ ) for solar hydrogen production. One of the nanostructuring techniques used were sol gel method, obtaining  $\text{TiO}_2$  nanoparticles which were deposited over a conductive glass substrate (FTO, fluorine tin oxide coated glass). Other methods used were the titanium foil anodization giving a 1D structure of  $\text{TiO}_2$  nanotubes (for this kind of 1D structure will be focus in the first paragraph) and 1D  $\text{TiO}_2$  nanorods grown on conductive glass by hydrothermal (this nanostructured material will be explained later). The aim to move from sol-gel method to 1D structures were related with the structure organization and how the electrons generated by the incident light are collected. In *Figure 3.1* is possible to observe the electron collection scheme comparing the two structures, nanoparticles and 1D structure.

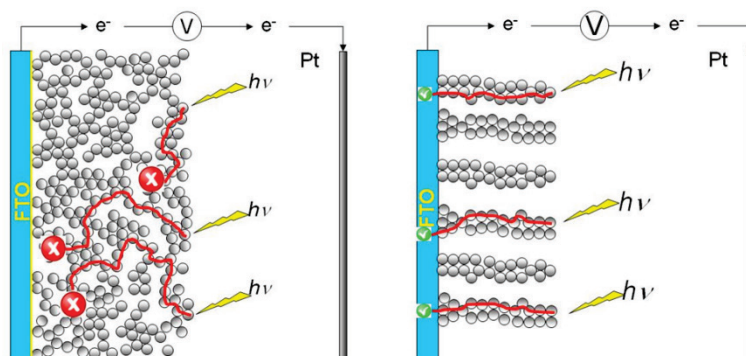


**Figure 3.1.** Scheme of the differences between the not organization layers obtained by sol-gel and the 1D nanostructuring (anodization or hydrothermal).

For the nanoparticle photoanodes, their numerous interparticle boundaries easily trap the charge carriers, which results in decrease in the carrier mobility and the carrier lifetime. When the nanoparticles are used in Dye Sensitize Solar Cells (DSSCs) the carrier transport is a trap-limited diffusion process. The electron diffusion coefficient is several orders of magnitude smaller than the expected value which is deduced from the physical properties of the  $\text{TiO}_2$  single crystalline bulk. [2]. Structures such as nanorods, nanotubes and nanowires have demonstrated a great potential of achieving high diffusion coefficient of carriers in electric devices, because of their unique one-dimensional (1D) structure [3].

Starting by the titanium nanotubes (TiNts), recently Schmuki collected all the recent relevant information about TiNts properties and main applications in a review [4], where among several synthetic strategies (deposition into templates of Anodic Aluminium Oxide –AAO–, hydrothermal, ...). The electrochemical anodization offers the key advantage that titanium dioxide

nanotubes are fabricated directly from the metal that acts as back contact. At the same time the technique can provide an easy control of the layer morphology (tube length and diameter) by changing the experimental conditions (electrolyte, applied voltage, temperature, etc.). Following the PhD work mentioned before, we focused on two non-aqueous electrolytes, dimethylsulfoxide (DMSO) [5,6] and ethyleneglycol (EG) [7].

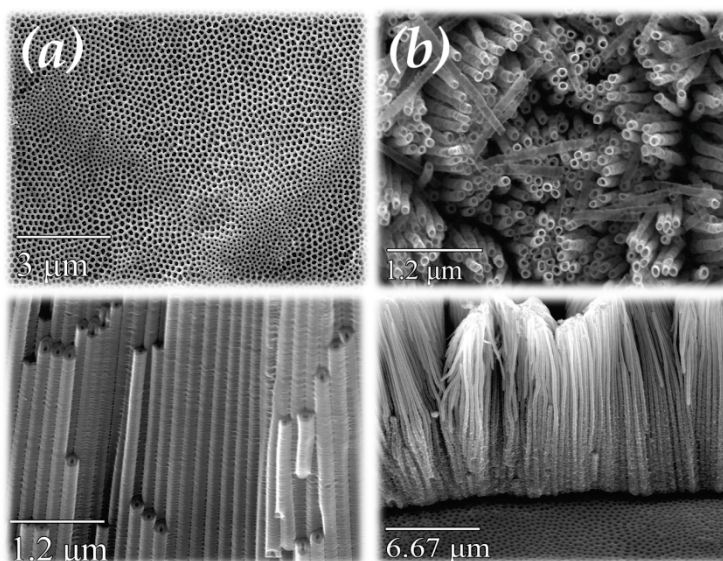
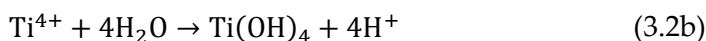
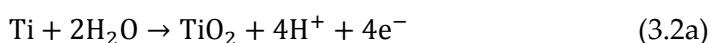


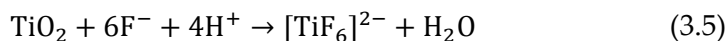
*Figure 3.2. SEM top view and cross section of TiNTs synthesized in (a) ethyleneglycol (EG) and (b) dimethylsulfoxide (DMSO) electrolyte.*

As seen in *Figure 3.2* when using EG as electrolyte (with  $\text{NH}_4\text{F}$ ), it is formed an uniform layer of straight nanotubes, where each wall is in direct contact with adjacent tubes; while for DMSO electrolyte (with HF), it is formed a bundle of individual and longer nanotubes, with higher surface area but poorer mechanical stability. The growth mechanism of these materials has been

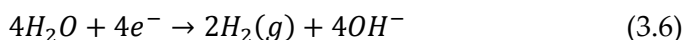
proposed in earlier works [8,9]. The reactions involved in the nanotubes generation changes in the presence of fluoride ion. Without these fluoride ions a compact dielectric oxide layer on the Ti surface is generated, preventing further growth of the oxide, following the equations 3.1 – 3.3:



When fluoride ions are present in the anodization process, it strongly affects the growth mechanism of the layer, generating water soluble  $[\text{TiF}_6]^{2-}$  species. The complexation occurs with the  $\text{Ti}^{4+}$  when is ejected at the oxide-electrolyte interface (migration through the oxide film, Eq. 3.4) and on the other hand, by the chemical attack over the formed  $\text{TiO}_2$ :



Simultaneously, at the counter electrode (Pt), the hydrogen evolution reaction takes place, Eq. 3.6:



The role of the fluoride ion is thus to maintain a thinner bottom oxide layer [10] by chemical etching of the oxide layer and

immediate complexation (solvatization) of  $\text{Ti}^{4+}$  species arriving at the oxide–electrolyte interface. On the other hand the small size of the fluoride ions competes with  $\text{O}^{2-}$  migration through the  $\text{TiO}_2$  bottom oxide. The fluoride ions can migrate two times faster than  $\text{O}^{2-}$  through the oxide lattice, generating a fluoride–rich layer at the metal–oxide interface [11]. The mechanism proposed by Macak *et al.* [12] is shown in *Figure 3.3*. The generation of the fluoride–rich layer has a very important role in the development of the tube morphology. This fluoride–rich layer and the effect of the water content modify the etching rate, been faster than the nanotubes growth rate. The separation of the tubes and the etching rate is determined by the fluoride concentration and the water content in the electrolyte (fluoride solubility).

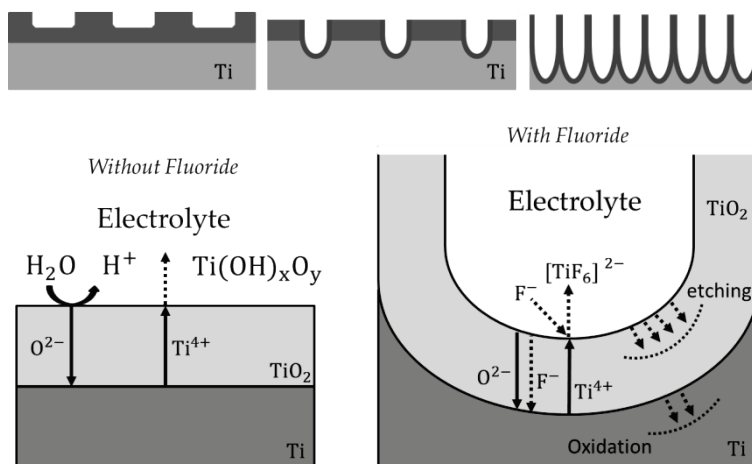


*Figure 3.3.* Scheme of the TiNTs generation mechanism, Macak *et al* [12].

### 3.2.1 Hierarchical TiNTs Synthesis by Anodization

In order to have a highly uniform layer of nanotubes, the importance of the two anodization steps was explained by Jessensky and Zhang [13,14]. Briefly, as illustrated in *Figure 3.4*, the first large anodization gives a patterned substrate and in the second one the nanotubes growth more uniform giving better shape and attachment to the substrate. With the patterned titanium foil the electric field and the morphology in the nanotubes growth have a regular distribution across the surface in the beginning of the anodization, avoiding the randomly electric field distribution using no patterned Ti foil. With the patterned sample the electric field occurs in the imprints generated in the first anodization, improving the uniformity and orderliness of the nanotubes [15]. There are many reported works explaining the positive effect over the TiNTs using the two anodization steps [14–20].

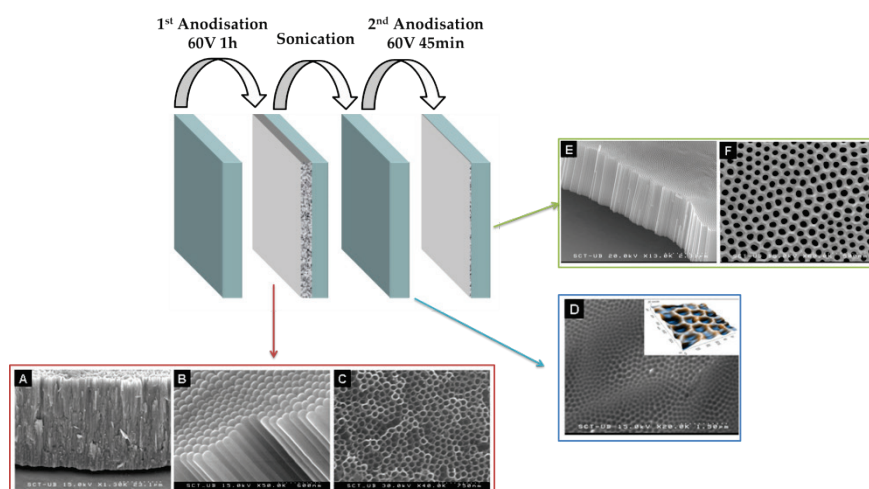


*Figure 3.4.* Scheme of TiNTs synthesis using the two step method.

In our work the two steps method was used but using two different electrolytes to take profit of the different morphologies for patterning (step 1) and layer growth (step 2). The objective was to increase the surface area of the nanotubes and at the same time to tune the surface morphology to generate light trapping centers [21–26]. The example of the different morphology is shown in *Figure 3.2*. When the anodization was carried on DMSO the TiNTs generated in this electrolyte are more separated with big pores (100 – 300 nm) and large length (*a*). When EG electrolyte is used a compact layer of nanotubes like a bee panel is generated with smaller pore sizes (*b*). For these hierarchical nanotubes the synthetic procedure follows this sequence: (1) anodization in DMSO, (2) nanotubes peeling off and (3) anodization in EG (*Figure 3.5*).

The materials used were: titanium foil (99.7%, 250  $\mu\text{m}$  thick, Sigma-Aldrich) was used as substrate to perform the anodization. The organic electrolytes used were dimethylsulfoxide (DMSO, 99.9%, Alfa Aesar) and ethyleneglycol (EG, 99.5%, Fluka), with added fluorhydric acid (HF,  $\geq 40\%$ , Sigma-Aldrich) or ammonium fluoride ( $\text{NH}_4\text{F}$ , 98%, Fluka). To clean the substrates, isopropanol, acetone and ethanol (Panreac) were used as well as hydrogen peroxide ( $\text{H}_2\text{O}_2$ , 33%, VWR International) for the detachment of nanotube layers (step 1).

The setup used in the anodization synthesis was shown in **Chapter II**, the cell used was a specific homemade design for exposing just one side of the titanium foil (working electrode), with

an exposed surface area of  $3.14 \text{ cm}^2$ , in a two-electrode configuration with platinum as counter electrode.

For the first anodization a solution containing 50 mL of DMSO, 2 vol% HF and 1 mL of Milli Q water ( $18.2 \text{ M}\Omega$ ) was prepared in a Teflon vessel and stirred during 1 h. Water was added to the electrolyte since it helps the nanotubes peel off the titanium foil to obtain the patterned substrate.

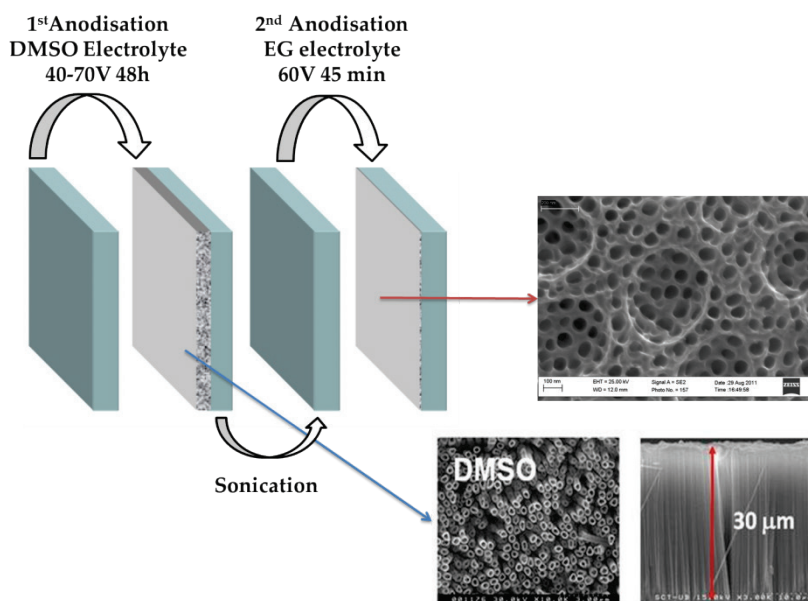


**Figure 3.5.** Hierarchical TiNTs synthetic route scheme using double anodization protocol in DMSO and EG electrolytes.

Afterwards, the solution was transferred to the anodization reactor where the cleaned Ti foil was incorporated and then, the anodization was started. To pattern the Ti metal substrate four voltages were selected: 40, 50, 60 and 70 V for the DMSO step in which the pore size increase with the voltage. To obtain a clean Ti

substrate the sample was immersed in water (with added  $\text{H}_2\text{O}_2$ ) and sonicated to peel off all the nanotubes, obtaining a clean and patterned surface with different pore size. The patterned substrate was rinsed with deionized water and dried under  $\text{N}_2$  stream. For the second anodization step, a solution containing 50 mL of EG, 0.3 wt%  $\text{NH}_4\text{F}$  and 3% in volume of Milli Q water (18.2 M $\Omega$ ) was prepared and kept under stirring during 1 hour. After, the electrolyte was transferred to the anodization reactor with the patterned Ti substrate. For this step the experimental conditions were the same for all the samples, with an applied voltage of 60 V during 45 min, obtaining the TiNTs compact layer with a bee panel organization. Afterwards, the sample was cleaned with a large amount of deionized water and dried under  $\text{N}_2$  stream. To obtain a reference sample the two steps was done but in this case only EG electrolyte was used using the same EG solution for the two steps. The voltage for the two steps was fixed at 60 V. The first anodization was done during 1 h and the second one using the same electrolyte 45 min.

All the samples were further dried in an oven at 200°C in air overnight. Finally, the samples were annealed at 500°C under air atmosphere during 2h (heating rate: 5°C/min) to crystalize the amorphous  $\text{TiO}_2$  obtained in the anodization to anatase.

#### **3.2.2 *Structural and Morphological Characterization***

To study the layer growth during the second anodization step in the hierarchical TiNTs some samples were prepared using only EG electrolyte, with two  $\text{NH}_4\text{F}$  concentrations (0.3 and 0.5 wt%) at

different anodization times in the second step. Later, the samples were cut to observe the cross section by SEM and the thickness of the samples at the different selected times. Cross section images and the anodization layer growth in the time interval studied (up to 45 min) using EG electrolytes are shown in *Figure 3.6*.

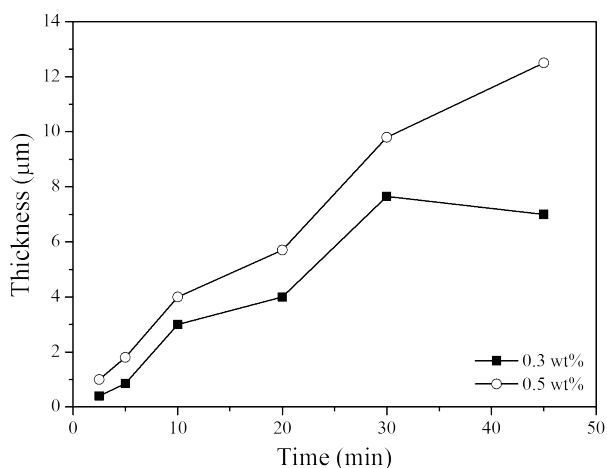
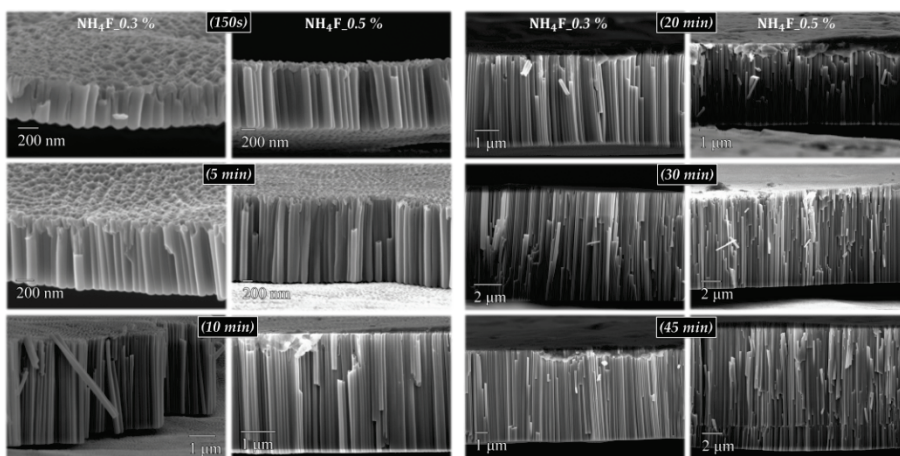


*Figure 3.6.* EG TiNTs cross section at different second anodization times, using electrolytes with different  $\text{NH}_4\text{F}$  concentration (0.3 wt% and 0.5 wt%). Plot of Layer thickness versus time of the hierarchical TiNTs using two ammonium fluoride concentrations.

In the plot is possible to observe a linear thickness growth with time up to 30 min for both electrolytes, with a slight tendency to decrease layer growth rate at 45 min. In all cases the samples obtained with 0.3 wt%  $\text{NH}_4\text{F}$  are thinner than the ones obtained with 0.5wt% electrolyte, indicating a lower dissolution rate mediated by the formation of  $[\text{TiF}_6]^{2-}$  complex. Thus, the concentration of free fluorine in the electrolyte is highly affecting the layer thickness, with is evidenced by the deviation of linearity at the longest anodization time. Since in the synthesis of these samples the electrolyte is reused, the layer growth for 0.3 wt% electrolyte was stopped and no variation in thickness was observed between 30 and 45 min. When using a fresh electrolyte (EG, 0.3 wt%  $\text{NH}_4\text{F}$ ) the thickness is around 10-11  $\mu\text{m}$  (instead of 7  $\mu\text{m}$  in the consecutive anodization), corroborating the need of free fluorine in the electrolyte for a progressive thickness growth. For the hierarchical nanotubes we select 45 min in the second anodization in EG with 0.3 wt%  $\text{NH}_4\text{F}$ , since it was optimum for photocatalytic reactions mentioned by Schmuki [4]. In this case, the first anodization in DMSO gives a patterned surface with a clearly different pore size compared with EG. SEM images in *Figure 3.7* of the samples give a view of the change in the morphology when the two electrolytes were used. An example of an AFM image was also shown, from which the value of the pore depth was obtained of the DMSO patterned surfaces.

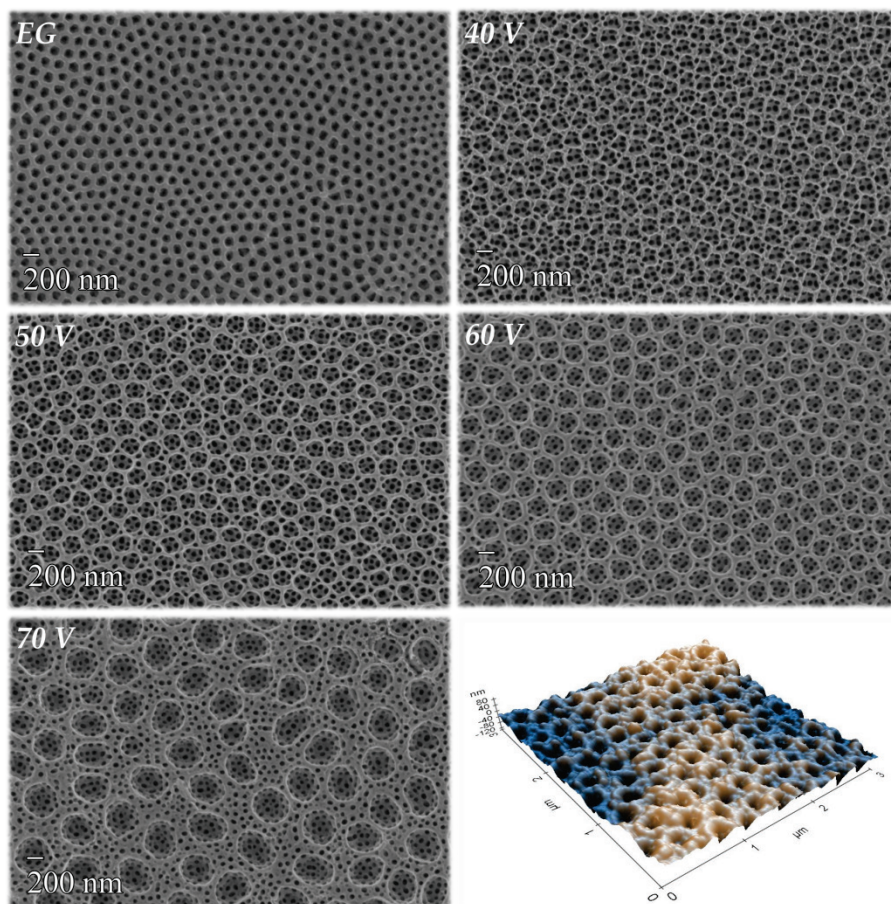


**Figure 3.7.** SEM images of the hierarchical nanotubes morphology obtained using the two different electrolytes and AFM example image of the DMSO patterned Ti surface.

The cross section of the hierarchical TiNTs can be observed in **Figure 3.8**, from which it can be depicted the thickness of each sample, ranging between 9.5 and 11  $\mu\text{m}$ .

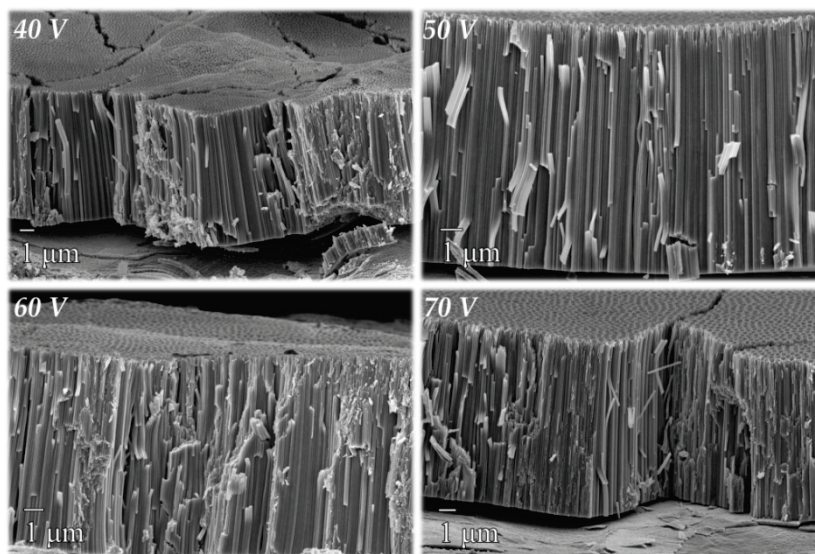


**Figure 3.8.** SEM cross section of hierarchical TiNTs at each voltage. The average of thickness for the samples is: 9.4, 11.6, 11.1 and 10.9  $\mu\text{m}$  for 40, 50, 60 and 70 V respectively.

As mentioned before, the objective of the big pore generation is to act as a light trapping hole. **Figure 3.9** shows the surface morphology of these light traps formed by concavities organized in a hexagonal distribution.

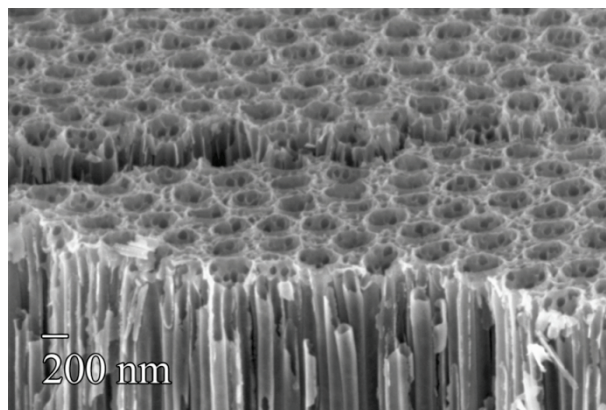


*Figure 3.9. Example SEM tilted top view to observe the surface morphology.*

To confirm the crystal structure of all the samples prepared, a XRD was done. After the thermal treatment at 500°C, the predominant crystal phase obtained was anatase, altogether with the presence of rutile phase at very low intensities (*Figure 3.10*). Some diffraction peaks corresponding to titanium substrate also appears. According to a previous study, the samples consist of a surface layer of anatase nanoholes (anodized film) on top of a rutile layer, formed during the annealing process [27].

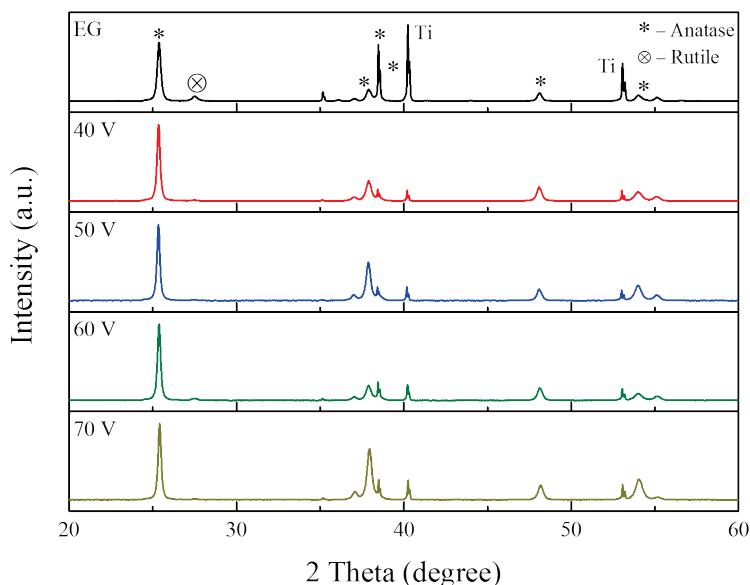


**Figure 3.10.** XRD pattern of the TiNTs samples prepared at different voltages in the first anodization step and the flat sample with only EG electrolyte.

In order to get the geometrical parameters of the patterned surfaces, using SEM images and AFM measurements is possible to obtain the values of pore size, wall thickness, DMSO pore depth and cross section of the nanotubes at each potential. With all these data a theoretical model could be postulated to obtain the surface increment of the hierarchical samples respect the EG (flat one). The DMSO pore organization of practically all the samples is like a bee panel, in other words, exhibits a hexagonal organization. The scheme of the theoretical model is shown in *Figure 3.11*.

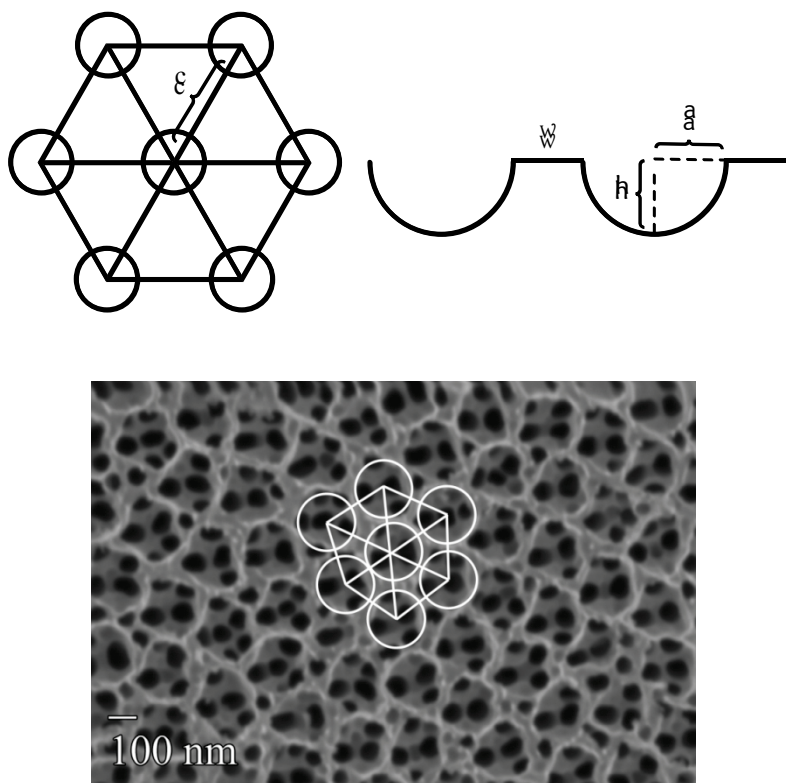


**Figure 3.11.** Theoretical model postulated for the surface area increment coming from the DMSO anodization. Second images the model applied over the 40 V sample.

There are different parameters used in the model  $c$  (distance between two pore center),  $a$  (pore radius),  $w$  (wall thickness) and  $h$  (pore depth). The following formulas were used for the calculation of the outer surface increment.

$$c = 2a + w \quad (3.7)$$

$$S_{\text{hexagon}} = \frac{3\sqrt{3}}{2} (2a + w)^2 \quad (3.8)$$

$$S_{pore} = 3\pi(a^2 + h^2) \quad (3.9)$$

$$S_{section} = 3\pi a^2 \quad (3.10)$$

$$S_{increment}(\%) = \frac{3(S_{pore} - S_{section})}{S_{hexagon}} \times 100 \quad (3.11)$$

The formulas used to obtain the value of the increment of surface area come from: Eq. 3.7 distance between the center of two pores, Eq. 3.8 hexagonal geometrical area, Eq. 3.9 and Eq. 3.10 a spherical approach which fits to the pore geometry to obtain the pore surface. When all of them are substituted in Eq. 3.11 the surface area percentage value is obtained. The number 3 in the Eq. 3.11 is the amount of pores which are included in the hexagonal model. Results of surface increment, including the geometric parameters, are summarized *Table 3.1*).

*Table 3.1. Average data obtained from SEM images and AFM topography with the corresponding error value, and the surface percentage increment for each sample ( $\emptyset$ , pore diameter; E, error.*

Sample	$\emptyset$ (nm)	E	$h$ (nm)	E	$w$ (nm)	E	$S_{\%}$
40 V	186	1.5	74	2.3	36	1.9	40
50 V	205	1.1	80	2.3	48	2.1	36
60 V	264	2.1	104	1.9	65	2.5	36
70 V	416	6.3	177	5	158	8.6	34

The data in *Table 3.1* shows the correspondent surface increment introduced in the DMSO anodization step. The value of  $S_{\%}$  was obtained taken as reference the sample with only EG anodization. When the data is analyzed is possible to observe the fact that when the voltage is increased the surface area percentage decrease using the postulated model. But in the case of the **70 V** sample the pore organization not fit under the hexagonal model, due to the pore disorganization obtained in the anodization step shown in *Figure 3.7*. This sample is forced to adjust to the model but the value of the surface increment for this sample is not the real one, when the adjustment is not done with this hexagonal model the values will be lower. The best value of surface increment using this model was obtained for the **40 V**, if the surface increment is correlated with the photoactivity the best value in photocurrent must be obtained.

### **3.2.3**    *Optical Characterization and PEC Measurements*

The optical characterization of  $\text{TiO}_2$  nanotubes was based on reflectance measurements, since the metallic foil substrate used is opaque and the transmittance in these samples is zero. The wavelength range selected for  $\text{TiO}_2$  was from 300 to 420 nm where the material is active. In *Figure 3.12* is possible to observe the optical response of the samples. The absorptance was calculated using the reflectance values and Eq. 3.12 and 3.13.

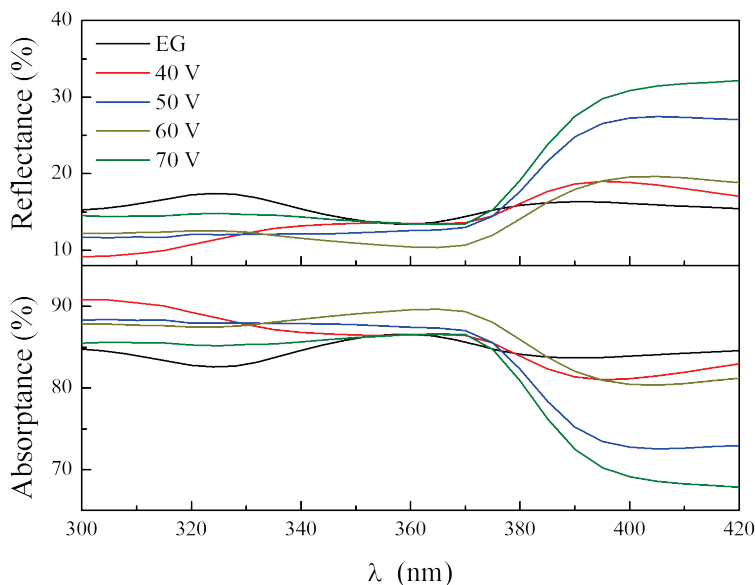


*Figure 3.12. UV - Visible experiments, reflectance and absorbance.*

The absorptance of a material is its effectiveness in absorbing radiant energy. Thus, it is the fraction of incident radiation that is absorbed at the material. Taking into account that all incident light can be either absorbed, reflected or transmitted:

$$1 = A + T + R \quad (3.12)$$

In our case, as mentioned before, the substrate is not transparent and the value of the transmittance is zero, therefore, the equation used was:

$$A = 1 - R \quad (3.13)$$

In all cases, in the range below 370 nm, the DMSO patterned samples gives lower values of reflectance than the EG which is flatter and reflects more the light. For the hierarchical TiNTs

samples there are no so much differences in the values. But between 300 – 330 the reflectance value of the **40 V** sample are lower compared with the rest but after increase and the others have lower values.

To corroborate if the surface structuration gives more photoactivity more experiments are required. The different measurements done and calculations are reported by Jaramillo *et al* [28]. In their review explain the different protocols and standards for PEC hydrogen production.

The first method used is the incident photon to current efficiency (IPCE), which gives the photocurrent collected per incident photon flux as a function of illumination wavelength. The IPCE for PEC devices is obtained from a chronoamperometry (potentiostatic) measurement. In this system a bias was applied (0.2 V *vs.* Ag/AgCl -1.23 V *vs* RHE: water splitting potential-) in a three electrode cell. This system measure the current that arises from subjecting the photoelectrode to monochromatic light at various wavelengths. This IPCE corresponds to the ratio of this photocurrent (converted to an electron rate) versus the rate of incident photons (converted from calibrated power of a light source). Calibrated monochromated light should be used for this experiment. With the data obtained from the experiments mentioned before ( $|j_{ph}(mAcm^{-2})|$ ) and Eq. 3.14 is possible to obtain the values of IPCE.

$$IPCE(\lambda) = \frac{|j_{ph}(mAcm^{-2})| \times 1239.8(V \times nm)}{P_{mono}(mWcm^{-2}) \times \lambda(nm)} \times 100 \quad (3.14)$$

Where  $1239.8 V \times nm$  is a multiplication of  $h$  ( $6.626 \cdot 10^{-34} J s$ , Planck's constant) and  $c$  ( $3 \cdot 10^8 m s^{-1}$ , speed of light),  $P_{mono}$  is the calibrated and monochromated illumination power intensity ( $mWcm^{-2}$ ) and  $\lambda$  (nm) is the wavelength at which this illumination power is measured. For PEC water-splitting IPCE describes the maximum possible efficiency which incoming radiation can produce hydrogen from water.

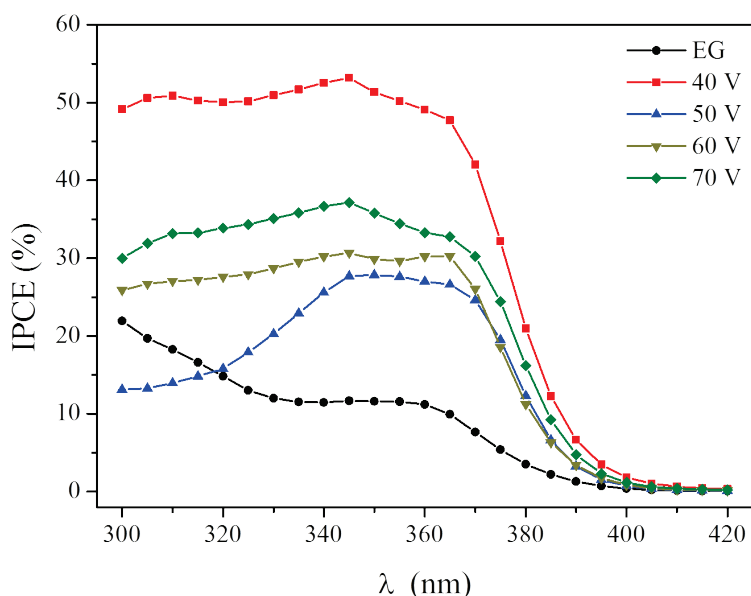
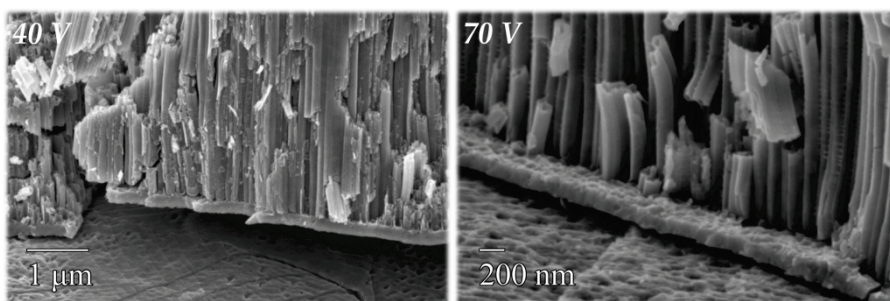


Figure 3.13. Incident photon-to-current efficiency (IPCE) of TiNTs, at 0.2V vs Ag/AgCl, 1M NaOH.

In Figure 3.13 for the hierarchical TiNTs higher values respect the EG flat sample were reached. The values of IPCE obtained have correlation with the surface area increment for the 40, 50 and 60 V because the theoretical model adjusts better to their pore distribution. In the case of the 40 V sample reach to the highest IPCE value. But in the case of the 70 V sample the IPCE is higher

than 50 and 60 V. The thickness of the TiNts layer is not the responsible because in these samples are quite similar as mentioned in *Figure 3.8*. The only difference between them is a thin compact oxide layer observed in SEM cross section images for the 70 and 40 V, for 50 and 60 this oxide layer does not appear. This oxide layer around 200 nm improves the contact of the nanotubes with the Ti substrate decreasing the resistance and improving the electrons collection [29].



*Figure 3.14. SEM images of 40 and 70 V compact oxide layer between the substrate and the nanotubes bottom.*

Using the IPCE plot is possible to obtain the effective band gap of our material. Following this formula Eq. 3.15:

$$\text{Band gap } (E) = \frac{h \times c}{\lambda} \quad (3.15)$$

Where  $h$  (Planck constant) is multiplied by  $c$  (speed of light) and divided between  $\lambda$  (cut off wavelength of the IPCE, nm) and using the conversion factor ( $1\text{eV} = 1.6 \cdot 10^{-19} \text{J}$ ) we obtain the values of the band gap for each sample. The values of the band gap are for all the samples are the same 3.16 eV corresponding with the anatase value ( $\approx 3.2 \text{eV}$ ).

The IPCE values include the losses from impinging photons that are reflected or transmitted. To measure the efficiency based on the absorbed photons is required the APCE (absorbed photon to current efficiency). This value helps to determine the optimum balance between maxima path length for photon absorption versus minimal effective  $e^-/h^+$  transport distance within the material. The data in *Figure 3.15* was obtained using this formula:

$$APCE = \frac{IPCE}{\eta_{e^-/h^+}} = \eta_{transport}\eta_{interface} \quad (3.16)$$

The factor  $\eta_{e^-/h^+}$  is the absorptance, obtained from the reflectance; this fraction is defined as the electro-hole ( $e^-/h^+$ ) pairs generated per incident photon flux. The values have the same order as in the IPCE but with an increment in all of them due to avoid the losses from the IPCE.

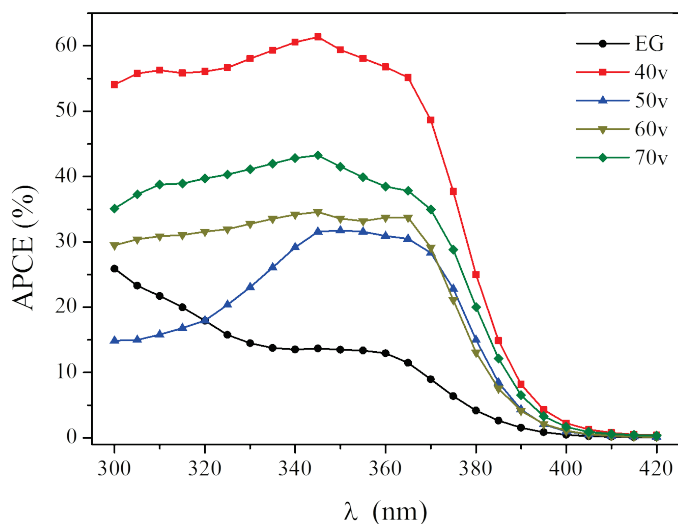


*Figure 3.15.* Absorbed photon-to-current efficiency (APCE) comparative values of the TiNts prepared.

The photocurrent density ( $j$ ) respect the wavelength (*Figure 3.16*) can be obtained when the IPCE is multiplied with the photon flux density of the AM 1.5G solar spectra over the range in which the material is active. For the  $\text{TiO}_2$  the optimal range is between 300 – 420 nm. The value of  $j(\lambda)$  can be obtained using this formula:

$$\int_{300}^{420} IPCE \times G(\lambda) d\lambda = \langle j_{\lambda} \rangle \quad (3.17)$$

Where  $G(\lambda)$  corresponds to the photon flux obtained from the AM 1.5G solar spectra in the mentioned wavelength range. The current density values obtained gives the total charge generated.

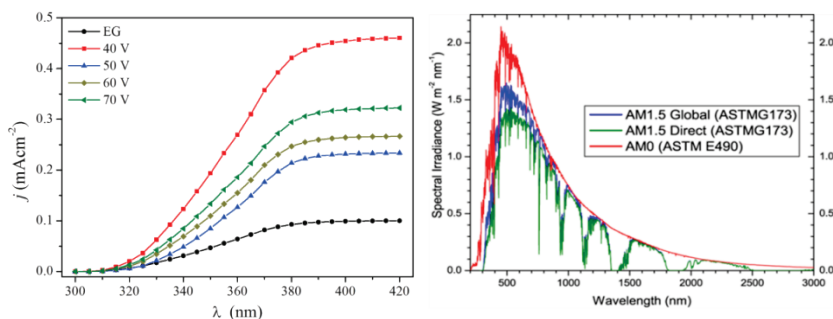


**Figure 3.16.** Current density integrated from IPCE values at 0.2 V (Ag/AgCl) using AM 1.5G solar spectra (300-420 nm) (<http://rredc.nrel.gov/solar/spectra/am1.5/>).

Photoelectrochemical measurements were done over the photoelectrodes to observe the current for the prepared samples using only EG and with the DMSO step. Linear-sweep voltammograms (LSV) were recorded under illumination of 100 mW cm<sup>-2</sup> (AM 1.5G), as shown in *Figure 3.17*.

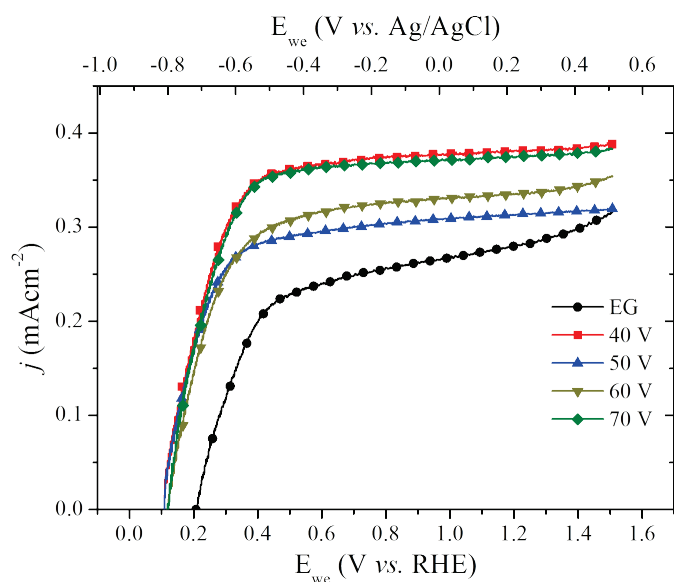


**Figure 3.17.** Linear Sweep Voltammetry (LSV) measurements in 1M of NaOH using AM 1.5G illumination source ( $100 \text{ mW cm}^{-2}$ ).

The potential was swept linearly at a scan rate of  $20 \text{ mV s}^{-1}$  between 0 and 1.5 V *vs.* RHE. Under illumination, at 1.23 V *vs.* RHE (corresponding to the potential of the reversible oxygen electrode), the current density is  $0.38 \text{ mA cm}^{-2}$  for the 40 V and 70 V sample showed higher photocurrent density throughout the potential window which suggested efficient charge separation. Another effect observed is the onset potential which shifts 0.1 V to more negative values in the hierarchical samples respects the flat sample. This onset potential shift gives better performance for the water splitting process. The EG sample only reach to  $0.28 \text{ mA cm}^{-2}$  at 1.23 V *vs.* RHE, while the 40V sample has a 135% higher photocurrent than the flat sample.

### **3.3 Titanium Dioxide Nanorods**

Nanowire/nanorods have demonstrated a great potential of achieving high diffusion coefficient of carriers in electric devices, because of their unique one-dimensional (1D) structure [30]. When a nanoparticle-based photoanode of DSSC is substituted with the nanorods based photoanode, it is expected that the nanorods will provide a ballistic pathway for the carriers and enhance the carrier transport [31–35]. In this work we focused on the anodization and hydrothermal synthesis due to the improvement over the electrons collection. In nanoparticle-based (as mentioned in TiNTs section) DSSCs, carrier transport mostly is through simple diffusion instead of drift force under built-in potential as in silicon solar cells. To conserve charge neutrality, cations in electrolyte make a corresponding movement through porous nanoparticle networks as electrons diffuse to the anode direction, and it is a type of ambipolar diffusion. The mobility of electrons usually is faster than that of cations, but electric field built from the position difference between electrons and cations will slow down the movement of electrons and eventually maintain equilibrium. In nanorod photoanodes, it is expected that the existence of radial and axial fields will guide electrons to go through nanorod and the ambipolar diffusion mode may be not valid. It is reported that the stable high fill factor (FF) and increasing short circuit current as the length of TiO<sub>2</sub> nanowire gets longer arise from the elongated lifetime of the carriers [36]. Kang et al. analyzed the effect of short nanorod based electrodes on DSSCs, and reported enhanced carrier

lifetime when the aspect ratio of the individual nanoparticles increases [37]. In contrast to the carrier lifetime, the improvement of the carrier transport has not been clearly observed in the nanorod based DSSCs. This is due to the unique microstructure of the nanowires grown by an oriented attachment technique, which includes locally formed necks and sudden turns in the electron path [38,39]. Enache-Pommer has examined carrier transport in single crystal ZnO nanowire, TiO<sub>2</sub> nanoparticles, polycrystalline TiO<sub>2</sub> nanowire, and single crystalline rutile nanowire [40]. The transport rate of carriers in ZnO nanowire is independent of illumination light, and is at least two orders faster than recombination rate [41]. The transport time of polycrystalline TiO<sub>2</sub> nanowires exhibit a similar power law dependence of illumination intensity as that of nanoparticles, although the ratio of recombination time to collection time is much larger than that in nanoparticles. It has been expected that single crystalline TiO<sub>2</sub> may make a difference. In contrast, for the single crystalline rutile nanorods, it is reported that the carrier transport is slower for the rutile nanorod than for the anatase P25 particles [42]. In collaboration with other groups [43], we overcome the main limitation for DSSCs cells using a rutile–hongquite core–shell system. The method used was electrodeposition of a layer of TiO over TiO<sub>2</sub> rutile nanorods, improving the energy conversion by a factor of 2.5. This overlayer introduced higher roughness factor and improved the electron injection from the dye to the TiO<sub>2</sub> nanorods.

### 3.3.1 *TiO<sub>2</sub> Nanorods Hydrothermal Synthesis Optimization.*

The hydrothermal method to obtain the TiO<sub>2</sub> nanorods was reported before by Wu *et al.* [44] and lately by Liu and Aydil [45]. In their work a hydrothermal method was developed to grow oriented single-crystalline rutile TiO<sub>2</sub> nanorod films on transparent conductive substrates studying different synthetic conditions. The growth parameters including growth time, growth temperature, initial reactant concentration, acidity, and types of additives could be selectively chosen to prepare TiO<sub>2</sub> nanorod film with desired lengths and densities. The small lattice mismatch between the FTO substrate and rutile TiO<sub>2</sub> plays a key role in driving the nucleation and growth of the rutile TiO<sub>2</sub> nanorods on FTO. Other review of the nanorods synthesis conditions was done by Kumar *et al.* [46] in this work they made a deep study of the growth mechanism of the TiO<sub>2</sub> over different glass substrates positioned at different angles position. The growth mechanism of the crystals is mainly determined by the relative growth of various crystal faces which is dependent on internal structure factors of a given crystal or on external conditions such as temperature, precursor concentration, pH. In rutile TiO<sub>2</sub>, every Ti atom is bound to six atoms of oxygen forming an octahedral chainlike structure. The growth rate depends on the number of corners and edge of the polyhedral. The growth rate of the crystal faces usually follows these sequence **(001) > (101) > (100) > (110)**.

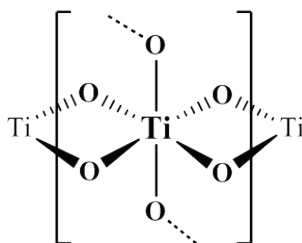
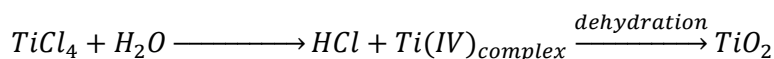


Figure 3.18.  $TiO_2$  octahedral complex as a chainlike structure.

The reaction growth of the  $TiO_2$  nanorods synthesis is based in a hydrolysis followed by a deshydration generating the nanostructured film.



When abundant amount of  $H^+$  from  $HCl$  is added restricts the supply of the growth and the rods does not been formed. The chlorine ion  $Cl^-$  restrict growth of the (110) faces further enhancing the growth along the (001) and (101) direction [45,47,48].

We study the different synthetic conditions for the  $TiO_2$  nanorods generation. The parameters fixed were the hydrothermal time (4h), and temperature  $200^\circ C$ . The synthesis was carried out on a fluorine tin oxide conductive glass substrate, FTO, ( $9\text{ cm}^2$ ) half of them masked with Teflon<sup>®</sup> tape to act as electrical contact afterwards. Once the synthesis was complete, the piece was cut obtaining three electrodes of  $1.5\text{ cm}^2$  (this is de geometrical area for all the photoanodes for the subsequent studies). The reactor used was filled until 60 mL of solution with different  $HCl$  concentration and titanium butoxide ( $Ti(OC_4H_9)_4$ ) (Fluka) as titania precursor (hydrothermal setup and images in **Chapter II**).

To obtain nanorods well aligned the conductive glass substrate was introduced in the Teflon reactor facing down with a 45° angle to avoid the formation of dandelion structures instead of nanorods [46]. A scheme of the synthesis pathway can be observed in *Figure 3.19*. After the synthesis the samples were subjected to a thermal treatment (2h at 500°C, in air) to improve the contact with the substrate and remove the chlorine impurities attached to the nanorods surface [49].

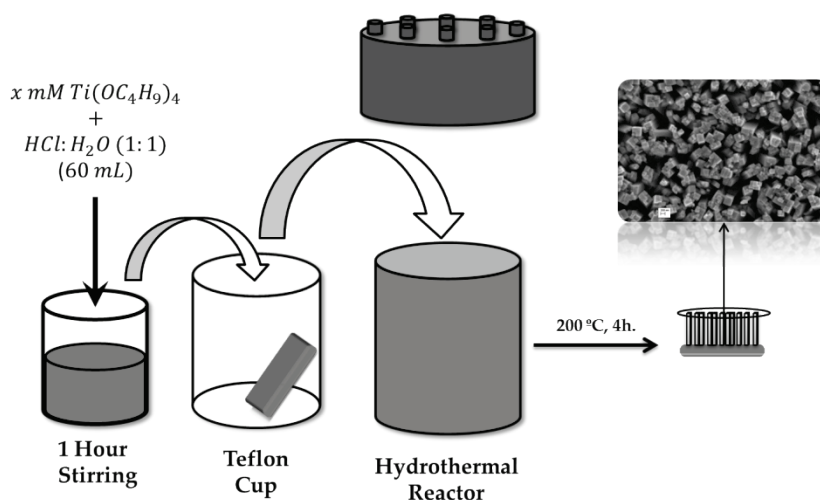


*Figure 3.19.* TiO<sub>2</sub> nanorods hydrothermal treatment synthesis pathway.

The parameters modified in the TiO<sub>2</sub> nanorods synthesis are summarized in the table below (*Table 3.2*).

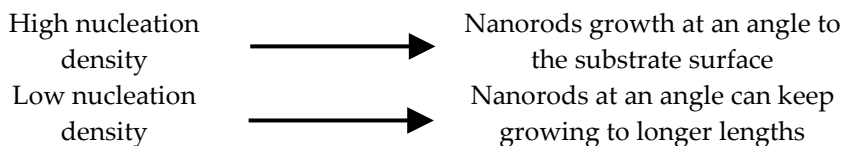
*Table 3.2. Hydrothermal synthesis conditions under study for the nanorods generation.*

<b>Ti(OC<sub>4</sub>H<sub>9</sub>)<sub>4</sub> (mM)</b>	<b>CaCl<sub>2</sub> (M)</b>
40	0.25
50	0.5
60	1
70	

### 3.3.1.1 Effect of Titanium Precursor Concentration

To observe the effect of the titanium precursor amount, we set the other experimental parameters. The ratio HCl:H<sub>2</sub>O was fixed to 50:50 without any added chlorine source. The different amount of precursor used was mentioned in *Table 3.2*.

The surface morphology obtained using the different concentration was followed by SEM images. The nanorods obtained have different densities, size and thickness. If the amount of titanium butoxide is increased it promotes rapid hydrolysis and TiO<sub>2</sub> is precipitated in the solution. Modifying the nucleation density it is possible obtain different rods morphologies.



In *Figure 3.20* is possible to observe the  $\text{TiO}_2$  nanorods morphology using different titanium precursor concentrations.

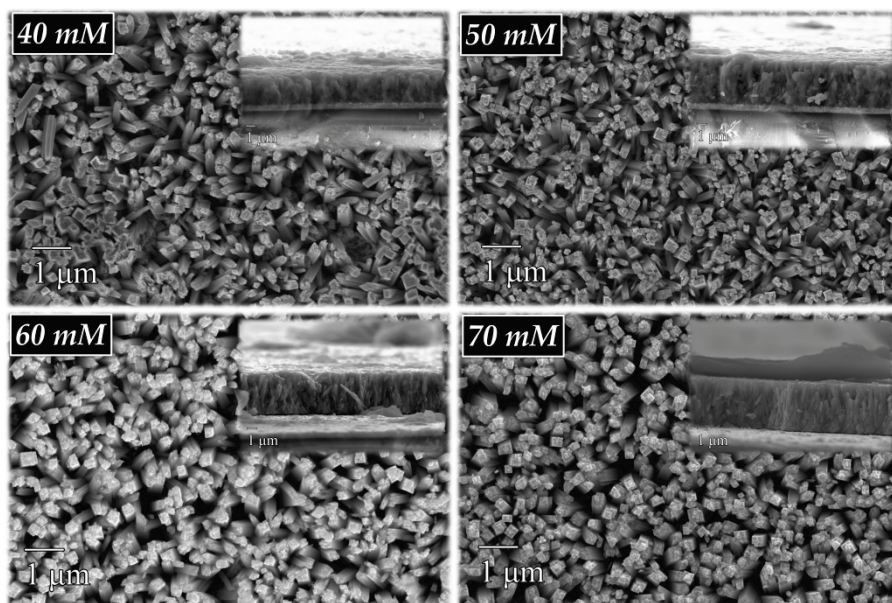


*Figure 3.20.* SEM top view and cross section images of the  $\text{TiO}_2$  nanorods with different precursor concentration.

In the top view images it is possible to observe an increase in the nanorods density when the titanium butoxide concentration is increased. The layer thickness and cross section values are shown in *Figure 3.21*. The rods shape is like a cuboid, whose edge sizes were measured taking the distance between two parallel sides.

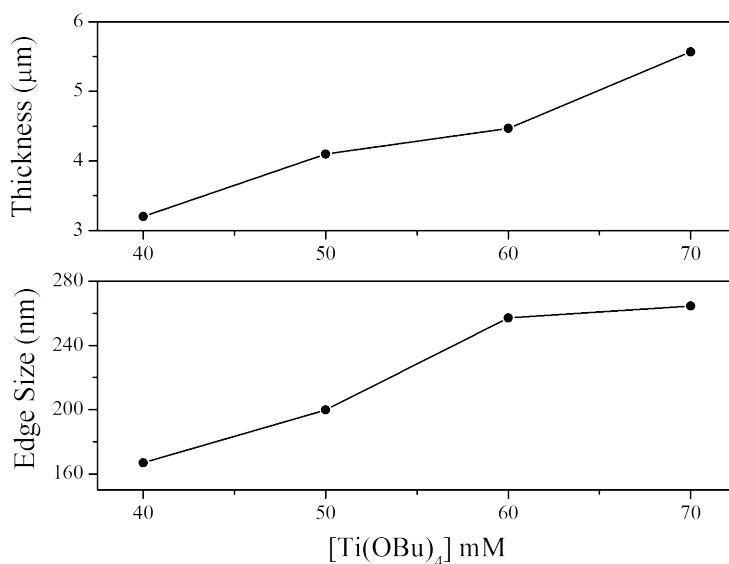


**Figure 3.21.** Cross section and nanorods edge size values evolution when the Ti concentration is increased.

The increment in the rods size goes with the precursor concentration. But, in the cross section values at 50 and 60 mM the tendency is similar.

XRD (*Figure 3.22*) analysis reveals that the crystal structure of the nanorods is mainly rutile TiO<sub>2</sub> with the preferential direction (101) and (002). The SnO<sub>2</sub> peaks observed come from the conductive glass substrate (fluorine tin oxide, FTO). If the ratio between TiO<sub>2</sub> and SnO<sub>2</sub> more intense peaks is possible to obtain an idea of the nanorods layer thickness, nevertheless the cross section values are more accurate.

When the SnO<sub>2</sub> peaks are compared with the TiO<sub>2</sub> peaks, is possible to observe that 40 and 50 mM have higher intensities for

the SnO<sub>2</sub> than 60 and 70 mM due to the layer thickness increment with the concentration (*Figure 3.21*).

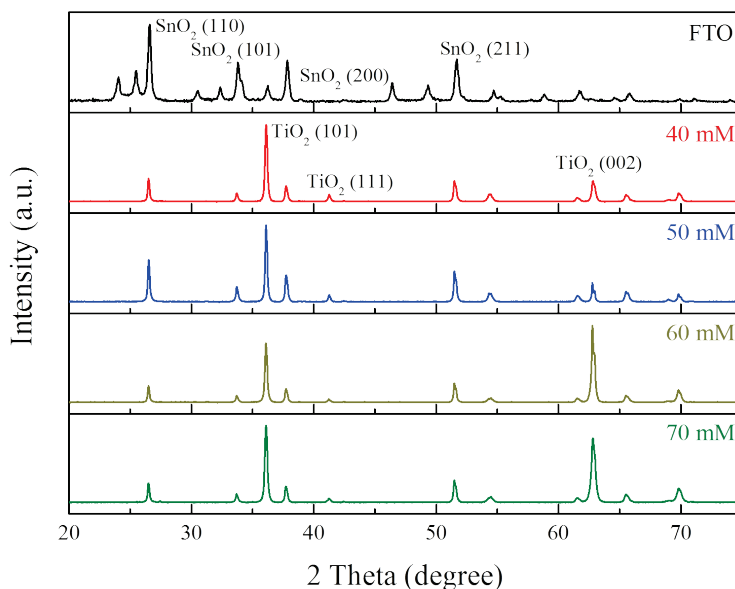


*Figure 3.22.* XRD patterns of the samples with the concentration modification.

The reported preferential direction is (001) but in our case when the TiO<sub>2</sub> nanorods are growth the (101) is the preferential face, due to the substrate. The SnO<sub>2</sub> substrate acts as seed for the TiO<sub>2</sub> nanorods growth and the more intense peak of the FTO after the (110) (direction which is suppressed by the Cl<sup>-</sup> presence) is the (101) and (200) but as mentioned before, by hydrothermal synthesis the (101) growth direction is more favored than (100), for this reason the more intense peak of TiO<sub>2</sub> in this direction is obtained. Consequently for 40 and 50 mM have this direction, however for 60 and 70 mM the (002) direction has higher intensity than the other two concentrations.

To observe the photoelectrochemical activity (*Figure 3.23*) a linear – sweep voltammetry (LSV) were done under 1 sun illumination ( $100 \text{ mW cm}^{-2}$ , AM 1.5G), under two experimental conditions: (1) direct illumination over the  $\text{TiO}_2$  surface (*Front*) and (2) through the conductive glass substrate (*Back*).

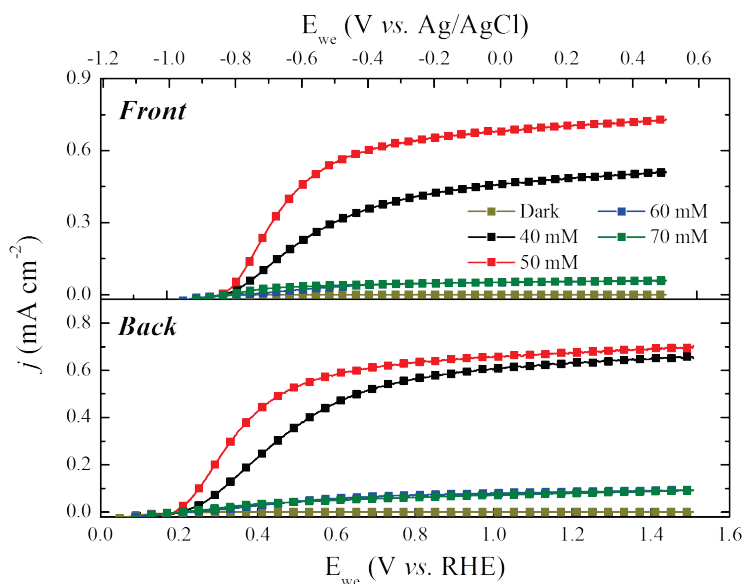


**Figure 3.23.** Linear – sweep voltammograms collected with a scan rate of  $20 \text{ mV s}^{-1}$  in dark and under illumination from the front and back part in  $1 \text{ M}$  of  $\text{NaOH}$ .

Taking the photocurrent values at  $1.23 \text{ vs. RHE}$ , in both illumination pathways (*Front* and *Back*) is the sample synthesized at  $50 \text{ mM}$  the most efficient, with slightly higher values under front illumination, since some UV light is absorbed by the glass substrate and FTO under back illumination. At  $60$  and  $70 \text{ mM}$  the current density is very low, probably due to the different orientation of the crystallites that does not favor electron collection to FTO.

3.3.1.2 *Chlorine Concentration Effect*

The aim to increase the amount of chlorine ions was to control the nanorods thickness, length and crystal orientation. As mentioned before the  $\text{Cl}^-$  ions block the nanorods growth in the (110) direction improving the (001) and (101). If the (110) direction could be block in a higher level, the nanorods could be thinner and the electrolyte can easily be in contact with the nanorod surface, potentially improving its photoactivity. Li *et al.* made a study about the effect in the  $\text{TiO}_2$  nanorods growth when some NaCl was incorporated in the hydrothermal process [45]. Due to the effect of the NaCl over the growth synthesis is decreasing the particle size [47]. In our synthesis conditions the nanorods growth was not successful using NaCl. As sequence, the chlorine compound source was changed to  $\text{CaCl}_2$ . The synthesis was done with the same hydrothermal conditions as used before. The 50 mM of titanium precursor was mixed in the Teflon cup with 0.25, 0.5 and 1 M of  $\text{CaCl}_2$ . In *Figure 3.24* is possible to observe the morphology and the cross section of the synthesized samples.

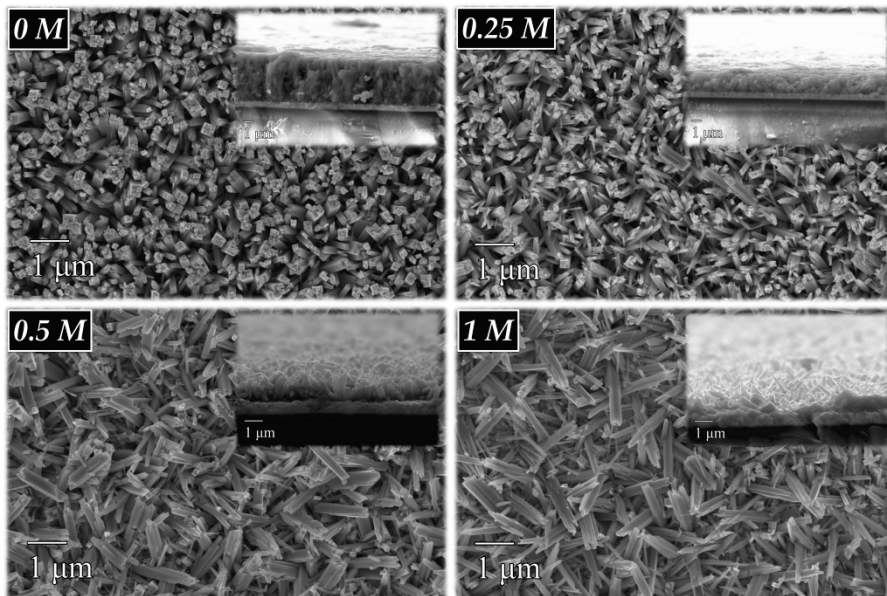


*Figure 3.24.* Top view and cross section obtained by SEM of the samples with 0, 0.25, 0.5 and 1 M of  $\text{CaCl}_2$ .

When the chlorine concentration was increased the  $\text{TiO}_2$  nanorods growth was suppressed in somehow, but the rods edge size and the density was reduced respect the sample without  $\text{CaCl}_2$ .

The values form the rods edge size and the layer thickness can be obtained from the SEM images. The plots to observe the tendency with the increase of the  $\text{CaCl}_2$  concentration can be observed in *Figure 3.25*.

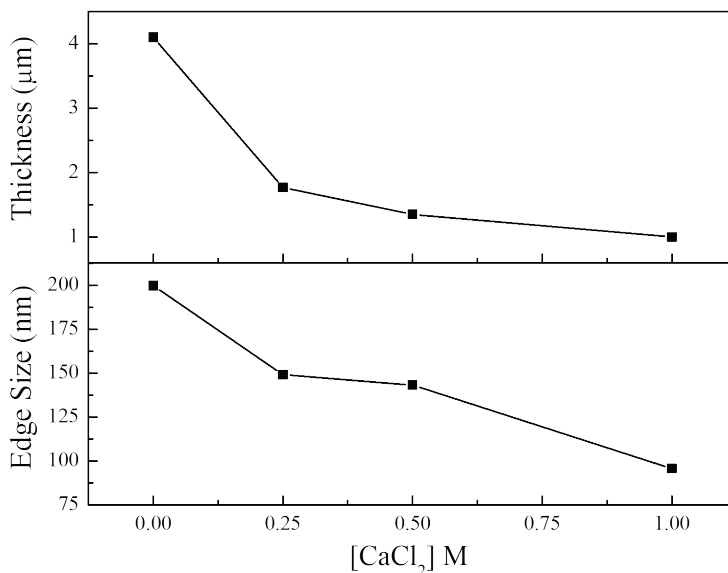


*Figure 3.25. TiO<sub>2</sub> nanorods edge size and layer thickness evolution with the CaCl<sub>2</sub> addition.*

As mentioned before, the tendency obtained from the edge size and thickness is the same, a decreasing respect the no added CaCl<sub>2</sub> sample. Chlorine ions block the growth in the (110) direction but does not enhance the growth in the (101) due to the decrease in the growth rate, and as sequence increasing the growing time.

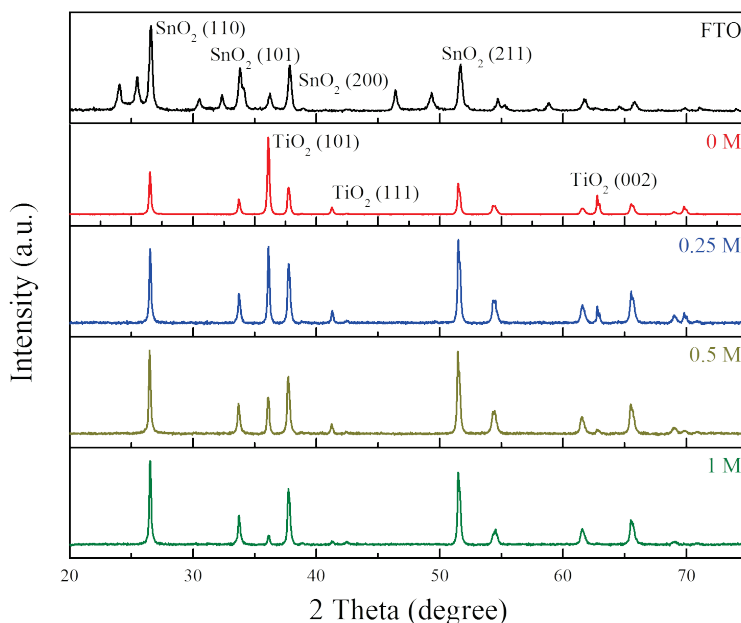


**Figure 3.26.** XRD patterns of the layer evolution from FTO to 0 M sample increasing the TiO<sub>2</sub> characteristic peaks.

The XRD patterns (**Figure 3.26**) show the evolution of the TiO<sub>2</sub> characteristic peaks from the FTO without TiO<sub>2</sub> nanorods, and the addition of different CaCl<sub>2</sub> concentrations; 0, 0.25, 0.5, 1, and 1 M. The TiO<sub>2</sub> (101) and (001) peaks are increasing when SnO<sub>2</sub> peaks decreasing due to the thickness of the TiO<sub>2</sub> nanorods layer which decrease in this order 0 M > 0.25 M > 0.5 M > 1 M > FTO.

For the photoelectrochemical (PEC) measurements a LSV experiment was done for all the samples to observe the photoactivity. Taken the values of current density at 1.23 V *vs.* RHE the values decrease with the chlorine concentration increment. The reason for this current density loss probably comes from the thinner layer and too low density of nanorods.

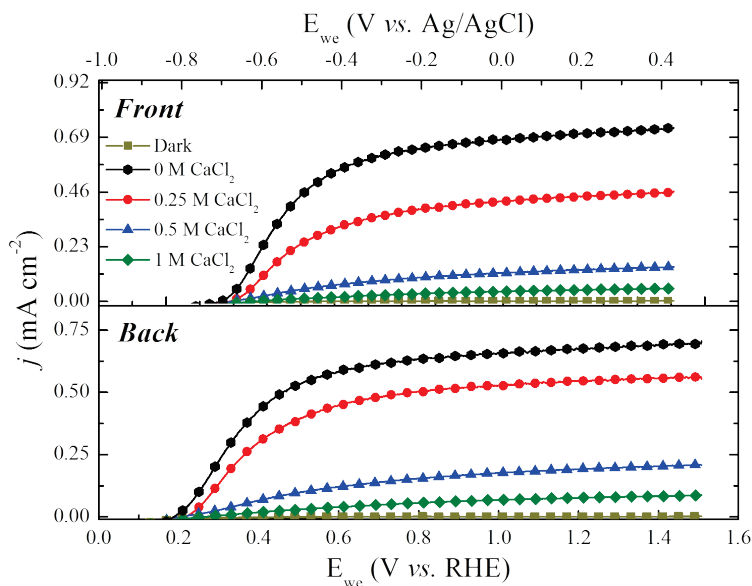


**Figure 3.27.** LSV measurements at  $20 \text{ mV s}^{-1}$  front and back illumination using  $100 \text{ mV s}^{-1}$  solar lamp AM 1.5G for the calcium chloride addition.

As mentioned before chlorine ions slow down the nanorods growth requiring more time to increase thickness and improving the current density of the photoelectrode. To prove if the current density increase keeping the rods size reduction respect the sample without  $\text{CaCl}_2$ , the hydrothermal time was increased from 4h to 5h in the same conditions ( $200^\circ\text{C}$ ). We only used two  $\text{CaCl}_2$  concentrations, 0.25 and 0.5 M to compare with the 4h samples.

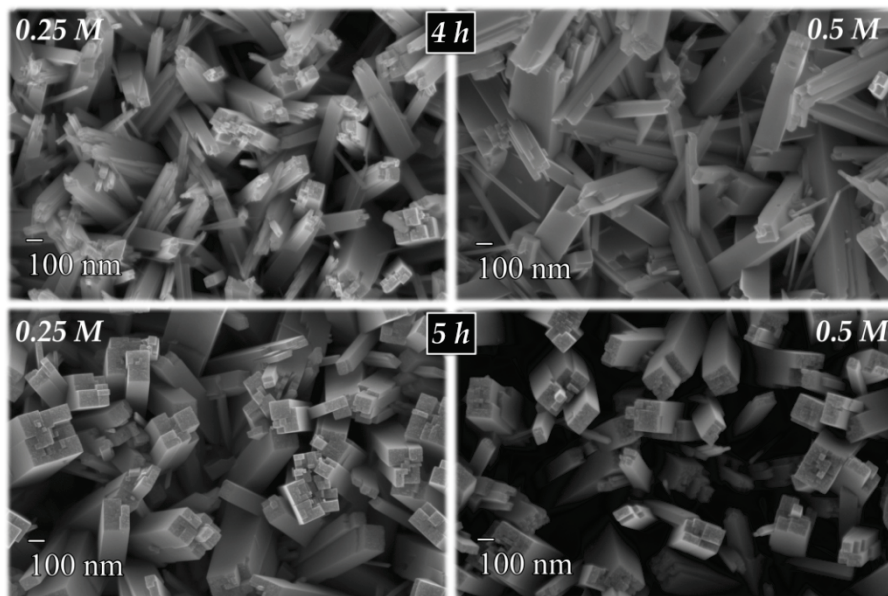


**Figure 3.28.** Top view images of the samples of 4 h and 5 h of hydrothermal synthesis with 0.25 and 0.5 M of  $\text{CaCl}_2$ .

When the hydrothermal time was increased to 5h the morphology of the nanorods obtained change. In **Figure 3.28** the samples synthesized during 4 and 5 hours can be compared. The shape for the 5h nanorods for the two  $\text{CaCl}_2$  concentrations is squarer than the 4h. In the case of the 4h samples the nanorods top have a triangular ending, but in the case of the 5h samples the top is more flat seem as if the top was cut. The rods edge size for the 0.25 M increase very low, however for 0.5 M the rods edge size increase around 70 nm more. The thickness values for both concentrations increase around 60 nm for both of them. In **Table 3.3** are summarized the average values for the rods edge size and the layer thickness.

**Table 3.3.** Rods edge size and layer thickness values from the 2h and 5h samples with 0.25 and 0.5 CaCl<sub>2</sub>.

	Edge Size (nm)		Thickness (μm)	
	0.25 M	0.5 M	0.25 M	0.5 M
4h	149	143	1,8	1,4
5h	153	214	2,4	1,9

To prove if the photoactivity of the samples was incremented due to the increase of the hydrothermal synthesis, LSV measurements were done under 100 mW cm<sup>-2</sup> illumination source.

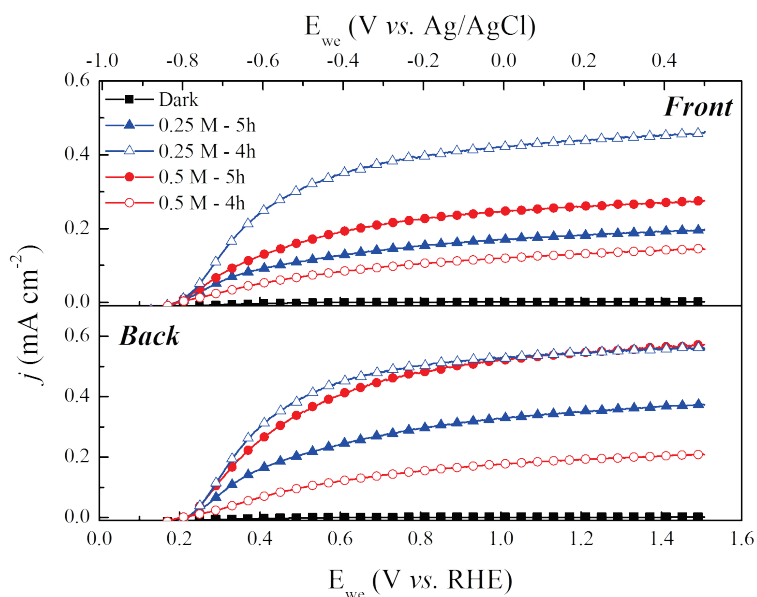


**Figure 3.29.** LSV measurements at 20 mV s<sup>-1</sup> comparative of the samples with 0.25 and 0.5 M of CaCl<sub>2</sub> from hydrothermal synthesis time of 2h and 5h in 1M NaOH.

In *Figure 3.29* was collected the current densities obtained from the LSV of the 5h and 4h samples with the  $\text{CaCl}_2$  to compare the photoactivity and how much was improved with the time increasing in the hydrothermal synthesis. The dark currents (black dotted line) are zero for all the samples. For the current density comparative we take the values at 1.23 V *vs.* RHE due to the water splitting potential. For the 0.25 M the increase of the hydrothermal time gives a decrease in the current density for both sides of the sample (back and front). The reason for this decrease could come from the concentration of  $\text{CaCl}_2$  effect. Because of when the hydrothermal synthesis time at the working conditions is around 6h starts to peel off the  $\text{TiO}_2$  layer generated from the substrate [45]. The suppression in the growing time at 0.25 M of  $\text{CaCl}_2$  is not enough and starts to degenerate the contact with the substrate. Nevertheless, when the  $\text{CaCl}_2$  concentration is de double (0.5 M) the growing rate is reduced more, blocking the degeneration of the  $\text{TiO}_2$  nanorods layer contact with the substrate. As sequence, allowing thicker  $\text{TiO}_2$  layers and bigger rods edge size which is optimal for the photon collection.

### 3.3.2 *TiO<sub>2</sub> Nanorods Doping*

#### 3.3.2.1 *Tin Doping*

Doping the materials with Sn or Sn<sup>4+</sup> is an attractive approach [50], especially for the TiO<sub>2</sub>, due to the small lattice mismatch between SnO<sub>2</sub> and TiO<sub>2</sub> leads to good structural compatibility and stability. The incorporation of Sn into the TiO<sub>2</sub> structure allows a crystal structure or shift its band edge [51–53] and growth of SnO<sub>2</sub>/TiO<sub>2</sub> core – shell nanoparticles [54] which can reduce the excitation recombination. But increasing the Sn doping upshifts the TiO<sub>2</sub> bandgap (SnO<sub>2</sub> has a bandgap of 3.8 eV) creating interface, which subsequently decrease the light absorption and the photogenerated charge separation. But if the amount of Sn is controlled in a low level in TiO<sub>2</sub> nanorods, can maintain or provide higher photon absorption efficiency than undoped TiO<sub>2</sub>, while at the same time can increase the charge carrier density increasing the photoactivity. Xu *et al.* incorporate small amount of Sn inside the TiO<sub>2</sub> nanorods enhancing the photoresponse in the UV region due to the increase of the charge carrier density [55]. To control the hydrolysis process of the Sn precursor and the reaction time is important to obtain an optimal density and quality of Sn/TiO<sub>2</sub> nanorods. High acidity helps to suppress the hydrolysis rate of SnCl<sub>4</sub> leading to a low Sn doping level.

In this case the titanium precursor concentration was fixed to 50 mM and 125 μL of a solution 0.1 M of SnCl<sub>4</sub> was added. To observe the Sn incorporation in the structure to enhance TiO<sub>2</sub> nanorods photoactivity the HCl:H<sub>2</sub>O ratio was modified (50:50, 40:60 and

30:70). However, when the acidity of the solution was changed and the water content is incremented, the hydrolysis rate increases with the immediate  $\text{TiO}_2$  precipitation and  $\text{SnCl}_4$  hydrolysis. On the other hand, if the amount of HCl is incremented, a lower pH media was reached and the hydrolysis is suppressed. Therefore the growth of oriented  $\text{TiO}_2$  nanorods requires slow hydrolysis of titanium precursor in a fairly strong acidic aqueous medium.

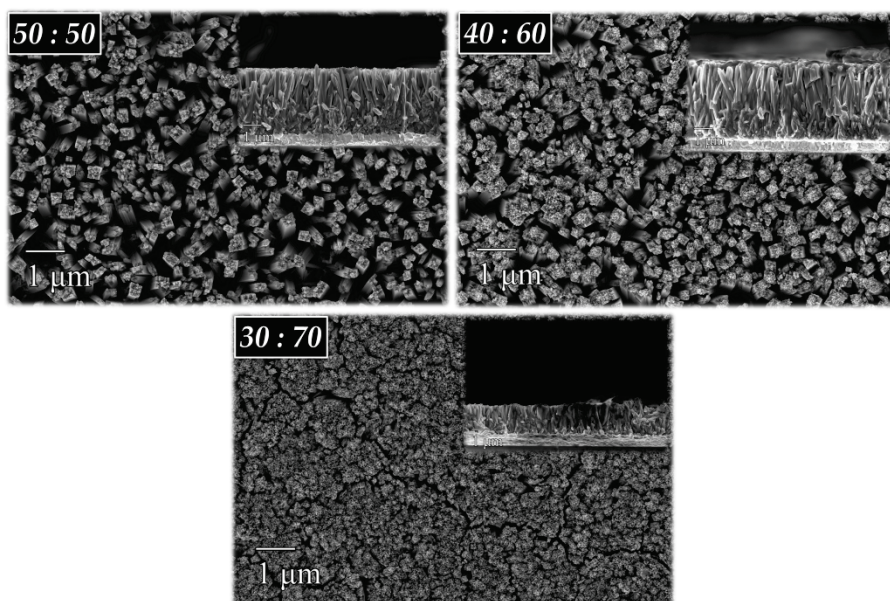


*Figure 3.30. Top view and cross section of the hydrochloric-water acid ratio samples with the amount of Sn incorporated in the solution.*

*Figure 3.30* shows the top view and the cross section images for each ratio. When the amount of hydrochloric acid was reduced, the  $\text{TiO}_2$  hydrolysis is faster increasing nanorods density giving more compact  $\text{TiO}_2$  layer and decreasing the layer thickness. In the opposite way, when the ration goes to 1:1 the density decrease and the length increase. This occurs due to the speed of precipitation of

the titanium precursor is higher at high water amount. The thickness value for each ratio was: 1.66, 4.15 and 3.53  $\mu\text{m}$  for 30:70, 40:60 and 50:50 respectively

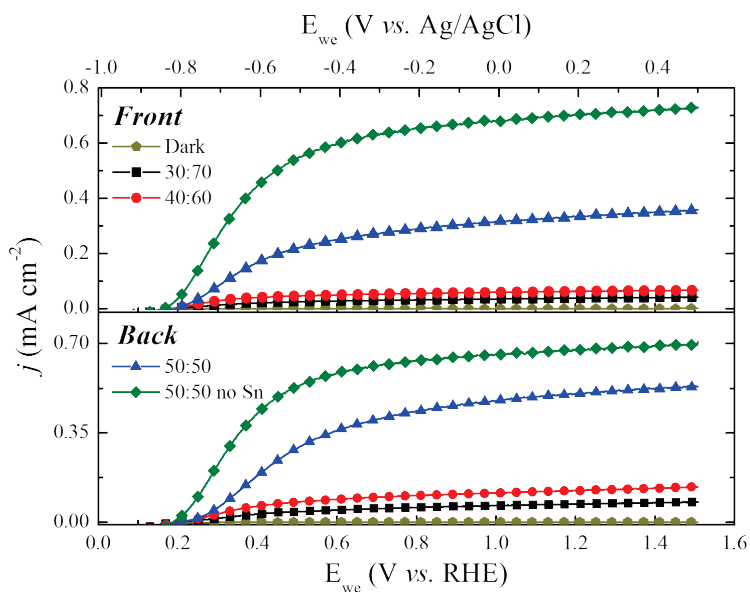


**Figure 3.31.** LSV measurements under illumination at  $20 \text{ mV s}^{-1}$  in  $1\text{M}$  of  $\text{NaOH}$  of the samples with Sn at different  $\text{HCl}:\text{H}_2\text{O}$  ratio and the  $\text{TiO}_2$  nanorods without Sn.

The current densities reached with the tin doped samples decrease compared with the bare  $\text{TiO}_2$  sample. The improvement effect of the Sn in the  $\text{TiO}_2$  structure was not observed, obtaining the opposite effect. However, it was possible to observe the pH effect over the  $\text{TiO}_2$  nanorods growth.

### 3.3.2.2 Vanadium Doping

The aim to incorporate vanadium is to increase the  $\text{TiO}_2$  photocatalytic activity. Yu *et al.* reported the enhance of the

hydroxyl ions adsorption on the surface due to the substitution of the  $\text{Ti}^{4+}$  with  $\text{V}^{5+}$  [56]. The  $\text{VO}_2$  band gap is 0.62 eV [57] with a rutile structure. The ionic radius of the  $\text{V}^{4+}$  is 0.072 nm very close to the  $\text{Ti}^{4+}$  in the rutile structure which have a value of 0.0745 nm [58]. By sol-gel method Zhao *et al.* prepare the first solid solution of titanium plus vanadium,  $\text{Ti}_{1-x}\text{V}_x\text{O}_2$  in anatase form improving the visible absorption respect the bare  $\text{TiO}_2$  [59]. In another work of Zhao *et al.* propose a gradient band gap design of  $\text{Ti}_{1-x}\text{V}_x\text{O}_2$  thin film electrode in which visible light photoresponses and photostability were observed [60]. Goodenough [61] prepare a molecular diagram for the rutile form of the  $\text{VO}_2$ . Phillips *et al.* suggest that the energy bandgap of  $\text{Ti}_{1-x}\text{V}_x\text{O}_2$  should be smaller than 2.5 eV, due to the top of O 2p valence band in  $\text{VO}_2$  is separated from the Fermi level by 2.5 eV and O 2p band. In  $\text{VO}_2$  should be broader than that in  $\text{TiO}_2$  due to the smaller distance of O – O in  $\text{VO}_2$ . In a recent work of Zhao *et al.* it was tested the photoelectrochemical properties of the solid solution at different Ti and V compositions. They study the evolution of the bandgap when the amount of vanadium is increased, using as reference the 3.2 eV of the anatase  $\text{TiO}_2$ .

The effect of the vanadium doping increases the donor density value and the photoconductivity. The positive shift in the onset potential reached in this work is due to the downing of the lowest level of conduction band with the vanadium incorporation (*Figure 3.32*). As summary, when a little amount of vanadium is incorporated decrease the photoresponse of the  $\text{TiO}_2$  due to the V 3d level in the bandgap promoting the electron-hole recombination

and it is not possible to use the visible light. When the amount of vanadium is increased the photoresponse increase too, allowing the utilization of visible light. With more increment a strong reduction of the bandgap could be obtained reaching to a semi-metallic behavior.

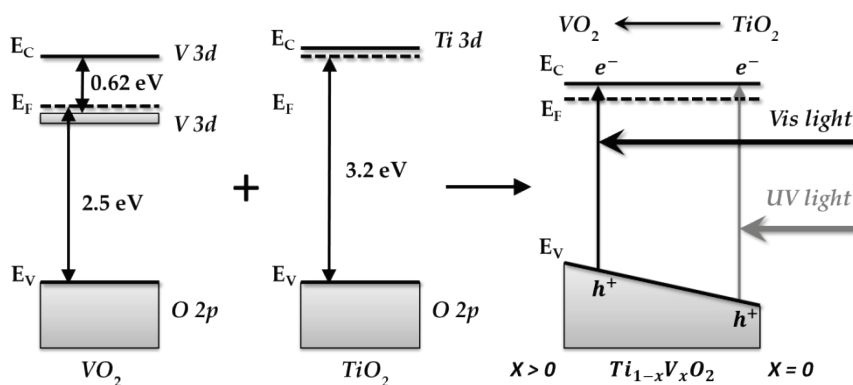


**Figure 3.32.** Gradient bandgap formation via solid solution reaction between semiconductors with different bandgaps.

Some reported works incorporate the vanadium into the  $\text{TiO}_2$  structure in thin films for organic compounds degradation observing an improvement in the visible range and the degradation activity [62–64]. Li *et al.* reported a method to incorporate vanadium into the rutile nanorods by a simple hydrothermal step. In the Li *et al.* work obtains a reduction of the  $\text{TiO}_2$  band gap as result of the incorporation in a very low percentage of vanadium ions. The presence of  $\text{V}^{+4}$  and  $\text{V}^{+5}$ .in the structure was corroborated by XPS. Under UV irradiation the activity of the incorporated vanadium samples are lower than the bare  $\text{TiO}_2$  due to the V doped sites acts as hole-recombination centers or as electron traps. But in the case of the visible irradiation

all the samples with V have activity; however the activity is different respect the oxidation state of the vanadium. When  $V^{+4}$  ions are in the structure improve the photocatalytic activity under the visible irradiation due to the electronic rich surface and as consequence, high concentration of the hydroxyl groups, in the opposite way the  $V_2O_5$  phase in the sample acts as electron-hole recombination center.

In our work, we tried to introduce vanadium into  $TiO_2$  rutile rods to enhance the response in the visible region. To obtain a photoelectrode is required to be growth over a FTO. 50 mM of titanium butoxide, in a 60 mL of HCl:H<sub>2</sub>O (1:1) solution and vanadium (IV) sulfate oxide hydrate (Alfa Aesar, 99.9%) was used as vanadium (IV) source at different molar ratio respect the Ti precursor. The hydrothermal conditions used were the same as the previous experiments (200°C during 4h and treatment at 500°C in air during 2h). The titanium:vanadium precursor ratio used for the synthesis is summarized in *Table 3.4*.

*Table 3.4. Titanium-Vanadium molar ratio used in the nanorods synthesis.*

<b>Molar Ratio (Ti:V)</b>
<b>1 : 0</b>
<b>1 : 0.5</b>
<b>1 : 1</b>
<b>1 : 2</b>

When the vanadium precursor was added to the acidic titanium solution the color change to blue due to indicating the presence of  $V^{4+}$  species, but when the synthesis was ended the solution

changed to green color, probably due to its partial oxidation to  $V^{5+}$  which is yellow but mixing both colors generate a green solution. The SEM images in *Figure 3.33* show how the shape of the nanorods was changed and the density was incremented when the molar ratio was increased. The morphology changes from square shape with only titanium precursor to a more rounded surface when the vanadium was added.

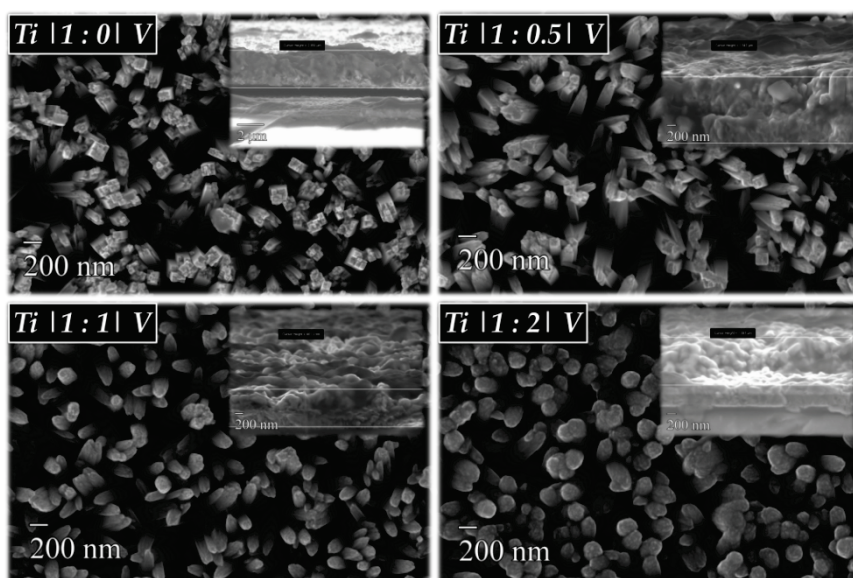


*Figure 3.33.* SEM images top view and cross section of the nanorods at the different vanadium molar ratio. Cross section values: 2.850, 1.547, 0.96 and 1.091  $\mu\text{m}$  for the 0, 0.5, 1 and 2 molar of vanadium respectively

The thickness of the  $\text{TiO}_2$  layers goes in the opposite way than the rods density. The layer decrease from 3  $\mu\text{m}$  to 1  $\mu\text{m}$ . The  $\text{TiO}_2$  nanorods growth somehow was suppressed in the presence of the vanadium precursor.

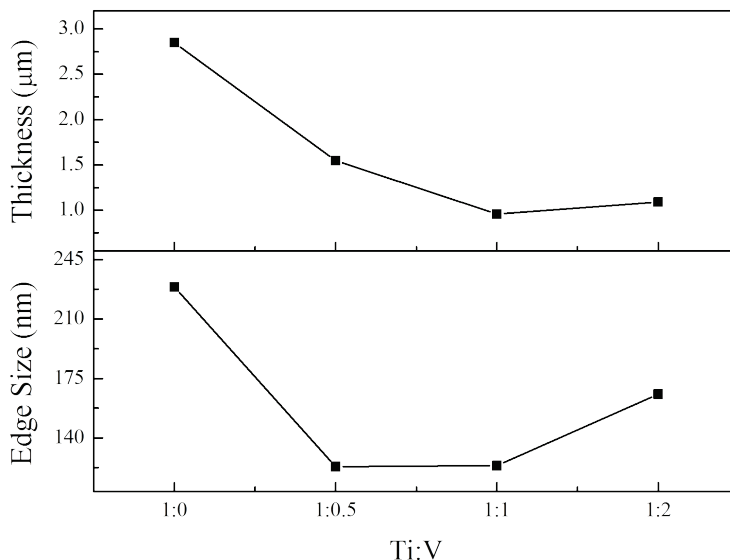


**Figure 3.34.** Average of cross section and nanorods diameter values at each Ti:V ratios under study.

In **Figure 3.34**, is possible to observe the evolution of the rods diameter and the layer thickness when the amount of vanadium was increased. The cross section and rods diameter values decrease with the amount of the vanadium until the 1:2 ratio which start to increase respect the other ratios with vanadium. But all of them are lower than the non doped  $\text{TiO}_2$ . To observe the crystal structure of the samples XRD and energy-dispersive X-ray spectroscopy (EDX) were done to obtain the crystallographic structure of the samples and to observe if there are some vanadium incorporated in the structure.

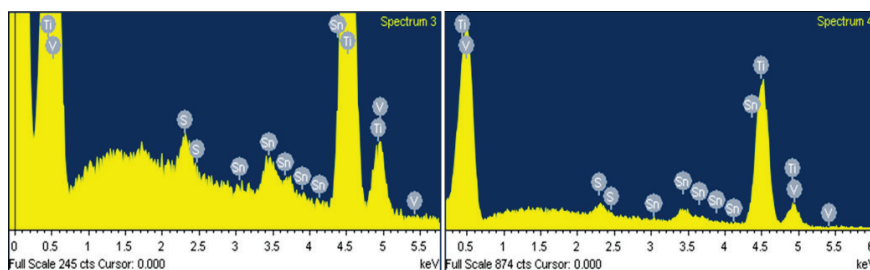
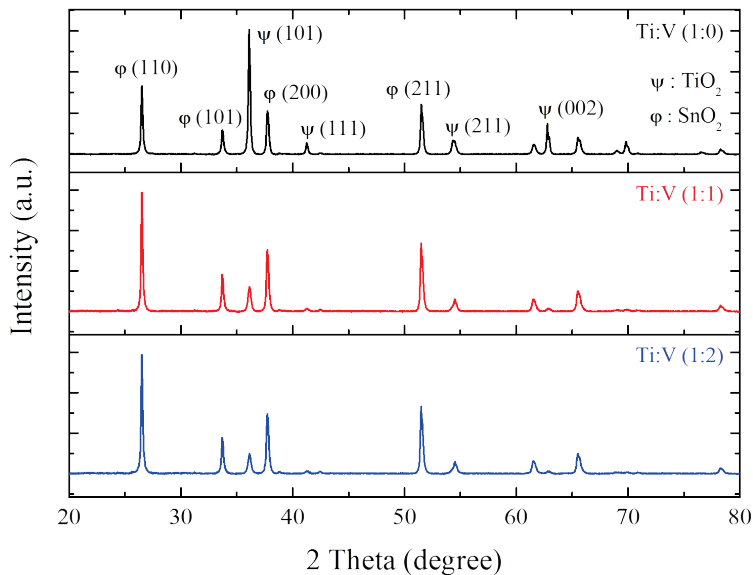


**Figure 3.35.** XRD pattern of the Ti:V samples at different molar ratio indicated and EDX spectra of the Ti:V-1:2 molar ratio.

In the XRD pattern (*Figure 3.35*) it is not possible to observe the vanadium, due to the small amount or high dispersions in the samples [65]. If  $\text{SnO}_2$  and  $\text{TiO}_2$  peaks are compared, they have correlation with the layer thickness obtained due to when the amount of vanadium was increased the  $\text{TiO}_2$  nanorods growth decrease. However, when in the EDX pattern is possible to observe

a very little amount of vanadium in the sample with 1:2 (Ti:V) molar ratio. The atomic percentage obtained was around 0.3%.

The optical measurements done over these samples were transmittance and reflectance. As mentioned before the absorbance can be obtained using Eq. (3.12) in this case the transmittance is not zero.

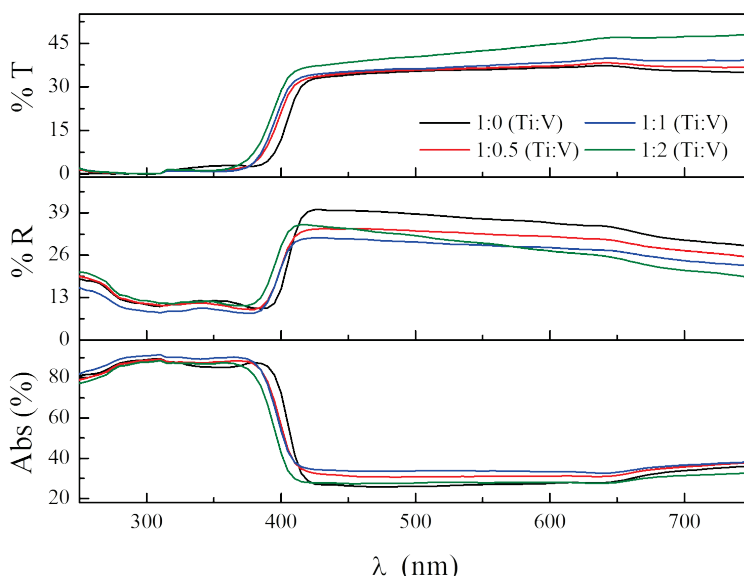


**Figure 3.36.** UV – vis transmittance (%T), reflectance (%R) and absorbance (Abs) spectra of the vanadium doped and no doped samples.

The values obtained in the optical experiments have no so much difference between them. There is not a clear enhance of the activity in the visible range neither in the  $\text{TiO}_2$  active wavelength range. The bandgap values obtained from the absorbance plot for each sample were 2.871, 2.858, 2.860 and 2.925 eV for 1:0, 1:0.5, 1:1 and 1:2 respectively. These values can be obtained from the

wavelength axes cut in the jump around 400 nm from the absorbance plot, Eq. (3.15).

For the PEC characterization, cyclic voltammetry (CV) was done for the samples between  $-0.4$  to  $1.6$  V *vs.* RHE at  $20$   $\text{mV s}^{-1}$ . The illumination source was fixed to  $100$   $\text{mW cm}^{-2}$  (AM 1.5G) in all the cases the illumination was done through the glass side (*back*).

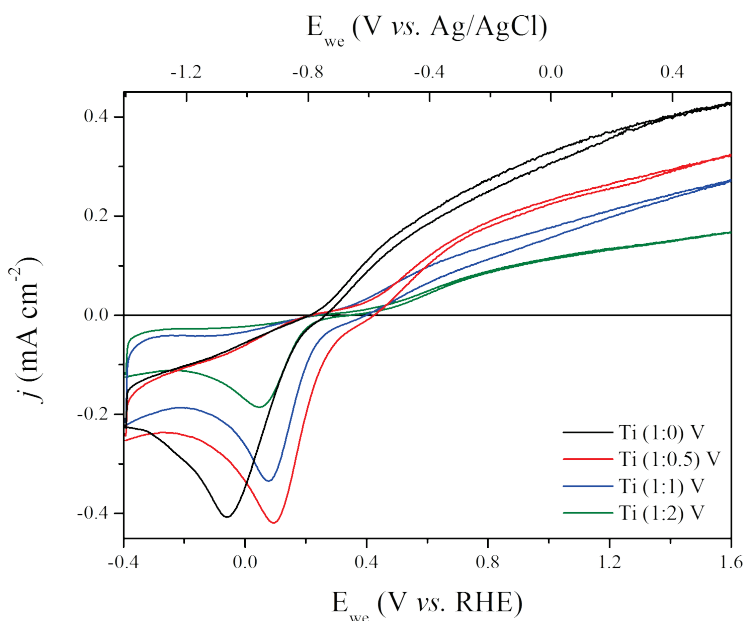


**Figure 3.37.** Cyclic-Voltamperometry (CV) at  $20$   $\text{mV s}^{-1}$  experiments under illumination of the incorporated vanadium samples in  $1$  M of NaOH.

In **Figure 3.37**, is shown the current density values of the vanadium doped samples under illumination. If we observe the values at  $1.23$  V *vs.* RHE the current density values obtained decrease from  $0.4$  to  $0.15$   $\text{mA cm}^{-2}$  from the undoped sample (1:0) to the more doped one (1:2). Additionally, the onset potential of the samples shifts to more positive values when the amount of

vanadium was increased (from 0.2 to 0.4 V). The reason for this shift to more positive values is due to a decreasing in the conduction band of the material [66]. The peak around 0 V corresponds to the reduction of oxygen generated in the OH<sup>-</sup> oxidation to O<sub>2</sub> at 1.23 V.

Subsequently, the IPCE measurements were done at 1.23 V *vs.* RHE bias potential using a monochromatic illumination source (back side).

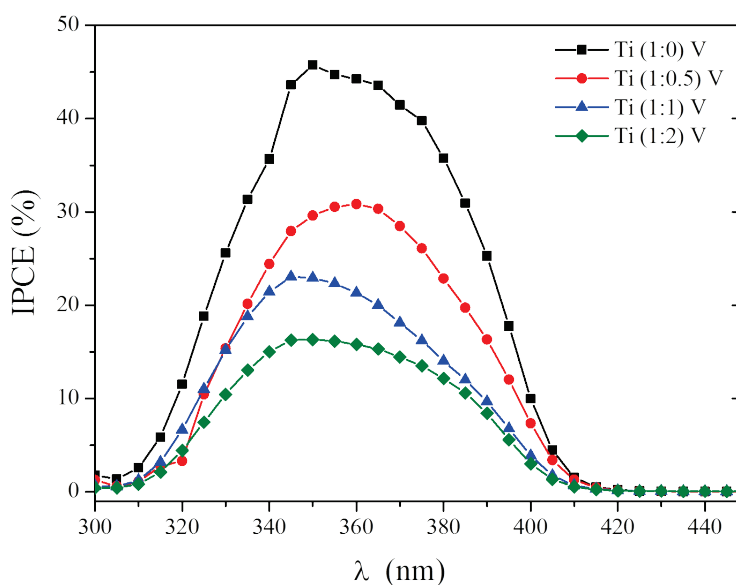


*Figure 3.38.* IPCE values for the samples, increasing the vanadium molar ratio taken at -0.2 V (1.23 V *vs.* RHE) *vs.* Ag/AgCl.

From the IPCE values in *Figure 3.38*, is possible to observe no shift to the visible range. The same tendency observed in the current densities obtained in the CV measurements was shown here, a decreasing in IPCE values when the vanadium molar ratio was increased. From the IPCE plot is possible to obtain the

bandgap values using the Eq. (3.15). The value of the bandgap obtained from the IPCE plot was the same for all the samples, 3.03 eV corresponding with the value of the rutile. There is no decreasing of the bandgap value of the samples due to the fail in the very low or no incorporation of the vanadium in the rutile structure of TiO<sub>2</sub> nanorods.

To determine the number of free carriers which gives idea of the conductivity level and carrier mobility (donor density, N<sub>D</sub>) Mott-Schottky plots were done. Using the Schottky plots is possible to obtain the flat band potential ( $E_{fb}$ ) which in the case of the n-type semiconductors is close to the Fermi level that is close to the conduction band [67]. The ideal sample to do M-S is with a single crystal material or high crystalline quality. To obtain the  $E_{fb}$  the Mott-Schottky (M-S) relationship involves the capacitance in the space charge layer ( $C_{sc}$ ) of the semiconductor electrode as a function of the applied potential ( $E$ ) and applying the relationship according to Eq. 3.18 [68]. To determine the values is very important to use the real area of the material [69]. For nanostructured materials is very complicated to obtain the real surface area value and for these reason, the values used are the geometrical surface area of the electrode.

$$\frac{1}{C_{sc}^2} = \frac{2}{\epsilon_r \epsilon_0 A^2 e N_D} \left( E - E_{fb} - \frac{kT}{e} \right) \quad (3.18)$$

In the relationship the parameters involved are  $\epsilon_r$  is the relative permittivity of the semiconductor (100 for rutile TiO<sub>2</sub>),  $\epsilon_0$  is permittivity in vacuum ( $8.85 \times 10^{-12} N^{-1}C^2m^{-2}$ ),  $A$  is the real surface area of the electrode,  $e$  is the charge of an electron ( $1.602 \times$

$10^{-19}$  C),  $N_D$  is the free carrier density,  $k$  is Boltzman constant ( $1.38 \times 10^{-23} J K^{-1}$ ),  $T$  is the temperature, and  $E$  the applied potential.

Electrochemical impedance spectroscopy (EIS) in dark has been performed in order to get the point by point Mott – Schottky plots at a single frequency over a range of potentials to determine the voltage dependence of the space charge capacitance. This experiment is repeated for more frequencies in the frequency range appropriate for the material [70–72].

From the M–S plots the flat band potential value and number of donor density ( $N_D$ ) were obtained. The high crystallinity of the  $TiO_2$  rutile nanorods gives the possibility to adjust to an ideal photoelectrode and the equivalent circuit can be simplified to a resistor (R) and a capacitor (C) in series. The R represents the resistance of the semiconductor bulk (for this resistance there are another contribution from the electrode connection to the potentiostat wires and the electrolyte), and the C correspond to the capacitance of the charge region ( $C_{sc}$ ).

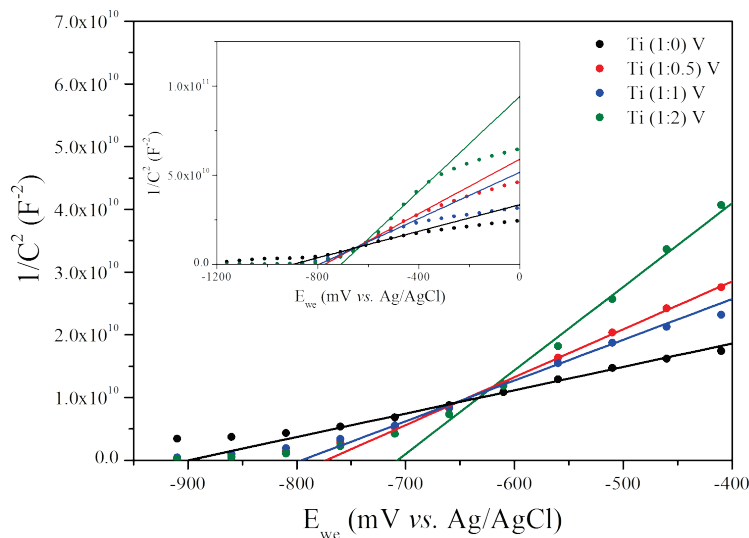


**Figure 3.39.** Mott-Schottky plots represented with the data obtained from the electrochemical impedance spectroscopy as function of potential versus reference electrode with for Ti:V ratios under study with the correspondent linear fit.

When the  $1/C_{sc}^2$  versus electrode potential ( $E$ ) is represented a linear fitting must be done in the linear part of the plot as shown in **Figure 3.39**. The fitted line must be extrapolated to  $1/C_{sc}^2 = 0$ . The X-intercept equals to  $E_{fb} + kT/e$  and the slope is proportional to the charge carrier concentration ( $N_D$ ) as shown in Eq. 3.19. This equation is obtained by substituting the relevant terms from Eq. 3.18.

$$N_D \text{ (cm}^{-3}\text{)} = \frac{1.41 \times 10^{32} \text{ (cm} \times \text{F}^{-2} \times \text{V}^{-1}\text{)}}{\epsilon_r \times A^2 \times \text{slope (F}^{-2} \times \text{V}^{-1}\text{)}} \quad (3.19)$$

The donor density and flat band potential obtained from the M-S are resumed in **Table 3.5**. For these experiments, a donor density of  $N_D = N_D^{\text{TiO}_2} = 1.5 \times 10^{17} \text{ cm}^{-3}$  to the nontreated sample was

assigned, which corresponds with a typical reported value for undoped rutile [73]. Considering in this case that all samples have a similar active surface area (the synthetic pathway was the same for all of them and for these samples it is hard to determine the real active area), we can extrapolate the donor density value using the relative M –S slopes:

$$N'_D = \frac{S^{TiO_2}}{S'} N_D^{TiO_2} \quad (3.20)$$

Where  $S^{TiO_2}$  and  $S'$  corresponds to the slopes of the nontreated and treated samples, respectively, and  $N'_D$  refers to the donor density of the treated sample

**Table 3.5.** Fundamental parameters calculated and obtained from the Mott - Schottky plots: Donor Density  $N_D$  and  $E_{fb}$  values.

Ti:V	Slope ( $F^{-2}mV^{-1}$ )	$E_{fb}$ (V vs.SHE)	$N_D(cm^{-3})$
1:0	$3.72 \times 10^7$	-0.70	$1.5 \times 10^{17}$
1:0.5	$7.63 \times 10^7$	-0.57	$7.31 \times 10^{16}$
1:1	$6.49 \times 10^7$	-0.60	$8.60 \times 10^{16}$
1:2	$1.33 \times 10^8$	-0.71	$4.20 \times 10^{16}$

All the doped samples present a decrease in the donor density reaching 1 order of magnitude lower than the nontreated sample. To determine the donor density of the nanostructured  $TiO_2$  photoelectrodes there are few reported works. For all the vanadium doped samples, as shown in *Figure 3.37* and *Figure 3.38*, the current density and IPCE values decrease with the doping level giving the reverse effect expected but correlated with the decrease in the donor density values. Another parameter which is possible

to calculate is the depletion width who gives an idea of the efficient separation of electrons and holes.

$$W = \sqrt{\frac{2\varepsilon_r\varepsilon_0|\phi_{SC}|}{eN_D}} \quad (3.21)$$

Where,  $\phi_{SC} \equiv E - E_{fb}$  is the maximum potential drop on the depletion layer. The values calculated for the vanadium doping samples are shown in **Table 3.6**.

*Table 3.6. Depletion region width at different applied potentials obtained from the Mott - Schottky plots.*

<i>W (nm) at (E - E<sub>fb</sub>)</i>					
<b>Ti:V</b>	<b>0.2 V</b>	<b>0.4 V</b>	<b>0.6 V</b>	<b>0.8 V</b>	<b>1 V</b>
<b>1:0</b>	121	172	210	243	271
<b>1:0.5</b>	174	246	301	348	389
<b>1:1</b>	160	227	278	320	358
<b>1:2</b>	230	324	398	459	513

To explain this effect is required to detail the processes involved in the mechanism of semiconductor photoactivity. These processes are:

- Charge carrier generation (charge separation, optical values)
- Charge carrier transport ( $N_D$ )
- Charge carrier transfer (charge transfer from semiconductor to the electrolyte to an acceptor species, in this case the water)

For our system the donor generation in which the absorptance is involved there are no differences between them as shown in *Figure 3.36*. For the donor transport ( $N_D$ ) when the doping amount was increased the level of donors decrease (decreasing the conductivity) translated to a loss in the photoactivity values in the material. However, for the compact structure of the rutile there is a possible formation of  $V^{5+}$  centers in the nanorods surface due to the segregation of vanadium in the hydrothermal synthesis. As mentioned before these centers could act as recombination centers, blocking the charge transfer to the water molecules in the electrolyte. For this reason, the current density and IPCE decrease with the doping level increment. Related to the depletion width values in *Table 3.6* the values increase with the potential and with the doping level, which is correlated by the decrease of the free carriers ( $N_D$ ). Considering the values of the width in the depletion region used the  $N_D$  value of the nontreated sample and the potential at which IPCE was collected, the value of the width at the depletion region was around 271 nm. Taking account that the nanorods mean width is around 230 nm, then the radius is too small for the potential to be fully drop within the semiconductor, and thus the assumption of a planar electrode type potential distribution cannot be considered herein [74]. Considering the Gärtner model [75] we assume that every hole entered or generated at the depletion layer does not recombine neither at the surface nor in the space charge layer. When the large values of  $\phi_{SC}$  can be correlated with the Gärtner model (large band bending,  $|E - E_{fb}| > 0$ ), but the model fails when the potential is close to the flat band

potential ( $E \approx E_{fb}$ ). Curiously, this problem is aggravated when the semiconductor excitation wavelength becomes shorter meaning that the electron – hole pairs are generated near the surface and so their probability for being trapped by surface states increases.

With  $E_{fb}$  obtained from the M – S plots also the bandgap values from the IPCE and absorptance is possible to build an energy bands position scheme for each sample to observe the shifting in the energy position (*Figure 3.40*). The undoped  $\text{TiO}_2$  was taken as reference to compare with the different band energy level position obtained in the doped samples. For these systems:  $E_F \cong E_{fb} \cong CB$  [67].

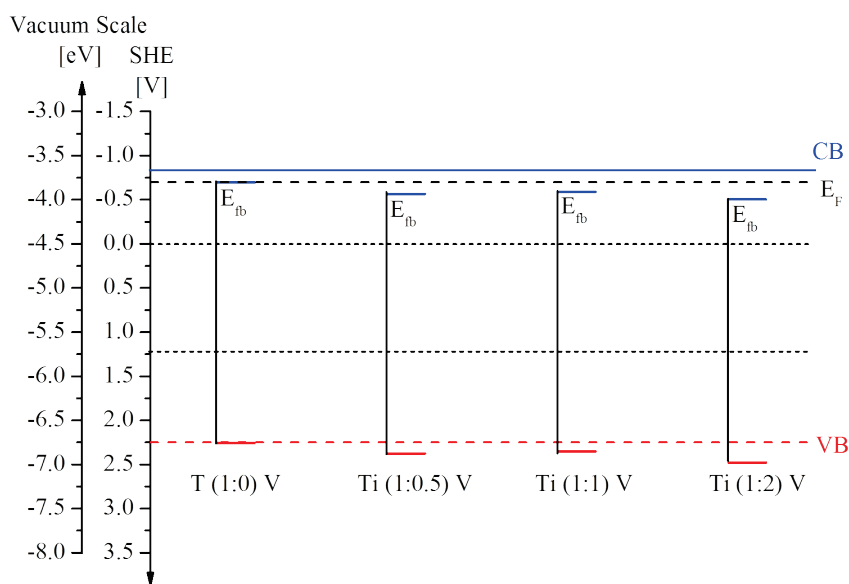


**Figure 3.40.** Energy bands position for the samples with different Ti:V molar ratio. The solid blue line (CB) corresponds to the undoped  $\text{TiO}_2$  conduction band and the red dotted line (VB) corresponds to the valence band.

In the figure the  $E_{fb}$  position decrease to more positive values comparing the nondoped and 1:2 doped samples. This effect support the onset potential shift to more positive values mentioned before [76]. But the band gap values are the same for all of them  $\approx 3 eV$  giving more positive values of the estimated valence band with the doped samples compared with the undoped one.

#### 3.3.2.3 *Nitrogen Doping*

Instead of hydrothermal doping, there is another method to incorporate other elements in the  $TiO_2$  nanorods structure, mentioned before [77]. The nitrogen doping can enhance the titanium dioxide efficiency. Some authors argued that the improvement reached comes from the bandgap narrowing due to the oxygen substitution by nitrogen [78], others consider that vacancy formation inherent to nitrogen doping [79] is responsible for such activity [80].

The synthesis pathway is the same as mentioned before for the rutile nanorods until the thermal treatment in air to eliminate any residue coming from the synthesis. The FTO glass size was  $4 \times 3 \text{ cm}^2$  after the thermal treatment mentioned before, the FTO glass with the nanorods was cut in four pieces of  $3 \text{ cm}^2$  ( $1 \times 3$ ), the real area immersed in the electrolyte was  $1.5 \text{ cm}^2$ . While one of these pieces was kept as reference sample and the others were treated under pure ammonia atmosphere at three different temperatures, 300, 400 and  $500^\circ\text{C}$  during 2h with a temperature ramp of  $5^\circ\text{C}/\text{min}$  and a gas flow of  $100 \text{ mL min}^{-1}$ .

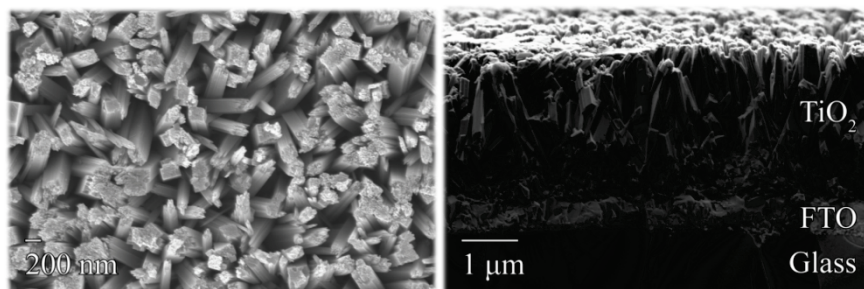


Figure 3.41. SEM top view and cross section images of the  $\text{TiO}_2$  nanorods obtained.

The nanorods layers obtained using 40 mM of titanium precursor gives have a 200 nm average width and 3  $\mu\text{m}$  length, corresponding approximately with the values obtained before.

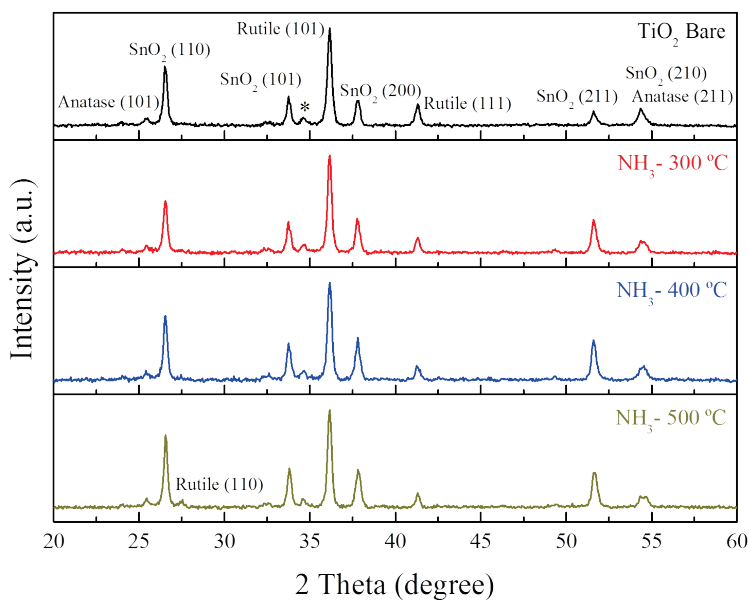
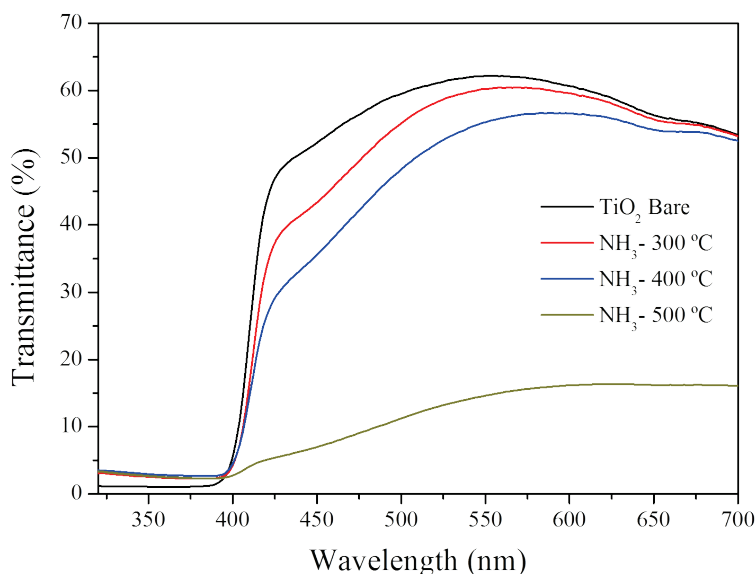


Figure 3.42. X-Ray diffraction spectra of samples treated at different temperatures in ammonia atmosphere.

For all the samples there are not remarkable crystallinity differences obtained after the annealing in ammonia atmosphere (*Figure 3.42*). The rutile phase polymorph was obtained with some small traces of anatase. A peculiar and interesting peak appears between  $\text{SnO}_2$  and  $\text{TiO}_2$  (101) peaks that can be attributed to  $\text{TiO}_2 - \text{SnO}_2$  solid solution formed in the FTO/nanorods interface indicating a good quality contact between the substrate and  $\text{TiO}_2$  nanorods.



*Figure 3.43.* UV-vis transmittance spectra of the ammonia treated samples at 300, 400 and 500 °C with the reference sample.

In addition, to observe if there are some improvements after the ammonia treatment UV-vis transmittance spectra was done (*Figure 3.43*). The results obtained show the expected absorption band for the bare  $\text{TiO}_2$  rutile phase and a new absorption band induced by

both the nitridation of the sample and the presence of intra bandgap states [78].

Ammonia treatments on  $\text{TiO}_2$  not only introduce new visible absorption bands [27,81,82] by creation of Ti – O – N bonds but also increase the n-doping character thanks to the reductive character of the ammonia (the same tendency using hydrogen treatment), as it partially decomposed to hydrogen and nitrogen at high enough temperatures.

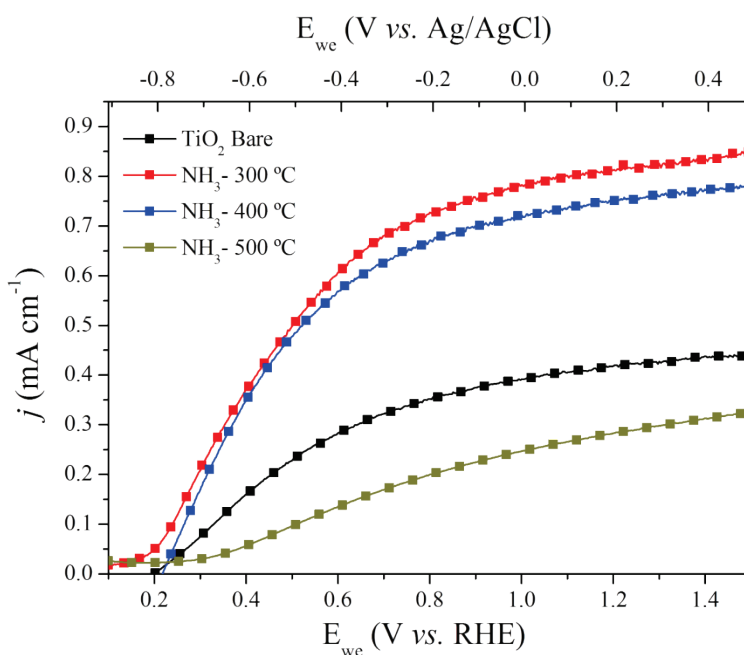


**Figure 3.44.** Comparative linear sweep voltammetry under illumination from 0.1 to 1.5 V vs RHE of the ammonia treated samples with the reference one.

Photoelectrochemical measurements (Figure 3.44) were conducted to evaluate the performance of the ammonia treated samples. The results obtained shows that ammonia treatments increase the photocurrent density up to 2-fold compared to bare

TiO<sub>2</sub> (NH<sub>3</sub> – 300°C). However, at higher temperatures, the effect was reversed; eventually resulting is a lower photocurrent density than the nontreated sample (NH<sub>3</sub> – 500°C). No significant changes were observed on the photocurrent onset potentials.

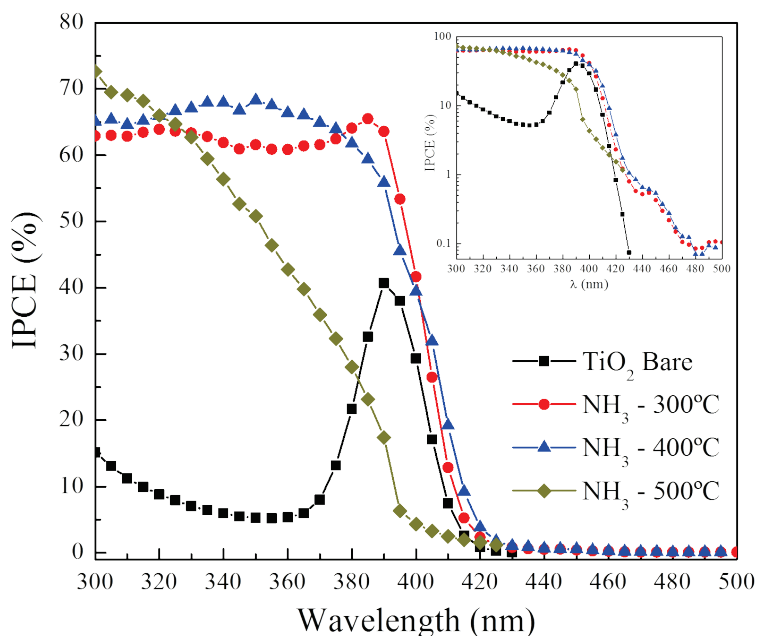


**Figure 3.45.** Incident photon-to-electron conversion efficiency (IPCE) taken at 0 V vs Ag/AgCl of the ammonia treated samples at 300, 400 and 500°C with the reference sample.

IPCE measurements (**Figure 3.45**) revealed that the increasing photocurrent density was mainly due to a more efficient photocurrent response of the UV part of the spectrum and to a lesser extent in the bandgap region also. Again, at 500°C the tendency was reversed, and it started to lose response in the bandgap region. Logarithmic representation of the IPCE results (inset in **Figure 3.45**) showed that, at 300 and 400°C, samples contained some response below the theoretical bandgap.

The origin of this sub-bandgap photoactivity relies on the visible absorption band aforementioned. However, this absorption band does not necessarily implies further photocatalytic activity as is has been stated [83]. For our samples IPCE measurements shows that the samples treated at 300 and 400°C actually presents photocatalytic activity under sub-bandgap excitation to some extent. In any case, nitrogen doping can introduce intra bandgap levels in the form of N 2p levels near the valence band that have shown photocatalytic activity [81,84,85].

The most relevant about IPCE results is the huge improvement on the activity in the UV region. Wang *et al.* [83] found a similar results by treating TiO<sub>2</sub> nanorods under hydrogen atmosphere, however, the reasons for such behavior were still not clear.

To understand deeply the material conductivity Mott – Schottky (M – S) plots were performed in order to approximately determine the number of free carriers (donor density,  $N_D$ ) and the flat band potential value (Eq. 3.18 and 3.19) for the samples with the ammonia treatment, to observe the correlation with the improvement of the IPCE and current density values.

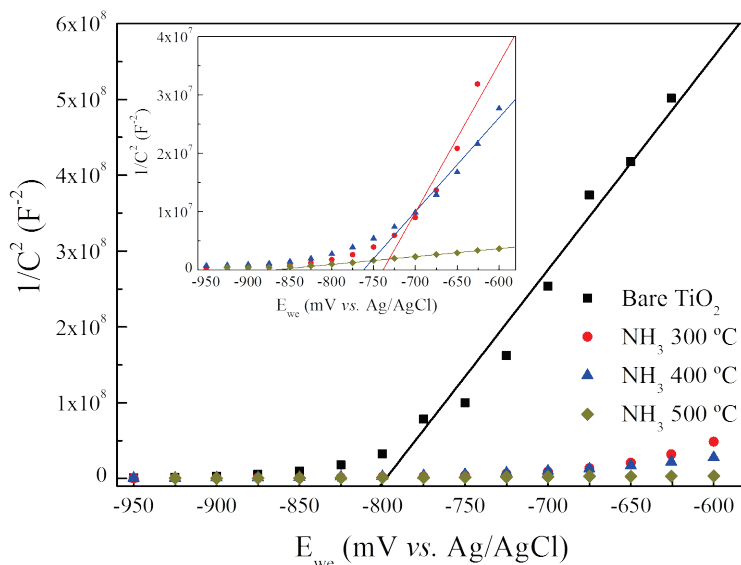


**Figure 3.46.** Mott - Schottky plots represented with the data obtained from the impedance spectroscopy measurements as a function of the applied potential versus reference electrode and the corresponding linear fit.

In **Table 3.7** are collected the data of the slopes, de donor density values and flat band potentials. The calculation of  $N_D$  was done using the approximation mentioned before in Eq. 3.20.

**Table 3.7.** Fundamental parameters calculated and obtained from the Mott - Schottky plots: Donor Density  $N_D$  and  $E_{fb}$  values.

Samples	Slope ( $F^{-2}mV^{-1}$ )	$E_{fb}$ (V vs. SHE)	$N_D$ ( $cm^{-3}$ )
TiO <sub>2</sub> Bare	$2.81 \times 10^6$	-0.82	$1.50 \times 10^{17}$
300°C – NH <sub>3</sub>	$2.55 \times 10^5$	-0.76	$1.65 \times 10^{18}$
400°C – NH <sub>3</sub>	$1.61 \times 10^5$	-0.79	$3.63 \times 10^{18}$
500°C – NH <sub>3</sub>	$1.35 \times 10^4$	-0.90	$3.12 \times 10^{19}$

For these samples when the temperature was increased under ammonia atmosphere the donor density value increase too. The tendency for all is the opposite as in the vanadium part, increasing the current density and IPCE values obtained compared with the bare sample.

The values of the depletion region obtained for these samples are resumed in *Table 3.8*.

*Table 3.8. Depletion region width at different applied potentials obtained from the Mott - Schottky plots.*

Samples	<i>W (nm) at (E – E<sub>fb</sub>)</i>			
	0.2 V	0.4 V	0.6 V	0.8 V
<b>TiO<sub>2</sub> Bare</b>	121	172	210	243
<b>300°C – NH<sub>3</sub></b>	36	51	63	73
<b>400°C – NH<sub>3</sub></b>	24	34	42	49
<b>500°C – NH<sub>3</sub></b>	8.4	11.9	14.6	16.8

Related with the explained in the vanadium doping in this case the value of the depletion region width for the nontreated sample have the same reference value as in vanadium (due to the approximation done), larger depletion width than the rods size and the potential is fully drop within the semiconductor. Giving a low electric field and the charge separation of electrons – hole pairs are generated close to the surface, increasing the recombination probability as mentioned before.

To understand this trend with the ammonia treatments the effect respect the donor density can be explained in two ways; (a) for shorter wavelengths the photogenerated electrons are formed

very close to the surface due to the higher absorption coefficient. Related to this an improvement in the separation of photogenerated electrons in the surface requires a decreasing of the depletion region and then, ensure that nanorods are not fully depleted giving a high potential drop in the electrolyte interface, giving an improvement of the separation of the photogenerated electrons from the surface. On contrary, at longer wavelengths, photons are absorbed deeper in the semiconductor and thus away from the surfaces avoiding and back-reaction. (b) When the donor density increases we are also shifting the Fermi level close to the conduction band and, consequently filling surfaces states located below the conduction band edge, acting as electron traps.

However, increasing the donor density too much would be deleterious because at higher wavelengths, photons are absorbed out from the depletion region. This limitation was clearly observed for the 500°C sample, in which the IPCE was maximum for shorter wavelengths, but for longer the response was almost annihilated. Besides, this behavior under long wavelengths could be understood as an apparent blue shift of the band gap material. At large doping level, the Fermi level eventually lies inside the conduction band by a certain quantity ( $\xi$ ). Since states below this energy are filled, electronic transitions to states below  $E_g + \xi$  are forbidden; hence, the absorption band edge should shift to higher energies (Burstein – Moss effect) [86]. Respect to the ammonia treatments a deeply study was published [77] where explain more parameters involved in the process of enhancing the titanium oxide nanorods efficiency for water splitting using ammonia treatments.

### 3.4 Conclusions

In summary of the chapter, we study two types of 1D nanostructures based on  $\text{TiO}_2$ , titanium nanotubes (TiNTs) and  $\text{TiO}_2$  nanorods. First TiNTs which are based on anatase obtained by anodization of a titanium foil. To improve the electrodes photoactivity the Ti foil was patterned with holes to act as light trap centers. To obtain this patterned substrate two different electrolytes in a two-step anodization process were used. In the first anodization to pattern the Ti foil surface, DMSO was used at four different voltages (40, 50, 60 and 70) obtaining bigger pores with the potential increment. In the second anodization step the electrolyte selected was EG which gives a very compact and hexagonal organization of the TiNTs. For comparison a sample obtained with the two anodization process was synthesized but using EG in both steps. A theoretical model was postulated to calculate the surface increment from the first anodization. For the **70 V** sample the model does not fit very well due to the pores disorganization. The **40 V** samples reach 40 % of surface increment compared with the flat sample. To prove if there is any increment in the photoactivity optical and photoelectrochemical (PEC) measurements were done to prove it. However, the optical data is possible to observe a lower reflectance values for the hierarchical TiNTs than the flat sample between 300 and 380. To observe the activity in the wavelength range where the material is active IPCE measurements was required. The data from IPCE for the **40 V** sample gives the best value followed by the **70 V**. In the case of the

LSV measurement have the same order in the current density. In the case of **40 V** sample this comes from the surface increment and the compact oxide layer generated at the bottom of the TiNTs layer. For the **70 V** could be for a better contact with the substrate due to a compact oxide layer generated in the bottom of the TiNTs because this sample has the lower surface increment but better photoactivity than **50** and **60 V** samples.

The second 1D nanostructured material based on TiO<sub>2</sub>, nanorods, have rutile as principal crystal phase. These samples are obtained by hydrothermal synthesis, growing a TiO<sub>2</sub> layer over a conductive glass substrate (FTO). For these samples a study of two hydrothermal synthesis conditions was done. The initial titanium precursor concentration and chlorine concentration addition were modified to observe the effect over the nanorods morphology and photoactivity. The Ti precursor used was titanium butoxide, the concentration used was 40, 50, 60 and 70 mM in an acidic aqueous solution (50:50, HCl:H<sub>2</sub>O). The hydrothermal temperature and time was fixed for all the concentrations (200°C, during 4h). In the LSV measurements the 50 mM under front and back illumination reach the best values followed by the 40 mM. The next condition is the concentration of Cl<sup>-</sup> ions, CaCl<sub>2</sub> was used for it because the NaCl suppress completely in our synthesis the TiO<sub>2</sub> nanorods growth. The concentrations used were 0.25, 0.5 and 1 M decreasing the nanorods edge size, density, layer thickness and photoactivity when the concentration was increased. However, we observe that chlorine ions decrease the growing time of the nanorods. Then the hydrothermal synthesis was extended to 5h for 0.25 and 0.5 M

reaching to thicker layers and bigger rods diameter. Only in the 0.5 M, the current density was improved to de double. The reason for this could come from the growing time decrease, because in the 0.25 is faster than 0.5 and when the hydrothermal time are close to 6 h the TiO<sub>2</sub> layers start to peel off. Therefore the contact of TiO<sub>2</sub> with the conductive glass could be affected decreasing the electro-collection and decreasing the current density. However for the 0.5 M allows higher hydrothermal times due to the growing speed decrease, reaching to better values in the current densities.

To improve the photoactivity of TiO<sub>2</sub> nanorods two materials were selected to introduce in the hydrothermal reaction, Sn and V. Both of them were incorporated in the hydrothermal solution. To improve the amount of Sn incorporated, the acidity of the hydrothermal solution was decreased. The ratio HCl:H<sub>2</sub>O used were: 50:50, 40:60 and 30:70. No tin incorporation was observed and the current densities from LSV measurement decrease with the acidity level reduction. The only effect observed was the acidity effect over the TiO<sub>2</sub> nanorods growth.

The other material incorporated under study was the vanadium. This metal can decrease the bandgap of TiO<sub>2</sub>, improving the absorption in the visible range. The vanadium precursor (VOSO<sub>4</sub>) was introduced in the hydrothermal solution at different Ti:V precursor molar ratio: 1:0.5, 1:1 and 1:2. The morphology of the TiO<sub>2</sub> nanorods generated changes to square shape to round. The density of the nanorods and the edge size were increased but the layer thickness decrease. The vanadium incorporation was observed by EDX at very low amount. However, in the optical

measurements no shift to visible range was observed and the current density values decrease with the increment of vanadium as the IPCE. To understand this effect Mott – Schottky measurements was done to obtain the flat band potential and the carrier density for the samples. The carrier density values decrease with the vanadium doping, translating to worst conductivity in the layer and not enhancing the photoactivity.

The limiting process in the photoactivity mechanism in the semiconductor is the charge carrier transfer from semiconductor to the electrolyte to an acceptor species ( $\text{H}_2\text{O}$ ). The charge carriers can be blocked by the presence of  $\text{V}^{5+}$  centers in the surface which acts as recombination center, decreasing the current density. The depletion region width for these samples are very large does not allowing the efficient separation of the electron – hole pair which are generated in the surface, with high probability to be trapped by surfaces states. As sequence with the  $\text{V}^{5+}$  possible presence acting as recombination centers and the generation of the electron – hole pair in the surfaces, the decrease of the photoactivity when the doping level increase is very pronounced. The flat band potential values obtained from the M – S plots, goes to more positive values which corresponds with the onset potential shift (to more positive values) in the LSV measurements with the vanadium increment.

On the other hand, the effect of the ammonia treatments to enhance the efficiency in the  $\text{TiO}_2$  nanorods was studied. For this case an improvement of the photoelectrochemical activity was reached by introducing more active surface states, which increase the holes average lifetime. For the  $300^\circ\text{C}$  sample was reached the

maximum IPCE and current density value ( $0.8 \text{ mA cm}^{-2}$  at  $1.23 \text{ V vs. RHE}$ ), nevertheless when the temperature of the ammonia treatment was increased to  $500 \text{ }^\circ\text{C}$  the free carriers were incremented and the Fermi level could be introduced in the conduction band shifting the absorption band to higher energies, decreasing the photoactivity of the material.

Consequently there are three options in the donor density level, (a) in the case of low donor density level, the maximum potential drop within the semiconductor is diminished. In this case the charge separation efficiency is lower, and thus surface recombination and back reaction kinetics are faster for photogenerated carriers created close to the surface (shorter wavelengths). In the case of larger wavelengths photogenerated carriers are efficiently separated because the material is fully depleted. (b) In the case of middle donor density levels, shorter space charge layer width, nanorods are no longer fully depleted, and the planar approximation is valid again and the maximum potential drop is higher. This fact and with the decreasing of the electron traps density due to the Fermi level position which shift close to the conduction band leads a more efficient charge separation. And the last, (c) with higher donor density levels the depletion region width is more localized nearby the nanorods surface, and therefore, those photogenerated charge carriers with shorter wavelengths are very efficiently separated but for longer wavelengths electrons and holes are photogenerated out from the depletion region.

Summarizing, the effect of the doping in the  $\text{TiO}_2$  nanorods studied in this chapter has two options (*Figure 3.47*). First, in the case of Sn or V doping there is not improvement in the photoactivity of the material. The reason for this is the generation of a flat band potential where the photoexcited electrons and holes are soon annihilated by their recombination, decreasing the efficiency of the material apart the depletion width region is too large and the electric field generated is small giving lower electron-hole separation. Second, the ammonia treatment effect which improves the photoactivity of the material. In this case there are a band bending which improves the electron-hole separation avoiding the recombination, in addition for this samples the depletion width region have the optimal length generating a high electric field. Consequently, improving the electron-hole separation and thus, decreasing the recombination and enhancing the photoactivity.

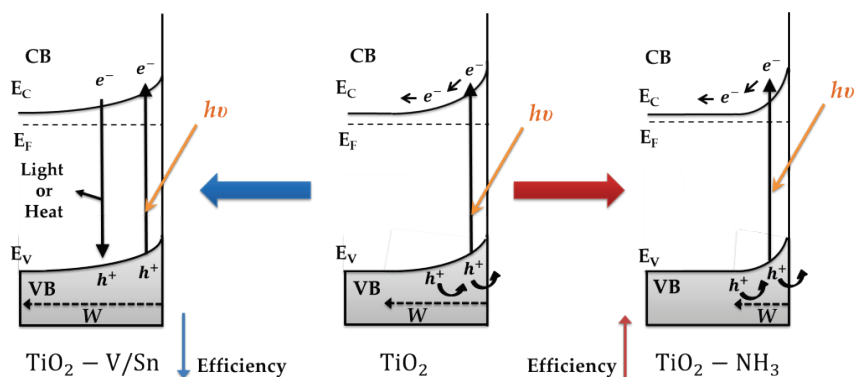


*Figure 3.47. Band bending scheme due to the two doping effect studied over titanium dioxide nanorods.*

### 3.5 References

- [1] Fàbrega Gallego C. *Síntesi i caracterització d'òxid de titani nanoestructurat per aplicacions energètiques*. Universitat de Barcelona; **2011**.
- [2] Solbrand A., Lindström H., Rensmo H., Hagfeldt A., Lindquist S.-E., Södergren S. *J Phys Chem B*. **1997**, 101, 2514.
- [3] Law M., Greene L.E., Johnson J.C., Saykally R., Yang P. *Nat Mater*. **2005**, 4, 455.
- [4] Lee K., Mazare A., Schmuki P. *Chem Rev*. **2014**, 114, 9385.
- [5] Ruan C., Paulose M., Varghese O.K., Mor G.K., Grimes C.A. *J Phys Chem B*. **2005**, 109, 15754.
- [6] Yoriya S., Paulose M., Varghese O.K., Mor G.K., Grimes C.A. *J Phys Chem C*. **2007**, 111, 13770.
- [7] Albu S.P., Ghicov A., Macak J.M., Schmuki P. *Phys Status Solidi – Rapid Res Lett*. **2007**, 1, R65.
- [8] Mor G.K., Varghese O.K., Paulose M., Shankar K., Grimes C. a. *Sol Energy Mater Sol Cells*. **2006**, 90, 2011.
- [9] Roy P., Berger S., Schmuki P. *Angew Chem Int Ed Engl*. **2011**, 50, 2904.
- [10] Macak J.M., Hildebrand H., Marten-Jahns U., Schmuki P. *J Electroanal Chem*. **2008**, 621, 254.
- [11] Albu S.P., Ghicov A., Aldabergenova S., Drechsel P., LeClere D., Thompson G.E., et al. *Adv Mater*. **2008**, NA.
- [12] Macak J.M., Tsuchiya H., Ghicov A., Yasuda K., Hahn R., Bauer S., et al. *Curr Opin Solid State Mater Sci*. **2007**, 11, 3.
- [13] Jessensky O., Müller F., Gösele U. *Appl Phys Lett*. **1998**, 72, 1173.
- [14] Zhang Z., Hossain M.F., Takahashi T. *Int J Hydrogen Energy*. **2010**, 35, 8528.
- [15] Li S., Zhang G., Guo D., Yu L., Zhang W. *J Phys Chem C*. **2009**, 113, 12759.
- [16] Wang D., Yu B., Wang C., Zhou F., Liu W. *Adv Mater*. **2009**, 21, 1964.
- [17] Wu H., Zhang Z. *Int J Hydrogen Energy*. **2011**, 36, 13481.
- [18] Ye M., Xin X., Lin C., Lin Z., Ye XK Lin, CJ Lin, ZQ M.D.X., Nanotubes S. *Nano Lett*. **2011**, 11, 3214.
- [19] Wang F., Liu Y., Dong W., Shen M., Kang Z. *J Phys Chem C*. **2011**, 115, 14635.

- [20] Wu H., Wang Y., Ma Y., Xiao T., Yuan D., Zhang Z. *Ceram Int.* **2015**, 41, 2527.
- [21] Ferry V.E., Verschuuren M.A., Li H.B.T., Verhagen E., Walters R.J., Schropp R.E.I., et al. *Opt Express*. **2010**, 18 Suppl 2, A237.
- [22] Müller J., Rech B., Springer J., Vanecek M. *Sol Energy*. **2004**, 77, 917.
- [23] Zhou D., Biswas R. *J Appl Phys*. **2008**, 103, 093102.
- [24] Berginski M., Hüpkens J., Schulte M., Schöpe G., Stiebig H., Rech B., et al. *J Appl Phys*. **2007**, 101, 074903.
- [25] Garnett E., Yang P. *Nano Lett.* **2010**, 10, 1082.
- [26] Campbell P., Green M.A. *J Appl Phys*. **1987**, 62, 243.
- [27] Fàbrega C., Andreu T., Güell F., Prades J.D., Estradé S., Rebled J.M., et al. *Nanotechnology*. **2011**, 22, 235403.
- [28] Chen Z., Jaramillo T.F., Deutsch T.G., Kleiman-Shwarsstein A., Forman A.J., Gaillard N., et al. *J Mater Res*. **2011**, 25, 3.
- [29] Yu D., Zhu X., Xu Z., Zhong X., Gui Q., Song Y., et al. *ACS Appl Mater Interfaces*. **2014**, 6, 8001.
- [30] Yang M. *Band Gap Engineering and Carrier Transport in Tio2 for Solar Energy Harvesting*. University of Pittsburgh; **2012**.
- [31] Lou Y., Chen J. *Nanosci Nanotechnol Lett.* **2014**, 6, 361.
- [32] Shankar K., Basham J.I., Allam N.K., Varghese O.K., Mor G.K., Feng X., et al. *J Phys Chem C*. **2009**, 113, 6327.
- [33] El Ruby Mohamed A., Rohani S. *Energy Environ Sci*. **2011**, 4, 1065.
- [34] Su Z., Zhou W. *J Mater Chem*. **2011**, 21, 8955.
- [35] Jun Y., Park J.H., Kang M.G. *Chem Commun*. **2012**, 48, 6456.
- [36] Jiu J., Isoda S., Wang F., Adachi M. *J Phys Chem B*. **2006**, 110, 2087.
- [37] Kang S.H., Choi S.-H., Kang M.-S., Kim J.-Y., Kim H.-S., Hyeon T., et al. *Adv Mater*. **2008**, 20, 54.
- [38] Penn R.L., Banfield J.F. *Geochim Cosmochim Acta*. **1999**, 63, 1549.
- [39] Cho H.J., Jung D. *Bull Korean Chem Soc*. **2011**, 32, 4382.
- [40] Enache-Pommer E. *Electron transport and recombination in nanowire dye-sensitized solar cells*. University of Minnesota; **2010**.
- [41] Grätzel M. *Inorg Chem*. **2005**, 44, 6841.
- [42] Enache-Pommer E., Liu B., Aydil E.S. *Phys Chem Chem Phys*. **2009**, 11, 9648.
- [43] Fan J., Fabrega C., Zamani R.R., Hao Y., Parra A., Andreu T., et al. *ACS Appl Mater Interfaces*. **2013**, 5, 9872.
- [44] Wu J.-M., Zhang T.-W., Zeng Y.-W., Hayakawa S., Tsuru K., Osaka A. *Langmuir*. **2005**, 21, 6995.
- [45] Liu B., Aydil E.S. *J Am Chem Soc*. **2009**, 131, 3985.

- [46] Kumar A., Madaria A.R., Zhou C. *J Phys Chem C*. **2010**, 114, 7787.
- [47] Cheng H., Ma J., Zhao Z., Qi L. *Chem Mater*. **1995**, 7, 663.
- [48] Lin J., Heo Y.-U., Nattestad A., Sun Z., Wang L., Kim J.H., et al. *Sci Rep*. **2014**, 4, 5769.
- [49] Fàbrega C., Andreu T., Tarancón A., Flox C., Morata A., Calvo-Barrio L., et al. *Int J Hydrogen Energy*. **2013**, 38, 2979.
- [50] Ling Y., Wang G., Wheeler D.A., Zhang J.Z., Li Y. *Nano Lett*. **2011**, 11, 2119.
- [51] Sayılkan F., Asiltürk M., Tatar P., Kiraz N., Şener Ş., Arpaç E., et al. *Mater Res Bull*. **2008**, 43, 127.
- [52] Vinodgopal K., Bedja I., Kamat P. V. *Chem Mater*. **1996**, 8, 2180.
- [53] Bedja I., Kamat P. V. *J Phys Chem*. **1995**, 99, 9182.
- [54] Pan J., Hühne S.-M., Shen H., Xiao L., Born P., Mader W., et al. *J Phys Chem C*. **2011**, 115, 17265.
- [55] Xu M., Da P., Wu H., Zhao D., Zheng G. *Nano Lett*. **2012**, 12, 1503.
- [56] Yu J.C., Lin J., Kwok R.W.M. *J Photochem Photobiol A Chem*. **1997**, 111, 199.
- [57] Nikolaiev A.V., Kostrubov Y.N., Andreev B. V. *Sov Physics-Solid State*. **1992**, 34, 1614.
- [58] Shannon R.D. *Acta Crystallogr Sect A*. **1976**, 32, 751.
- [59] Zhao G., Kozuka H., Lin H., Yoko T. *Thin Solid Films*. **1999**, 339, 123.
- [60] Zhao G., Kozuka H., Lin H., Takahashi M., Yoko T. *Thin Solid Films*. **1999**, 340, 125.
- [61] Goodenough J.B. *J Solid State Chem*. **1971**, 3, 490.
- [62] Klosek S., Raftery D. *J Phys Chem B*. **2001**, 105, 2815.
- [63] Zhou J., Takeuchi M., Zhao X.S., Ray A.K., Anpo M. *Catal Letters*. **2006**, 106, 67.
- [64] Sene J.J., Zeltner W.A., Anderson M.A. *J Phys Chem B*. **2003**, 107, 1597.
- [65] Mohamed M.M., Al-Esaimi M.M. *J Mol Catal A Chem*. **2006**, 255, 53.
- [66] Sato N. *Electrochemistry at Metal and Semiconductor Electrodes - Chapter 6*. Elsevier; **1998**.
- [67] Cardon F., Gomes W.P. *J Phys D Appl Phys*. **1978**, 11, L63.
- [68] Orazem M.E., Tribollet B. *Angew Chemie Int Ed*. **2009**, 48, 1532.
- [69] Chen Z., Jaramillo T.F., Deutsch T.G., Kleiman-Shwarscstein A., Forman A.J., Gaillard N., et al. *J Mater Res*. **2011**, 25, 3.
- [70] Van de Krol R. *J Electrochem Soc*. **1997**, 144, 1723.
- [71] Harrington S.P., Devine T.M. *J Electrochem Soc*. **2008**, 155, C381.

- [72] Cooper G. *J Electrochem Soc.* **1982**, 129, 1973.
- [73] O'Regan B., Moser J., Anderson M., Graetzel M. *J Phys Chem.* **1990**, 94, 8720.
- [74] Albery W.J. *J Electrochem Soc.* **1984**, 131, 315.
- [75] Gärtner W.W. *Phys Rev.* **1959**, 116, 84.
- [76] Sivula K. *J Phys Chem Lett.* **2013**, 4, 1624.
- [77] Fàbrega C., Monllor-Satoca D., Ampudia S., Parra A., Andreu T., Morante J.R. *J Phys Chem C.* **2013**, 117, 20517.
- [78] Asahi R., Morikawa T., Ohwaki T., Aoki K., Taga Y. *Science.* **2001**, 293, 269.
- [79] Livraghi S., Paganini M.C., Giamello E., Selloni A., Di Valentin C., Pacchioni G. *J Am Chem Soc.* **2006**, 128, 15666.
- [80] Finazzi E., DiValentin C., Selloni A., Pacchioni G. *J Phys Chem C.* **2007**, 111, 9275.
- [81] Wang J., Tafen D.N., Lewis J.P., Hong Z., Manivannan A., Zhi M., et al. *J Am Chem Soc.* **2009**, 131, 12290.
- [82] Diwald O., Thompson T.L., Zubkov T., Walck S.D., Yates J.T. *J Phys Chem B.* **2004**, 108, 6004.
- [83] Wang G., Wang H., Ling Y., Tang Y., Yang X., Fitzmorris R.C., et al. *Nano Lett.* **2011**, 11, 3026.
- [84] Torres G.R., Lindgren T., Lu J., Granqvist C.-G., Lindquist S.-E. *J Phys Chem B.* **2004**, 108, 5995.
- [85] Hoang S., Berglund S.P., Hahn N.T., Bard A.J., Mullins C.B. *J Am Chem Soc.* **2012**, 134, 3659.
- [86] Burstein E. *Phys Rev.* **1954**, 93, 632.

# Chapter IV

Dark Reaction:

$\text{CO}_2$  Electroreduction

with Cu-Based

Electrodes

<b>4. Dark Reaction: CO<sub>2</sub> Electroreduction with Cu-Based Electrodes</b> .....	<b>161</b>
<b>4.1 Chapter Overview</b> .....	<b>161</b>
<b>4.2 Copper Based Electrodes as Catalyst</b> .....	<b>162</b>
<b>4.2.1 Cu Mesh as Gas Diffusion Electrode (GDE) and Copper Foil Electrode for CO<sub>2</sub> Reduction</b> .....	<b>162</b>
4.2.1.1 <i>Electrocatalytic Reduction of CO<sub>2</sub> in KHCO<sub>3</sub> and NaHCO<sub>3</sub> over a Copper Surface</i> .....	<b>167</b>
4.2.1.2 <i>Electrolyte Concentration Effect and Cu foil experiments</i> .....	<b>175</b>
<b>4.2.2 Cu<sub>x</sub>O Mesh as Gas Diffusion Electrode</b> .....	<b>179</b>
4.2.2.1 <i>Electrocatalytic reduction of CO<sub>2</sub> in KHCO<sub>3</sub> and NaHCO<sub>3</sub> over a Copper Oxide (Cu<sub>x</sub>O) surface</i> .....	<b>182</b>
4.2.2.2 <i>Electrochemical evolution of the Cu<sub>x</sub>O layers in the CO<sub>2</sub> reduction</i> .....	<b>192</b>
<b>4.3 CO<sub>2</sub> Pre-Humidification Effect</b> .....	<b>201</b>
<b>4.4 Conclusions</b> .....	<b>207</b>
<b>4.5 References</b> .....	<b>209</b>

## **4. Dark Reaction: CO<sub>2</sub> Electroreduction with Cu-Based Electrodes**

### **4.1 Chapter Overview**

In this chapter we are going to discuss the electrochemical CO<sub>2</sub> reduction activity over a copper based electrode using hydrogen carbonate salts as supporting electrolyte, the cations used were sodium and potassium. The first electrode selected was pristine copper due to the interest in methane production. We characterized the samples by SEM and XRD to visualize the surface morphology and the crystal structure of the electrodes. Afterwards, the electrochemical process was studied to understand the activity of these electrodes. Chronopotentiometric (CP) experiments were done at different current densities to observe the activity as a function of the reached potential.

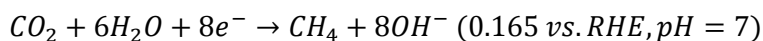
The second cathode under study was copper oxide. During the electrochemical reduction experiments these electrodes suffered a reduction of the different copper oxide layers generated during the thermal synthesis, leading to a catalytically active copper that enables carbon dioxide reduction. With this type of electrodes a time-dependence test was done to carefully study these crystallographic changes at each potential plateau. To check the structure and surface morphology SEM images and XRD experiments were done at different times using two electrolytes to elucidate the effect of cations in the oxide layer reduction process.

Finally the in last section of this chapter it was studied the impact on the faradaic efficiency of the CO<sub>2</sub> gas stream humidification before the introduction in the electrochemical cell.

## **4.2 Copper Based Electrodes as Catalyst**

### *4.2.1 Cu Mesh as Gas Diffusion Electrode (GDE) and Copper Foil Electrode for CO<sub>2</sub> Reduction*

Copper electrodes in the electrochemical carbon dioxide reduction have a high interest due to the catalytic selectivity for the hydrocarbons production, compared with other metals used as mentioned in **Chapter I**. The aim to use the copper electrode is the focus on methane production by an electrochemical process. The methane generated, would potentially be stored and distributed using the existing infrastructure of natural gas network. Only this metal has high selectivity for this product. In this work a study of the cations effect used in in the supporting electrolyte over the electrochemical CO<sub>2</sub> reduction process was done.



The characteristic property of this material to produce hydrocarbons was first reported by Hori *et al.* [1], who studied the absorption strength of the CO over different metals and copper presented an average strength respect to the rest of the metals. Recently Jaramillo *et al.* [2] have reported about the binding energy

for CO and how impacts in the catalyst behavior: copper stabilizes the CO intermediate enough for the evolution to hydrocarbons.

Thermodynamic requirements for methane production are not very high compared with the rest of hydrocarbons (*Table 1.2*). However, the reaction involves the charge transfer of eight electrons, and thus, is kinetically less favorable than other less reduced products, like carbon monoxide (2 electrons) or ethylene (12 electrons) formation as result of a different reaction pathway. Hori [3] carried out some experiments where the potential of the CO reduction over a Cu surface was controlled. In this work the authors stated that the partial current density of ethylene formation is in agreement with the pH in the electrolyte, while methane production is proportional to the proton activity. The rate determining step in CH<sub>4</sub> formation involves a second electron transfer to a hypothetical intermediate species such as COH in an electrochemical equilibrium with a CO adsorbed on the electrode and a proton from the electrolyte [4,5]. A mechanism for the methane formation postulated by Hori is shown in *Figure 4.1*.

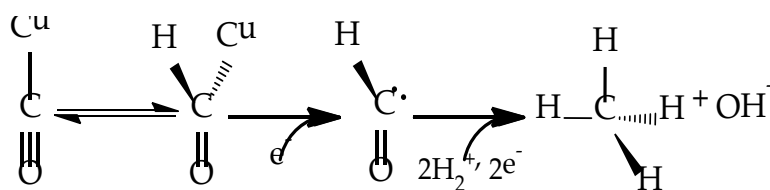


*Figure 4.1.* Molecular mechanism of the electrochemical reduction of the carbon monoxide to methane over a copper surface obtained from Hori work [3].  $H_2^+$  corresponds to  $H_2^+$  or a combined  $H_{(ads)} + H^+$ .

Density functional theory (DFT) calculations made by Pussana [6] explain some pathways for CO<sub>2</sub> electroreduction to CH<sub>4</sub> on Cu

(211),  $\text{Cu}_3\text{Ag}$  (211), and  $\text{Cu}_3\text{Au}$  (211) associated with the standard hydrogen electrode model. Adsorbed  $\text{CO}^*$ ,  $\text{HCO}^*$ ,  $\text{HOCO}^*$ , and  $\text{OH}^*$  species were found to be the key intermediates that require an optimum binding energy among them to achieve an effective catalyst decreasing the overpotential for the methane formation. Nevertheless, their natures are not quite related  $\text{HCO}^*$  and  $\text{CO}^*$  adsorptions are insensitive with the surface affinity toward O or C, while  $\text{HOCO}^*$  and  $\text{OH}^*$  are strongly related to surface affinity toward O, creating a great challenge in the search for effective catalysts. In the case of the  $\text{OH}^*$  Pussana pointed out the electrode poisoning due to the high affinity over surfaces like Cu, being an important limiting step the  $\text{OH}^*$  removal. Peterson and Nørskov presented DFT studies [7] indicating that the key enabling step in the formation of hydrocarbons from  $\text{CO}_2$  is the protonation of adsorbed CO to form adsorbed CHO. If the adsorbed CHO can be stabilized relative to adsorbed CO the necessary overpotential can be significantly reduced, which will be translated directly into a more efficient process. In other work Peterson and Nørskov explained several strategies as result of their research for the overpotential improvement relative to a copper surface [8].

Since the reaction is highly dependent on surface quality and purity, two copper electrodes were used: a copper mesh (*Cu-GDE*) and a high purity copper foil (*Cu*, 99.9999%), Both electrodes were precleaned either with HCl to remove native oxides (*Chem*) or by a subsequent electropolishing treatment (*Epol*) (explained in **Chapter II**) prior to electrochemical test. The characterization of the electrodes was done by SEM and XRD before and after the

electrochemical test. *Figure 4.2* shows the electrode surface morphology. In the images is possible to notice the different electrodes morphology with the two pretreatments done.

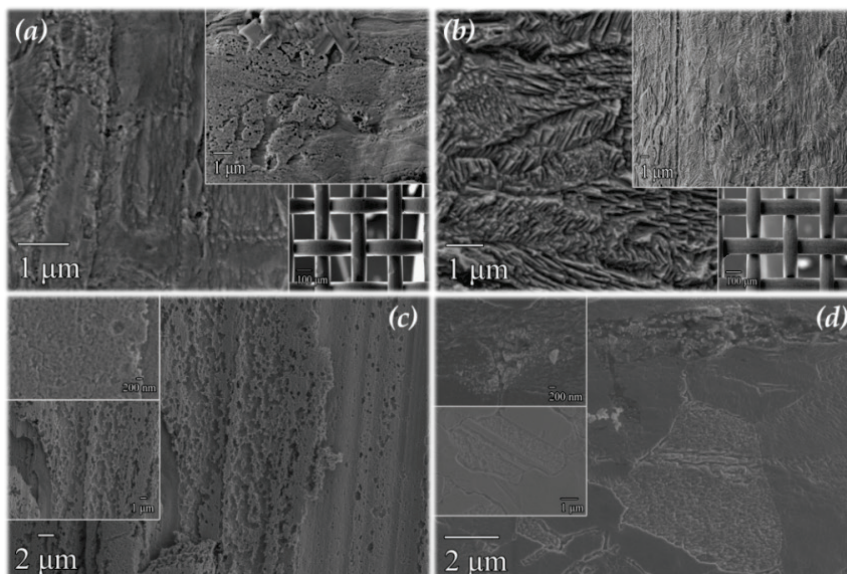


*Figure 4.2.* Metallic copper electrodes SEM images before electrochemical test: (a) Cu-GDE-Chem, (b) Cu-GDE-Epol, (c) Cu-Chem and (d) Cu-Epol.

The crystal facets obtained after the electrode conditioning using the two methods were confirmed by XRD and they are shown in *Figure 4.3*. For all of them the same pattern was obtained with the maximum intensity for the (111) direction, but in the case of the electropolished high purity copper (Cu-Epol) the maximum intensity was for the (200) direction, (parallel to (100) direction).

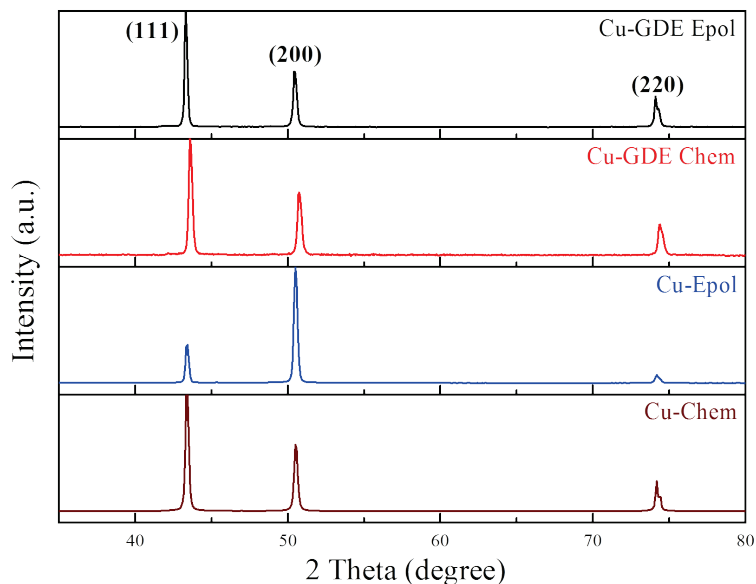


**Figure 4.3.** XRD pattern of the different treatments done over the metallic copper electrodes used in the  $\text{CO}_2$  reduction experiments before any test.

The dependence of the crystal facets is crucial for the methane formation. In reported works over single crystal copper electrodes (111), (110) and (100) explains which is the favored crystallographic face for the methane production [9] the order is  $(111) > (110) > (100)$ . Later Hori *et al.* [10–12] reported a serial of studies where explain the selectivity of the (100) face for the ethylene, (111) for the methane formation and in the case of (110) the activity is in between, in these works it is remarked the effect of the atomic configuration of the electrode surface over the product selectivity. Relative to the Cu (100) there is a reported DFT study by Calle-Vallejo and Koper [13] about the formation mechanism for the  $\text{C}_2\text{H}_4$ , EtOH and acetaldehyde (MeCHO) from CO. Respectively about the mechanism proposed in the paper Koper made

remarkable experimental observation about the CO reduction, while the CH<sub>4</sub> formation depends on the pH value on the SHE reference electrode concerning to the proton-electron transfer in the case of the C<sub>2</sub>H<sub>4</sub> there is no pH influence as mentioned before by Hori [3].

### *4.2.1.1 Electrocatalytic Reduction of CO<sub>2</sub> in KHCO<sub>3</sub> and NaHCO<sub>3</sub> over a Copper Surface*

For the carbon dioxide reduction tests the electropolished copper mesh (*Cu-GDE-Epol*) was selected to eliminate the impurities [14] in a GDE configuration explained in **Chapter II**. The results of the Chronopotentiometric (CP) working potential measurements are shown in *Figure 4.4*. In this figure is possible to observe the evolution of the working electrode potentials in the two supporting electrolytes used for the tests, NaHCO<sub>3</sub> and KHCO<sub>3</sub>. The typical concentration used in the electrochemical CO<sub>2</sub> conversion in reported works is 0.1 or 0.5 M. The anolyte used was either NaOH or KOH, depending on the catholyte cation. In these experiments the anolyte and the catholyte was fixed at 0.5 M to have a high ionic conductivity in the electrolyte. Both compartments were separated by a Nafion® 117, pretreated with anolyte solution overnight.

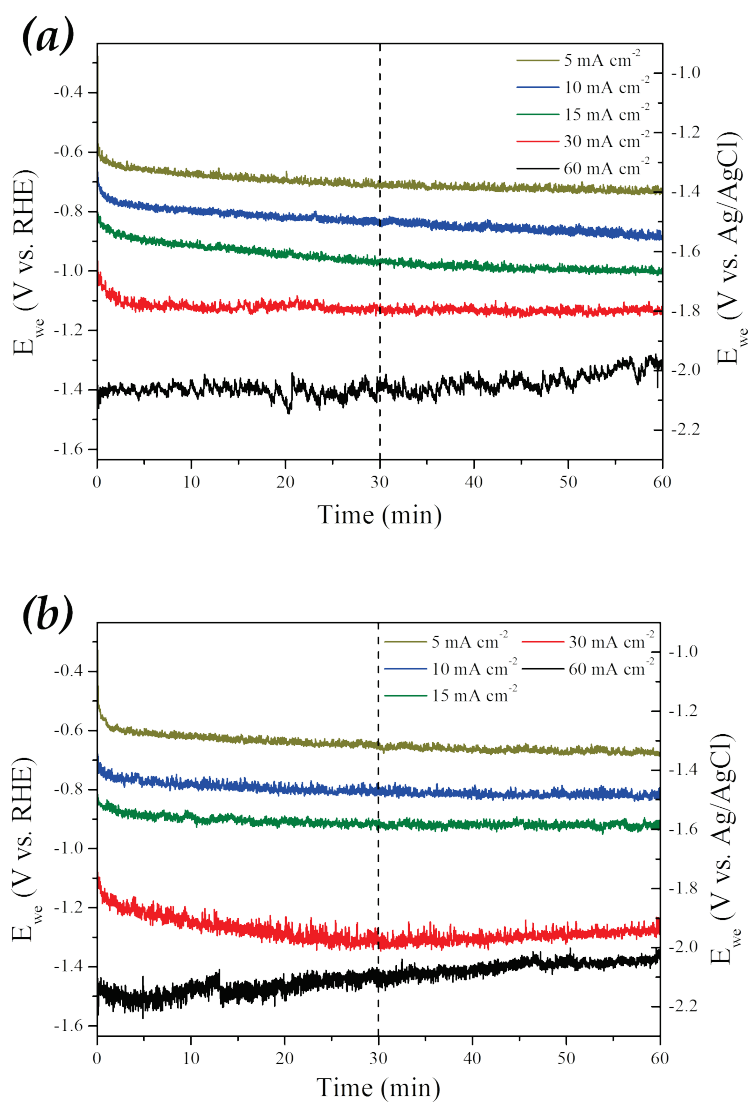


**Figure 4.4.** Cu-GDE-Epol electrode potential versus time during the electrochemical  $\text{CO}_2$  reduction in (a)  $\text{KHCO}_3$  and (b)  $\text{NaHCO}_3$  at different current densities, indicated in the figure.

In **Figure 4.4** is possible to observe a shift in the potential to more negative values when at higher current densities when the

cation changes from potassium to sodium. As mentioned before, the electrolytes have the same concentration and anion, but the differences are in the positive ions involved for the charge compensation. The reason for this potential increment is explained by Wu *et al.* [15], in their work a deeper study of the electrolyte effect in the carbon dioxide reduction using tin (Sn) as catalysts was done. They made a correlation between the ionic radius with the dielectric constant. The dielectric constant of an aqueous solution increase with the cation size (Pauling radius, Na<sup>+</sup> = 0.95 Å, K<sup>+</sup> = 1.33 Å) and as consequence is giving lower electrode potentials in the case of the potassium electrolyte and increasing in the sodium.

There is a large possibility in the products generation from carbon dioxide reduction going from gaseous products as H<sub>2</sub>, CO, CH<sub>4</sub>, C<sub>2</sub>H<sub>4</sub>, etc. to liquid products as formic acid, methanol, ethanol, etc. Jaramillo *et al.* [16] reported a deep analysis of the different products obtained over a copper surface, using a very similar electrochemical cell setup. The mayor products obtained in the test was H<sub>2</sub>(g), CH<sub>4</sub>(g), [HCOO]<sup>-</sup>(liq.), CO(g) and C<sub>2</sub>H<sub>4</sub>(g). As result of their study they conclude that in the reaction rate and selectivity for the C<sub>2+</sub> products there are two critical factors: (1) the coverage and chemical identities of C<sub>1</sub> and C<sub>2</sub> surface species play major roles in determining which C<sub>2+</sub> products are formed and, (2) the possibility of the enol-like species as reaction intermediates. In our work the interest goes to the gaseous products which were measured by a MicroGC coupled to the exit of the electrochemical cell, considering as the only products obtained.

The yield of an electrochemically generated product is expressed in terms of the so-called faradaic efficiency or yield defined as follows [9]. In an electrolysis experiment, a number of coulombs passed through the cell. The charge is simply the product of the current ( $A \text{ cm}^{-2}$ ) and time (seconds,  $s$ ) or the integral over time.

$$Q = \int I dt \quad (4.1)$$

In principle all the products of the reaction can be identified and quantified in a given time interval. The faradaic efficiency is defined as the ratio of the number of coulombs required to form the amount of a product determined by chemical analysis to the total charge in the specified time interval. In an ideal system, the sum of the faradaic efficiencies for all products must reach 100% and the products are said to be in faradaic balance.

In our case to calculate the faradaic efficiency we start with the amount of ppm reached in the gas chromatography measurements for the gaseous products generated. As mentioned before our interest is focused on this products and no liquid analysis was done. First with the amount of ppm for one product ( $Y$ ) is transformed to  $\text{mol}_{e^-} \cdot \text{min}^{-1}$  with this formula:

$$\text{ppm}_Y = X_{\mu L/L_{mix}} \times \frac{L}{10^6 \mu L} \times \text{Flow} (L_{mix} \text{ min}^{-1}) \times \left( \frac{P}{T \times R} \right) \times n_{e^-} \quad (4.2)$$

Where  $Flow$  is the gas flow injected into the electrochemical cell,  $P$  is the pressure ( $1 \text{ atm}$ ),  $T$  ( $K$ ) is the temperature ( $25^\circ\text{C}$ ),  $R$  is the gas constant ( $0.082 \text{ atm L/K mol}$ ) and  $n_{e^-}$ , are the electrons involved to obtain the product  $Y$  (**Chapter I**).

After the Eq. 4.2, is possible to obtain the partial current density of the product  $Y$ , ( $j_Y$ ) following the Eq. 4.3:

$$j_Y(\text{mA cm}^{-2}) = \frac{X_{\text{mol e}^-/\text{min}} \times F \times Z}{A} \quad (4.3)$$

Where  $Z$  is a conversion factor ( $16.7 \text{ mA min/A s}$ ),  $F$  is the faradaic constant ( $96485.4 \text{ C (A s)/mol e}^-$ ) and  $A$  is the electrode area ( $\text{cm}^2$ ). To obtain a faradaic balance without measuring the liquid products require the normalization of the partial current of each product ( $j_{\bar{y}}$ ) to not overpass the 100% faradaic efficiency.

$$j_{\bar{y}} = \frac{j_Y}{\sum j_{\text{each product}}} \times j_{\text{Total}} \quad (4.4)$$

Where  $j_{\text{Total}}$ , is the total current density applied to the working electrode ( $\text{mA cm}^{-2}$ ) and  $\sum j_{\text{each product}}$ , is the sum of the partial current densities of all products measured. To obtain the faradaic efficiency ( $FE$ ) is needed to divide the normalized partial current density between the absolute value of the total current density applied.

$$FE (\%) = \frac{j_{\bar{y}}}{|j_{\text{Total}}|} \times 100 \quad (4.5)$$

Whit the equations explained before all the faradaic efficiencies values were obtained for the electrochemical experiments with metallic copper and coper oxide electrodes.

In **Figure 4.5** is possible to observe the faradaic efficiencies of the  $\text{CO}_2$  reduction using metallic copper (mesh) electrode ( $\text{Cu-GDE-Epol}$ ). When the data is analyzed is possible to observe the differences in the faradaic efficiencies values in each electrolyte,

reaching to higher values in the case of the potassium one. The products obtained in the  $\text{CO}_2$  electrochemical conversion was analyze by gas chromatography obtaining hydrogen ( $\text{H}_2$ ) as the mayor product, carbon monoxide ( $\text{CO}$ ), methane ( $\text{CH}_4$ ) and ethylene ( $\text{C}_2\text{H}_4$ ). The selectivity of the copper electrode corresponds with the crystallographic faces obtained in the XRD. Obtaining methane due to the high intensity of the (111) peak, and ethylene in the case of the (100).

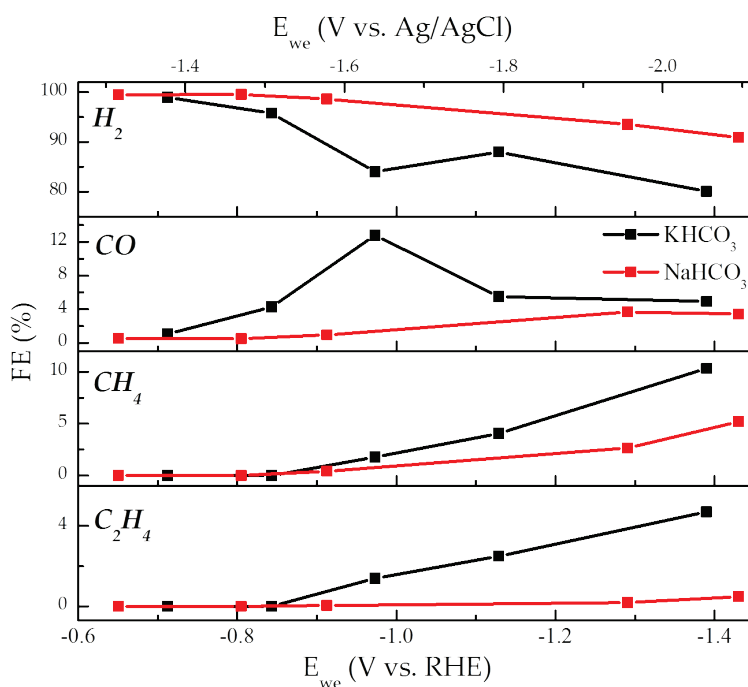


**Figure 4.5.** Faradaic efficiencies obtained in the electrochemical  $\text{CO}_2$  reduction using copper mesh as GDE in potassium and sodium hydrogencarbonate electrolyte.

The different activity in the carbon dioxide conversion is related to the negative (anion) and positive ions (cation) used in the

aqueous electrolyte. Ogura [17] in his work is focus on the mechanism of the ethylene production, but in one part of the work he explains that the CO<sub>2</sub> is attracted to the electrode on account of the electron flow from the adsorbed anion to the vacant orbital of CO<sub>2</sub>. This attraction may cause the structural transformation of CO<sub>2</sub> from the linear form to the bend. The occurrence of the X<sub>ads</sub><sup>-</sup> – C bond results in the weakening of the C – O bond and the chemical activation of CO<sub>2</sub> occurs. Ogura uses halide as electrolyte and he explain the different specific absorption ability for different anions (*Figure 4.6.*) involved in the inner Helmholtz plane to block the proton absorption and enhancing the overpotential of the hydrogen evolution. In our experiment the anion used is the same in both cases ([HCO<sub>3</sub>]<sup>-</sup>) changing only the cation.

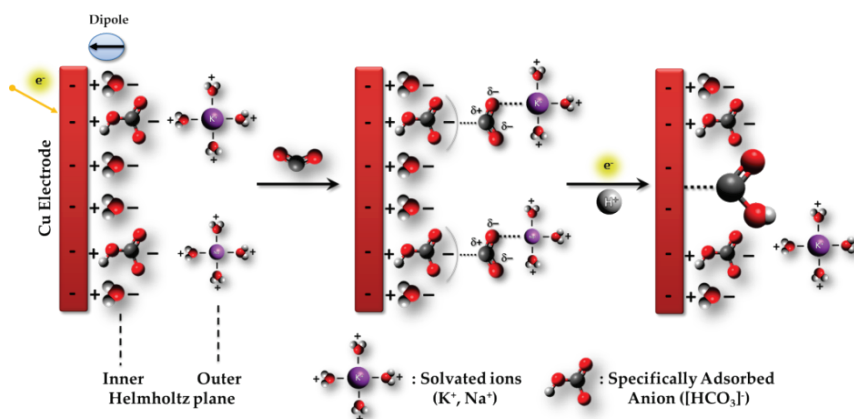


*Figure 4.6. Electric double layer attraction of the CO<sub>2</sub> and formation of the formate radical by the inner-sphere mechanism proposed by Ogura [17] adapted for the ions used in ours experiments.*

The same work explain the importance of the cation involved in the charge compensation of the X<sub>ads</sub><sup>-</sup> – CO<sub>2</sub> in the inner Helmholtz

plane. But to compensate the charges the solvated cations cannot approach to the electrode further the outer Helmholtz plane for a closer approach. The sizes of the solvated cations have an important influence in the charge compensation. Corresponding with the cations size used in ours the hydration degree should increase in this order,  $K^+ < Na^+$  due to the Lewis acid power and polarization power, which are related with the charges and size of the cations. Relative to charges both cations have the same however relative to size; potassium has a bigger radius and as result, lower polarization power compared with sodium. Due to this evidence, in  $K^+$  the water molecules around are more labile and detachable than around  $Na^+$ . As sequence the interaction of  $K^+$  with the nucleophilic oxygen of the  $CO_2$  becomes possible as shown in *Figure 4.6*. The stabilization of the  $CO_2$  in the double layer enhances the acceptance of the electrons coming from the cathode improving the efficiency of the electrochemical process. Thorson *et al.* [18] made a deep research about the cation effect over the efficiencies in the electrochemical conversion of  $CO_2$  to  $CO$ . Following this work they made a comparative between different halides and hydroxide salts with the alkali metals as cations. In addition they explain the same idea of the stabilization in the Helmholtz plane of the intermediate specie involved in the  $CO_2$  reduction reaction.

As mentioned in **Chapter I** the limiting step in the reaction is:



This  $\text{CO}_2^-$  may be stabilizing by the cation adsorbed in the electrode by ion pairing. Subsequently to this, there is an improvement in the current density with the overpotential reduction derivation, increasing the faradaic efficiency. As conclusion Thorson explains that using small cations ( $\text{Na}^+$ ) the  $\text{H}_2$  evolution is favored, as result, lower faradic efficiencies are obtained for CO. However, with large cations ( $\text{K}^+$ ) the CO production is favored and somehow the  $\text{H}_2$  evolution is suppressed rising with high faradaic efficiencies for CO.

### *4.2.1.2 Electrolyte Concentration Effect and Cu foil experiments*

The aim to use a copper foil with high level of purity as electrode is to improve the faradaic efficiency for the methane production. Due to the impurities coming from the copper or the electrolyte used [14,19,20] could reduce the catalytic activity. The setup for this electrode must be changed because it is not possible to assemble like a gas diffusion electrode. The carbon dioxide gas source must to be bubbled in the electrolyte (catholyte) to keep the concentration of these gas constant, due to the low solubility of the  $\text{CO}_2$  in the aqueous media ( $1.45 \text{ g L}^{-1}$  at  $25 \text{ }^\circ\text{C}$ ). To improve the solubility value there are two common pathways: the pressure and temperature increment or moving to another kind of electrolytes. One of this electrolytes could be ionic liquids, where the carbon dioxide could be dissolved by physisorption avoiding the competition of the  $\text{CO}_2$  reduction reaction with the bond strength in the chemisorption process [21–23]. As sequence, opening the molecule and decreasing the energy requirements for the process.

For all the electrochemical experiments the current density was set at  $30 \text{ mA cm}^{-2}$  during one hour to secure that the product obtained from the  $\text{CO}_2$  reduction are representative to analyze by gas chromatography, the surface of the electrode was  $1 \text{ cm}^2$  and the electrolyte selected was  $\text{KHCO}_3$  (due to the better activity compared with sodium). First of all the  $\text{CO}_2$  flow must be fixed to the optimal condition trying to keep constant  $\text{CO}_2$  concentration in the electrolyte because in this kind of setup is the critical point. For comparing the activity of different electrolyte concentration in this test the flow optimization was done over  $0.1 \text{ M}$  of  $\text{KHCO}_3$ .

In *Figure 4.7* is represented the activity of the  $\text{CO}_2$  reduction at different  $\text{CO}_2$  bubbling flows. Accordingly with the data,  $\text{CH}_4$  is only appreciable at higher gas flow rates, precisely at  $50$  and  $100 \text{ mL min}^{-1}$  the activity is more stable compared with the rest of them. Using  $0.1 \text{ M}$  of  $\text{KHCO}_3$  the working electrode potential is around  $-3.4$  to  $-3.8 \text{ V vs. Ag/AgCl}$  for the flow rate experiments due to the decrease in the electrolyte conductivity [15]. To decrease this overvoltage generated in the flow rate tests the electrolyte concentration is increased to  $0.5 \text{ M}$  to improve the conductivity and subsequently the faradaic efficiency.

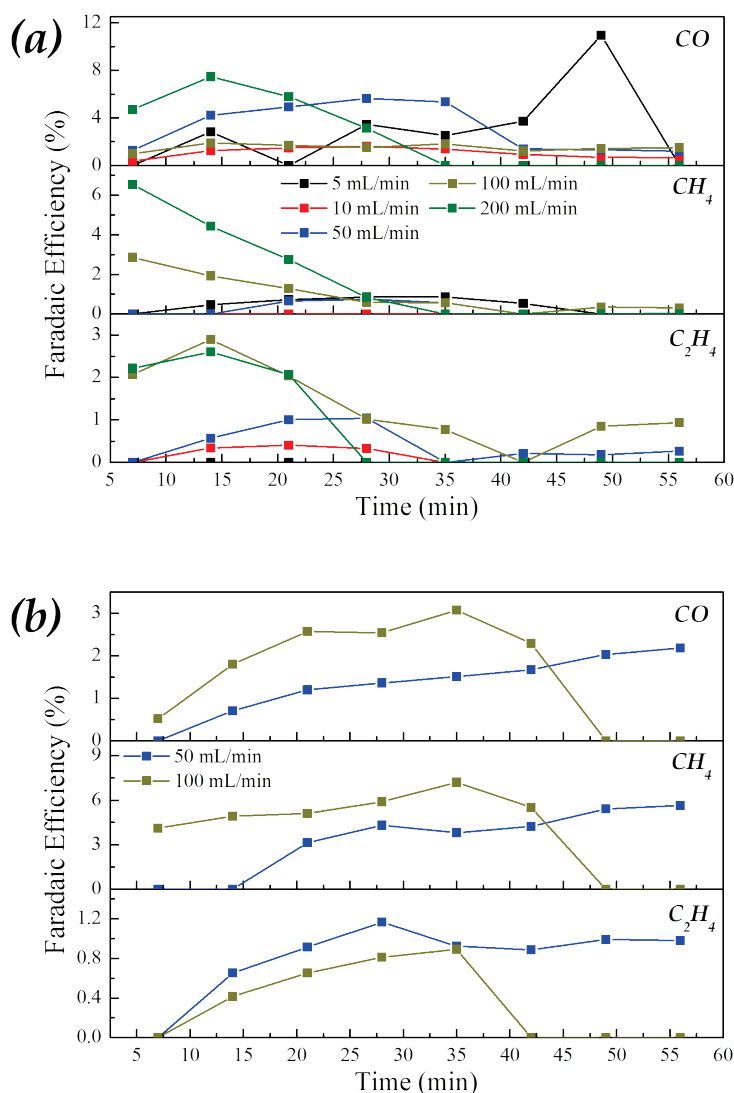


**Figure 4.7.** (a) Faradaic efficiencies of CO<sub>2</sub> reduction over high purity copper foil (Cu-Chem) at different CO<sub>2</sub> bubbling flow rates in the catholyte (0.1 M). (b) Faradaic efficiencies of the CO<sub>2</sub> reduction over high purity copper foil at 50 and 100 mL min<sup>-1</sup> CO<sub>2</sub> bubbling flow rates in the catholyte (0.5 M).

When the electrolyte concentration was increased the methane activity improves reaching to higher values with better stability.

The potential of the working electrode in these experiments was reduced considerably archiving values around  $-2$  V vs Ag/AgCl with similar voltages values obtained in the gas diffusion setup. We should mention that the copper electrode only have the chemical treatment (HCl : H<sub>2</sub>O) for the surface cleaning (*Chem*). Using the same pretreatment over the copper mesh an electropolishing was done to the copper foil to improve the activity over the methane production. The evolution of the different parameters modified to reach the best conditions is shown in *Figure 4.8*.

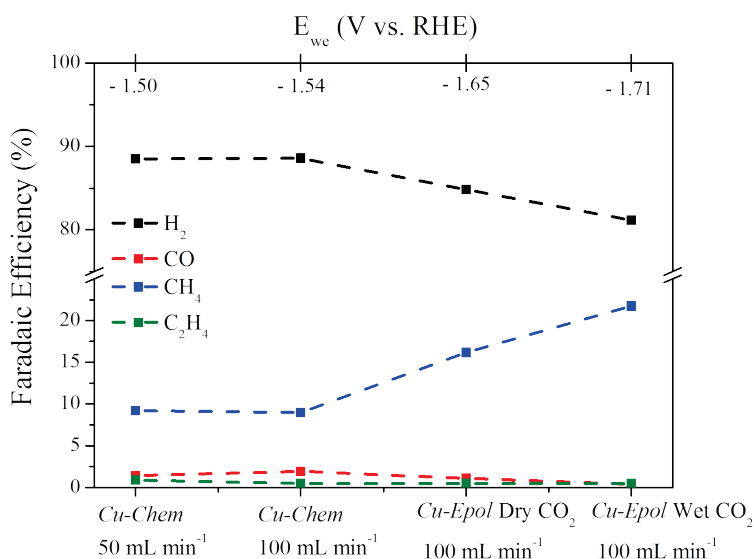


*Figure 4.8.* Copper foil activity evolution changing the CO<sub>2</sub> bubbling flow in the electrolyte and after the surface treatment.

In this plot is possible to observe the methane production at the different modified parameters. We start first with the modification of the bubbling flow rate to the optimal conditions using only the chemical surface cleaning. After the surface electropolishing was

done, increasing more the activity and at the end the humidification of the CO<sub>2</sub> gas stream before the entrance to the catholyte. The last condition included will be studied later in a separated section. The maximum efficiency obtained using the metallic copper electrode is 20% for methane using the best conditions for the copper foil electrode in which the predominant crystal face is (200) –parallel to (100)- where ethylene must have the best efficiency due to the explained before. But in our electrode before the electropolish treatment the predominant face was (111) which improves the methane activity. Hori *et al.* [12] explain that the introduction of (100) planes over basal system of (111) does not enhance so much the activity for ethylene keeping the activity for methane. In summary, using a copper foil is complicated make longer electrochemical tests due to a mass transfer problem (solubility in water) of CO<sub>2</sub> and the large potential required for the methane formation with a high efficiency. If a copper electrode with high purity level could be implemented in a GDE setup then it could be possible to enhance the efficiency for methane in the CO<sub>2</sub> reduction.

#### **4.2.2 *Cu<sub>x</sub>O Mesh as Gas Diffusion Electrode***

The problem with the metallic copper is the large overvoltage needed to obtain methane with high efficiency ( $> 0.7 V$  vs. NHE) [5]. This large overvoltage must be reduced for the scalability of the process to decrease the energy requirements and giving the possibility to couple with a photoactive anode to implement it in a photoelectrochemical cell for the artificial photosynthesis process.

The copper oxide electrodes were used by some researchers for the CO<sub>2</sub> reduction electrolysis. The oxides were reduced to Cu<sup>0</sup> in situ during the CO<sub>2</sub> reduction catalysis, but only transient changes in the CO<sub>2</sub> product distribution attributed to oxide catalysis were observed [24,25]. Li and Kanan [26] shown the CO<sub>2</sub> reduction properties of Cu<sup>0</sup> electrodes resulting from copper oxide reduction vary widely depending on the properties of the initial oxide layer. The copper oxide was done by high annealing temperature and the result of the layer reduction is an electrode that catalyzes energy-efficient CO<sub>2</sub> reduction with stability to the deactivation phenomena. In our case, as result of the thermal treatment in air at 500 °C during one hour using a metallic copper mesh, we obtain a thick copper oxide layer with nanowires [27]. The copper mesh was used to obtain a uniform oxide layer because in a copper foil the oxide layer generated suffers surface tensions generating the oxide layer peel off. In addition, with the copper oxide mesh is possible to assemble the electrode in a gas diffusion electrode.

The characterization to observe the surfaces morphology was done by SEM. In *Figure 4.9* is possible to observe the surface of the copper oxide electrode after the thermal synthesis before any carbon dioxide reduction experiment.

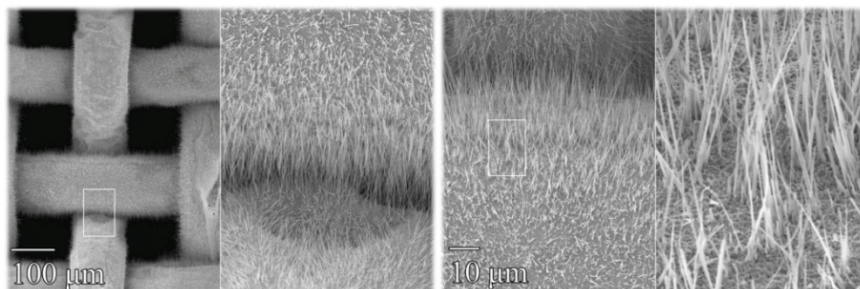


*Figure 4.9. Cu<sub>2</sub>O electrode images before the CO<sub>2</sub> electrochemical test.*

XRD was used to confirm structure of the oxides layers obtained in the thermal synthesis. The pattern obtained has the characteristic peaks expected for the copper oxide (II), (I) and the metallic copper substrate (*Figure 4.10*).

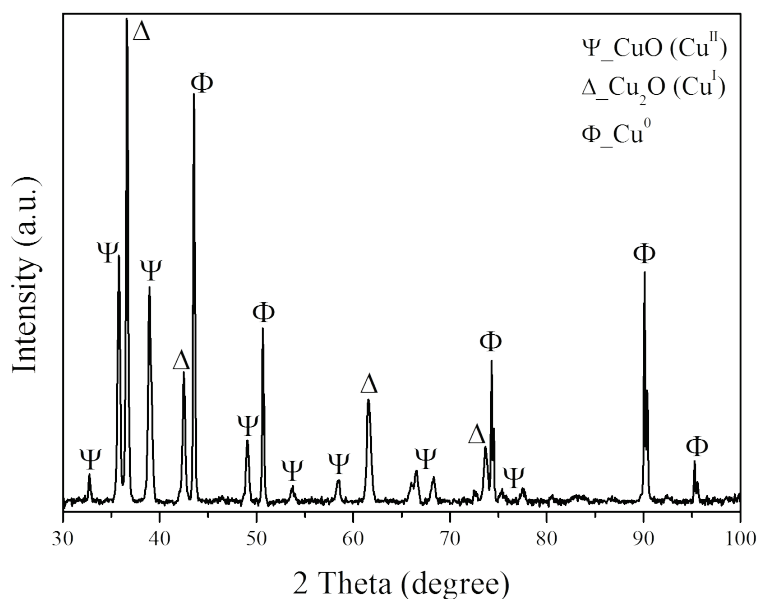


*Figure 4.10. XRD pattern of the Cu<sub>x</sub>O electrode before the electrochemical CO<sub>2</sub> reduction.*

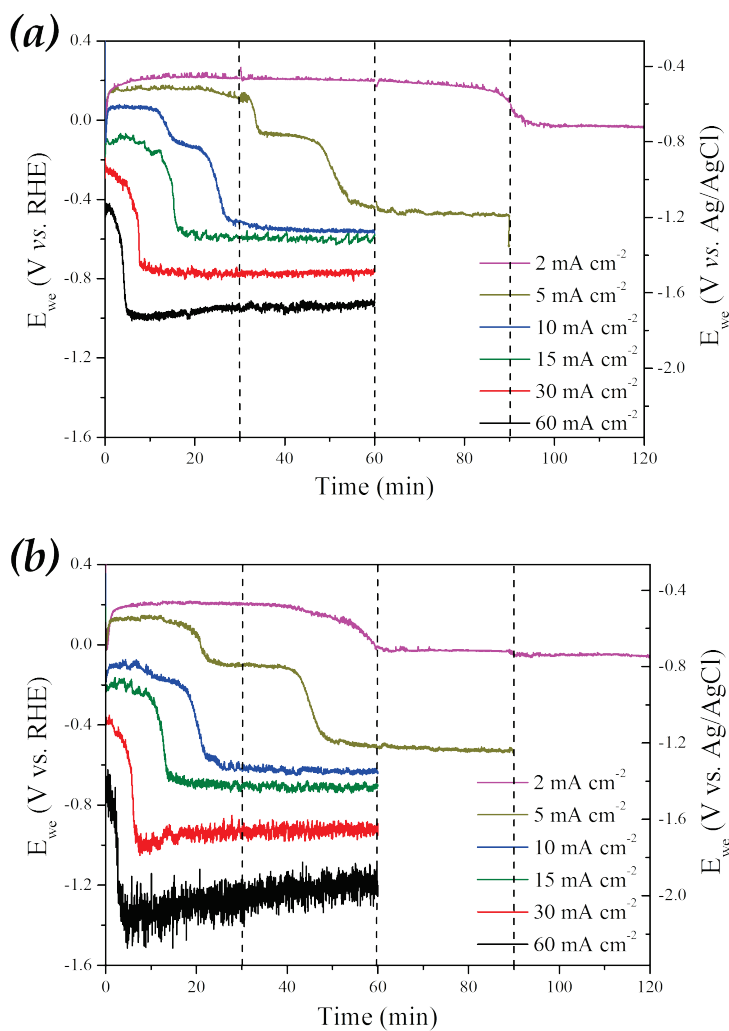
Table 4.1 shown all the peaks measured for all the oxides generated over the copper electrode in a core shell organization.

Table 4.1. XRD crystal faces of the copper oxide electrode before CO<sub>2</sub> electroreduction test.

$\psi\_CuO (Cu^{II})$				$\Delta\_Cu_2O (Cu^I)$		$\Phi\_Cu^0$	
(h k l)	2 $\theta$ (°)	(h k l)	2 $\theta$ (°)	(h k l)	2 $\theta$ (°)	(h k l)	2 $\theta$ (°)
1 1 0	32	0 2 2	66	1 1 1	36	1 1 1	43
0 0 2	35	-3 1 1		2 0 0	42	2 0 0	50.6
-1 1 1	35.7	3 1 0		2 2 0	62	2 2 0	74
1 1 1	38.9	1 1 3	68	3 1 1	73	3 1 1	90
2 0 0	46	2 2 0				2 2 2	95
-2 0 2	49	0 0 4	75				
0 2 0	53	-2 2 2	76				
2 0 2	58						

#### 4.2.2.1 Electrocatalytic reduction of CO<sub>2</sub> in KHCO<sub>3</sub> and NaHCO<sub>3</sub> over a Copper Oxide (Cu<sub>x</sub>O) surface

The Chronopotentiometric (CP) experiments done were carried out at the same electrochemical conditions as in the metallic copper electrode applying different current densities (2 – 60 mA cm<sup>-2</sup>) to the working electrode.



**Figure 4.11.** *Cu<sub>x</sub>O* electrode potential versus time during the electrochemical CO<sub>2</sub> reduction in (a) KHCO<sub>3</sub> and (b) NaHCO<sub>3</sub> at different current applied.

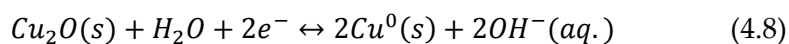
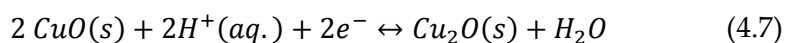
In **Figure 4.11** is possible to observe a big decay in the working electrode potential due to the oxide layer reduction into the electroactive copper (Cu<sup>0</sup>) and a small shift to more negative potentials in the sodium electrolyte (explained in **Figure 4.6**). In both plots the second voltage drop is evident (the CuO reduction

step) but the first jump ( $\text{Cu}_2\text{O}$  reduction) only is possible to observe at lower values of current density. In the potential evolution at 60 and 30  $\text{mA cm}^{-2}$  the first decay is very fast and it is not remarkable for both electrolytes. At 15  $\text{mA cm}^{-2}$  the first drop starts to be slightly visual only in the potassium electrolyte. In the case of 10 and 5  $\text{mA cm}^{-2}$  the two steps of the oxides reduction layer are more obvious in the potassium one due to slower oxide layer reduction. Using sodium, the oxide reduction is faster as seen in *Figure 4.11 (b)*. This difference in the oxide layer reduction speed will be further studied lately (4.2.2.2). The markdown at 2  $\text{mA cm}^{-2}$  takes more than two hours to reach to the stable copper surface in the test only reach to the second level in both electrolytes.

DFT calculations done by Asthagiri *et al* [28] over a  $\text{Cu}_2\text{O}$  (111) explain the preference for a Cu terminated surface and the favorability to reduce it thought O –vacancy formation are related with the thermodynamic driving force given by the Pourbaix diagram, to the reduction of the  $\text{Cu}_2\text{O}$  electrode to metallic copper under  $\text{CO}_2$  electroreduction conditions. The oxide layer reduction is favored and faster than the  $\text{CO}_2$  reduction reaction. For this reason, in this region only  $\text{H}_2$  evolution in low range is measured. Kenis *et al.* [29] made a electrochemical study of the behavior for Cu (core)/CuO (shell) catalyst using 1 M of  $\text{KHCO}_3$ . The catalyst is transformed between various oxidation states of copper, Cu,  $\text{Cu}^{\text{I}}$  and  $\text{Cu}^{\text{II}}$ . Nakayama *et al.* [30,31] develop a electroanalytical method to elucidate the copper oxides reduction mechanism using a strongly alkaline electrolyte. In this case the shape of the plots obtained has the same tendency like ours but with more negative

potentials due to the strong basic pH used. This transformation between the copper oxidation states was deep studied by Takanabe *et al.* [32], they study the properties of the Cu<sub>2</sub>O using different annealing conditions for photoelectrochemical [33,34] and electrocatalytic applications. In this work they do an electrochemical study of the evolution in the oxide layers at the same pH conditions (7.9, in our case 7.8) and corresponding with their black sample (obtained at the same conditions like ours) the shape of the CP obtained is very similar to ours.

The two plateaus observed clearly at lower current densities in *Figure 4.11* correspond to the copper oxide species obtained in the thermal synthesis. The corresponding reactions of the oxides reduction are shown below reaching to electroreduced copper as Cu<sup>0</sup> where the CO<sub>2</sub> reduction activity starts.



At the end of the electrochemical experiment all the samples were characterized by SEM and X-ray diffraction. First we start by the copper surface images shown in *Figure 4.12*. In the pictures the surfaces in both electrolytes have not so much differences. The copper oxide wires obtained in the thermal treatment disappear partially reaching to a rough surface with many cracks in the oxide layer over all the mesh.

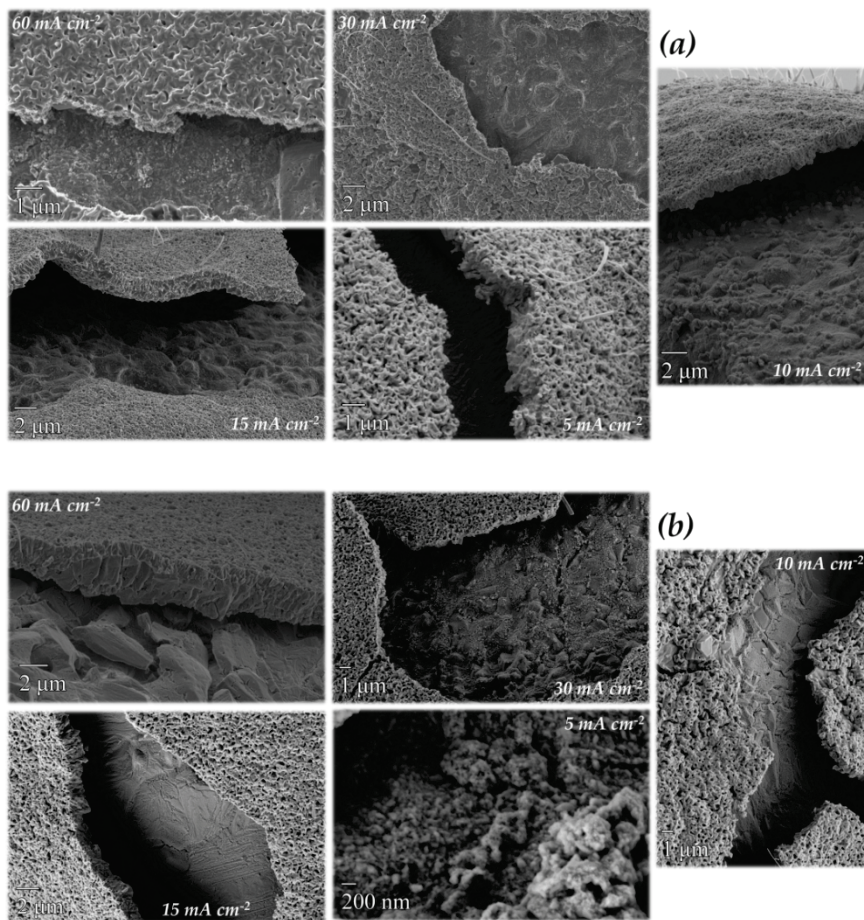


**Figure 4.12.** Copper oxide electrodes SEM images after one hour of electrochemical test at different currents densities applied (a)  $\text{KHCO}_3$  and (b)  $\text{NaHCO}_3$ .

The corresponding XRD patterns of the images in **Figure 4.12** are shown in **Figure 4.13**. There are no so much differences between them, only in (a) at  $j_5$  (220) crystal face intensity is higher than the rest of the other peaks. However, in the other samples the most intensity peak is the (111) corresponding with electroreduced

copper (Cu<sup>0</sup>). In the case of the oxide layer only a very small peak is observable at low current densities.

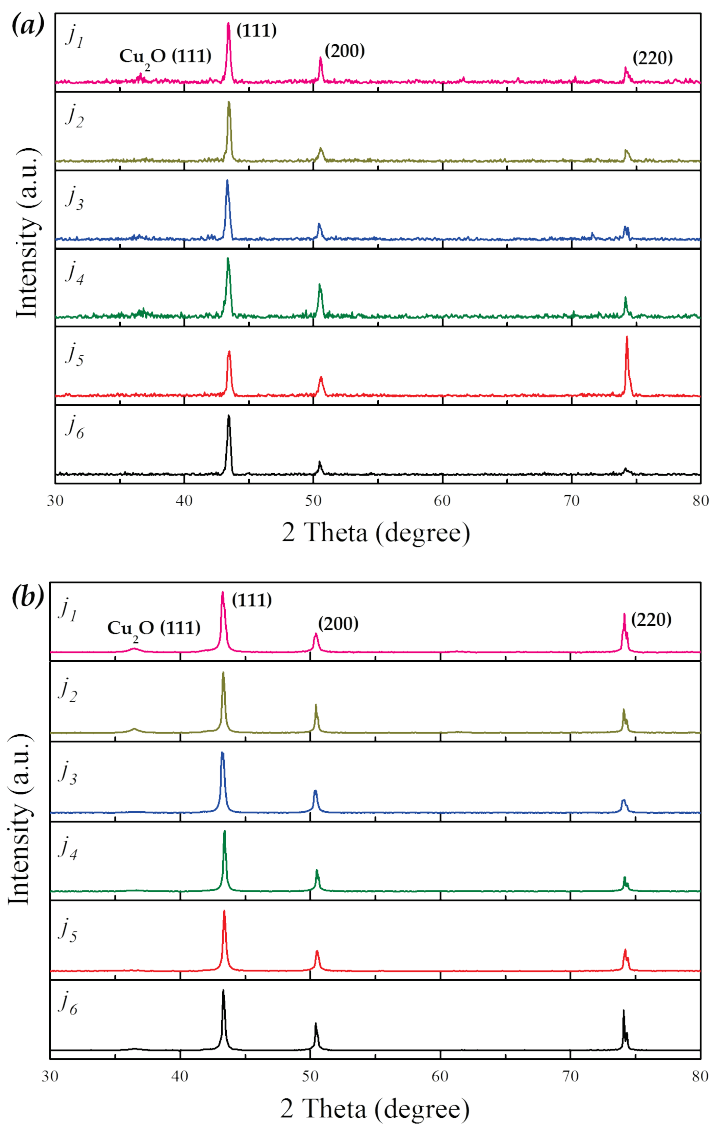


**Figure 4.13.** XRD pattern of the Cu<sub>x</sub>O electrode after 60 min for  $j_3$  to  $j_5$ , 90 min for  $j_2$  and 120 min for  $j_1$  of galvanostatic test at different currents densities applied ( $j_1 - j_6$  corresponding with 2, 5, 10, 15, 30 and 60 mA cm<sup>-2</sup>). (a) KHCO<sub>3</sub> and (b) NaHCO<sub>3</sub>..

As mentioned before the CO<sub>2</sub> reduction activity in these electrodes does not start before the third voltage drop in the working electrode potential. The selectivity for this reduced copper should be the same, as metallic copper due to the most intense crystal faces obtained in the XRD which favor the methane production. However it was found that, in our case, the activity of these electrodes suppress the methane production giving only selectivity for: H<sub>2</sub>, CO, C<sub>2</sub>H<sub>4</sub> and C<sub>2</sub>H<sub>6</sub>. In these experiments the liquid phase was not measured again, but there are liquid products which is possible to obtain with these reduced copper electrodes. These liquid products can be methanol [25,35], formate (HCOO<sup>-</sup>) reported by Kanan, Takanabe and Qiao [26,32,36] obtained at low overpotentials.

As mentioned before (section 4.2.1) CO is considered as intermediate specie in the electrochemical CO<sub>2</sub> reduction. In a reported work done by Kanan [37] they study the CO reduction to liquid fuel using oxidized copper. The products obtained were multi-carbon oxygenates (ethanol, acetate and *n*-propanol) at a modest potentials  $-0.25\text{ V}$  to  $-0.5\text{ V vs. RHE}$ . *Figure 4.14* shows the faradaic efficiencies obtained using the copper oxide electrode using 0.5 M of potassium and sodium hydrogen carbonate as electrolyte.

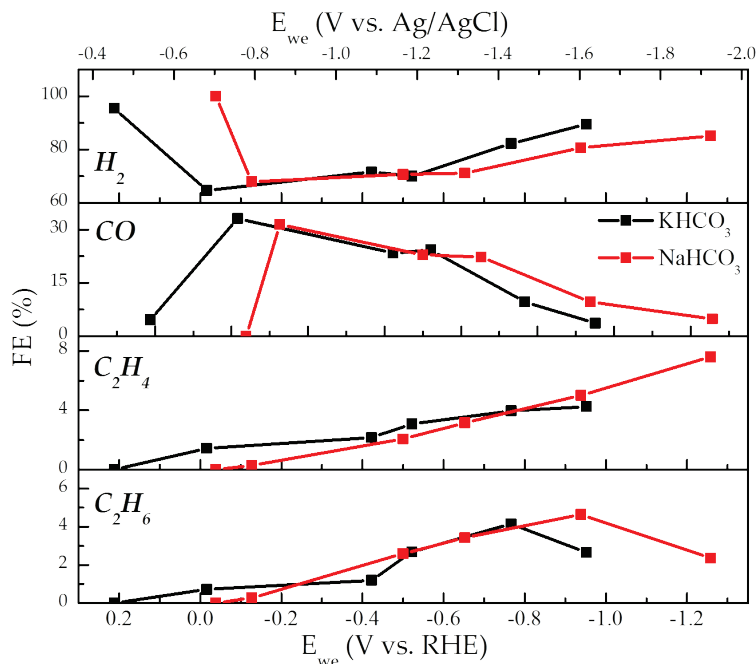
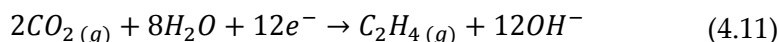
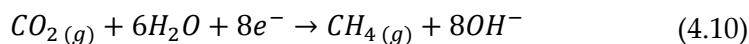


**Figure 4.14.** *Cu<sub>x</sub>O* GDE faradaic efficiencies using NaHCO<sub>3</sub> (red line) and KHCO<sub>3</sub> (black line) electrolytes.

The expected shift in the potentials using sodium instead potassium is obtained in these experiments too. Results suggest that the positive ions have the same effect over the Helmholtz double layer in the surface of this electrode. There are no so much differences in the faradaic efficiencies values between the two electrolytes. But in terms of potential there is a decrease of 0.2 V at high current densities, reaching to the same faradaic efficiency value in the case of the ethane productivity with lower potential. Related to the ethylene production, in sodium electrolyte can reach better values but the voltage is increased to values around  $-1.2$  V vs. RHE. In the CO production we found a peak of activity at lower potentials around  $-0.1$  V vs. RHE. However the CO activity

starts to decrease when the other carbon products start to be produced. Nevertheless H<sub>2</sub> evolution has the highest efficiency, following by CO, ethylene (C<sub>2</sub>H<sub>4</sub>) and ethane (C<sub>2</sub>H<sub>6</sub>). Taking account that the methane production is completely suppressed the electrode surface does not act like metallic copper. In the XRD patterns of the electrode after the electrochemical test (*Figure 4.13*) is possible to observe a very small peak of Cu<sub>2</sub>O practically in all of them. In reported work by Lee *et al.* [38] demonstrate the selectivity towards C<sub>2</sub>H<sub>4</sub> at low overpotential, they support that they obtain a stable Cu<sub>2</sub>O layer on the top of the bulk Cu<sub>2</sub>O – derived Cu. This decrease of the oxygen concentration in the Cu<sub>2</sub>O electrode during the electrolysis gives many oxygen-vacant structures distributed randomly over the Cu<sub>2</sub>O-derived bulk layer. These vacancies are the responsible for the reactivity for ethylene formation. They support that the Cu<sub>2</sub>O depletion could be done due to these reactions:



The hydroxide ions (OH<sup>-</sup>) generated at the electrode surface in the CO<sub>2</sub> reduction gives an instantaneous rise in the local pH closer to the surface layer as active sites [14,4,39]. But is demonstrated that in this electrolytic conditions the Cu<sub>2</sub>O reduction to Cu is suppressed [35,40,41]. And in other reported works the Cu<sub>2</sub>O shows a good stability in alkaline media during cathodic potential in the

oxygen reduction reaction [42,43]. Maybe this increase in the pH at the surface gives the selectivity for ethylene, due to correlation with the pH increment [44,45].

Relative to the Cu<sub>2</sub>O structural transformation and stability during the CO<sub>2</sub> electrolysis many different reported works studied this effect. Kim *et al.* reports the CuO and Cu<sub>2</sub>O reduction reaction with H<sub>2</sub> using DFT calculations combined with X-ray diffraction and X-ray absorption to study the mechanism involved in the reduction of these oxides. They conclude that in the case of the CuO under hydrogen can be reduced directly to metallic copper. But in the Cu<sub>2</sub>O the reduction is more complicated due to the easily formation intermediates species or suboxides. Maimaiti *et al.* found in their DFT calculations that the loss of superficial oxygen is thermodynamically favorable in copper oxide reduction and support that the reduction of CuO to Cu at the surface is more energetically difficult than in the bulk phase [46]. Wu *et al.* made a DFT study of the CO<sub>2</sub> adsorption on the oxygenated vacancies in a Cu<sub>2</sub>O (111) surface. They conclude after the theoretical calculations that the dissociative CO<sub>2</sub> adsorption on the oxygen vacancy surface is unfeasible. But they found that these oxygen vacancies are active sites and the CO<sub>2</sub><sup>δ-</sup> radical anion can be formed. This CO<sub>2</sub> reduction reaction intermediate has low adsorption energy and due to his high reactivity it can easily leave off the adsorption sites [47] giving the decrease in the potential values, corresponding with the data shown.

### 4.2.2.2 Electrochemical evolution of the $\text{Cu}_x\text{O}$ layers in the $\text{CO}_2$ reduction

A structural study for the copper oxide electrode to observe the evolution of the copper oxide surfaces at the different potentials plateaus observed in *Figure 4.11* was done to demonstrate the cation effect over the oxide layer reduction. Both electrolytes were used to observe if there is any effect coming from the cations. The chronopotentiometric experiments were carried out at  $10 \text{ mA cm}^{-2}$ . At this current density ( $j$ ) value is possible to observe the two potential decays for both electrolytes and at the potential reached there is activity for the  $\text{CO}_2$  reduction. All the tests were done using different electrodes synthesized at the same time, with the same methodology and fresh electrolyte for each experiment. The CP experiments were stopped at different times ( $t_1$ ,  $t_2$  and  $t_3$ ) corresponding to the middle point in each copper oxide potential plateau. The characterization at the different steps was done by SEM to observe the surface morphology evolution at each potential and XRD to observe the evolution of the copper oxide structure until reaching the active copper surface ( $\text{Cu}^0$ ).

First of all, we start with the  $\text{KHCO}_3$  the data of the working electrode potential vs. time is shown in *Figure 4.15* with the corresponding SEM surface images done at the different stop times indicated in the plots.

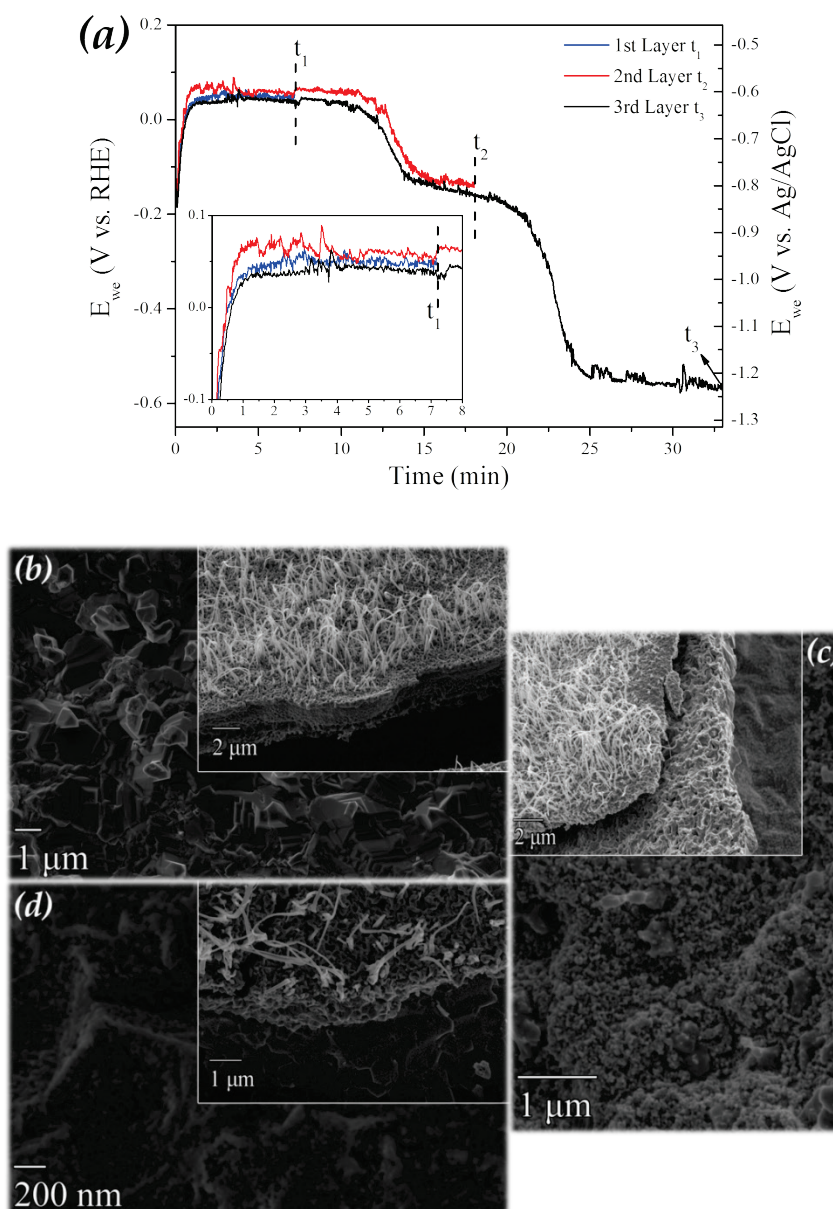


**Figure 4.15.** (a) CP experiment stopped at 8, 18 and 32 minutes corresponding  $t_0$   $t_1$ ,  $t_2$  and  $t_3$  to observe the oxide layer reduction. The SEM images (b)-(d) correspond at the stopped time respectively.  $\text{KHCO}_3$  electrolyte.

The images in *Figure 4.15* showed the electrode surface at different times. The low magnification image shows the copper surface evolution, where the roughness and the porosity increase with time. In the high magnification images, there are no so much differences in the copper oxide surface and some wires obtained in the thermal treatment still appearing. Additionally, an XRD (*Figure 4.15*) at each time was done corresponding with the images (b), (c) and (d).

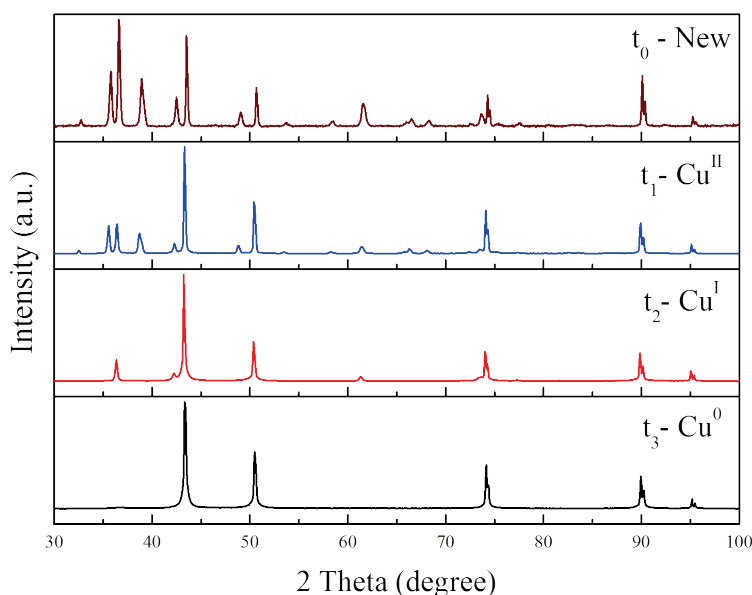


*Figure 4.16.* XRD patterns of the  $\text{Cu}_x\text{O}$  electrode at different times to observe the corresponding oxide layer ( $\text{KHCO}_3$ ).

*Figure 4.16* shows different states of the  $\text{Cu}_x\text{O}$  electrode surface at four times ( $t_0 - t_3$ ), which corresponds to fresh  $\text{Cu}_x\text{O}$ ,  $\text{Cu}^{\text{II}}$ ,  $\text{Cu}^{\text{I}}$  and  $\text{Cu}^0$  species respectively. First of all at  $t_0$  the copper oxide electrode fresh prepared (brown line). At  $t_1$  the blue line pattern corresponds to  $\text{CuO}$ , the peaks position are like at  $t_0$  but with lower

peak intensity respect Cu (II) and Cu (I) oxides. At  $t_2$  (red one) part of the corresponding peaks of CuO disappears completely, maintaining only the Cu<sub>2</sub>O characteristic peaks. At  $t_3$ , pattern corresponds to metallic copper surface where the oxide layers disappear completely. The crystallographic faces of each oxide and the reduced metallic copper are shown in *Table 4.2*.

*Table 4.2. XRD peaks of the crystallographic direction of each layer in KHCO<sub>3</sub> electrolyte.*

CuO (Cu <sup>II</sup> )		Cu <sub>2</sub> O (Cu <sup>I</sup> )	Cu <sup>0</sup>
(110) - 32.5°	(202) - 58.3°	(111) - 36°	(111) - 43°
(-111) - 35.6°	(-113) - 61.6°	(200) - 42°	(200) - 50°
(111) - 38.7°	(022) - 65.8°	(220) - 61°	(220) - 74°
(200) - 38.9°	(-311) - 66.3°	(311) - 73°	(311) - 89°
(-202) - 48.8°	(220) - 68.1°		

Subsequently, we move to sodium electrolyte to observe the effect of this cation over the copper oxide layer evolution. As mentioned before and showed in *Figure 4.11* between both electrolytes is possible to observe a difference in the oxide layer reduction rate, going faster in the case of sodium electrolyte. To corroborate and evaluate this effect, the same time-test of the oxide layers evolution done in potassium electrolyte was done moving to sodium in this case.

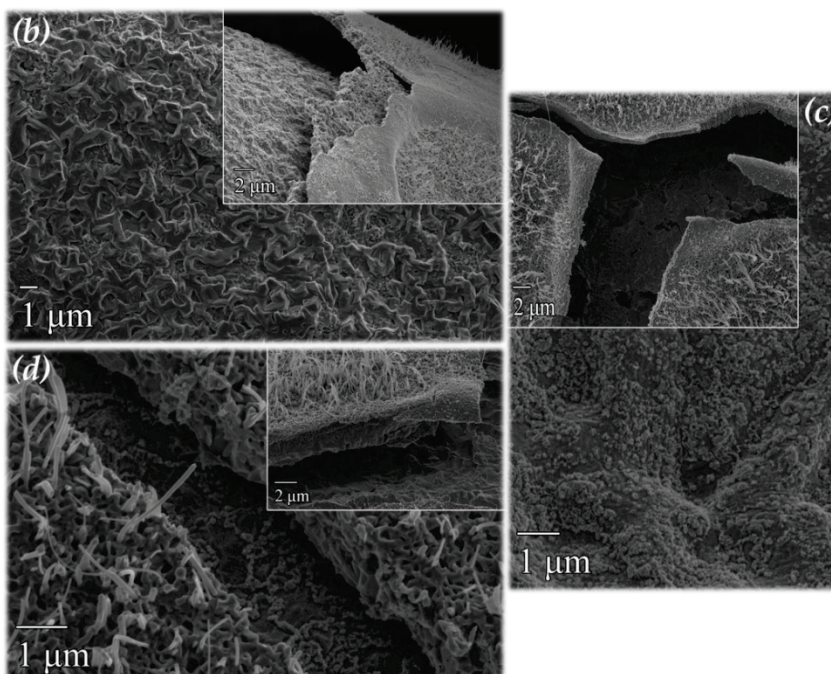
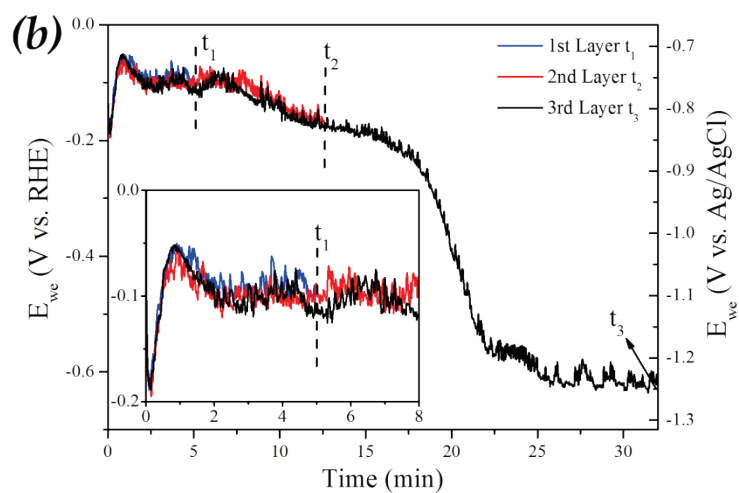
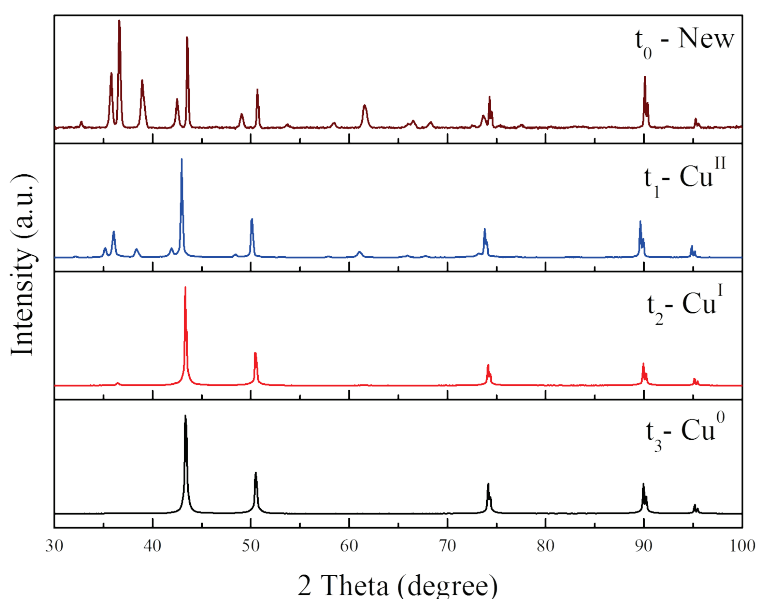


Figure 4.17. (a) CP experiment stopped at 5, 12.5 and 32 minutes corresponding to  $t_1$ ,  $t_2$  and  $t_3$  to observe the oxide layer reduction the images (b)-(d) corresponds with the stopped times.

*Figure 4.17* shows the working electrode potential versus time (a) of the copper oxide evolution at the three times when the experiment was stopped. The plot shape is different compared with the potassium one. In this plot the first plateau is not very clear been too fast the reduction using sodium. The SEM images (b)-(d) correspond with  $t_1$ ,  $t_2$  and  $t_3$  respectively. Apparently there are no so much differences in the surface compared with the potassium images in *Figure 4.15* only at low magnification the surface roughness changes a little. In the *Figure 4.15 (d)* the surface looks like more porous and in *Figure 4.17 (d)* have a deposited material over the metallic copper surface looking like veins.



*Figure 4.18.* XRD patterns of the  $Cu_xO$  electrode at different times to observe the corresponding oxide layer in  $NaHCO_3$ .

To corroborate the evolution of the oxide layer, each samples was analyzed by XRD (*Figure 4.18*), to do the evaluation of the

peaks evolution of the oxide layer using  $\text{NaHCO}_3$ . Taking as reference the  $t_0$  pattern (new electrode) the oxide layer reduction is clearly faster than using  $\text{KHCO}_3$  electrolyte (**Figure 4.16**). In the XRD pattern at  $t_1$  (blue line) corresponding with  $\text{Cu}^{\text{II}}$ , the first peaks pair does not have the same intensity, decreasing faster the left one. This peak corresponds to the external  $\text{CuO}$  layer. At  $t_2$  (red line) the pattern corresponds with  $\text{Cu}^{\text{I}}$  and the peaks are not as intense as in **Figure 4.16**. The completely reduced copper ( $\text{Cu}^0$ ) at  $t_3$  have the same pattern as the potassium one. When **Table 4.2** and **Table 4.3** are compared is possible to observe the oxide peaks evolution in both electrolytes. For the  $\text{CuO}$  pattern the (-113) and (220) cannot be measured. And for the  $\text{Cu}_2\text{O}$  only the (311) direction disappear at the time when the experiment was stopped.

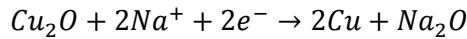
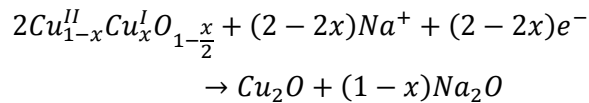
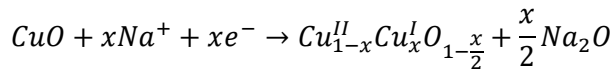
**Table 4.3.** XRD peaks of the crystallographic direction in each layer in  $\text{NaHCO}_3$  electrolyte.

CuO ( $\text{Cu}^{\text{II}}$ )		$\text{Cu}_2\text{O}$ ( $\text{Cu}^{\text{I}}$ )	$\text{Cu}^0$
(110) - 32.5°	(-202) - 48.8°	(111) - 36°	(111) - 43°
(-111) - 35.6°	(202) - 58.3°	(200) - 42°	(200) - 50°
(111) - 38.7°	(022) - 65.8°	(220) - 61°	(220) - 74°
(200) - 38.9°	(-311) - 66.3°		(311) - 89°

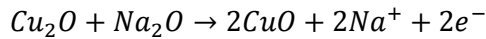
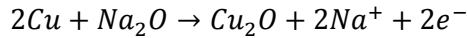
The reason for the enhance in the oxide layer reduction in the case of the sodium ion could be due to the smaller cation size that allows intercalation into metal oxides. There are reported works on lithium ion batteries [48,49] and recently for sodium ion batteries [50,51] in which copper oxide (II) is used as anode material. In these reported works the sodium ions can intercalate in the  $\text{CuO}$

structure in the discharge step and subsequently recovering the structure in the charge step, releasing the sodium ions. The mechanism in the sodium ion batteries was reported by Chen *et al.* [52]. Herein, the author explains the reaction mechanism carefully in the charge and discharge steps.

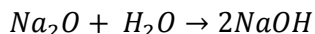
Discharge reactions:



Charge reactions:



In our case when the reduction potential was applied over the copper oxide electrode is working like in the discharging step reactions. The sodium ions can react with the copper oxide layer helping in the oxide layer reduction following the discharge reactions explained above. In the batteries media, the electrolyte is not aqueous where Na<sub>2</sub>O generated is stable. However, in our setup we use an aqueous media and the sodium oxide is not stable dissolving via this reaction:



The sodium hydroxide in situ generated by the sodium oxide dissolution can modify the local pH at the electrode surface. Besides, the continuous CO<sub>2</sub> flow passing through the electrode (GDE setup) can react with the sodium hydroxide generated:



This method was used to dissolve the CO<sub>2</sub> into the aqueous media reported before [53]. In the case of potassium, the same can happen but due to the bigger ionic radius it cannot be introduced into the copper oxide structure and for this reason the oxide layer reduction in the potassium media is not enhanced as in sodium electrolyte. For the charge compensation of free HCO<sub>3</sub><sup>-</sup> when the sodium was being incorporated in the CuO structure the protons from the anode part can go through the Nafion® membrane to compensate the hydrogen carbonate ion, generating CO<sub>2</sub> plus water. However these HCO<sub>3</sub><sup>-</sup> ions “destroyed” are regenerated again by the reaction between NaOH and CO<sub>2</sub>, keeping constant the hydrogen carbonate concentration.

### 4.3 CO<sub>2</sub> Pre-Humidification Effect

In the photocatalytic CO<sub>2</sub> reduction is well known that the gas must be bubbled through DI water to include the necessary H<sub>2</sub>O to carry on the CO<sub>2</sub> reduction reaction. The importance in the ratio between H<sub>2</sub>O and CO<sub>2</sub> was studied by Dimitrijevic *et al.* [54]. In their work explain separately the effect of the water and the carbonates generated. They use electron paramagnetic resonance technique to study both species. They finally conclude that the water in the two forms observed (dissociated on the surface of TiO<sub>2</sub> and in subsequent molecular layers) having three roles. The first one is the stabilization of charges (preventing electron-hole recombination). Second, it acts as an electron donor (reaction of water with photogenerated holes to give OH radicals). Third, acting as an electron acceptor (formation of H atoms in a reaction of photogenerated electrons with protons on the surface,  $-\text{OH}_2^+$ ). The CO<sub>2</sub> dissolved forming carbonates/bicarbonates competes with water for photogenerated holes and thus can act as hole scavenger. CO<sub>3</sub><sup>-</sup> radicals are relatively strong one-electron oxidation agents. Another reported effect is the CO<sub>2</sub> activation by the water, to increase the capture capacities over alkali metal-based sorbents. In this systems is very important the formation of hydrogen carbonates to increase the CO<sub>2</sub> adsorption capacity of these materials [55,56]. Another reported work based on metalorganic framework materials for CO<sub>2</sub> adsorption they study the role of the water coordinated over the metallic center, which improves the adsorption over a Cu center being possible to tune the behavior of

these material for the CO<sub>2</sub> capture or coordination [57]. How does the water acts over the CO<sub>2</sub> molecule? Some theoretical studies suggest the CO<sub>2</sub> and water cannot react forming carbonic acid due to the high energy barrier (200 kJ mol<sup>-1</sup>) [58–60]. However, the theory and the experimental shows that a planar H<sub>2</sub>O – CO<sub>2</sub> van der Waals complex is generated in the gas stream, through the interaction of the oxygen lone pairs on the water molecule with the 2π<sub>u</sub> antibonding orbital at the carbon dioxide [58–64]. For this complex the binding energy was estimated around 12 – 33 kJ mol<sup>-1</sup>. The intramolecular distances and the angles of the individual molecules in the complex not suffer an important modification, only there is a bending of 2.8° in the O – C – O angle. The van der Waals complex (H<sub>2</sub>O)<sub>2</sub> – CO<sub>2</sub> in the gas phase does not react to form carbonic acid [58,59,65] but when another water molecule is attached to the complex gives a bending in the O – C – O angle of 7.2° [58]. When hydrogen bonding is generated over the oxygen of the CO<sub>2</sub> molecule as result of the coordination of a second water molecule, decreases the energy barrier associated in the O – C – O bending. This effect is linked with the catalytic effect occurring in solution [58–61,64,66]. Henderson [67] in his work explain that the acid sites on the surface may assist in perturbing the physisorbed H<sub>2</sub>O – CO<sub>2</sub> complex bound transiently on the surface in a precursor state. In addition, the chemically adsorbed water molecules may also form hydrogen bonding interactions with such a complex to facilitate the O – C – O bending. The perturbations of the complex might then lead the carbonic/bicarbonate formation at the surface.

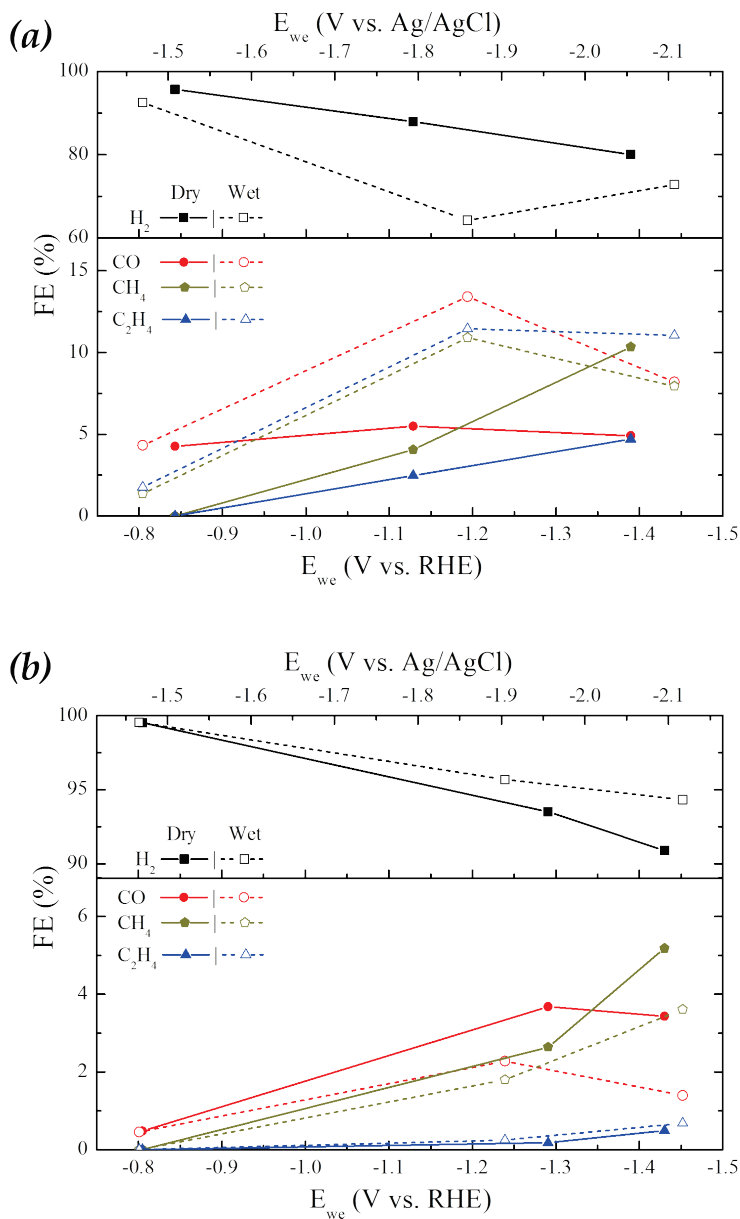


**Figure 4.19.** Metallic copper faradaic efficiencies using dry and wet CO<sub>2</sub> stream in potassium (a) and sodium (b) hydrogen carbonate electrolyte.

The electrochemical test was carried out during 1 hour at different applied current densities (60, 30 and 10 mA cm<sup>-2</sup>) using dry and wet CO<sub>2</sub> stream in a GDE setup. First the copper electrode is used as catalyst in this test series. When *Figure 4.19* is analyzed it could be observed the CO<sub>2</sub> humidification effect over the faradaic efficiencies for both electrolytes. In the potassium plot (*a*), the faradaic efficiency of the carbonaceous products is increased using the humidified stream. But the potentials reached are a little bit more negative. In the sodium case (*b*) the increase of the water content in the CO<sub>2</sub> stream gives the opposite behavior expected. The faradaic efficiencies obtained under these conditions are a little bit lower for carbon products but the potential shifts to more positive values. The effect of the ions in the double Helmholtz layer could be incremented. For sodium the stabilization of the layer could be more complicated because of the water increment blocking the Na<sup>+</sup> approaching to the adsorbed CO<sub>2</sub> decreasing the efficiency. Nevertheless, for the potassium ion effect corresponds with the expected, the enhancing of the faradaic efficiencies. The reason for this increment in the efficiency could be due to: (1) improvement in the CO<sub>2</sub> adsorption over the surface as explained before, (2) the O – C – O angle binding activating the molecule generating easily an increment of HCO<sub>3</sub><sup>-</sup> concentration in the electrode surface. Hori reported that the electrolyte concentration have an important influence in the methane and ethylene production ratio [3].

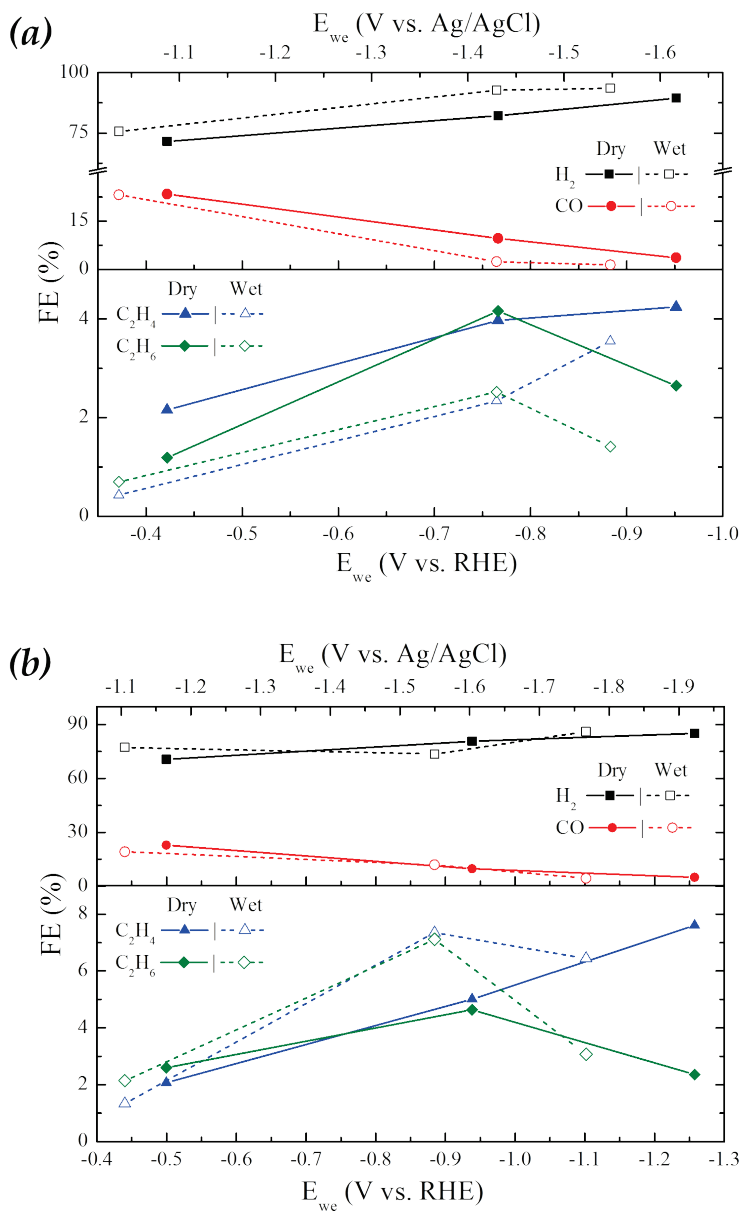


**Figure 4.20.** Copper oxide electrode faradaic efficiencies using dry and wet CO<sub>2</sub> stream in potassium (a) and sodium (b) hydrogen carbonate electrolyte.

In *Figure 4.20*, for potassium (*a*) the efficiencies decrease when the water is incorporated in the gas stream. The only positive effect using wet gas (in potassium) compared with the dry one, is a shift to more positive potential values clearly observed at higher potentials. In sodium (*b*) the hydrogen and carbon monoxide efficiencies are quite similar. But in the case of the ethylene and ethane around  $-0.9$  V (*vs.* RHE) there is an increment in the faradaic efficiency using wet gas. The potential using sodium is higher as mentioned before. The potential reached for all the products obtained using humidified  $\text{CO}_2$  stream decrease respect to the dry one. The faradaic efficiency using wet gas at high potential decrease a little respect to dry gas, however, the potential is reduced  $0.15$  V. The reason for the efficiency increment using sodium electrolyte with the copper oxide could be related to the angle bending in the  $\text{CO}_2$  molecule, due to the two molecules water coordination. In the oxide layer the water is preferentially adsorbed over the oxygen vacancies competing with the  $\text{CO}_2$  adsorption. Over this surface the effect over the Helmholtz layer goes in the opposite way. For potassium with the big size and low polarizing power the water can be easily detached and adsorbed in the surface decreasing the faradaic efficiency. For sodium which has higher polarizing power (small size) in the case of dry gas the effect over the Helmholtz layer was negative, nevertheless, now is interesting because can block the adsorption of water over the surface allowing an easier  $\text{CO}_2$  adsorption than in potassium. As consequence, an increase in the faradaic efficiencies was reached.

## 4.4 Conclusions

As conclusion, we studied and support the effect of the positive ions used in the CO<sub>2</sub> electrochemical reaction over the two types of electrodes. First we focused on the metallic copper due to the interest for methane production, using a GDE setup. For these experiments we observe how the potassium increases the faradaic efficiency and decrease the potential requirements for the CO<sub>2</sub> reduction reaction. The ions action over the Helmholtz layer generated over the electrode surface have the ability to stabilize the CO<sub>2</sub> adsorbed in the surface. In sodium due to the high polarizing power the water is strongly attached blocking the coordination of the adsorbed CO<sub>2</sub> giving a worst stabilization. For potassium the water coordinate weakly and can desorb better allowing the stabilization of adsorbed CO<sub>2</sub> enhancing the faradaic efficiencies with a decrease in the potential values. The importance of the electrode treatment and the purity is shown too. A highly copper electrode was used in a different electrochemical setup. The difference was the incorporation pathway of CO<sub>2</sub>, because in these experiments was constantly bubbled into the electrolyte to keep the concentration constant. Using this electrode we reach to 20% of faradaic efficiency in methane production.

The interest for change to copper oxide is to decrease the potential values for the CO<sub>2</sub> electrochemical reduction. The metallic copper potential requirements to obtain a reasonable faradaic efficiency are very high and are not energetically viable. In the case of the copper oxide the potentials decrease 0.2 V with NaHCO<sub>3</sub> and

for  $\text{KHCO}_3$  the potential shift 0.4 V (*vs.* RHE) to more positive values. But using the oxide as electrodes the activity does not start until the oxide layer is reduced reaching to an activated copper ( $\text{Cu}^0$ ). The selectivity of this electrode goes to ethylene and ethane and no methane is measured. The oxide layer reduction was studied apart because in the sodium electrolyte the time to reach to the active copper surface compared with the potassium decrease. The reason for this difference comes from the sodium intercalation into  $\text{CuO}$ . The small radius in sodium allows introduced inside the structure, helping in the oxide layer reduction until to a  $\text{Cu}_2\text{O}$  small layer which is stable and could be responsible for the selectivity for  $\text{C}_2\text{H}_4$  instead of  $\text{CH}_4$  production.

In the final part of the chapter the effect of the  $\text{CO}_2$  solvation before the entrance in the electrochemical cell was treated. The  $\text{CO}_2$  molecule can be bended when two water molecules are coordinated improving the adsorption, and the carbonate/bicarbonate generation. This carbonates are essential for the reduction reaction to decrease the energy activation, improving the efficiency and decreasing the potential values. For the copper electrode only in the potassium electrolyte the  $\text{CO}_2$  solvation has a positive effect over the methane efficiency and potential values. But in the case of the  $\text{Cu}_2\text{O}$  the effect goes in the opposite way and only in the sodium electrolyte the potential shift to positive values increasing the faradaic efficiencies for ethylene and ethane.

## 4.5 References

- [1] Hori Y., Kikuchi K., Suzuki S. *Chem Lett.* **1985**, 1695.
- [2] Kuhl K.P., Hatsukade T., Cave E.R., Abram D.N., Kibsgaard J., Jaramillo T.F. *J Am Chem Soc.* **2014**, 136, 14107.
- [3] Hori Y., Takahashi R., Yoshinami Y., Murata A. *J Phys Chem B.* **1997**, 101, 7075.
- [4] Hori Y. Electrochemical CO<sub>2</sub> Reduction on Metal Electrodes. In: Vayenas CG, White RE, Gamboa-Aldeco ME, editors. *Mod. Asp. Electrochem.*, Springer New York; **2008**, p. 89–189.
- [5] Hori Y., Murata A., Takahashi R. *J Chem Soc Faraday Trans 1 Phys Chem Condens Phases.* **1989**, 85, 2309.
- [6] Hirunsit P. *J Phys Chem C.* **2013**, 117, 8262.
- [7] Peterson A. a., Abild-Pedersen F., Studt F., Rossmeisl J., Nørskov J.K. *Energy Environ Sci.* **2010**, 3, 1311.
- [8] Peterson A. a., Nørskov J.K. *J Phys Chem Lett.* **2012**, 3, 251.
- [9] Sullivan B.R. *Electrochemical and Electrocatalytic Reactions of Carbon Dioxide.* **1993**.
- [10] Hori Y., Wakebe H., Tsukamoto T., Koga O. *Surf Sci.* **1995**, 335, 258.
- [11] Hori Y., Takahashi I., Koga O., Hoshi N. *J Phys Chem B.* **2002**, 106, 15.
- [12] Hori Y., Takahashi I., Koga O., Hoshi N. *J Mol Catal A Chem.* **2003**, 199, 39.
- [13] Calle-Vallejo F., Koper M.T.M. *Angew Chemie - Int Ed.* **2013**, 52, 7282.
- [14] Tang W., Peterson A.A., Varela A.S., Jovanov Z.P., Bech L., Durand W.J., et al. *Phys Chem Chem Phys.* **2012**, 14, 76.
- [15] Wu J., Risalvato F.G., Ke F.-S., Pellechia P.J., Zhou X.-D. *J Electrochem Soc.* **2012**, 159, F353.
- [16] Kuhl K.P., Cave E.R., Abram D.N., Jaramillo T.F. *Energy Environ Sci.* **2012**, 5, 7050.
- [17] Ogura K. *J CO<sub>2</sub> Util.* **2013**, 1, 43.
- [18] Thorson M.R., Siil K.I., Kenis P.J. a. *J Electrochem Soc.* **2013**, 160, F69.
- [19] Manthiram K., Beberwyck B.J., Alivisatos A.P. *J Am Chem Soc.* **2014**, 136, 13319.
- [20] Hori Y., Konishi H., Futamura T., Murata A., Koga O., Sakurai H., et al. *Electrochim Acta.* **2005**, 50, 5354.
- [21] Lei Z., Dai C., Chen B. *Chem Rev.* **2014**, 114, 1289.

- [22] Supasitmongkol S., Styring P. *Energy Environ Sci.* **2010**, 3, 1961.
- [23] Torralba-Calleja E., Skinner J., Gutiérrez-Tauste D. *J Chem.* **2013**, 2013.
- [24] Frese K.W. *J Electrochem Soc.* **1991**, 138, 3338.
- [25] Le M., Ren M., Zhang Z., Sprunger P.T., Kurtz R.L., Flake J.C. *J Electrochem Soc.* **2011**, 158, E45.
- [26] Li C.W., Kanan M.W. *J Am Chem Soc.* **2012**, 508, 504.
- [27] Jiang X., Herricks T., Xia Y. *Nano Lett.* **2002**, 2, 1333.
- [28] Nie X., Griffin G.L., Janik M.J., Asthagiri A. *Catal Commun.* **2014**, 52, 88.
- [29] Lan Y., Gai C., Kenis P.J.A., Lu J. *ChemElectroChem.* **2014**, 1, 1577.
- [30] Nakayama S., Kimura A., Shibata M., Kuwabata S., Osakai T. *J Electrochem Soc.* **2001**, 148, B467.
- [31] Nakayama S., Kaji T., Shibata M., Notoya T., Osakai T. *J Electrochem Soc.* **2007**, 154, C1.
- [32] Garcia-Esparza A.T., Limkrailassiri K., Frederic L., Rasul S., Yu W., Lin L., et al. *J Mater Chem A.* **2014**, 1.
- [33] Paracchino A., Laporte V., Sivula K., Grätzel M., Thimsen E. *Nat Mater.* **2011**, 10, 456.
- [34] Walter M.G., Warren E.L., McKone J.R., Boettcher S.W., Mi Q., Santori E.A., et al. *Chem Rev.* **2010**, 110, 6446.
- [35] Chang T.-Y., Liang R.-M., Wu P.-W., Chen J.-Y., Hsieh Y.-C. *Mater Lett.* **2009**, 63, 1001.
- [36] Qiao J., Jiang P., Liu J., Zhang J. *Electrochem Commun.* **2014**, 38, 8.
- [37] Li C.W., Ciston J., Kanan M.W. *Nature.* **2014**, 508, 504.
- [38] Kim D., Lee S., Ocon J.D., Jeong B., Lee J.K., Lee J. *Phys Chem Chem Phys.* **2015**, 17, 824.
- [39] Hori Y., Murata A., Takahashi R., Suzuki S. *J Chem Soc Chem Commun.* **1988**, 17.
- [40] Shin H.S., Song J.Y., Yu J. *Mater Lett.* **2009**, 63, 397.
- [41] Ko C.K., Lee W.G. *Surf Interface Anal.* **2010**, 42, 1128.
- [42] Xu Y., Wang H., Zhu R., Liu C., Wu X., Zhang B. *Chem Asian J.* **2013**, 8, 1120.
- [43] Li Q., Xu P., Zhang B., Tsai H., Zheng S., Wu G., et al. *J Phys Chem C.* **2013**, 117, 13872.
- [44] Murata A., Hori Y. *Bull Chem Soc Jpn.* **1991**, 64, 123.
- [45] Hori Y., Murata A., Takahashi R., Suzuki S. *J Am Chem Soc.* **1987**, 109, 5022.

- [46] Maimaiti Y., Nolan M., Elliott S.D. *Phys Chem Chem Phys.* **2014**, 16, 3036.
- [47] Wu H., Zhang N., Wang H., Hong S. *Chem Phys Lett.* **2013**, 568-569, 84.
- [48] Martin L., Martinez H., Poinot D., Pecquenard B., Le Cras F. *J Power Sources.* **2014**, 248, 861.
- [49] Zhou X., Shi J., Liu Y., Su Q., Zhang J., Du G. *J Alloys Compd.* **2014**, 615, 390.
- [50] Chen K., Song S., Xue D. *Cryst Eng Comm.* **2015**, 17, 2110.
- [51] Lu Y., Zhang N., Zhao Q., Liang J., Chen J. *Nanoscale.* **2015**, 7, 2770.
- [52] Wang L., Zhang K., Hu Z., Duan W., Cheng F., Chen J. *Nano Res.* **2014**, 7, 199.
- [53] Varela A.S., Schlaup C., Jovanov Z.P., Malacrida P., Horch S., Stephens I.E.L., et al. *J Phys Chem C.* **2013**, 117, 20500.
- [54] Dimitrijevic N.M., Vijayan B.K., Poluektov O.G., Rajh T., Gray K.A., He H., et al. *J Am Chem Soc.* **2011**, 133, 3964.
- [55] Hayashi H., Taniuchi J., Furuyashiki N., Sugiyama S., Hirano S., Shigemoto N., et al. *Ind Eng Chem Res.* **1998**, 37, 185.
- [56] Lee S.C., Choi B.Y., Ryu C.K., Ahn Y.S., Lee T.J., Kim J.C. *Korean J Chem Eng.* **2006**, 23, 374.
- [57] Yazaydin A.O., Benin A.I., Faheem S.A., Jakubczak P., Low J.J., Willis R.R., et al. *Chem Mater.* **2009**, 21, 1425.
- [58] Jonsson B., Karlstrom G., Wennerstrom H., Forsen S., Roos B., Almlöf J. *J Am Chem Soc.* **1977**, 99, 4628.
- [59] Ha T.K. *J Am Chem Soc.* **1984**, 106, 599.
- [60] Merz K.M. *J Am Chem Soc.* **1990**, 112, 7973.
- [61] Jönsson B., Karlström G., Wennerström H. *Chem Phys Lett.* **1975**, 30, 58.
- [62] Peterson K.I., Klemperer W. *J Chem Phys.* **1984**, 80, 2439.
- [63] Damewood J.R., Kumpf R.A., Muhlbauer W.C.F. *J Phys Chem.* **1989**, 93, 7640.
- [64] Zhang N.R., Shillady D.D. *J Chem Phys.* **1994**, 100, 5230.
- [65] Peterson K.I., Suenram R.D., Lovas F.J. *J Chem Phys.* **1991**, 94, 106.
- [66] Jönsson B., Karlström G., Wennerström H., Roos B. *Chem Phys Lett.* **1976**, 41, 317.
- [67] Henderson M.A. *Surf Sci.* **1998**, 400, 203.



# Chapter V

## Photoelectrochemical PEC Cell Assembling

<b>5</b>	<b>Photoelectrochemical (PEC) Cell Assembling.....</b>	<b>215</b>
<b>5.1</b>	<b>Evaluation of Photoanodes .....</b>	<b>215</b>
<b>5.2</b>	<b>Evaluation of Cathodes.....</b>	<b>219</b>
<b>5.3</b>	<b>Evaluation of the Overall Process.....</b>	<b>222</b>

## 5. Photoelectrochemical (PEC) Cell Assembling

As final point of the work, the PEC cell assembling requires a potential evaluation for each individual component separately, to observe the energy requirements for the complete cell. First of all the photoanode (light part) is evaluated to obtain the potential working conditions where the efficiency is higher. After, the cathode evaluation (dark part) was done to select the most efficient working potential for the CO<sub>2</sub> reduction process. And finally the potential values are used for the overall process to observe the external potential requirements for the complete cell with the photo-effect enhancement.

### 5.1 Evaluation of Photoanodes

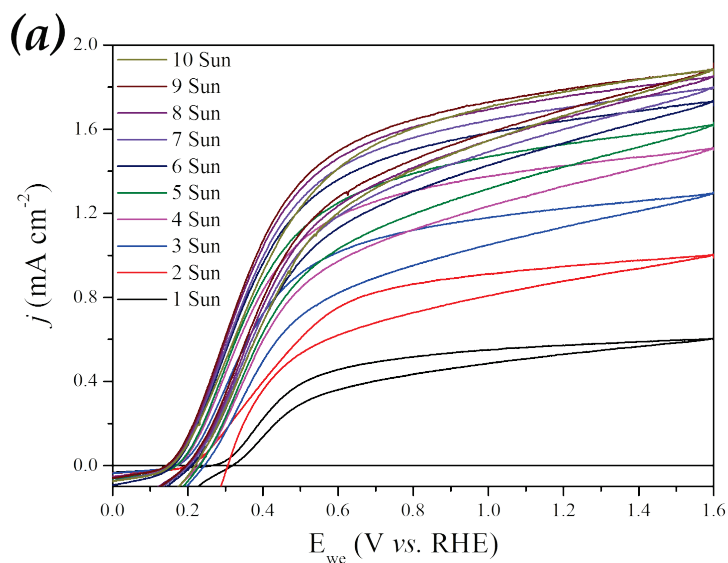
The reaction under interest involved in this part of the PEC cell is shown below:



The materials studied in **Chapter III** were thought for use them as photoanode in the PEC cell. First, the anodization of titanium metal was considered to produce titania nanotubes. However, the lack of adherence under long term operation in the PEC cell and low photoactivity was the main motivation to focus on the synthesis of titanium dioxide nanorods, obtained by hydrothermal,

which have better photoactivity (around 4 times more). Additionally, due to the way to assemble in the PEC cell setup a transparent conductive substrate is required for the back illumination. In addition, the nucleation of TiO<sub>2</sub> rutile nanorods is favored on the FTO surface, since SnO<sub>2</sub> also has a rutile crystalline structure, and thus, it is assured a direct contact between the semiconductor and the conductive substrate.

As explained before, CO<sub>2</sub> reduction to any carbonaceous product is an electron-mediated reaction, and then the current density photogenerated is an important parameter that will determine the CO<sub>2</sub> conversion. To enhance the photogenerated current density using undoped TiO<sub>2</sub> nanorods is possible, increasing the power input (*Figure 5.1*).



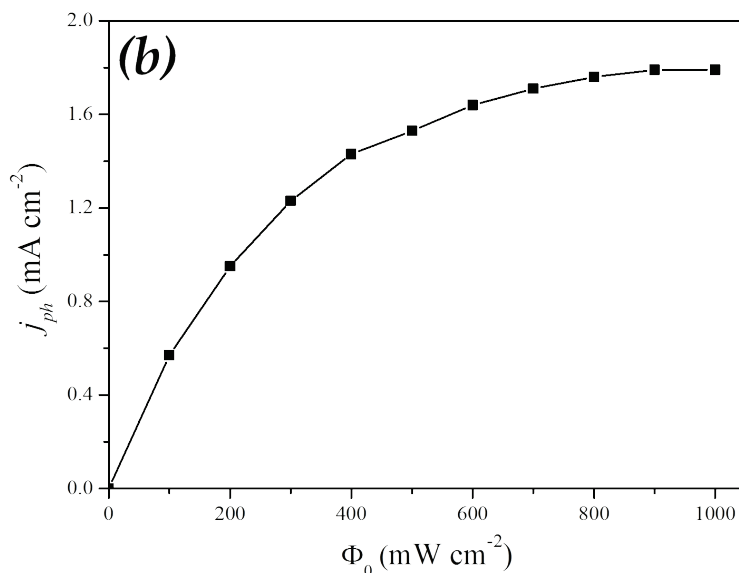


**Figure 5.1.** (a) Polarization curves of  $\text{TiO}_2$  nanorods under different light intensities (1 to 10 Sun) in 1 M NaOH electrolyte. (b) Photocurrent generated at 1.23 V vs. RHE at different light intensities.

In **Figure 5.1** is shown the polarization curves of the bare  $\text{TiO}_2$  photoanode under different light intensities. It can be seen that light concentration, the photocurrent density generated increase linearly up to three sun, reaching at limit value at six suns.

If a sample which reaches to higher values respect the bare one at one sun is used, could be possible to reach to higher values with the solar concentration method. In our work we focus on the successful nitrogen doping by thermal treatment. The best sample is  $\text{NH}_3 - 300^\circ\text{C}$  who reach the highest value of photogenerated current density (**Figure 5.2**). Over this sample we focus due to reach a similar value of two sun ( $200 \text{ mW cm}^{-2}$ ) respect bare  $\text{TiO}_2$ .

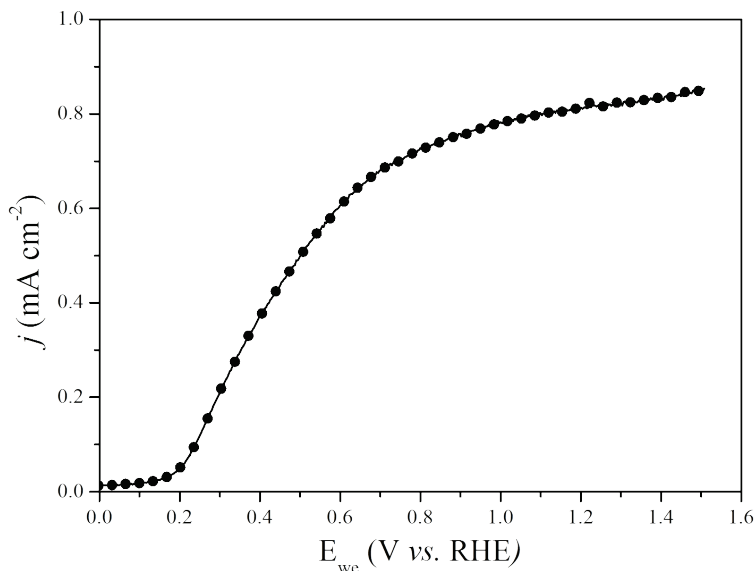


**Figure 5.2.** LSV at  $20 \text{ mV cm}^{-2}$  of the sample threated at  $300^\circ\text{C}$  under ammonia under one sun AM 1.5G in 1 M NaOH electrolyte.

For the sample evaluation not only the conversion must be taken into account. Also, the energy consumption using the photoanode is evaluated. Then power output ( $\text{mW cm}^{-2}$ ) for water oxidation taking into account the electrical external bias required was calculated using the formula:

$$\begin{aligned} \text{Efficiency} &= \frac{j_{ph}(E_{redox} - E_{bias})}{\text{Photonflux}} \times 100 \\ &= \frac{j_{ph}(1.23 - E_{RHE})}{\text{Photonflux}} \times 100 \end{aligned} \quad (5.1)$$

Which is called applied bias photon-to-current efficiency (ABPE), where the potential scale of photoanode must be referred to RHE scale and the redox potential of water oxidation is then 1.23V.

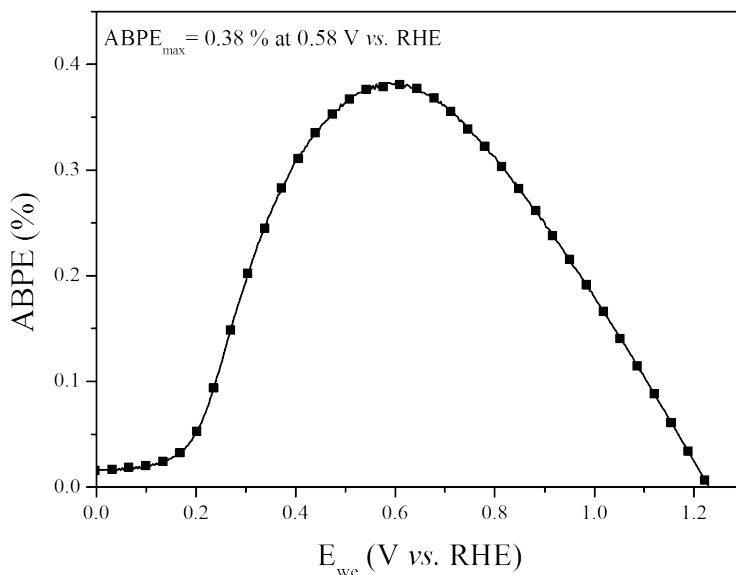
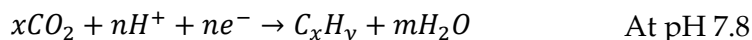


*Figure 5.3.* ABPE solar efficiency of the sample treated at 300°C under ammonia atmosphere.

*Figure 5.3* shows the ABPE for the NH<sub>3</sub> – 300°C sample. This plot is a useful tool to adjust the optimum polarization of the photoanodes to harvest the maximum power from the solar radiation. According to the data, the polarization of the NH<sub>3</sub> – 300°C nanorods must be set at 0.58 V *vs.* RHE. As mentioned before, the NH<sub>3</sub> – 300°C photoanode assembled to a PEC device will be more efficient in terms of energy consumption despite its low conversion rate.

## 5.2 Evaluation of Cathodes

The general reaction involving the cathodes studied in **Chapter IV** is shown below:



On the other compartment, copper based cathodes were considered to electrocatalyse the reduction of  $\text{CO}_2$  to  $\text{C}_1$  and  $\text{C}_2$  hydrocarbons. Our interest was focus on the methane ( $\text{CH}_4$ ) production but, as shown in **Chapter IV** there are different carbon products generated by  $\text{CO}_2$  electroreduction. The potential values for the working electrode (Cu-based electrodes) and counter electrode (DSA) are shown in *Figure 5.4*.

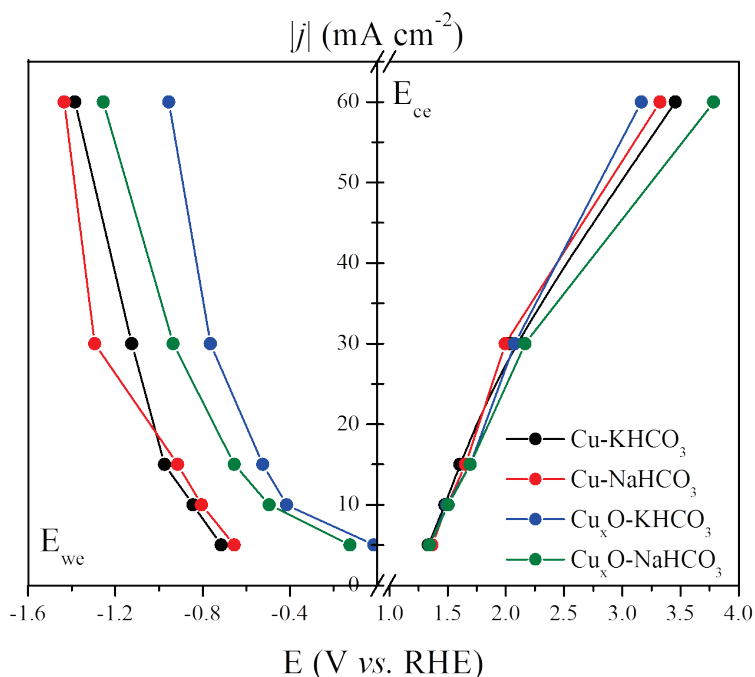


**Figure 5.4.** Polarization curves of the working (Cu based electrodes) and counter (DSA) electrode, with the electrolyte indicated in the figure (at 0.5 M concentration).

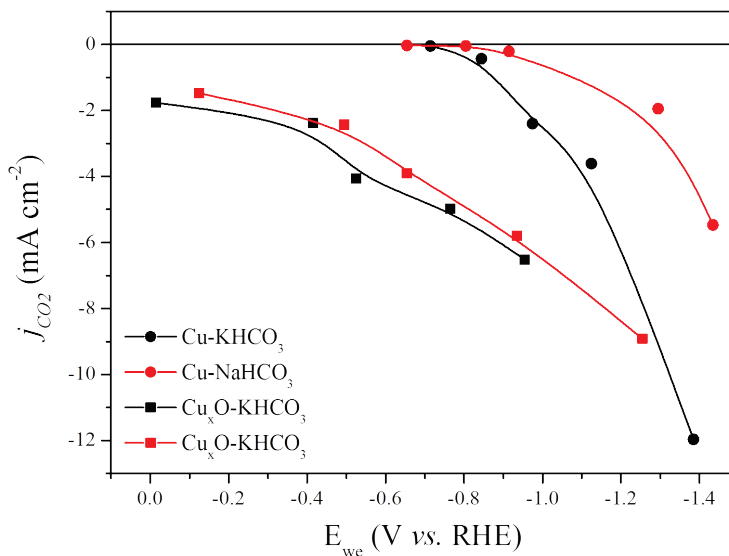


**Figure 5.5.**  $CO_2$  partial current density of the copper based electrodes and electrolytes used in **Chapter IV**.

The cathodes used were a pure copper and copper oxide mesh, using  $KHCO_3$  or  $NaHCO_3$  as catholytes. **Figure 5.4** shows the cathode polarization curves. In the graph, it is represented the overall polarization (current density  $-j$  vs. cathode and anode potential), while in **Figure 5.5**, it is represented the  $CO_2$  partial current density ( $j_{CO_2}$ ), to compare the activity of a certain cathode.  $j_{CO_2}$  was calculated taking into account the GC analysis of the products obtained ( $CO$ ,  $CH_4$ ,  $C_2H_4$ , ...) and the number of electrons involved in the half-reaction. As in the PEC cell it aqueous electrolyte was used, hydrogen evolution reaction is a competitive process with the  $CO_2$  reduction, decreasing the efficiency in the process.

As seen in **Figure 5.4**, for copper oxide mesh, the electrode is more easy to polarize (more current density at less negative

electrode potential) and more prone the CO<sub>2</sub> conversion. Additionally, when comparing both electrolytes, KHCO<sub>3</sub> electrolyte is giving a higher carbon dioxide conversion for the copper mesh, but for the copper oxide mesh, NaHCO<sub>3</sub> reaching to better conversion values. In any case, it is needed a high polarization of the cathode in both electrodes used, ranging from -1.1 to -1.40 V vs. RHE for the metallic copper and from -0.70 to 1.25 V vs. RHE for the copper oxide electrodes.

### 5.3 Evaluation of the Overall Process

In order to evaluate the process performances, and the benefit from photoactivated process, it was considered the energy consumption of the electroreduction process. *Figure 5.6* shows that the external bias polarization required for CO<sub>2</sub> conversion to methane for copper electrode and ethylene for copper oxide electrode, as majority products. In the range where the copper potential is between -1.1 to -1.40 V vs. RHE, the cell voltage is ranged between -3 and -5 V. However, the copper oxide between -0.70 to 1.25 V vs. RHE the cell voltage is ranged -2.5 to -5 V.

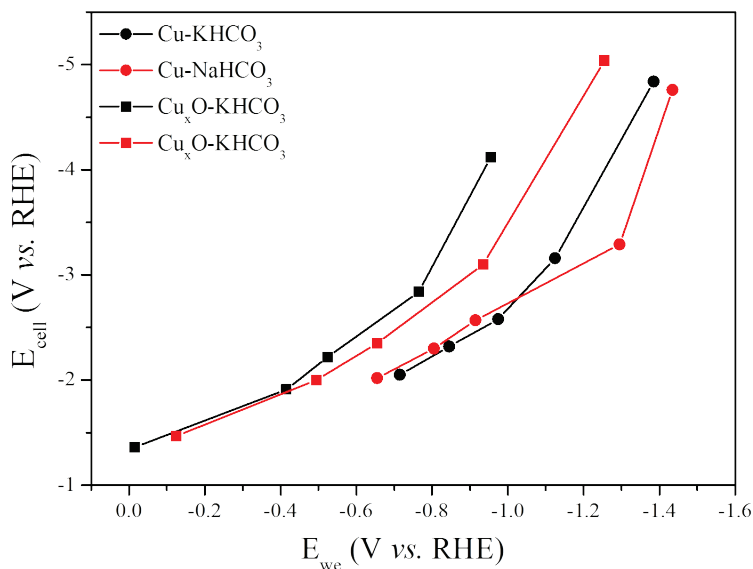


*Figure 5.6.* Cell polarization for the copper based electrodes used a dimensional stable anode (DSA) in dark.

When theoretically the nanorods sample  $\text{NH}_3 - 300^\circ\text{C}$  is coupled with the copper cathodes (*Table 5.1*), it was found that the bias voltage required is in the range of 1 – 1.7 V under one sun illumination.

Table 5.1. Process performance of PEC cell with the electrodes under study.

WE	$E_{we}$ (V) vs. Ag/AgCl (pH 7.8)	$E_{\text{photoanode}}$ at max. eff. (V) vs. Ag/AgCl (pH 13.6)	Optimum $E_{\text{cell}}$ (V)
<b>Cu</b> – $\text{KHCO}_3$	-2.05	-0.43	-1.62
	-1.77	(0.58 vs. RHE)	-1.34
<b>Cu</b> – $\text{NaHCO}_3$	-2.10	-0.43	-1.67
	-1.96		-1.53
<b>Cu<sub>x</sub>O</b> – $\text{KHCO}_3$	-1.62	-0.43	-1.19
	-1.43		-1.00
<b>Cu<sub>x</sub>O</b> – $\text{NaHCO}_3$	-1.92	-0.43	-1.49
	-1.60		-1.17

The photoactivated process was implemented for the conversion of carbon dioxide to methane for the copper cathode. However in the copper oxide cathode the selectivity changes to ethylene, as mentioned in **Chapter IV** in these electrodes the methane production is suppressed.

In terms of energy consumption, in the case of a 100% faradic efficiency to methane and ethylene (and without hydrogen as competitive reaction), the energy consumption per mol will be between 46 and 54  $\text{W h mol}^{-1}$  and 36 and 49  $\text{W h mol}^{-1}$  of methane and ethylene produced respectively, using  $\text{TiO}_2$  as photoanode.

Another approximation to enhance de activity in the  $\text{CO}_2$  reduction due to the large current density requirements is with the variation of the photoanode/cathode area ratio. This method is similar to the solar concentration but without increasing the intensity of the power source, as consequence, decreasing the

overall energy requirements. But if both concentration methods could be coupled is possible to increase the efficiency in the CO<sub>2</sub> photoelectrochemical reduction using TiO<sub>2</sub> nanorods (*Figure 5.7*).

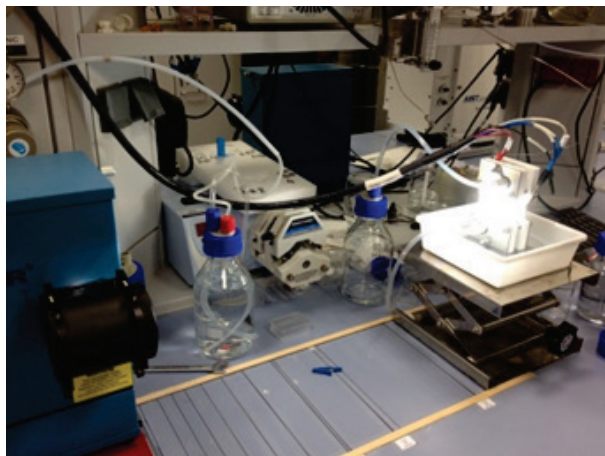


*Figure 5.7. PEC cell with the photoanode and Cu cathode assembled.*

In our system the limiting part is the photoanode due to the low current density photogenerated. For this reason the area of the photoanode will be bigger than the cathode. As shown in **Chapter IV** and in the evaluation of cathodes the best efficiencies are around  $-2$  to  $-1.4$  V *vs.* Ag/AgCl for both electrodes at  $-60$  and  $-30$  mA cm<sup>-2</sup> of current density using 10 cm<sup>2</sup> of electrode. If the cathode area is decreased to 1 cm<sup>2</sup> the current density requirements will be 10 times lower, been possible, coupled with the sun concentration, the photoelectrochemical process. This method leads to a patent application of a photoelectrochemical cell (*EP14382541.2, 19/12/2014*).

As future work over the photoelectrochemical CO<sub>2</sub> reduction must be focus on two ways, (a) the generation of more efficient photoanodes, which can give more power to the CO<sub>2</sub> reduction

part, but keeping the negative onset potential or going to more negative values to decrease the external potential requirements, ideally, reaching the zero bias system. (b) Respectively, for the CO<sub>2</sub> reduction part the copper catalyst must be enhanced to improve the catalytic activity, decreasing the potential requirements for the reaction.

# Chapter VI

## Conclusions



## 6. Conclusions

This thesis is devoted to prove the concept of the CO<sub>2</sub> reduction to CH<sub>4</sub> with a decreasing in the voltage requirements using a photoelectrochemical cell. The work developed in this thesis was devoted to the study of its individual components: **nanostructured photoanodes**, focused on **TiO<sub>2</sub>**, and **copper based cathodes for electrochemical CO<sub>2</sub> reduction**, as well as their implementation and evaluation in a photoelectrochemical (PEC) cell for CO<sub>2</sub> reduction. Experimental, technological and theoretical aspects were covered to attain this purpose. The most relevant achievements are listed below,

**Hierarchical TiNTs** synthesis by anodization using two organic electrolytes to enhance the photoactivity

- An improvement over TiNTs (based on anatase) was done by a surface patterning of the Ti foil; the **holes generated acts as light trap centers**. In the first anodization, DMSO was used at four different voltages (40, 50, 60 and 70) obtaining bigger pores with the potential increment. In the second anodization step the electrolyte selected was EG which gives a very compact and hexagonal organization of the TiNTs. A **theoretical model** was postulated to calculate the surface increment from the first anodization. For the **40 V** samples **40% of surface increment** was obtained. Correlated to this, the values of current density (LSV experiments) and IPCE for the **40 V** sample gives the best values, followed by the **70 V**.

- A **compact oxide layer** is generated in the bottom of the TiNTs and the substrate improving the contact. In the case of **40 V** sample this compact oxide layer coupled with the surface increment enhance more the photoactivity. In the case of **70 V** has this oxide layer too giving better photoactivity than **50** and **60 V** samples which have higher surface increment.

**TiO<sub>2</sub> nanorods fabrication and evaluation** of the synthetic conditions by hydrothermal technique.

- The initial titanium precursor concentration was modified to observe the effect over the nanorods morphology and photoactivity. The Ti precursor used was **titanium butoxide**, the concentration used was 40, 50, 60 and 70 mM in an acidic aqueous solution (50:50, HCl:H<sub>2</sub>O). The hydrothermal temperature and time was fixed for all the concentrations (200°C, during 4h). In the LSV measurements the 50 mM under **front** and **back illumination** reach the best values followed by the **40 mM**.
- The next condition is the concentration of **Cl<sup>-</sup>** ions. The concentrations used were 0.25, 0.5 and 1 M of CaCl<sub>2</sub> decreasing the **nanorods edge size, density**, layer thickness and photoactivity when the concentration was increased. However, we observe that **chlorine ions decrease the growing rate** of the nanorods. Then the hydrothermal synthesis was extended to 5h for 0.25 and 0.5 M reaching to thicker layers and bigger rods diameter. Only in the 0.5 M,

the current density was improved to de double. For 0.5 M allows **higher hydrothermal times** due to the growing rate decrease, **reaching to better values** in the current densities.

**TiO<sub>2</sub> nanorods doping** by hydrothermal reaction or **thermal treatment**, to enhance the **photoactivity** in the material.

- To improve the amount of **Sn** incorporated, the acidity of the hydrothermal solution was decreased. The ratio HCl:H<sub>2</sub>O used were: 50:50, 40:60 and 30:70. No tin incorporation was observed and the current densities from LSV measurement decrease with the acidity level reduction. The only effect observed was the **acidity effect** over the **TiO<sub>2</sub> nanorods growth**.
- **Vanadium** can decrease the bandgap of TiO<sub>2</sub>, improving the absorption in the **visible range**. The morphology of the TiO<sub>2</sub> nanorods generated changes to square shape to round. The carrier density values decrease with the vanadium doping, translating to worst conductivity in the layer and not enhancing the photoactivity. The **depletion region width** for these samples are **very large** does not allowing the efficient separation of the electron – hole pair which are **generated in the surface**, with high probability to be **trapped by surfaces states**. As sequence with the V<sup>5+</sup> possible presence acting as recombination centers and the generation of the electron – hole pair in the surfaces, the decrease of the photoactivity when the doping level increase is very pronounced. The **flat**

**band** potential values obtained, goes to **more positive values** which corresponds with the **onset potential shift**.

- **Ammonia treatments** enhance the efficiency in the TiO<sub>2</sub> nanorods. For this case an improvement of the photoelectrochemical activity was reached by introducing more active surface states that increase the holes average lifetime. For the 300°C sample was reached the maximum IPCE and current density value compared with the others temperatures (**0.8 mA cm<sup>-2</sup> at 1.23 V vs. RHE**). The ammonia treatment generates a **band bending** plus an **optimal length** in the **depletion region width** generating a **high electric field, improves the electron-hole separation**, avoiding the recombination and enhancing the photoactivity.

Hydrogen carbonate electrolytes (K<sup>+</sup> and Na<sup>+</sup>) effect in the CO<sub>2</sub> reduction using **copper based electrodes**.

- **Metallic copper electrodes** were studied for the methane production using a GDE setup. We observed how the potassium increases the faradaic efficiency and decrease the potential requirements for the CO<sub>2</sub> reduction. A highly purity copper electrode was used in a different electrochemical setup (CO<sub>2</sub> constant bubbling into the electrolyte) obtaining a maximum **faradaic efficiency of 20% for methane** generation.
- **Copper oxide electrodes** were selected to **decrease the potential requirements** in the CO<sub>2</sub> electrochemical reduction. In the case of the copper oxide the potentials decrease 0.2 V

with  $\text{NaHCO}_3$  and for  $\text{KHCO}_3$  the potential shift 0.4 V (vs. RHE) to more positive values compared with the metallic copper. However the **selectivity** of these cathodes goes to **ethylene and ethane**.

- Another effect observed related to the **copper oxide cathodes** is the **oxide reduction layer** reaching to an **activated copper ( $\text{Cu}^0$ )**. In sodium electrolyte takes lower times to reach to the active copper surface and the reason for this comes from the **cation intercalation into  $\text{CuO}$** . The sodium due to the small radius can be introduced inside the structure helping in the oxide layer reduction until to a stable  **$\text{Cu}_2\text{O}$  thin layer** which could be the responsible for the **selectivity** for the  **$\text{C}_2\text{H}_4$**  instead of  **$\text{CH}_4$** .

**$\text{CO}_2$  solvation effect** before the entrance in the electrochemical cell.

- The  $\text{CO}_2$  molecule can be bended when two water molecules are coordinated improving the molecule adsorption and the carbonate / bicarbonate generation. For the copper electrode only in the potassium electrolyte the  $\text{CO}_2$  solvation has a positive effect over the methane production efficiency and potential values. But in the case of the  $\text{Cu}_2\text{O}$  the effect goes in the opposite way, for potassium, only in sodium the potential shift to positive values increasing the faradaic efficiencies of ethylene and ethane.

Finally, an evaluation of the **photoelectrochemical (PEC) cell assembling** was presented.

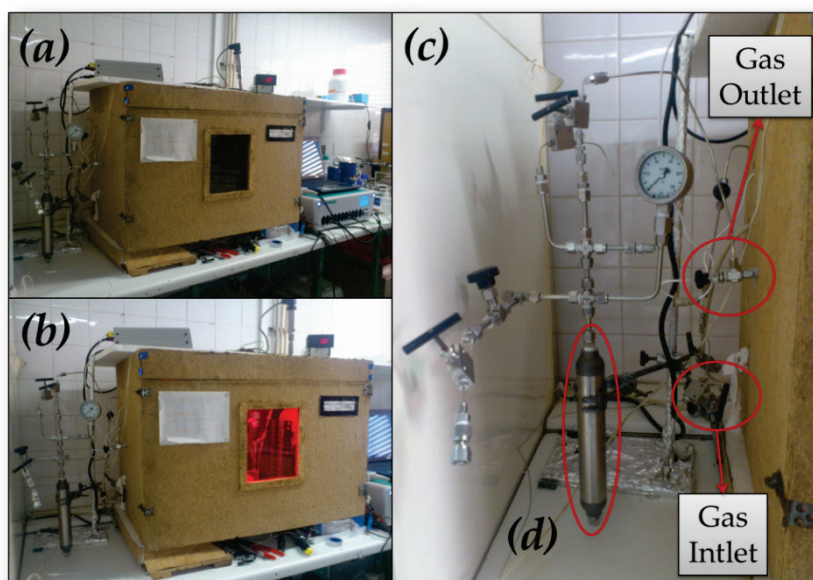
- First the photoanode working potential evaluation at the maximum efficiency was done. For the **300°C sample** from the **ammonia** treatment is **0.58 V vs. RHE**. Second, the copper cathodes potential were evaluated obtaining the values of potential with the best efficiencies for the CO<sub>2</sub>. In this case the values selected for **metallic copper** were in the range of **-1.38 to 1.10 V vs. RHE** and for copper oxide cathodes were in the range of **-1.25 to -0.76 V vs. RHE**. Finally an evaluation of the energy requirements for the complete PEC cell assembling was done to observe which external potential is required. In terms of energy consumption, for 100% faradic efficiency to methane and ethylene (and without hydrogen as competitive reaction), the **energy consumption per mol** will be between **46 and 54 Wh mol<sup>-1</sup>** and **36 and 49 Wh mol<sup>-1</sup>** of methane and ethylene produced respectively, using **TiO<sub>2</sub> as photoanode**.

# Annexes

A.	Electrochemical Reduction of Supercritical CO <sub>2</sub> in Ionic Liquids.....	237
B.	Characterization and Analysis Techniques.....	241
B.1.	Gas Chromatography (GC) .....	241
B.2.	Scanning Electronic Microscopy (SEM) .....	245
B.3.	Atomic Force Spectroscopy (AFM) .....	246
B.4.	X – Ray Diffraction (XRD).....	247
B.5.	Thermal Treatments .....	249
B.6.	Diffuse Reflectance Ultraviolet – Visible Spectroscopy (UV – Vis).....	251
C.	Calculations .....	253
C.1.	Mott – Schottky plots .....	253
C.2.	Electrochemical Standard Potential and Gibbs Energy ( $\Delta Gf^\circ$ ).....	259
	References.....	265

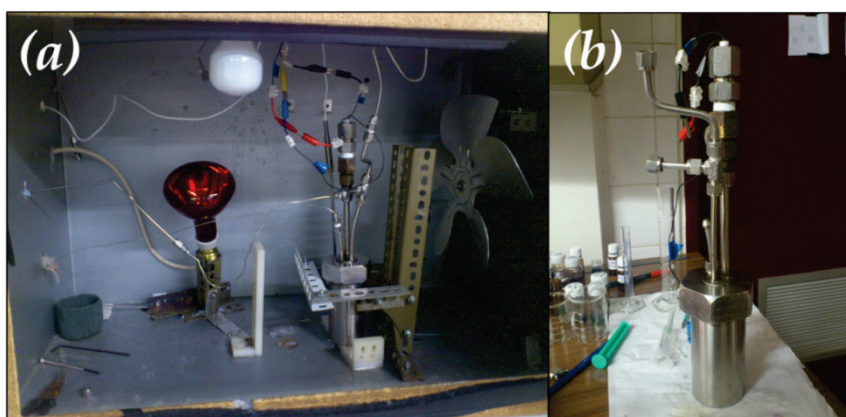
## A. Electrochemical Reduction of Supercritical CO<sub>2</sub> in Ionic Liquids

These tests were done during the stay in Portugal at the FCT Universidade Nova de Lisboa. The work done in Portugal was the optimization of a reactor (under pressure and temperature) for CO<sub>2</sub> electroreduction using supercritical CO<sub>2</sub> in ionic liquids as electrolytes. We performed the first test under a very preliminary test conditions focused to the reactor optimization rather than to have definitive results. The reactor used in these serial of test is shown in *Figure A.1*.



*Figure A.1. Supercritical CO<sub>2</sub> reactor setup. (a) reactor off (b) image with a running experiment and (c) the supercritical CO<sub>2</sub> inlet and the reactor outlet for the produced gas collection after the reaction. (d) Chiller to condensate CO<sub>2</sub> for the separation from the gaseous products obtained in the reaction.*

The internal view of the reactor is shown in *Figure A.2*. For the heating systems an infrared lamp was used at 40 °C. The pressure was set at 60 bars using a pressure controller (approximately the value was 65 bars to assure 60 bars in the reactor). The reactor was a stainless-steel reactor with the sealed electric connections for the reference, working and counter electrode and with a pipe to introduce the supercritical CO<sub>2</sub> in the ionic liquid (*Figure A.2, (b)*). The electrodes used are shown in (*c*) (*Figure A.2*). A zinc plate was used as counter electrode (0.5 cm<sup>2</sup>), the reference electrode was a silver wire and the working electrode a carbon cloth in two forms, circular (1.145 cm<sup>2</sup>) and rectangular (0.5 cm<sup>2</sup>).



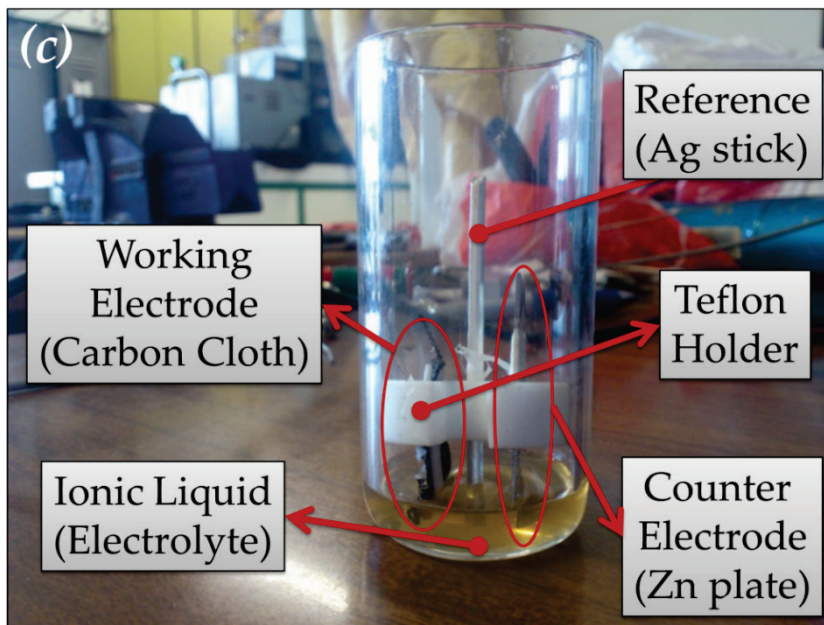


*Figure A.2. (a) Inside view of the reactor composed by, infrared lamp for heating, a fang to homogenize the heat and the reactor. (b) Image of the electrochemical reactor. (c) Glass cup with the electrodes and the ionic liquid.*

The electrochemical parameters for the ionic liquids used were: 20, 50 and 100  $\text{mV s}^{-1}$  scan speed and two potential windows were selected, from -2 to 2 V and -3 to 3 V to observe the electrochemical stability of the ionic liquid [1,2]. The ionic liquids selected for the preliminary test are shown in *Figure A.3*.

The contribution was the assembly of the new setup and defining the boundary conditions of the electrochemical tests. This work was done in the framework of CEOPS (FP7-NMP) project.

Annex A

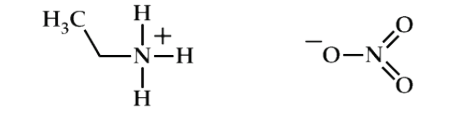
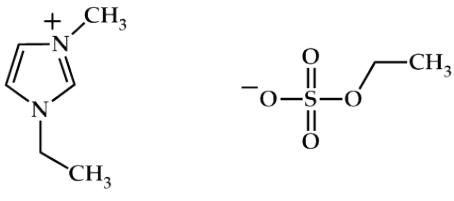
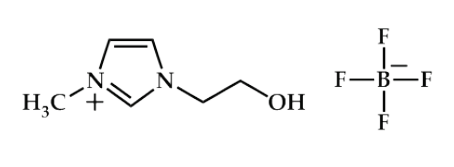
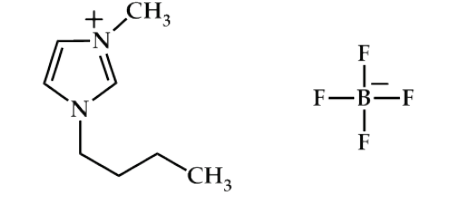
	<p>Ethyl Ammonium Nitrate (EAN, &gt;97% )</p>
	<p>1-Ethyl-3-Methyl-Imidazolium Ethyl Sulfate (<b>ECOENG 212</b>, 99%)</p>
	<p>1-(2-Hydroxyethyl)-3- Methylimidazolium Tetrafluoroborate (<b>HOEMIMBF4</b>, 98%)</p>
	<p>1-Butyl-3-Methyl-Imidazolium Tetrafluoroborate (<b>BMIMBF4</b>, &gt;98%)</p>

Figure A.3. Ionic Liquids used in the supercritical CO<sub>2</sub> electrochemical experiments.

## **B. Characterization and Analysis Techniques**

**Characterization techniques** are fundamental tools in material science to study the structure and the properties of the materials and understand their behavior. The different structural techniques routinely used to characterize the samples under study were exposed in this annex.

### **B.1. Gas Chromatography (GC)**

The gas chromatography is a physical separation method used in analytical chemistry for separating and analyzing compounds that can be vaporized without decomposition. The basic use for the GC is Obtaining the quantitative compositions of the mixture introduced [3,4].

The basic operation in chromatography is based on the separation capacity of a solid or liquid (*stationary phase*), due his physical properties, of the components in a sample (*mobile phase* – moving phase, liquid or gas). The different types or chromatography depends on the physical phase of the mobile phase, which could be liquid (LC) or gas (GC). On the other hand, the different nature of the stationary phase determines the mechanism in the components separation. If the stationary phase is solid, the adsorption strength of the material over the different molecules gives the separation performance. However, if the

stationary phase is liquid the separation performance is given by the solubility properties.

In this thesis we work with gas chromatograph (*Figure B.1*) which use a flow-through narrow tube known as *column*, through which different chemical constituents of a sample pass in a gas stream (*carrier gas*, mobile phase,) at different rates depending on their various chemical and physical properties and their interaction with a specific column filling, called *stationary phase*. As the chemicals exit the end of the column, they are detected and identified electronically. The function of the stationary phase in the column is to separate different components, causing each one to exit the column at a different time (*retention time*). Other parameters that can be used to alter the order or time of retention are the carrier gas flow rate, column length and the temperature.

In a GC analysis, a known volume of gaseous *analyte* is injected into the "entrance" (head) of the column, usually using a *microsyringe* (or, solid phase microextraction fibers, or a gas source switching system). As the carrier gas (normally inert gas as He and Ar) sweeps the analyte molecules through the column, this motion is inhibited by the *adsorption* of the analyte *molecules* either onto the column walls or onto packing materials in the column.

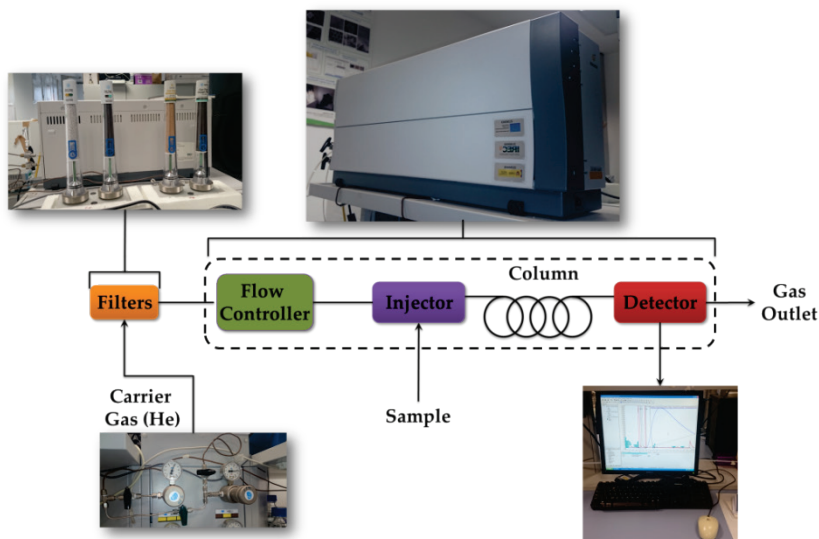


Figure B.1. Basic diagram of the components of micro-GC system.

The rate at which the molecules progress along the column depends on the strength of *adsorption*, which in turn depends on the type of molecule and on the stationary phase materials. Since each type of molecule has a different rate of progression, the various components of the analyte mixture are separated as they progress along the column and reach the end of the column at different times (*retention time*). A detector is used to monitor the outlet stream from the column; thus, the time at which each component reaches the outlet and the amount of that component can be determined. Generally, substances are identified (qualitatively) by the order in which they emerge (elute) from the column and by the retention time of the analyte in the column.

The GC detector must have specific properties as, sensibility, stability in a large range of concentrations for the different

molecules and long term stability. In this thesis thermal conductivity detectors (TCD) were used. These kinds of detectors measure the conductivity differences between the pure carrier gas and the mixture of the carrier gas with the analyte. This type of detector are commonly used for the analysis of permanent gases ( $H_2$ , CO, etc.) and light hydrocarbons. The electric signal from the detector is transformed by the software to a chromatogram, which represents the concentration of the different species of the sample versus the retention time. The peak area obtained (Gaussian shape) are correlated lineally with the analyte concentrations. However, to obtain this correlation a calibration of the machine is required. The calibration is done using reference gases with known concentrations.

The machine used in this thesis is a multichannel Varian 490 Micro-GC with four columns with the correspondent TCD detectors to analyze the maximum amount of molecules; lately we use only three channels in the system. The specifications and conditions of the micro-GC are resumed in *Table B.1*. The micro-GC was calibrated to quantify  $H_2$ , CO, short chain hydrocarbons ( $CH_4$ ,  $C_2H_4$  and  $C_2H_6$ ) and some alcohols ( $CH_3OH$  and  $C_2H_5OH$ ) from some reference gas bottles (Abelló-Linde). The concentrations of the reference bottles were <1% for all of them except  $H_2$ ; 1 and 3 % for CO and  $H_2$  to increase the range; 100%  $H_2$  for large amounts. For methane a 20% bottle in He was used for the large range of concentrations.

*Table B.1. Experimental conditions of the micro-GC using a thermal conductivity detector (TCD). The carrier gas for all channels was Helium and the columns have heating system.*

Channel	Column type	Temperature (°C) Injector/Column	Analytes
1	Molsieve 5Å-10m (M5Å_BF)	50/80	H <sub>2</sub> , CO, CH <sub>4</sub>
2	PPQ (10m)	70/40	Hydrocarbons C <sub>1</sub> – C <sub>3</sub>
3	CP-Sil 5 CB (6m)	110/100	Alcohols

## **B.2. Scanning Electronic Microscopy (SEM)**

Scanning electron microscopy (SEM) utilizes a focus beam of high-energy electrons to generate a variety of signals at the surface of the solid sample, coming from the electron-sample interaction. The beam of electrons which typically have energy from ~eV to keV is focused by a series of electromagnetic lenses to an spot size up to 1 nm. The accelerated electrons impact with the sample and cause electrons to be scattered from the sample due to elastic or inelastic events. Low energy electrons resulting from inelastic scattering are secondary electrons and it is the most common imaging mode. Due to their low energy (< 50 eV) these electrons are generated few nanometers from the surface and contain information about the morphology and the topography of the sample. Backscattered electrons (BSE) are higher energy electrons produced by elastic scattering interactions. Since elements with different atomic number backscatter different, BSE is commonly

used to illustrate contrast of samples with different chemical composition. Finally, X-rays are produced when the electron beam removes an inner shell electron of the sample, causing a higher energy electron to fill the shell and releasing energy. These characteristic X-rays are used to identify the composition and abundance of the elements of the sample.

In this work, SEM routinely used to investigate the morphology of the samples before and after the electrochemical tests, generally using a ZEISS AURIGA. SEM-EDX line profile was performed to observe the incorporation of new materials in the TiO<sub>2</sub> nanorods structure (*Chapter III*) (Zeiss Auriga – Inca).

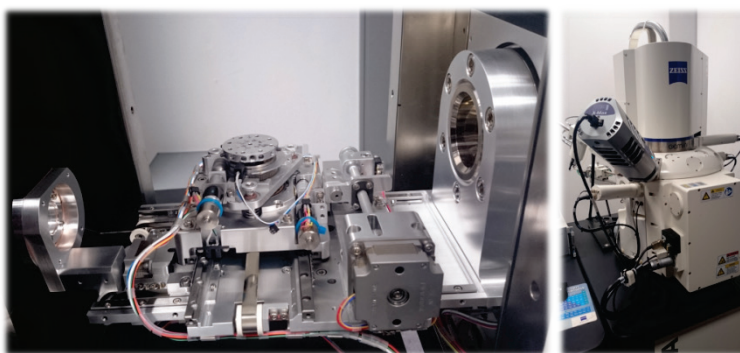


*Figure B.2. Image of the SEM used in this thesis.*

### **B.3. Atomic Force Spectroscopy (AFM)**

For the 3D high resolution topography done over the samples under study in *Chapter III* an atomic force spectroscopy XE – 100 from Park Systems Co. with the non-contact setup was used.



*Figure B.3. AFM image of the machine used in this thesis.*

#### **B.4. X – Ray Diffraction (XRD)**

X-ray crystallography is a non-destructive characterization technique in which the pattern collected is produced by exposition of a crystal to X-rays. If the wavelength of the X-rays launched is on the order of magnitude of the interatomic distances of the crystal, the X-rays will diffract with a specific direction and intensity and therefore, the so-generated diffraction pattern is specific of the atomic and molecular structure of the crystal under study. The connection between the diffraction peak position and the distance between atomic planes in the crystals comes from the Bragg law:

$$n\lambda = 2d_{hkl} \sin \theta \quad (\text{B.1})$$

Where  $n$  are an integer number,  $\lambda$  X-Ray wavelength,  $d_{hkl}$  atomic plane distance and  $\theta$  Bragg angle.

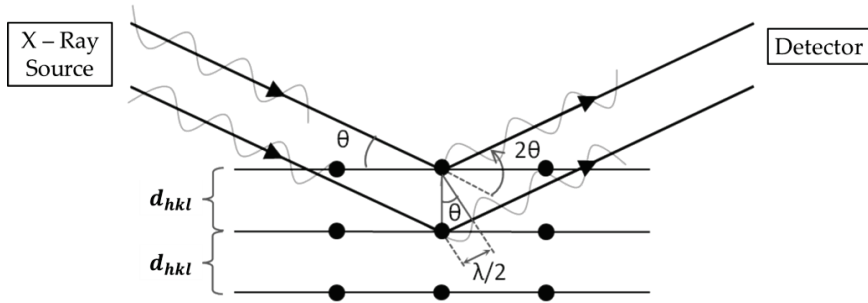


*Figure B.4. Scheme of X-Ray diffraction interaction with the crystallographic planes.*

A qualitative and quantitative analysis of the patterns allows identifying the crystalline phase and determining the lattice parameter. An analysis of the peak shape gives information about the crystallite size distribution, the micro-strain or the extended defect concentration. Williamson and Hall proposed a method for deconvoluting size and strain broadening by analysis of the peak width as function of  $2\theta$  [5]. According to the Scherrer and Wilson equation [6].

$$\beta \cos \theta = \frac{4K\lambda}{3D} + 4\varepsilon \sin \theta \quad (\text{B.2})$$

Where,  $\beta$  is the integral breadth of a reflection (in radians),  $K$  is the Scherrer constant (equals 0.89 for spherical grains),  $\lambda$  is the X-ray wavelength,  $\theta$  is the diffraction angle,  $D$  is the crystallite size and  $\varepsilon$  is the microstrain

The plot  $\beta \cos \theta$  on the y-axis and  $4 \sin \theta$  on the x-axis allows to linear fit the data and extracts the crystallite size and the strain, but in this thesis was not used. X-ray diffraction (XRD) was routinely used **in this thesis** to identify and further, corroborate the phase of

all materials. Different equipments were used, but generally the scans were performed at room temperature, using copper  $K\alpha$  radiation, in the  $2\theta$  range from 20 to  $100^\circ$ . Most of the XRD patterns were obtained from a Bruker D8 automated diffractometer, with a nickel filter and Lynx Eye detector the working anode conditions were 40 kV – 40 mA. The radiation was  $Cu\ k\alpha$ ,  $\lambda = 1.5418\ \text{\AA}$ .

For the crystal structure identification is possible to use the data bases available on the market. Normally are included in the program for spectra acquisition and treatment. In this thesis the data based used was JCPDS from *International Centre of Diffraction* (ICDD).



*Figure B.5. Image of the Bruker D8 automated diffractometer.*

## **B.5. Thermal Treatments**

For the thermal treatments under controlled atmospheres ( $H_2$  (5% in Ar),  $O_2$ , ammonia gas ( $NH_3$ ) and Ar) a stainless steel cell, to avoid the gas corrosion, coupled with a glass or quartz tubular

pipe with controlled gas flow passing through the cell was used. This setup can be used in horizontal and vertical tubular furnaces (Carbolite, HST 12/300 – 1200 °C max Temp). For the vertical configuration a holder is required to support the sample. For the atmosphere treatments a big oven with ramping (5 °C/min) controller was used (Lenton, AWF 12/5 – 1200 °C max Temp).



*Figure B.6. Furnace used in the thesis. Left side the controlled atmosphere and right one atmospheric oven.*

## B.6. Diffuse Reflectance Ultraviolet – Visible Spectroscopy (UV – Vis)

In a UV – Vis spectroscopic measurements, light absorption as a function of wavelength provides information about electronic transitions occurring in the material. The incident intensity ( $I_0$ ) is possible to be reflected ( $I_R$ ), absorbed ( $I_A$ ) or transmitted ( $I_T$ ) using the Kirchhoff radiation law :

$$I_0 = I_R + I_A + I_T \Rightarrow I_A = I_0 - I_T - I_R \quad (\text{B.3})$$

In  $I_R$  is included specular and diffuse reflectance, therefore after multiple dispersions in the sample come back to the surface (Figure B.7). For opaque samples  $I_T = 0$ . The diffuse reflectance is a perfect technique to measure powder and crystalline samples (high dispersion) [7].

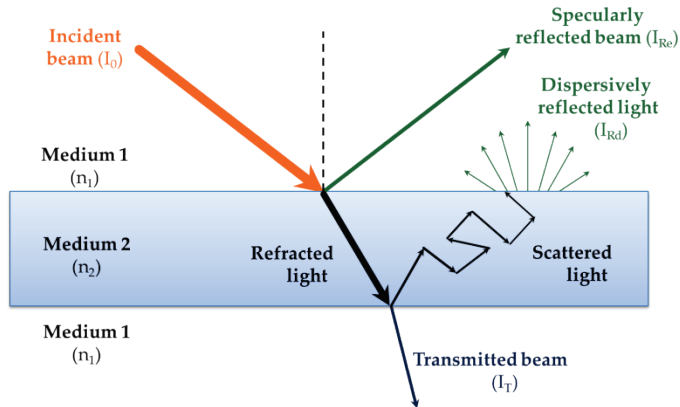
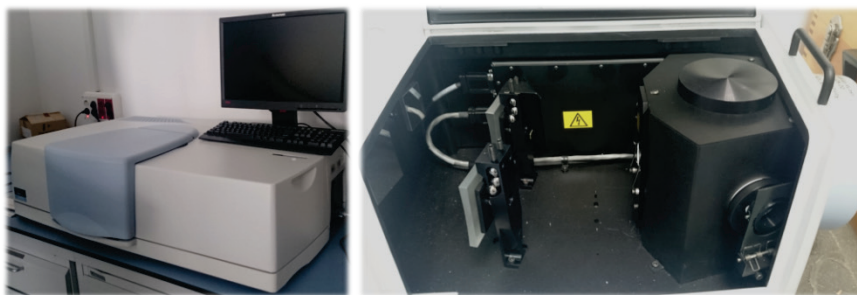
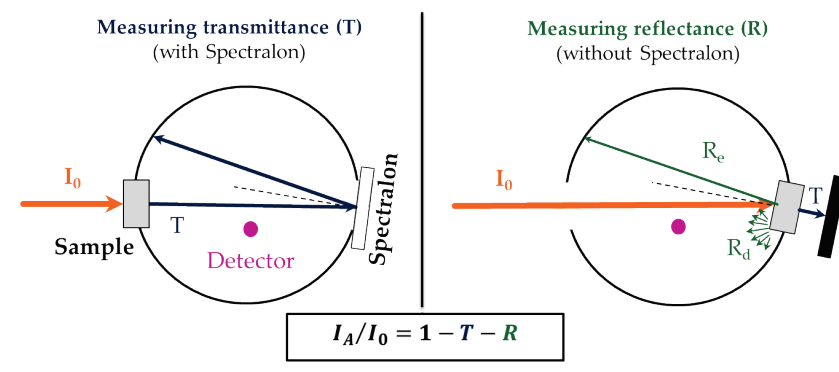


Figure B.7. Scheme included the reflectance, absorbance and transmittance of a transparent sample.

## Annex B

For this thesis, a Perkin Elmer Lambda 950 spectrometer with two lamps (tungsten and D2) and the integrating sphere (Ulbricht's sphere) accessory which allow the diffuse reflectance measurements was used [8].

**Integrating sphere (150 mm):** recovers all dispersed (scattered) light by **multiple reflections** of light mediated by the white inner coverage (BaSO<sub>4</sub>, teflon, etc).



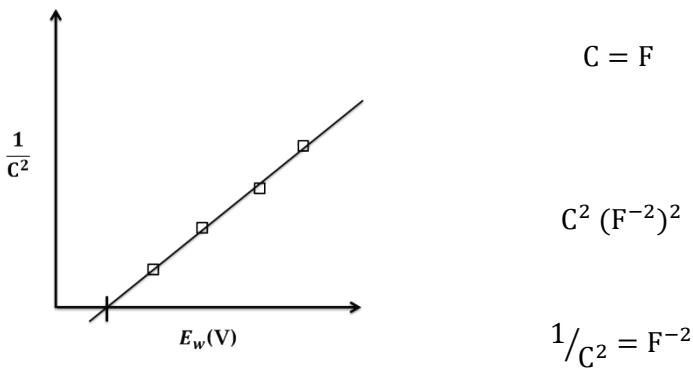
**Figure B.8.** Scheme of integrating sphere setup and image of the UV-Vis spectrometer.

## C. Calculations

In this part of the thesis are included some short explanations and basic calculations for Mott-Schottky plots and Gibbs energy formation for the reactions involved in the CO<sub>2</sub> reduction and the water oxidation.

### C.1. Mott – Schottky plots

Assuming an ideal and simplified model, from the Schottky plots it is straightforward to deduce relevant parameter of the semiconductor such as the doping density ( $N_D$ ) depending on the N or P type of semiconductor [8]. Another parameter which is possible to obtain is the flat band potential ( $E_{fb}$ ). Those plots measure the capacitance of the material changing the applied voltage.



Herein in the representation, was considered the capacitance. Respect of the potential variations over the semiconductor in the space charge region occurs a bending of the conduction and valence bands.

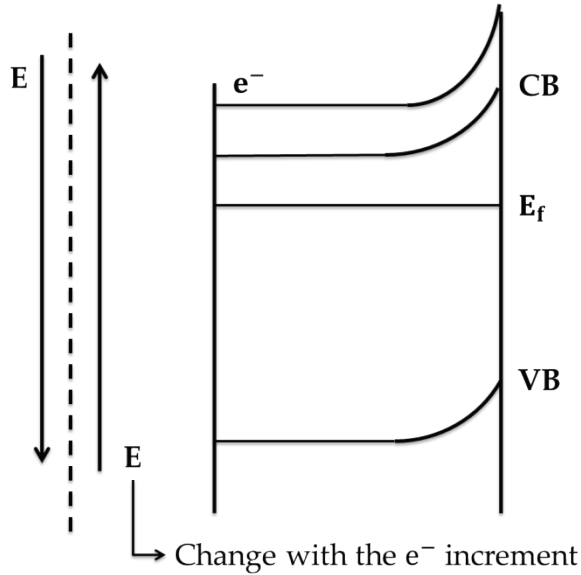


*Figure C.1. Scheme of the band bending in an n-type semiconductor.*

When the potential is changed it is possible to obtain the capacitance, the program of the Parstat software gives directly  $C^{-2}$ .

Electrical Model ( $\alpha = proportional$ )

$$C \propto \frac{1}{\sqrt{E - E_{fb}}} \rightarrow C^2 \propto \frac{1}{E - E_{fb}} \quad (C.1)$$

When the data from the potentiostat are represented we obtain curves at different frequencies. One of these frequencies is selected and the slope in the straight part of the S generated gives the values for  $N_D/N_A$  and  $E_{fb}$ .

$$\frac{1}{C^2} \propto (E - E_{fb}) \quad (C.2)$$

From the plot is possible to obtain,

$$y = \frac{1}{C^2} (F^{-2}) \text{ and } x = E(V) \quad (C.3)$$

The equation required to calculate the parameters under study is:

$$\frac{1}{C^2} = \frac{2}{N_D A^2 e \epsilon_s} \left[ (E - E_{fb}) - \frac{kT}{e} \right] \quad (C.4)$$

Where  $e$  is the charge of an electron ( $1.602 \times 10^{-19}C$ ),  $k$  is Boltzmann constant ( $1.38 \times 10^{-23} JK^{-1}$ )  $T$  is the temperature in Kelvin degrees (K) and  $\epsilon_s$  is the static dielectric constant ( $\epsilon_m \epsilon_0$ , product of the vacuum permittivity ( $8.85 \times 10^{-12} F m^{-1}$ ) with the material dielectric constant, 100 for rutile  $TiO_2$  [9]). From the representation of the Schottky plots the regression line obtained is:

$$\frac{1}{C^2} (\mathbf{Y}) = \left[ \frac{2}{N_D A^2 e \epsilon_s} \left( -E_{fb} - \frac{kT}{e} \right) \right] (\mathbf{a}) + \frac{2}{N_D A^2 e \epsilon_s} (\mathbf{b}) \times E(\mathbf{X}) \quad (C.5)$$

From the regression line slope is and corresponding with  $b$  is possible to obtain the donors value,

$$b = \frac{2}{N_D A^2 e \epsilon_s} \rightarrow N_D (cm^{-3}) \quad (C.6)$$

For the flat band potential is required the intercept with the X (E) axes, when  $y = 0$ , and solving the Eq. (B.5) with this condition:

$$E_{fb} = E - \frac{kT}{e} (0.0257 V \text{ at } 25^\circ C) \quad (C.7)$$

$N_D$ , gives the material conductivity, at higher values the conductivity is better giving high current density. The shape of the Schottky plots changes depending on the semiconductor type (Figure C.2).

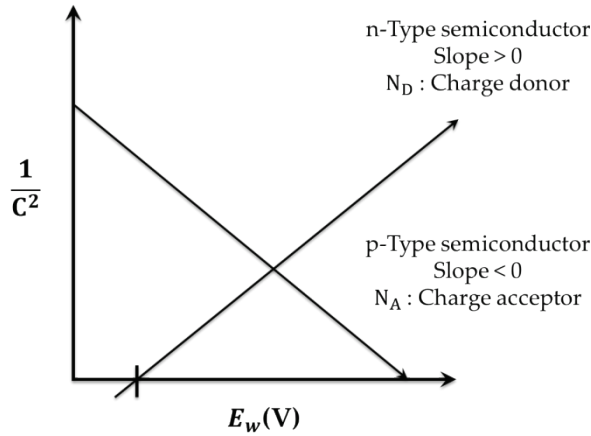
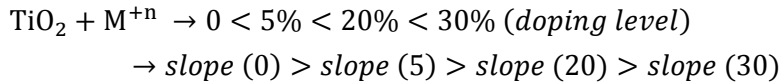


Figure C.2. Schottky plot for each type of semiconductor.

An example of tendencies when for example; if a titanium oxide rods are doped with any material, the charge donors number goes with the doping level.



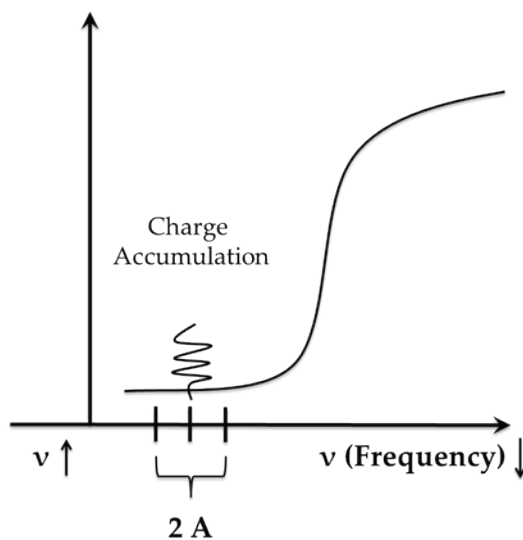
The values for the  $N_D$  goes in the opposite way then the slope, when the slope increases the charge donors value decrease. The values accepted for the donors number for  $\text{TiO}_2 \sim 10^{17} - 10^{18} \text{ cm}^{-3}$ .

For the experimental setup is required a potential working range, the parameters are:

- Scan Definition
  - o AC amplitude (A)
  - o Frequency, scan rate
- Initial DC Potential  $\rightarrow -1400 \text{ mV } (-1.4 \text{ V})$ 

*Potential window for the CV, is not required to reach to the maximum potential value, only upper then the onset potential.*
- Final DC Potential  $\rightarrow 0 \text{ mV } (0\text{V})$ 

*Modify the frequencies range, the effect change with the frequencies ( $\nu$ ).*



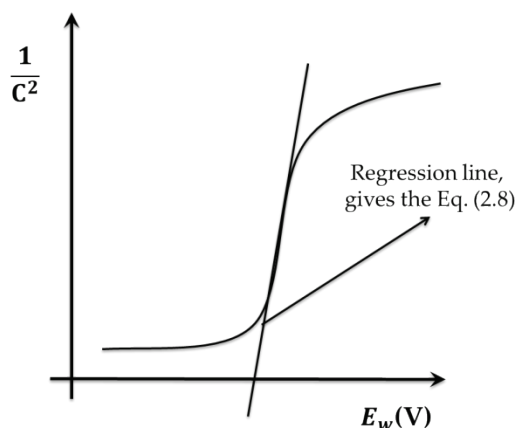


**Figure C.3.** First image, scheme of the Schottky plots measurements. Second image, regression line used for the donors number and flat band potential calculation, obtained from the Schottky measurements.

When the flat band and band gap (**Chapter III**) values are obtained is possible to build a band diagram. To move from potential into absolute potential scale in vacuum:

$$E(eV) = -eE(V \text{ vs. RHE}) - 4.5 \quad (\text{C.8})$$

The 0 in the electrochemical scale (V vs. RHE) corresponds to  $-4.5$  eV in the potential energy in vacuum. To move from V to eV is required to divide between the electron elementary charge, but first must be multiply by the same value keeping the same.

Example:

$$E(eV) = -1.5 \text{ V vs. RHE}; E(eV) = -(1.5) - 4.5 = -3eV$$

$$E(eV) = -E(V \text{ vs. RHE}) - 4.5$$

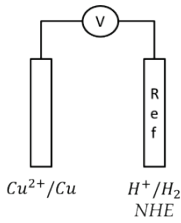
$$1 \text{ V} = 1 \text{ J C}^{-1}, e \times E(V) = C \times (\text{J C}^{-1}) = J (\text{jules})$$

To obtain the values for the band diagram, the flat band potential value obtained from the Schottky plots correlates with the conduction band of the material and with the band gap is possible to obtain the valence band.

$$E_{CB} - E_{VB} = E_g(\text{Band gap}) \quad (\text{C.9})$$

## C.2. Electrochemical Standard Potential and Gibbs Energy ( $\Delta G_f^\circ$ )

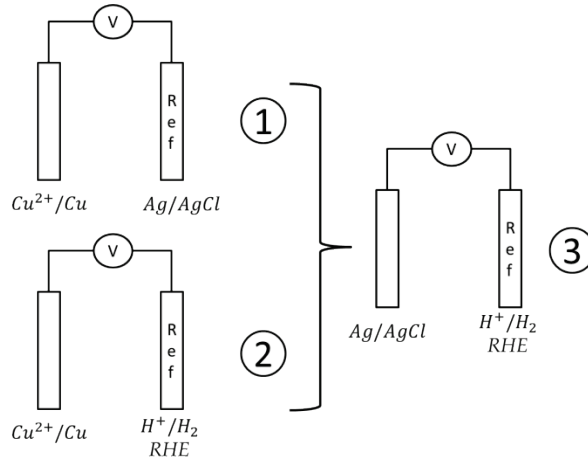
The calculations required to move from one reference electrode to other are shown below. For these calculations we take a Cu/Cu<sup>2+</sup> system as example, and the objective is passing from Ag/AgCl to RHE [10].



$$\begin{aligned} \Delta E_{NHE} &= E_{(Cu^{2+}/Cu)} - E_{Ref} \\ &= E_{(Cu^{2+}/Cu)} - E_{(H^+/H_2)} \end{aligned}$$

$$\Delta E_{(Ag/AgCl)} = E_{(Cu^{2+}/Cu)} - E_{(Ag/AgCl)}$$

$\Delta E$  corresponds to the measured potential in the experiment.



The formula with the configuration of the draw (1 = 2 + 3):

$$\Delta E_{(Ag/AgCl)} = E_{(Cu^{2+}/Cu)} - E_{(Ag/AgCl)} + E_{(Ag/AgCl)} - E_{(H^+/H_2)}$$

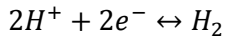
$$\Delta E_{(Ag/AgCl)} = E_{(Cu^{2+}/Cu)} - E_{(H^+/H_2)}$$

$$\Delta E_{(Ag/AgCl)} + E_{(Ag/AgCl)}^\circ = E_{(H^+/H_2)}^*$$

$$NHE \rightarrow a_{H^+} = 1$$

$$pH = -\log[H^+]$$

$$RHE \rightarrow a_{H^+} \neq 1$$



Standard conditions (1 atm, 25°C)

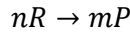
$E_{RHE}$  and Nernst equation:

$$E_{RHE} = E_{(H^+/H_2)}^\circ + \frac{0.059(2.3RT)}{2(n)} \log \frac{[H^+]^2}{P_{H_2}} = E_{(H^+/H_2)}^\circ - 0.0592 \times pH$$

If the last formula is substituted in the star one (\*) we obtain this formula at the end:

$$E_{RHE} = \Delta E_{(Ag/AgCl)} + 0.0592 \times pH + E_{(Ag/AgCl)}^{\circ}$$

To obtain the potential values of the reactions under study in this thesis we use the Gibbs energy values from the thermodynamic data [10]. For this we need the Hess law, which is possible to obtain the values of  $\Delta G_f^0$  for each reaction. The free Gibbs energy is as standard state for this reason, is possible to calculate for a general reaction using this Eq. (B.10).



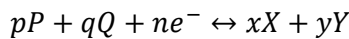
$$\Delta G_{f-reaction}^0 = \sum m \times \Delta G_{f-products}^0 - \sum n \times \Delta G_{f-reactants}^0 \quad (C.10)$$

To calculate the standard potential at pH 0 for the reaction the Nernst law is required to apply.

$$\Delta G_{f-Reaction}^0 = -n \cdot F \cdot \Delta E_{Reaction}^0 \quad (C.11)$$

The calculations done in **Chapter I** to obtain the potential values for the CO<sub>2</sub> reduction products and, as reference, H<sub>2</sub> and O<sub>2</sub> evolution at different pH are shown below.

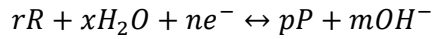
Nernst equation for a generic reaction is given by Eq. (B.12)



$$E_R = E_R^\circ + \frac{2.3RT}{nF} \log \left[ \frac{(a_P)^p (a_Q)^q}{(a_X)^x (a_Y)^y} \right] \quad (\text{C.12})$$

In the formula,  $E_R^\circ$  standard potential calculated from the Gibbs free energy,  $R$  is the gas constant ( $8.314 \text{ J mol}^{-1} \text{ K}^{-1}$ ),  $T$  in the temperature (K),  $n$  in the electrons involved in the reaction and the logarithmic part is the activities of the reduction and oxidation species.

For the Basic media calculations, using Nernst equation:



$$E = E^\circ + \frac{0.0592}{n} \log \left[ \frac{(a_R)^r (a_{H_2O})^x}{(a_P)^p (a_{OH^-})^m} \right]$$

The activities for R, H<sub>2</sub>O, and P are equivalent to 1. The reactions change to:

$$\begin{aligned} E &= E^\circ + \frac{0.0592}{n} \log \left( \frac{1}{(a_{OH^-})^m} \right) \rightarrow E \\ &= E^\circ + \frac{0.0592}{n} (-m \times \log(a_{OH^-})) \end{aligned}$$

$$E = E^\circ + \frac{m \times 0.0592}{n} (-\log(a_{OH^-}))$$

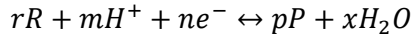
$$pH = -\log a_{H^+}, \quad pOH = -\log a_{OH^-}$$

$$E = E^\circ + \frac{m \times 0.0592}{n} \times pOH \quad pH + pOH = 14 \text{ (} pK_w \text{)}$$

$$E = E^\circ + \frac{m \times 0.0592}{n} \times (14 - pH)$$

$$E = E^\circ + \frac{m}{n} \times (0.8288 - 0.0592 \times pH), \quad \text{Basic Media (pH 14)}$$

Using the same general reaction for the acid media the calculations change a bit. The approximation in the activities is the same as in the basic media.



$$E = E^\circ + \frac{0.0592}{n} \log \left[ \frac{(a_R)^r (a_{H^+})^m}{(a_P)^p (a_{H_2O})^x} \right]$$

$$E = E^\circ + \frac{0.0592}{n} (m \times \log(a_{H^+})) \quad pH = -\log a_{H^+}$$

$$E = E^\circ - \frac{m \times 0.0592}{n} \times pH, \quad \text{Acid Media (pH0)}$$

The values obtained for the reactions under study for both media are resumed in

*Table C.1* and *Table C.2*.

**Table C.1.** Calculated standard potentials in acid media.

<b><i>CO<sub>2</sub>(g) Reduction Half Reactions</i></b>	<b><i>E° (V vs. SHE)</i></b>
$\text{CO}_2 + \text{H}^+ + 2\text{e}^- \leftrightarrow \text{HCOO}^-$	-0.22
$\text{CO}_2 + 2\text{H}^+ + 2\text{e}^- \leftrightarrow \text{CO} + \text{H}_2\text{O}$	-0.10
$\text{CO}_2 + 6\text{H}^+ + 6\text{e}^- \leftrightarrow \text{CH}_3\text{OH} + \text{H}_2\text{O}$	0.03
$\text{CO}_2 + 8\text{H}^+ + 8\text{e}^- \leftrightarrow \text{CH}_4 + 2\text{H}_2\text{O}$	0.18
$2\text{CO}_2 + 12\text{H}^+ + 12\text{e}^- \leftrightarrow \text{C}_2\text{H}_4 + 4\text{H}_2\text{O}$	0.06
$2\text{CO}_2 + 12\text{H}^+ + 12\text{e}^- \leftrightarrow \text{C}_2\text{H}_5\text{OH} + 3\text{H}_2\text{O}$	0.09
$2\text{CO}_2 + 14\text{H}^+ + 14\text{e}^- \leftrightarrow \text{C}_2\text{H}_6 + 4\text{H}_2\text{O}$	0.14
<b><i>H<sub>2</sub> Reduction Half Reaction</i></b>	
$2\text{H}^+ + 2\text{e}^- \rightarrow \text{H}_2$	0.00

**Table C.2.** Calculated standard potentials in basic media and pH 7

<b><i>CO<sub>2</sub>(g) Reduction Half Reactions</i></b>	<b><i>E° (V vs. SHE)</i></b>	<b><i>E (V vs. RHE)</i></b>
$\text{CO}_2 + \text{H}_2\text{O}(l) + 2\text{e}^- \leftrightarrow \text{HCOO}^-(aq.) + \text{OH}^-(aq)$	-0.64	-0.43
$\text{CO}_2 + \text{H}_2\text{O} + 2\text{e}^- \leftrightarrow \text{CO}(g) + 2\text{OH}^-$	-0.93	-0.52
$\text{CO}_2 + 5\text{H}_2\text{O} + 6\text{e}^- \leftrightarrow \text{CH}_3\text{OH}(aq.) + 6\text{OH}^-$	-0.80	-0.38
$\text{CO}_2 + 6\text{H}_2\text{O} + 8\text{e}^- \leftrightarrow \text{CH}_4(g) + 8\text{OH}^-$	-0.65	-0.24
$2\text{CO}_2 + 8\text{H}_2\text{O} + 12\text{e}^- \leftrightarrow \text{C}_2\text{H}_4(g) + 12\text{OH}^-$	-0.76	0.06
$2\text{CO}_2 + 9\text{H}_2\text{O} + 12\text{e}^- \leftrightarrow \text{C}_2\text{H}_5\text{OH}(aq.) + 12\text{OH}^-$	-0.74	-0.33
$2\text{CO}_2 + 10\text{H}_2\text{O} + 14\text{e}^- \leftrightarrow \text{C}_2\text{H}_6(g) + 14\text{OH}^-$	-0.68	0.14
<b><i>H<sub>2</sub> Reduction Half Reaction</i></b>		
$2\text{H}_2\text{O}(l) + 2\text{e}^- \rightarrow \text{H}_2(g) + 2\text{OH}^-(aq.)$	-0.83	-0.41

## References

- [1] Rosen B.A., Zhu W., Kaul G., Salehi-Khojin A., Masel R.I. *J Electrochem Soc.* **2012**, 160, H138.
- [2] Salehi-Khojin A., Jhong H.-R.M., Rosen B.A., Zhu W., Ma S., Kenis P.J.A., et al. *J Phys Chem C.* **2013**, 117, 1627.
- [3] Harvey D. *Modern Analytical Chemistry.* **1999**.
- [4] Meyers R.A. *Encyclopedia of Physical Science and Technology, Volumen 8.* **2002**.
- [5] Williamson G., Hall W.. *Acta Metall.* **1953**, 1, 22.
- [6] Als-Nielsen J., McMorrow D. *Elements of Modern X-ray Physics, Second Edition - Als-Nielsen - Wiley Online Library.* **2011**.
- [7] Gauglitz G., Vo-Dinh T. *Handbook of Spectroscopy.* **2006**.
- [8] Chen Z., Dinh H.N., Miller E. *Photoelectrochemical Water Splitting: Standards, Experimental Methods, and Protocols.* New York, NY: Springer New York; **2013**.
- [9] Fàbrega C., Monllor-Satoca D., Ampudia S., Parra A., Andreu T., Morante J.R. *J Phys Chem C.* **2013**, 117, 20517.
- [10] Bard A.J., Parsons R., Jordan J. *Standard Potentials in Aqueous Solution.* **1985**.

D.	Resumen de la Tesis.....	267
D.1.	Introducción.....	267
D.1.1.	<i>Producción de Combustibles Solares Mediante Fotorreducción de CO<sub>2</sub></i> .....	269
D.1.2.	<i>Fotoánodos para la Ruptura del Agua Mediante Energía Solar (Reacción Luminosa)</i> .....	271
D.1.3.	<i>Electrorreducción de CO<sub>2</sub> (Reacción Oscura)</i> .....	272
D.1.4.	<i>Objetivos de la Tesis</i> .....	273
D.2.	Reacción Luminosa: Fotoánodos para la Ruptura de Agua.....	273
D.2.1.	<i>Nanotubos de Óxido de Titanio, TiNTs</i> .....	273
D.2.2.	<i>Nanohilos de Óxido de Titanio</i> .....	276
D.2.3.	<i>Dopaje de Nanohilos</i> .....	279
D.3.	Reacción Oscura: Electrorreducción de CO <sub>2</sub> con Electrodo Basado en Cobre .....	284
D.4.	Ensamblado de la Celda PEC.....	288
D.5.	Conclusiones.....	290
D.6.	Bibliografía .....	298

## **D. Resumen de la Tesis**

### **D.1. Introducción**

Los gases de efecto invernadero provenientes del sector energético representan alrededor de dos tercios de las emisiones totales del efecto invernadero. El uso de los combustibles fósiles en el sector energético continúa siendo más del 80% y las emisiones de CO<sub>2</sub> proveniente del mismo están alrededor del 90%. Es necesario, por tanto, una acción efectiva en el sector para tratar el problema del cambio climático.

El coste tecnológico de las energías renovables se han reducido notablemente, pero aún sigue siendo muy importante el soporte por parte de la administración pública para el desarrollo de las mismas.

Para la reducción del CO<sub>2</sub> de la atmósfera existen dos métodos posibles:

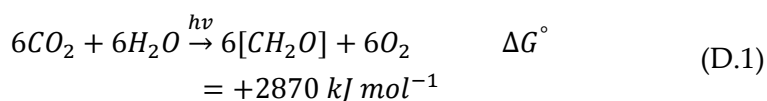
(1) la captura y secuestro de carbono (CCS), que se basa en la separación y captura del CO<sub>2</sub> de las plantas energéticas e industriales, para luego transportar el CO<sub>2</sub> a zonas adecuadas para su inyección en formaciones subterráneas para el almacenaje permanente [1,2]

(2) la captura y utilización de carbono (CCU). Este tipo de tecnología toma el CO<sub>2</sub> para convertirlo en un producto de valor añadido, introduciéndolo en el ciclo económico del carbono [3]. Los métodos más importantes dentro de esta tecnología para la reutilización del CO<sub>2</sub> son:

- (a) Carbonatación Mineral.
- (d) Utilización del  $CO_2$  para generar productos de valor añadido a través de algas.
- (e) Conversión del  $CO_2$ : materia prima química.

Ambas tecnologías (CCUS) pueden jugar un papel importante en la reducción del cambio climático con el añadido, en el caso de las CCU, de reducir la demanda energética junto con las renovables y otros tipos de tecnologías [4].

Dentro de la tecnología CCU, el método de conversión de  $CO_2$  a materia prima química, existe un proceso similar en la naturaleza, la *fotosíntesis*. La fotosíntesis se basa en la producción de carbohidratos usando energía solar para la generación de energía en las plantas. El proceso involucra la incorporación del carbono en la biosfera y actúa también como fuente de  $O_2$  para la atmósfera.



Desde el punto de vista tecnológico este proceso sería muy interesante para la revalorización del  $CO_2$  usando energía solar, pudiendo almacenar energía en enlaces químicos (**fotosíntesis artificial**).

Un concepto bastante interesante relativo a la fotosíntesis artificial es el concepto de refinería solar, la cual se basada en la economía circular del  $CO_2$ . Este concepto se basa en la captura y reciclaje (mediante diferentes metodologías) del  $CO_2$  proveniente de los combustibles fósiles hacia productos de valor añadido. La energía requerida para el proceso se suministraría mediante energía solar (térmica solar, fotovoltaica o fotones). Mediante este

concepto el  $\text{CO}_2$  generado sería completamente reciclado a productos con valor añadido, cerrando el ciclo del  $\text{CO}_2$ , similar a la fotosíntesis.

### D.1.1. Producción de Combustibles Solares Mediante Fotorreducción de $\text{CO}_2$

Existen dos tipos de vías para la reducción del  $\text{CO}_2$  reducción usando materiales semiconductores (*Figura D.1*), (1) mediante fotocatalisis directa y (2) mediante procesos fotoelectroquímicos (PEC).

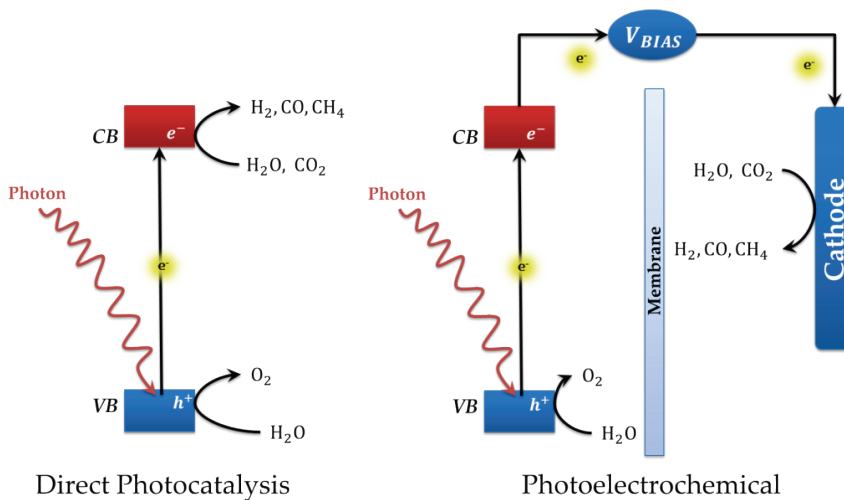


**Figura D.1.** Esquemas de la conversión fotocatalítica directa (Direct Photocatalysis) y fotoelectroquímica (Photoelectrochemical) para la reducción de  $\text{CO}_2$  o  $\text{H}_2\text{O}$ .

Para la conversión fotocatalítica directa, la reducción y la oxidación se dan en la superficie del material. El problema de este proceso es la proximidad de las reacciones teniendo una alta probabilidad de que los productos generados se vuelvan a oxidar

como la alta probabilidad de procesos de recombinación del par electrón-hueco fotogenerados al tener tan próximas las dos reacciones [5]. Para poder evitar la reoxidación de los productos reducidos podemos usar el método fotoelectroquímico, donde el proceso de reducción y oxidación están separados físicamente por una membrana de intercambio iónico evitando el proceso de reoxidación y mediante la aplicación de un potencial externo se pueden evitar procesos de recombinación.

Los materiales semiconductores son idóneos para esto debido a que es posible generar una caída de potencial en la superficie del material pudiendo modular el ancho de banda en la zona de depleción. En el caso de valores altos de anchura en la zona de depleción dan lugar a un alto campo eléctrico, generando una mejor separación de los pares electrón ( $e^-$ )-hueco ( $h^+$ ) fotogenerados, evitando los procesos de recombinación y, por lo tanto, mejorando las eficiencias en la reducción del  $\text{CO}_2$  o  $\text{H}_2\text{O}$  respecto a la conversión directa [6]. El efecto de que puede introducir un ánodo fotoactivo en un electrolizador clásico se puede observar en la *Figura D.2*.

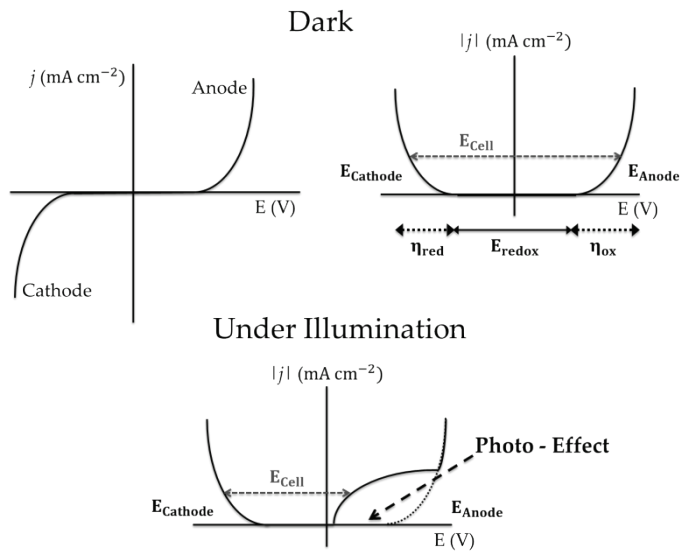


**Figura D.2.** Esquema del efecto de la introducción de un fotoelectrodo en una configuración fotoelectroquímica (PEC) en oscuridad (Dark) y bajo iluminación (Under illumination).

### D.1.2. Fotoánodos para la Ruptura del Agua Mediante Energía Solar (Reacción Luminosa)

Dentro de los semiconductores basados en óxidos metálicos el  $TiO_2$ , tanto en anatasa como en rutilo (estructuras cristalográficas estables) tienen valores teóricos de densidad de corriente como eficiencia de conversión solar a hidrogeno (STH) más bajos que otros óxidos metálicos comúnmente utilizados como la hematita ( $Fe_2O_3$ ) y el óxido de wolframio (VI) ( $WO_3$ ). En cambio tanto la estabilidad del  $TiO_2$  como la posición energética de la banda de conducción [7], favorable para la reducción de  $CO_2$  (o  $H_2O$ ) pudiéndose dar espontáneamente, como el valor más negativo del potencial de inicio (onset potential), es posible reducir el potencial

externo necesario requerido en la celda fotoelectroquímica (*Figure 1.19*) mejorando la eficiencia energética global del proceso [8]; siendo mayor en el caso del  $\text{TiO}_2$  comparado con los otros óxidos metálicos ( $\text{Fe}_2\text{O}_3$  y  $\text{WO}_3$ ).

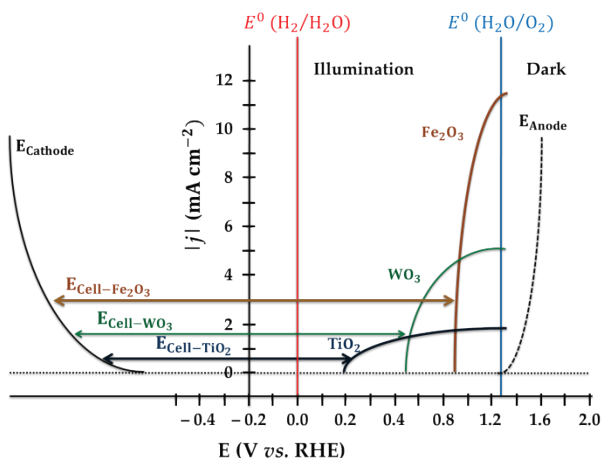


*Figura D.3.* Esquema mostrando el efecto cualitativo del potencial de inicio del fotoánodo en el rendimiento global del potencial en una celda PEC para los óxidos metálicos mencionados. La línea discontinua representa un ánodo en oscuridad.

### D.1.3. Electroreducción de $\text{CO}_2$ (Reacción Oscura)

La variedad de productos que se pueden obtener de la reducción de  $\text{CO}_2$  en medio acuoso va desde productos líquidos (ácido fórmico, diferentes alcoholes como isopropanol, metanol...), hidrocarburos de cadena corta (metano, etano, etileno) hasta monóxido de carbono que es un componente del gas de síntesis [9,10]. Sin embargo, el factor limitante en la reducción de  $\text{CO}_2$  es la formación del radical aniónico  $\text{CO}_2^{\cdot-}$  como especie intermedia la cual requiere un alto sobrepotencial, reduciendo la eficiencia del

proceso. Para la producción de hidrocarburos solo hay un metal con las propiedades adecuadas para que se dé lugar el proceso: el cobre (Cu) [11].

#### *D.1.4. Objetivos de la Tesis*

Esta tesis se ha desarrollado para comprobar el concepto de reducción del CO<sub>2</sub> a metano mediante un mecanismo fotocatalítico el cual mejora el balance energético total al reducir los valores de potencial requeridos. El trabajo desarrollado intenta primero usar las características de materiales fotoactivos nanoestructurados, permitiendo obtener mejoras en el área superficial como en la colección de fotones. En segundo lugar, se ha investigado cátodos de cobre y óxido de cobre para la electroreducción de CO<sub>2</sub> a metano. Como parte final, se ha realizado una evaluación de los requerimientos de potencial externo para una celda fotoelectroquímica completa usando estos fotoánodos y cátodos para la reducción de CO<sub>2</sub>.

## **D.2. Reacción Luminosa: Fotoánodos para la Ruptura de Agua.**

### *D.2.1. Nanotubos de Óxido de Titanio, TiNTs*

Este tipo de fotoánodos están basados en anatasa como principal estructura cristalográfica, obtenidos mediante anodización de una placa de titanio. Para mejorar la eficiencia en la absorción de energía solar se ha realizado un marcado de la superficie generando agujeros que actúan como trampas de luz y así

aumentando la superficie activa del material. Para ello en el proceso de anodización se han utilizado dos electrolitos orgánicos en dos pasos: en el primero, para generar los agujeros, se ha utilizado dimetilsulfóxido (DMSO) a diferentes voltajes (40, 50, 60 y 70 V); y en el segundo se ha usado etilenglicol para obtener nanotubos con una perfecta organización hexagonal a un mismo voltaje en todas las muestras (60 V), *Figura D.4.*

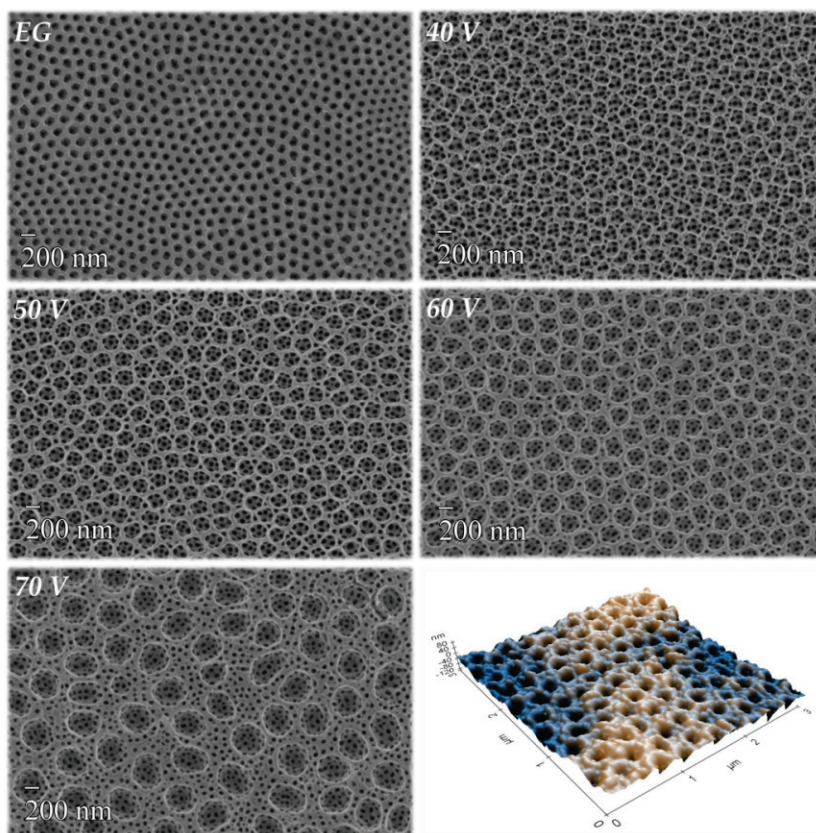


*Figura D.4.* Imágenes de SEM de las estructuras jerárquicas de nanotubos, junto con una imagen de AFM de la superficie de una muestra de titanio marcada por la anodización en DMSO.

Para estudiar el aumento de superficie en las muestras se ha realizado un modelo teórico, donde la muestra **40 V** llega a un aumento del 40% de superficie respecto a una muestra sin el tratamiento con DMSO. Para comprobar si la mejora superficial se traduce en un incremento en la fotoactividad se han realizado medidas ópticas y fotoelectroquímicas. En las medidas ópticas se ha observado una disminución de la reflexión en la zona de absorción del material, y en el caso de las de IPCE (eficiencia de los fotones incidentes sobre la generación de corriente, el cual determina el valor de la energía de los fotones para generar fotoelectrones a distintas longitudes de onda) aumentan los valores al realizar el tratamiento con DMSO, *Figura D.5*.

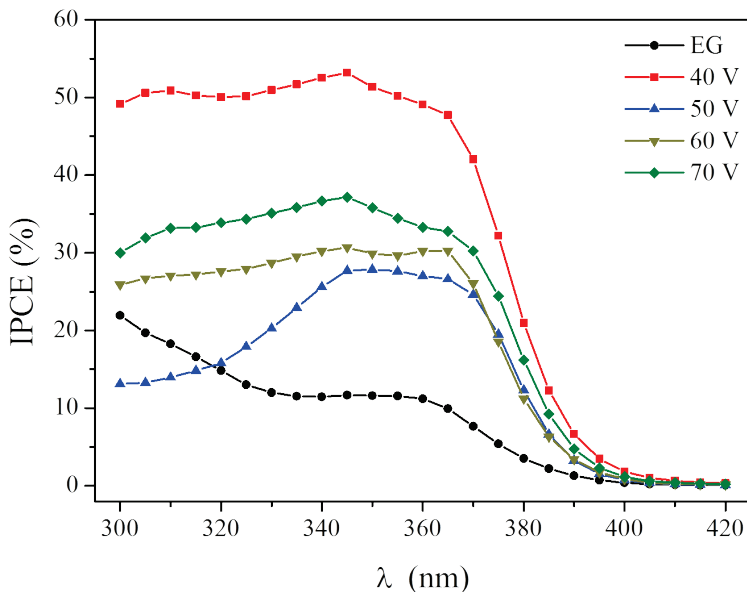


*Figura D.5.* IPCE de los nanotubos con estructuras jerárquicas medidas a 0.2 vs. Ag/AgCl en 1M de NaOH.

Tanto las medidas PEC como en el IPCE siguen la misma tendencia. Como se puede observar en la *Figura D.5*, la muestra **70 V** tiene un valor mayor que **50 V** y **60 V** (36% de aumento superficial para ambos) con un aumento de superficie menor (34%). En este caso, tanto para la muestra **40 V** como para **70 V** se ha encontrado una capa compacta de óxido al fondo de los nanotubos la cual mejora la adherencia y el contacto con el sustrato metálico, mejorando de este modo la colección de electrones fotogenerados [12], *Figura D.6*.

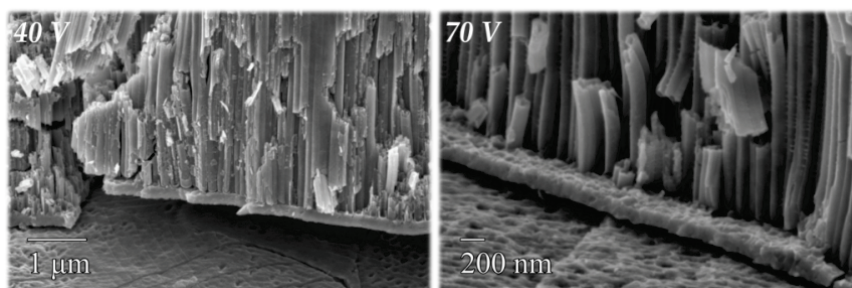


*Figura D.6.* Imágenes de SEM de las muestras 40 V y 70 V donde se puede observar la capa de óxido compacto entre el sustrato metálico y el fondo de los nanotubos.

### **D.2.2. Nanohilos de Óxido de Titanio**

Este tipo de fotoánodos se basan en rutilo como principal fase cristalina, obtenidos mediante síntesis hidrotérmal sobre un sustrato de vidrio conductor (FTO). En este caso, se ha realizado un estudio sobre dos condiciones de síntesis; la concentración inicial del precursor de titanio y el aumento de concentración de cloruros ( $\text{Cl}^-$ ) añadiendo  $\text{CaCl}_2$ .

En la primera condición de síntesis se han fijado tres parámetros; la acidez del medio (50:50, HCl: H<sub>2</sub>O), la temperatura de horno (200°C) y el tiempo de síntesis (4h). Las concentraciones de precursor de titanio utilizadas fueron 40, 50, 60 y 70 mM, *Figura D.7.*

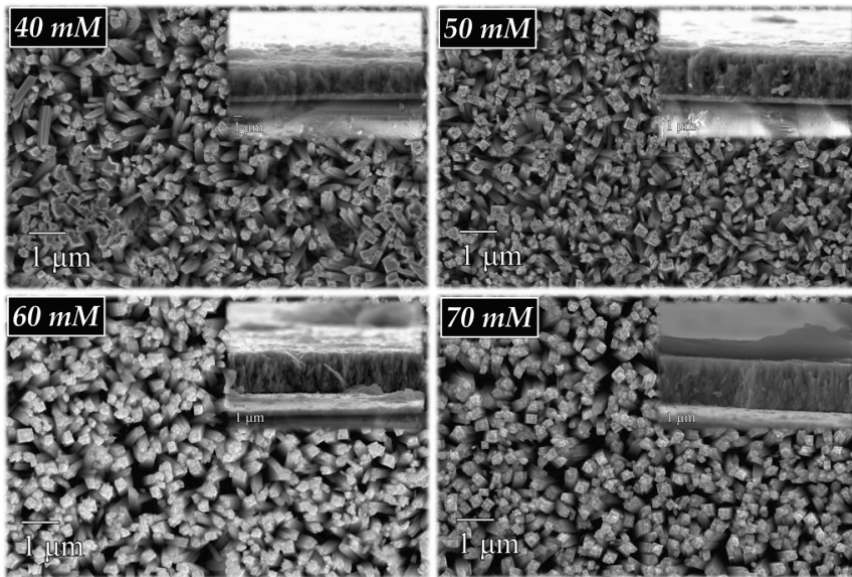


*Figura D.7.* Imágenes de SEM de la sección transversal y vista desde arriba de los nanohilos de TiO<sub>2</sub> usando diferentes concentraciones de precursor.

La actividad fotoelectroquímica (*Figura D.8*) se ha podido observar mediante una voltamperometría de barrido lineal (LSV) bajo un sol de potencia de iluminación (100 mW cm<sup>-2</sup>, AM 1.5G), utilizando dos modos de iluminación, trasera (a través del FTO, *Back*) y delantera (*Front*).

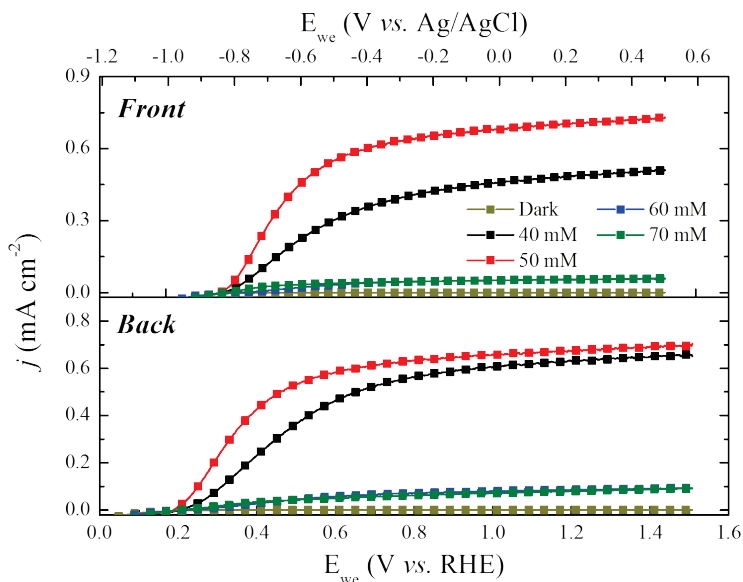


**Figura D.8.** LSV medido a una velocidad de escaneo de  $20 \text{ mV s}^{-1}$  en oscuridad y bajo iluminación desde la parte frontal y la trasera de la muestra en  $1\text{M}$  de  $\text{NaOH}$ .

La muestra de  $50 \text{ mM}$  tanto en la configuración trasera como frontal obtiene el valor más alto respecto al resto de muestras.

La segunda condición de síntesis bajo estudio, es el aumento de la concentración de cloruros para controlar el grosor y la longitud de los nanohilos. Para ello se han añadido diferentes concentraciones de  $\text{CaCl}_2$ ,  $0.25$ ,  $0.5$  y  $1 \text{ M}$ . Con estos experimentos se ha podido observar la reducción del borde de los nanohilos, la densidad y el grosor de la capa como la reducción de la fotoactividad con el aumento de la concentración.

Se ha podido observar también que los cloruros ralentizan el crecimiento de los nanohilos, necesitando más tiempo de síntesis. Por este motivo, se realizaron unas síntesis usando únicamente  $0.25$

y 0.5 M de  $\text{CaCl}_2$  para observar si con el aumento del tiempo se mejoraba la densidad de corriente fotogenerada. En este caso, se encontró que solo usando 0.5 M mejoran los valores de densidad de corriente fotogenerada.

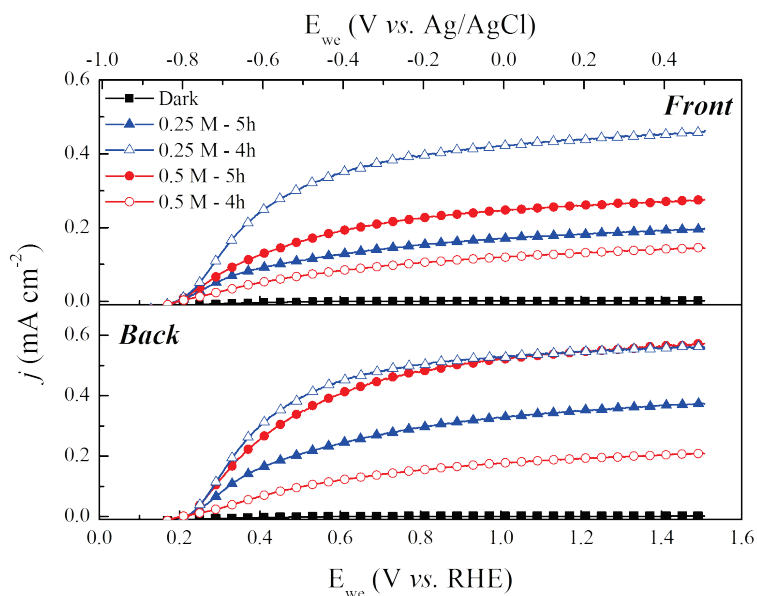


**Figura D.9.** LSV a  $20 \text{ mV s}^{-1}$  comparando las muestras con 0.25 y 0.5 M de  $\text{CaCl}_2$  con 4 y 5h de síntesis hidrotérmica en 1M de NaOH.

### D.2.3. Dopaje de Nanohilos

Para la mejora de la fotoactividad en los nanohilos de  $\text{TiO}_2$  usando la síntesis hidrotérmica se ha intentado incorporar estaño (Sn) y vanadio (V). En el caso del Sn, la mejora a los nanohilos se focaliza en incrementar la conductividad del material y así reduciendo el proceso de recombinación [13–16]. Pero en este caso no se obtuvo ninguna mejora en las densidades de corriente

fotogeneradas. Únicamente se pudo observar el efecto de la modificación del pH sobre el crecimiento de los nanohilos.

La idea de incorporar vanadio en la estructura del material es para reducir el ancho de banda prohibida (bandgap) del  $\text{TiO}_2$  y así poder mejorar la absorción en la parte visible del espectro [17]. En este caso, se prepararon tres disoluciones para la síntesis hidrotermal con diferentes proporciones molares de los respectivos precursores: Ti:V (1:0.5, 1:1, 1:2). Con esta síntesis la morfología de los nanohilos se modificó, pasando de una aspecto cuadrado a más redondeado, *Figura D.10*.

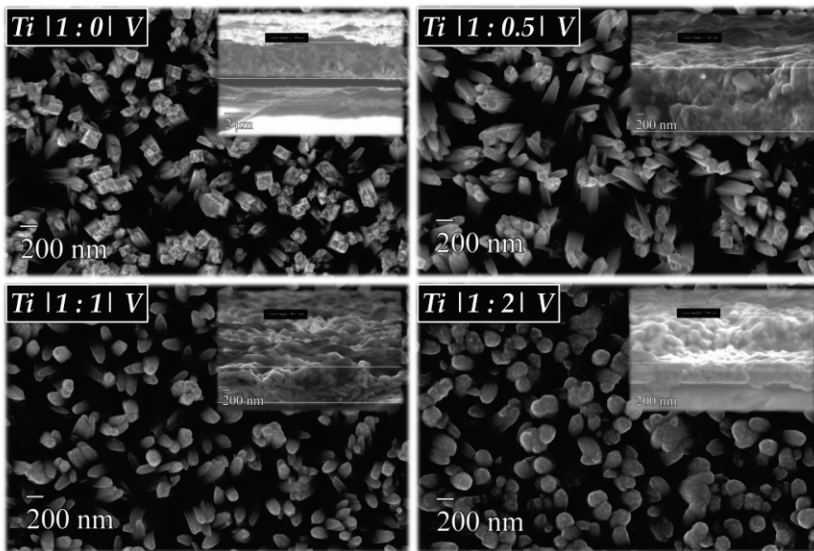


*Figura D.10.* Imágenes de la sección transversal y vista desde arriba obtenida por SEM de los nanohilos obtenidos con los diferentes ratios molares de vanadio: titanio.

Para determinar si se obtuvo alguna mejora en la actividad de los nanohilos sintetizados, se realizaron medidas ópticas, fotoelectroquímicas y de IPCE. Los resultados en las medidas

ópticas no dieron ninguna absorción en la parte del visible, en cambio, en las PEC e IPCE se dio una disminución de los valores a medida que se aumenta la proporción de vanadio.

Para Sn y V, no se ha encontrado ninguna mejora en la fotoactividad del material. Esto se debe a la generación de un potencial de banda plano (flat band) donde los electrones y huecos fotogenerados se recombinan rápidamente, reduciendo la eficiencia del material. En el caso del vanadio, se genera una zona de deplexión muy ancha [18] en la cual no se puede realizar una separación eficiente del par electrón–hueco los cuales se generan en la superficie con una alta probabilidad de que se dé el proceso de recombinación. A parte la presencia de especies de  $V^{5+}$  que actúan como centros de recombinación reducen aún más la fotoactividad del material.

Otro método para el dopaje de los nanohilos es mediante tratamientos térmicos de amoníaco (dopaje con nitrógeno) [19–21]. Con este método si se ha conseguido una mejora en la actividad fotoelectroquímica del material. Para la muestra obtenida a 300°C tanto el valor de IPCE como de densidad de corriente ( $0.8 \text{ mA cm}^{-2}$  at 1.23 V *vs.* RHE) son máximos respecto al resto (400, 500°C y sin tratamiento), *Figura D.11*.

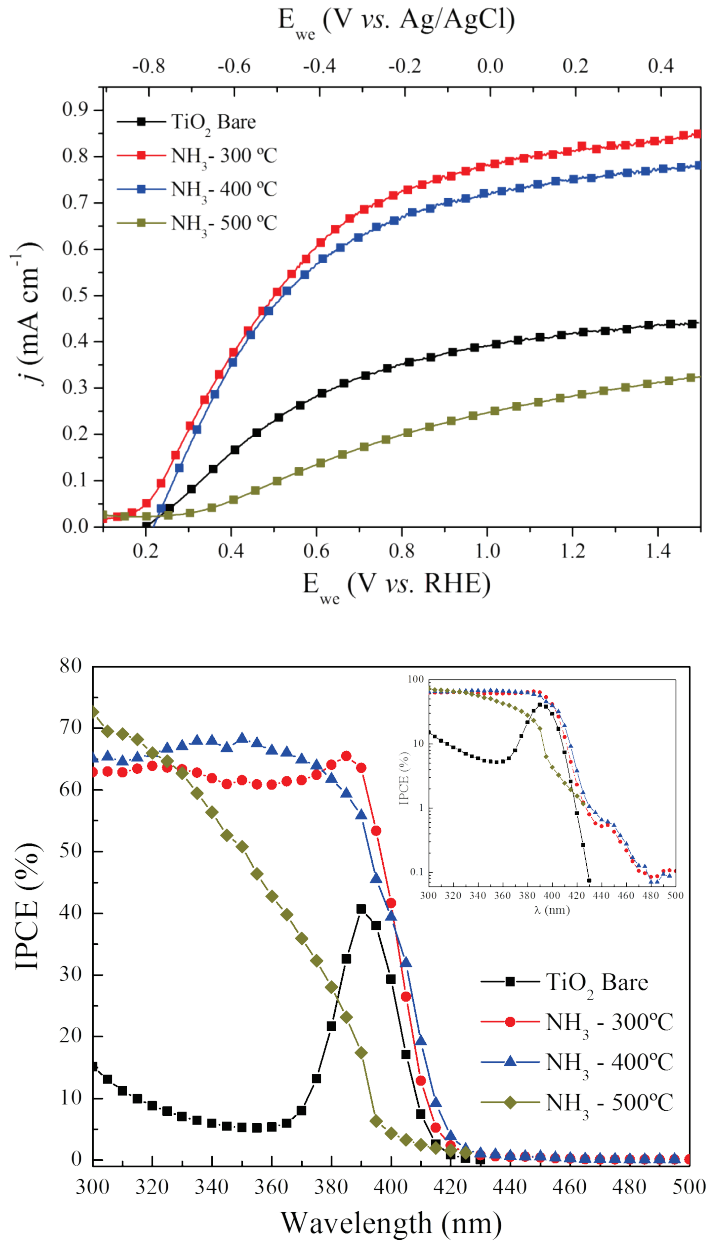


**Figura D.11.** El Gráfico de arriba corresponde a medidas LSV de las muestras tratadas con amoníaco y con la muestra blanco. En el de abajo está el IPCE obtenido a 0 V vs. Ag/AgCl de las mismas muestras.

En el caso de la muestra tratada a 500°C, la actividad decae debido a que los portadores de carga se incrementan mucho y el nivel de Fermi se puede introducir en la banda de conducción moviendo la banda absorción a niveles energéticos más altos, reduciendo la fotoactividad del material.

Para el tratamiento con amoníaco se dan tres opciones dependiendo del nivel de densidad de portadores:

(a) Cuando la densidad de portadores es baja, hay una reducción en la caída máxima de potencial dentro del semiconductor. En este caso la eficiencia en la separación de cargas es baja y los procesos de recombinación superficiales como las cinéticas de las reacciones inversas (back reactions) son más rápidas para los portadores fotogenerados cerca de la superficie. Por lo tanto, para longitudes de onda largas los portadores fotogenerados son separados eficientemente debido a que el material está completamente deplectado.

(b) En el caso de que la densidad de portadores sea media, hay una menor anchura en la capa de separación de carga, los nanohilos no están completamente deplectados y la aproximación de electrodo plano es válida pudiendo obtener valores mayores en la caída máxima de potencial. Este hecho, más el decrecimiento de la densidad de trampas electrónicas, debido a que la posición del nivel de Fermi se mueve cerca de la banda de conducción, permite una mejor separación de cargas.

(c) Para altas densidades de portadores, la anchura de la zona de depleción está más localizada cerca de la superficie y como consecuencia los portadores de carga fotogenerados son

eficientemente separados a longitudes de onda cortas. En cambio a longitudes de onda mayores los electrones y huecos son fotogenerados fuera de la zona de depleción. Con un alto nivel de dopaje, el nivel de Fermi eventualmente se junta con la banda de conducción en cierta medida ( $\xi$ ) mientras que los estados por debajo de este nivel energético se llenan, las transiciones electrónicas a estados por debajo de  $E_g + \xi$  están prohibidas, por lo tanto el borde de la banda de absorción debería moverse a energías mayores (efecto de Burstein – Moss)[22].

### **D.3. Reacción Oscura: Electroreducción de CO<sub>2</sub> con Electrodo Basado en Cobre**

En este caso, se ha realizado un estudio de la reducción electroquímica del CO<sub>2</sub> usando cátodos de cobre en una configuración de electrodos de difusión de gas (GDE) con dos pretratamientos previos: químico (disolución HCl:H<sub>2</sub>O, 3:1) y electropulido en H<sub>3</sub>PO<sub>4</sub> (85%) [9,23]. En principio se ha realizado un estudio del efecto de los cationes (K<sup>+</sup> y Na<sup>+</sup>) de los electrolitos acuosos utilizados. En el primer caso se ha enfocado el estudio en el cátodo de cobre metálico electropulido debido al interés en la producción de metano [11]. En estos experimentos se ha podido observar como la reacción llevada a cabo en el electrolito con potasio, mejora la eficiencia farádica y reduce el potencial requerido para la reacción de reducción de CO<sub>2</sub>, *Figura D.12*.

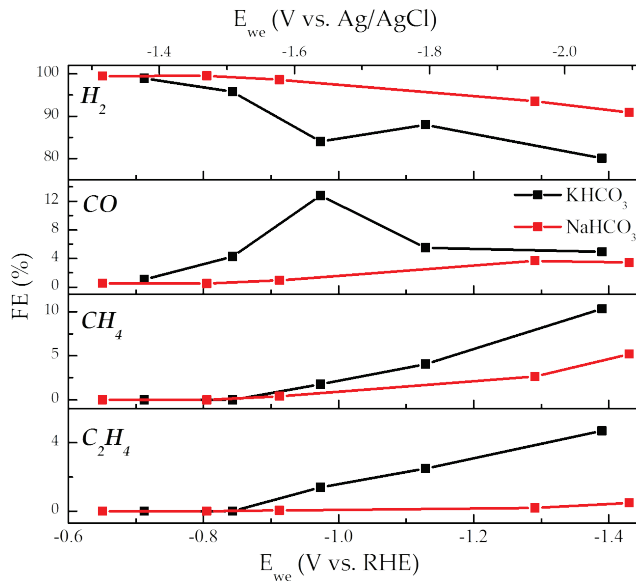


**Figura D.12.** Comparativa de las eficiencias farádicas de los productos carbonosos obtenidos en la reducción electroquímica del  $CO_2$  usando una malla de cobre como GDE en hidrogeno carbonato de potasio y sodio como electrolito.

El efecto de los iones sobre la capa de Helmholtz generada en la superficie del electrodo tiene la habilidad de estabilizar el  $CO_2$  absorbido, **Figura D.13**.

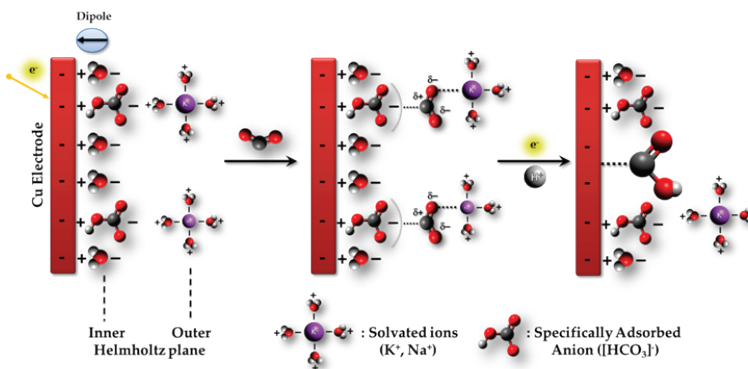


**Figura D.13.** Atracción del  $CO_2$  por la doble capa electrónica y formación del radical formiato debido al mecanismo de esfera interna propuesto por Ogura [24] adaptado para los iones que se han utilizado en estos experimentos.

En el caso del sodio, debido a la alta característica polarizante del catión, el agua se coordina fuertemente, bloqueando la coordinación del  $\text{CO}_2$ , desfavoreciendo su estabilización. En cambio para el potasio el agua se coordina débilmente pudiéndose desorber fácilmente, permitiendo una mejor estabilización del  $\text{CO}_2$  y por ello la eficiencia farádica se incrementa además de desplazar el potencial a valores más positivos. Otro experimento se ha realizado usando una placa de cobre de alta pureza con una configuración diferente al GDE. En este caso el método de inyección de  $\text{CO}_2$  ha sido mediante burbujeo constante en el electrolito para poder mantener constante la concentración de  $\text{CO}_2$ . Con este tipo de electrodo se ha podido llegar a una eficiencia farádica de un 20% para metano.

Los potenciales necesarios en el caso de cobre metálico son muy altos para obtener una eficiencia farádica razonable, haciéndolo energéticamente inviable. Por ello se ha cambiado al siguiente tipo de cátodos utilizados, una malla de cobre oxidada mediante tratamiento térmico, el interés en el uso de óxido de cobre es la reducción del valor de potencial necesario para la reducción electroquímica del  $\text{CO}_2$ . Para este caso los potenciales se han reducido 0.2 V con  $\text{NaHCO}_3$  y para  $\text{KHCO}_3$  se ha desplazado 0.4 V (vs. RHE) hacia valores más positivos, *Figura D.14*.

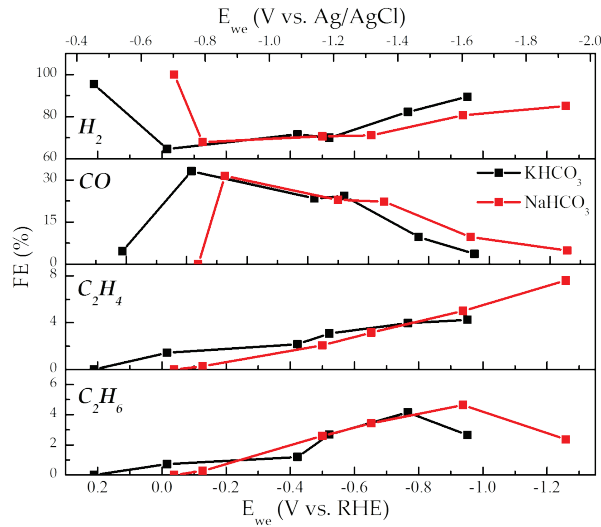


**Figura D.14.** Gráfico comparativo de las eficiencias farádicas obtenidas usando un electrodo de óxido de cobre en la configuración GDE en electrolitos de sodio (línea roja) y potasio (línea negra).

Utilizando estos electrodos de óxido de cobre, la reducción de  $\text{CO}_2$  no comienza hasta que la capa de óxido es reducida [25–27] hasta llegar a una superficie de cobre activada ( $\text{Cu}^0$ ). Sin embargo, la selectividad de estos cátodos cambia, obteniendo etileno y etano en vez de metano.

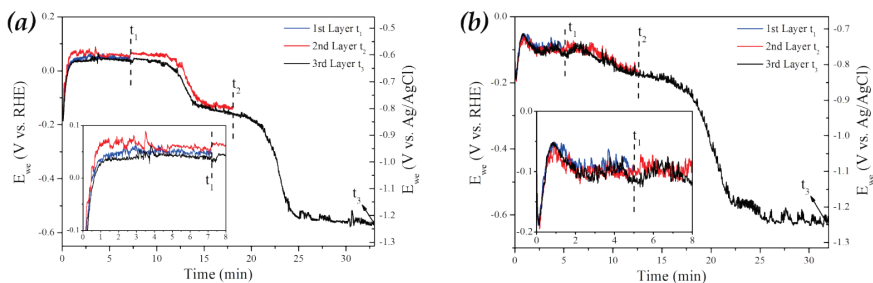


**Figura D.15.** Experimentos cronopotenciométricos (CP) para observar la reducción de la capa óxido de cobre en, (a) electrolito de potasio y (b) electrolito de sodio, parado a 9, 19 y 32 min que corresponden con  $t_1$ ,  $t_2$  y  $t_3$  respectivamente.

La reducción de la capa de óxido de cobre se ha estudiado a parte debido a que usando el electrolito de sodio la existe un efecto que ayuda a la reducción de la capa de óxido, que en el electrolito de potasio no aparece, *Figura D.15*.

La razón de este efecto viene dado por la intercalación de los cationes de sodio en la estructura del CuO [28–30]. El sodio al tener un menor radio se puede introducir en la estructura del óxido permitiendo ayudar en la reducción de la capa de óxido de cobre (II) hasta llegar a una capa fina estable de Cu<sub>2</sub>O [31–33], que es el responsable de la selectividad hacia C<sub>2</sub>H<sub>4</sub> en vez de CH<sub>4</sub>.

Por último, se ha estudiado el efecto de la solvatación de la molécula de CO<sub>2</sub> [34–40] previa inyección en la celda electroquímica. El enlace de la molécula de CO<sub>2</sub> se puede doblar cuando dos moléculas de agua se coordinan mejorando la absorción del CO<sub>2</sub> como la generación de especies carbonato/bicarbonato. Estas especies basadas en carbonatos son necesarias para reducir la energía de activación del proceso, mejorando así la eficiencia como el desplazamiento del potencial de trabajo a valores más positivos.

#### **D.4. Ensamblado de la Celda PEC**

Para poder evaluar el rendimiento y el aporte de la integración de los fotoánodos, es necesario tener en cuenta el consumo energético del proceso de electroreducción de CO<sub>2</sub>. En la *Figura D.16* se puede observar el potencial externo necesario para la conversión de CO<sub>2</sub> a metano para el caso de los electrodos de cobre y etileno para los de óxido de cobre, como productos principales.

En el rango de mayor eficiencia farádica el potencial esta entre -1.1 to -1.40 V *vs.* RHE, y el potencial de celda requerido esta entre -3 and -5 V, y para el óxido de cobre el potencial del cátodo está entre -0.70 to 1.25 V *vs.* RHE y el de celda entre -2.5 to -5 V.

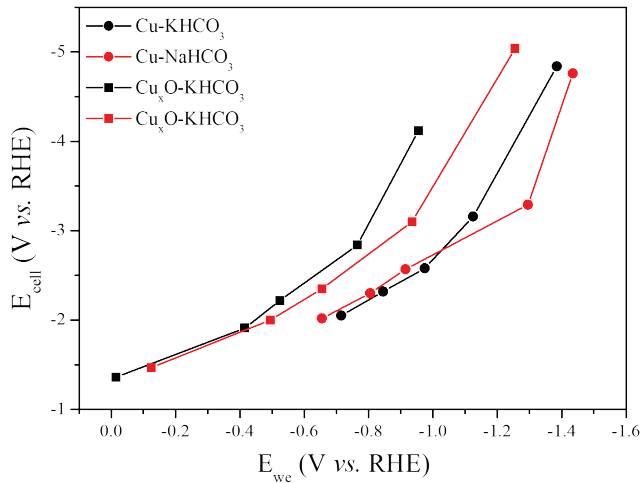


**Figura D.16.** Polarización de celda necesaria para los electrodos basados en cobre bajo estudio usando un electrodo comercial (DSA) en oscuridad.

Cuando se realiza una evaluación teórica de los valores de potencial donde el fotoánodo tiene mayor eficiencia (en este caso la muestra de nanohilos NH<sub>3</sub> – 300°C) es posible obtener el valor del potencial externo necesario utilizando la mejora proveniente de la iluminación en la celda de electrólisis (*Tabla D.4.1*), el rango de voltaje requerido esta entre 1–1.7 V usando un sol de potencia (100 mW cm<sup>-2</sup>).

*Tabla D.4.1. Valores de potenciales de trabajo de los electrodos estudiados y potencial de celda fotoelectroquímica óptimo para la reducción de CO<sub>2</sub>.*

WE	E <sub>we</sub> (V) vs. Ag/AgCl (pH 7.8)	E <sub>fotoánodo a máx eff.</sub> (V) vs. Ag/AgCl (pH 13.6)	E <sub>cell</sub> (V) óptima
Cu – KHCO <sub>3</sub>	-2.05	-0.43	-1.62
	-1.77	(0.58 vs. RHE)	-1.34
Cu – NaHCO <sub>3</sub>	-2.10	-0.43	-1.67
	-1.96		-1.53
Cu <sub>x</sub> O – KHCO <sub>3</sub>	-1.62	-0.43	-1.19
	-1.43		-1.00
Cu <sub>x</sub> O – NaHCO <sub>3</sub>	-1.92	-0.43	-1.49
	-1.60		-1.17

Relacionado con el consumo energético global, para una eficiencia farádica del 100% a metano en el caso de cobre metálico y etileno para óxido de cobre, el consumo energético por mol estaría entre 46 y 54 W h mol<sup>-1</sup> y 36 y 49 W h mol<sup>-1</sup> para el metano y etileno producido respectivamente, utilizando nanohilos de TiO<sub>2</sub> como fotoánodos.

## D.5. Conclusiones

El trabajo desarrollado en esta tesis se ha centrado en el estudio de diferentes **nanoestructuras** para preparar **fotoánodos** basados en TiO<sub>2</sub>, y explorando el comportamiento de **cátodos** basados en **cobre** para la **reducción electroquímica del CO<sub>2</sub>**, como su implementación y evaluación en una celda fotoelectroquímica (PEC) completa, teniendo en cuenta los aspectos tecnológicos,

experimentales y teóricos. Los logros más relevantes obtenidos se muestran a continuación.

Síntesis de estructuras **jerárquicas basadas en TiNTs** mediante anodización, usando dos electrolitos orgánicos para mejorar la fotoactividad.

- Se ha realizado una mejora sobre los TiNTs (anatasa) mediante un marcado de la superficie de la placa de Ti, los **agujeros generados hacen de centros trampa para la luz**. Para calcular el aumento de superficie por parte de la primera anodización se ha postulado un **modelo teórico**. Para la muestra **40 V** se obtuvo un **incremento de superficie de un 40%** respecto a la muestra plana. Relacionado con este incremento, los valores de densidad de corriente medidos por LSV e IPCE para la muestra **40 V** obtiene los valores más altos seguido de la muestra **70 V**.
- Se ha observado la generación de una **capa compacta de óxido** al final de los TiNTs que mejora el contacto con el sustrato. Esta capa únicamente aparece para las muestras **40 V** y **70 V**. En el caso de la muestra **40 V** el incremento de la superficie activa más la generación de esta capa de óxido da lugar a la mayor mejora en la fotoactividad. A continuación le sigue la muestra **70 V** ya que tiene esta capa de óxido obteniendo mejor fotoactividad que las muestras **50** and **60 V** que tienen un incremento de superficie algo mayor.

**Fabricación y evaluación** de las condiciones de síntesis de **nanohilos de TiO<sub>2</sub>** mediante síntesis hidrotermal.

- La concentración inicial del precursor de Ti se ha modificado para estudiar el efecto sobre la morfología y fotoactividad de los nanohilos. Las concentraciones de **butóxido de titanio** utilizadas han sido 40, 50, 60 and 70 mM en una solución acuosa a pH ácido (50:50, HCl:H<sub>2</sub>O). La temperatura y el tiempo utilizados para la síntesis hidrotérmal se fijaron para todos los experimentos (200°C, durante 4h). En las medidas de LSV la muestra con **50 mM** en ambas configuraciones de iluminación (trasera o delantera) llegaron a los valores más altos de las muestras estudiadas, seguida de la de **40 mM**.
- La siguiente condición de síntesis fue la modificación de la concentración de iones **Cl<sup>-</sup>**. Las concentraciones utilizadas en este caso fueron 0.25, 0.5 and 1 M de CaCl<sub>2</sub> reduciendo el tamaño del borde, la densidad y el grosor de capa de los nanohilos. También se observó la reducción de la fotoactividad al aumentar la concentración de cloruros. Además en presencia de cloruros el tiempo de crecimiento de los nanohilos se ve aumentado, por lo tanto se realizaron síntesis más largas (5h) únicamente a dos concentraciones 0.25 y 0.5 M obteniendo capas más gruesas con nanohilos más grandes. Pero únicamente en el caso de **0.5 M** se encontró una mejora en la densidad de corriente, aproximadamente el doble respecto a 4h. Utilizando 0.5 M ha permitido utilizar **mayores tiempos de síntesis** hidrotérmal debido a la reducción en la velocidad de crecimiento, pudiendo **mejorar los valores** de densidades de corriente fotogeneradas.

**Dopaje de nanohilos de TiO<sub>2</sub>** mediante síntesis hidrotermal o **tratamiento térmico** en amoníaco para mejorar la fotoactividad del material.

- Para mejorar la cantidad de **Sn** que se quiere incorporar a la estructura, el pH de la solución de síntesis hidrotermal se redujo. Las proporciones de HCl:H<sub>2</sub>O usados fueron: 50:50, 40:60 and 30:70. En este caso, no se observó ninguna incorporación de Sn y las densidades de corriente medidas se redujeron respecto a la muestra sin Sn. El único efecto encontrado fue la modificación del **crecimiento de los nanohilos de TiO<sub>2</sub>** al **modificar el pH**.
- Usando **Vanadio** es posible reducir el ancho de la banda prohibida del TiO<sub>2</sub>, mejorando la absorción del material en el **rango del visible**. Aparte, la morfología de los nanohilos obtenidos se modificó, pasando de un aspecto cuadrático a más redondeado. Los valores de densidad de portadores se vieron reducidos al incrementar el dopaje de vanadio, traducándose esto a una peor conductividad en el material reduciendo la fotoactividad del mismo. La posible presencia de estados de V<sup>5+</sup> actuando como centros de recombinación y añadido al hecho de la baja eficiencia en la separación del par electrón–hueco generado en la superficie del material debido a la generación de una **zona de depleción** muy ancha para esta muestra, el cual genera un **bajo campo eléctrico** que a su vez genera una baja separación electrón–hueco, dando lugar a una rápida recombinación entre ambos. Por este motivo, la caída en la fotoactividad con el aumento del

dopaje es muy pronunciada. En el caso del valor del potencial de la banda plana (*Flat Band*), va hacia valores más positivos correspondiendo con el desplazamiento en el potencial de inicio (*onset potential*) de las muestras en las medidas fotoelectroquímicas.

- **Los tratamientos con amoníaco** mejoran la eficiencia en los nanohilos de TiO<sub>2</sub>. En este caso, se han introducido una mayor cantidad de estados superficiales activos, los cuales incrementan el tiempo de vida medio de los huecos, mejorando la actividad fotoelectroquímica. Para la muestra tratada a 300°C se ha alcanzado el máximo valor de IPCE respecto a las demás, como en la densidad de corriente (**0.8 mA cm<sup>-2</sup> a 1.23 V vs. RHE**). Los tratamientos con amoníaco generan un doblado de banda (**band bending**) el cual mejora la separación del par electrón–hueco evitando la recombinación. Aparte en este caso la zona de depleción (**depletion región width**) tiene un tamaño óptimo el cual genera un alto campo eléctrico, mejorando también la separación del par electrón–hueco y como consecuencia mejorando la fotoactividad.

Efecto de los electrolitos de hidrógeno carbonato de K<sup>+</sup> y Na<sup>+</sup> en la **reducción de CO<sub>2</sub>** utilizando **electrodos basados en cobre**.

- **Electrodos de cobre metálico** se han estudiado para la producción de metano. En estos experimentos se ha observado como el electrolito de potasio mejora las eficiencias farádicas y reduce el potencial en la reacción de

reducción de  $\text{CO}_2$ . A parte se ha utilizado un cátodo de cobre de alta pureza en una configuración diferente a la GDE (el  $\text{CO}_2$  se ha burbujeado constantemente en el electrolito) obteniendo la máxima eficiencia farádica obtenida para la producción de metano con este tipo de electrodos, **20%**.

- **Electrodos de óxido de cobre** se han seleccionado para poder **reducir los potenciales necesarios** para la reducción electroquímica del  $\text{CO}_2$ . Para estos cátodos los potenciales se reducen 0.2 V en  $\text{NaHCO}_3$  y para  $\text{KHCO}_3$  el potencial se desplaza 0.4 V (vs. RHE) a valores más positivos respecto a los de cobre metálico. Sin embargo, la **selectividad** de estos cátodos va hacia **etileno** y **etano** suprimiendo la producción de metano.
- Un efecto observado en **cátodos de óxido de cobre** es la **reducción de la capa de óxido** generada hasta un **cobre activado ( $\text{Cu}^0$ )**. En el electrolito con sodio la reducción de esta capa de óxido se ve favorecida debido a la posible **intercalación de los cationes de sodio en la estructura del  $\text{CuO}$** . El sodio al tener un radio más pequeño que el potasio se puede introducir en la estructura del óxido de cobre ayudando en la reducción de la capa de óxido hasta una **capa fina** estable de  **$\text{Cu}_2\text{O}$** , pudiendo ser el responsable de la **selectividad** hacia  **$\text{C}_2\text{H}_4$**  en vez de  **$\text{CH}_4$** .

**Efecto de solvatación de la molécula de  $\text{CO}_2$** , a la entrada en la celda electroquímica, en la eficiencia de reducción de  $\text{CO}_2$ .

- El ángulo de enlace de la molécula de CO<sub>2</sub> se puede doblar al coordinarse dos moléculas de agua, mejorando la absorción de la molécula y la generación de especies carbonato/bicarbonato. En el caso del cobre metálico, únicamente en el electrolito de potasio la solvatación de la molécula de CO<sub>2</sub> da lugar a un efecto positivo en la eficiencia de la producción de metano como en los valores de potencial de trabajo. Sin embargo, para el óxido de cobre el efecto va en el sentido opuesto para potasio. En cambio para el electrolito con sodio el potencial de trabajo va hacia valores más positivos y se puede observar un aumento en la eficiencia farádica para el etileno y etano.

Finalmente se ha presentado la posibilidad de **ensamblado de la celda fotoelectroquímica (PEC) completa** con los electrodos estudiados.

- Se ha realizado una evaluación de potencial de trabajo del fotoánodo donde la eficiencia es máxima, para la muestra **tratada en amoníaco a 300°C** es a **0,58 V vs. RHE**. Después, se han evaluado los potenciales de trabajo de los cátodos de cobre donde la eficiencia para la reducción de CO<sub>2</sub> es más alta. Para el **cobre metálico** los potenciales están entre **-1.38 to 1.10 V vs. RHE** y para el **óxido de cobre** entre **-1.25 to -0.76 V vs. RHE**. Por último, se ha realizado la evaluación de los requerimientos energéticos necesarios (valor de potencial externo necesario) para el ensamblado de ambos electrodos en la celda completa. Hablando en términos de consumo

energético, para el caso de una eficiencia farádica del 100% a metano y etileno para cobre metálico y óxido de cobre respectivamente (sin la evolución de hidrógeno como reacción competitiva), el **consumo de energía por mol** estaría entre **46 y 54 Wh mol<sup>-1</sup>** y **36 y 49 Wh mol<sup>-1</sup>** para la producción de **metano** y **etileno** producido en cada electrodo respectivamente, utilizando el fotoánodo de **nanohilos de TiO<sub>2</sub>**.

## D.6. Bibliografia

- [1] OECD/IEA. *Redrawing the Energy-Climate Map: World Energy Outlook Special Report*. Paris: **2013**.
- [2] OECD/IEA. *Southeast Asia Energy Outlook: World Energy Outlook Special Report*. Paris: **2013**.
- [3] Styring P., Jansen D., de Coninck H., Reith H., Armstrong K. *Carbon Capture and Utilisation in the green economy*. **2011**.
- [4] Cuéllar-Franca R.M., Azapagic A. *J CO2 Util.* **2015**, 9, 82.
- [5] Ohtani B. *Catalysts*. **2013**, 3, 942.
- [6] Mor G.K., Shankar K., Paulose M., Varghese O.K., Grimes C.A. *Nano Lett.* **2005**, 5, 191.
- [7] Scanlon D.O., Dunnill C.W., Buckeridge J., Shevlin S.A., Logsdail A.J., Woodley S.M., et al. *Nat Mater.* **2013**, 12, 798.
- [8] Walter M.G., Warren E.L., McKone J.R., Boettcher S.W., Mi Q., Santori E.A., et al. *Chem Rev.* **2010**, 110, 6446.
- [9] Kuhl K.P., Cave E.R., Abram D.N., Jaramillo T.F. *Energy Environ Sci.* **2012**, 5, 7050.
- [10] Kuhl K.P., Hatsukade T., Cave E.R., Abram D.N., Kibsgaard J., Jaramillo T.F. *J Am Chem Soc.* **2014**, 136, 14107.
- [11] Hori Y., Kikuchi K., Suzuki S. *Chem Lett.* **1985**, 1695.
- [12] Yu D., Zhu X., Xu Z., Zhong X., Gui Q., Song Y., et al. *ACS Appl Mater Interfaces.* **2014**, 6, 8001.
- [13] Sayilkan F., Asiltürk M., Tatar P., Kiraz N., Şener Ş., Arpaç E., et al. *Mater Res Bull.* **2008**, 43, 127.
- [14] Vinodgopal K., Bedja I., Kamat P. V. *Chem Mater.* **1996**, 8, 2180.
- [15] Bedja I., Kamat P. V. *J Phys Chem.* **1995**, 99, 9182.
- [16] Pan J., Hühne S.-M., Shen H., Xiao L., Born P., Mader W., et al. *J Phys Chem C.* **2011**, 115, 17265.
- [17] Zhao G., Kozuka H., Lin H., Yoko T. *Thin Solid Films.* **1999**, 339, 123.
- [18] Albery W.J. *J Electrochem Soc.* **1984**, 131, 315.
- [19] Asahi R., Morikawa T., Ohwaki T., Aoki K., Taga Y. *Science.* **2001**, 293, 269.
- [20] Livraghi S., Paganini M.C., Giamello E., Selloni A., Di Valentin C., Pacchioni G. *J Am Chem Soc.* **2006**, 128, 15666.
- [21] Finazzi E., DiValentin C., Selloni A., Pacchioni G. *J Phys Chem C.* **2007**, 111, 9275.

- [22] Burstein E. *Phys Rev.* **1954**, 93, 632.
- [23] Chen C.S., Handoko A.D., Wan J.H., Ma L., Ren D., Yeo B.S., et al. *Catal Sci Technol.* **2014**, 2.
- [24] Ogura K. *J CO2 Util.* **2013**, 1, 43.
- [25] Nie X., Griffin G.L., Janik M.J., Asthagiri A. *Catal Commun.* **2014**, 52, 88.
- [26] Nakayama S., Kimura A., Shibata M., Kuwabata S., Osakai T. *J Electrochem Soc.* **2001**, 148, B467.
- [27] Nakayama S., Kaji T., Shibata M., Notoya T., Osakai T. *J Electrochem Soc.* **2007**, 154, C1.
- [28] Chen K., Song S., Xue D. *CrystEngComm.* **2015**, 17, 2110.
- [29] Lu Y., Zhang N., Zhao Q., Liang J., Chen J. *Nanoscale.* **2015**, 7, 2770.
- [30] Wang L., Zhang K., Hu Z., Duan W., Cheng F., Chen J. *Nano Res.* **2014**, 7, 199.
- [31] Chang T.-Y., Liang R.-M., Wu P.-W., Chen J.-Y., Hsieh Y.-C. *Mater Lett.* **2009**, 63, 1001.
- [32] Shin H.S., Song J.Y., Yu J. *Mater Lett.* **2009**, 63, 397.
- [33] Ko C.K., Lee W.G. *Surf Interface Anal.* **2010**, 42, 1128.
- [34] Ha T.K. *J Am Chem Soc.* **1984**, 106, 599.
- [35] Jonsson B., Karlstrom G., Wennerstrom H., Forsen S., Roos B., Almlöf J. *J Am Chem Soc.* **1977**, 99, 4628.
- [36] Merz K.M. *J Am Chem Soc.* **1990**, 112, 7973.
- [37] Jönsson B., Karlström G., Wennerström H. *Chem Phys Lett.* **1975**, 30, 58.
- [38] Peterson K.I., Klemperer W. *J Chem Phys.* **1984**, 80, 2439.
- [39] Damewood J.R., Kumpf R.A., Muhlbauer W.C.F. *J Phys Chem.* **1989**, 93, 7640.
- [40] Zhang N.R., Shillady D.D. *J Chem Phys.* **1994**, 100, 5230.



## **Financial Support Acknowledgments**

I gratefully acknowledge IREC fellowship that made this doctoral project possible. The work was partially supported by MINECO project ENE2012-3651, the European Regional Development Funds (FEDER), the Framework 7 program under the projects CEOPS (FP7-NMP-2012-309984), SOLAROGENIX (FP7-NMP-2012-310333) and Repsol, SA.

# Scientific Contributions

## Patent

1. M.D. Hernandez-Alonso; G. Penelas; T. Andreu; E. Irtem; A. Parra; C. Fàbrega; J. R. Morante. *Photoelectrochemical Cell*. Europe Patent Council (EPC), 1360 (EP14382541.2), Appl. 14382541.2, 19 December 2014. Repsol S.A.

## Publications

1. Fàbrega C., Monllor-Satoca D., Ampudia S., Parra A., Andreu T., Morante J.R. "Tuning the Fermi Level and the Kinetics of Surface States of TiO<sub>2</sub> Nanorods by Means of Ammonia Treatments". *J. Phys. Chem. C*. 2013, 117, 20517. (DOI: 10.1021/jp407167z).
2. Fan J., Fàbrega C., Zamani R.R., Hao Y., Parra A., Andreu T., et al. "Enhanced Photovoltaic Performance of Nanowire Dye-Sensitized Solar Cells Based on Coaxial TiO<sub>2</sub>@TiO Heterostructures with a Cobalt (II/III) Redox Electrolyte." *ACS Appl. Mater. Interfaces*. 2013, 5, 9872. (DOI: 10.1021/am402344d).

## Conferences

1. Andrés Parra, Erdem Irtem, J.R. Morante and Teresa Andreu. *Cu and Cu<sub>x</sub>O Electrodes for Selective CO<sub>2</sub> Conversion into Hydrocarbons in Different Electrolytes*. Poster session presented at: 2015 E-MRS Spring Meeting & CEOPS Summer School; 2015 May 10<sup>th</sup> to 15<sup>th</sup>; Lille (France).
2. Parra, A.; Fàbrega, C.; Monllor D.; Andreu, T.; Morante, J.R. *Ti-<sub>x</sub>V<sub>x</sub>O<sub>2</sub> nanorod photoanodes for photoelectrochemical devices*. Oral communication presented at: IPS-20, 20<sup>th</sup> International Conference on Photochemical Conversion and Storage of Solar Energy; 2014 July 27<sup>th</sup> – August 1<sup>st</sup>, Berlin (Germany).
3. Parra, A.; Fàbrega, C.; Monllor D.; Andreu, T.; Morante, J.R. *Hierarchical nanostructures of TiO<sub>2</sub> via multistep electrochemical techniques for PEC applications*. Oral communication presented at: XIII Congreso Nacional de Materiales; 2014 June 18<sup>th</sup> – 20<sup>th</sup>, Barcelona (Spain).
4. T. Andreu, M. Manzanares, A. Parra, C. Fàbrega, J.R. Morante. *On the role played by catalytic metallic additives on TiO<sub>2</sub> for the photoreduction of CO<sub>2</sub>*. Oral communication presented at: International Conference on New Advances in Materials Research for Solar Fuels Production; 2013 July, Granada (Spain).
5. Parra, A.; Fàbrega, C.; Andreu, T.; Morante, J.R. *Hierarchical Nanostructures of TiO<sub>2</sub> via Multistep Electrochemical Techniques for PEC Applications*. Oral communication presented at: 2012 MRS

- Spring Meeting - Symp Q: Titanium Dioxide Nanomaterials; 2012 April 13<sup>th</sup>, San Francisco (United States of America).
6. Andreu, T.; Parra, A.; Fàbrega, C.; Ibañez, M.; Nafria, R.; Cabot, A.; Morante, J.R. *How to Boost the Efficiency of CO<sub>2</sub> Photoreduction by Using Bimetallic Catalyst Nanoparticles*. Oral communication presented at: 2012 MRS Spring Meeting - Symp U: Materials for Catalysis in Energy; 2012 April 10<sup>th</sup>, San Francisco (United States of America).
  7. Andreu, T.; Fàbrega, C.; Manzanares, M.; Parra, A.; Morante, J.R. *Strategies for the Enhancement of Carbon Dioxide Solar Photoreduction*. Oral communication presented at: International Conference on Nanostructured Systems for Solar Fuel Production (SolarFuel12); 2012 March 25<sup>th</sup>, Mallorca (Spain).
  8. Fàbrega, C.; Parra, A.; Andreu, T.; Morante, J.R. *Heterostructured Photoanodes Based on Chalcogenides over TiO<sub>2</sub> Nanorods Arrays*. 2011 MRS Fall Meeting - Symp Z: Functional Metal-Oxide Nanostructures; 2011 November 29<sup>th</sup>, Boston (United States of America).
  9. Andreu, T.; Parra, A.; Fàbrega, C.; Ibañez, M.; Nafria, R.; Cabot, A.; Morante, J.R. *Enhanced Photoreduction of CO<sub>2</sub> Using Bimetallic Nanoparticles as Catalyst*. Oral communication presented at: 2011 MRS Fall Meeting - Program - Symp E: Advanced Materials for Solar-Fuel Generation; 2011 November 28<sup>th</sup>, Boston (United States of America).
  10. Parra, A.; Andreu, T.; Morante, J.R. *Enhanced Photoreduction of CO<sub>2</sub> using metallic Nanoparticles*. Oral communication presented at: XXVII Trobades Científiques de la Mediterrània; 2011 September 29<sup>th</sup>, Mahón (Spain).

